

# Physics of Cosmological Reionization and Structure Formation in the Universe

---

By  
**Sourav Mitra**

**Enrolment Number: PHYS08200804002**  
**Harish-Chandra Research Institute, Allahabad**

*A thesis submitted to the*  
*Board of Studies in Physical Sciences*  
*In partial fulfillment of requirements*  
*For the degree of*  
**DOCTOR OF PHILOSOPHY**  
*of*  
**HOMI BHABHA NATIONAL INSTITUTE**



**July, 2013**

---



# **CERTIFICATE**

This is to certify that the Ph.D. thesis titled 'Physics of cosmological reionization and structure formation in the Universe' submitted by Sourav Mitra is a record of bona fide research work done under my supervision. It is further certified that the thesis represents independent work by the candidate and collaboration was necessitated by the nature and scope of the problems dealt with.

Date:

**Dr. Tirthankar Roy Choudhury**

Thesis Adviser



## **STATEMENT BY AUTHOR**

This dissertation has been submitted in partial fulfillment of requirements for an advanced degree at Homi Bhabha National Institute (HBNI) and is deposited in the Library to be made available to borrowers under rules of the HBNI.

Brief quotations from this dissertation are allowable without special permission, provided that accurate acknowledgement of source is made. Requests for permission for extended quotation from or reproduction of this manuscript in whole or in part may be granted by the Competent Authority of HBNI when in his or her judgment the proposed use of the material is in the interests of scholarship. In all other instances, however, permission must be obtained from the author.

Date:

**Sourav Mitra**

Ph.D. Candidate



## **DECLARATION**

This thesis is a presentation of my original research work. Whenever contributions of others are involved, every effort is made to indicate this clearly, with due reference to the literature and acknowledgement of collaborative research and discussions. The work is original and has not been submitted earlier as a whole or in part for a degree or diploma at this or any other Institution or University. This work was done under guidance of Dr. Tirthankar Roy Choudhury, at Harish Chandra Research Institute, Allahabad.

Date:

**Sourav Mitra**

Ph.D. Candidate



*To My Friends & Family ...*



## ACKNOWLEDGEMENTS

It would not have been possible to write this thesis without the help and support of the kind people around me. It is a pleasant aspect that I have now the opportunity to express my gratitude to all of them.

First of all, I would like to convey my sincere thanks and appreciation to my thesis supervisor Dr. Tirthankar Roy Choudhury for his continuous support and patience towards me through my PhD life, not to mention his advice, criticism and unsurpassed knowledge in this subject. Working with him has been a great pleasure and I sincerely hope to do more productive work with him in the future. It has been really a privilege being his student. Thank you Sir for everything.

Besides my supervisor, my earnest thanks goes to Prof. Andrea Ferrara for his insightful comments and timely suggestions. His uncompromising attitude towards the quality of work has always been a source of inspiration for me. Without your immense help this thesis would never have been an enriching experience. Also I would like to thank Prof. Jasjeet Singh Bagla for being with us. His meticulous comments were of enormous help to me. I would take this opportunity to express my deep gratitude to Girish Kulkarni, Jaswant Kumar Yadav, Stefania Pandolfi, Prof. Alessandro Melchiorri, Suman Majumdar and Tapomoy Guha Sarkar for their collaboration on parts of this research. I would also like to thank Anjan Da, it was a great experience to discuss scientific as well as non-scientific problems with you. Special thanks to Prof. Xiaohui Fan and Prof. Jane Charlton for permitting me to use some published figures in this thesis.

I would like to acknowledge the financial, academic and technical support of Harish-Chandra Research Institute (HRI). Thanks to all the academic and non-academic staff of HRI who are giving their best for a smooth working atmosphere.

How can I forget to thank all my HRI friends who made my journey entertaining and amusing with their valuable (!) thoughts? I will never forget how to discuss on pointless and meaningless things for hours over a cup of tea. Thank you Niyogi, Dhiraj, Jonthu, Tarat, Manoj, Rambha, Pandu, Hochi, Satya, Atri Da, JD, Sanjay Da, Mama, Shamik Da, Subho Da and Anirban Da for being with me whenever and for whatever I needed.

Special thanks also to my University friends - Banerjee, Kaka, Jyoti Da, Joy Da, Bagchi, Chiku Da, Arghya Da, Shikhar mama, Bachcha Da and my school friends - Uja, Hodo, Diganta, Gantait and the list goes on!

Not only this thesis, but also my life after school would not have been complete without one person, my best friend - Akash. I am in debt to you throughout the journey of my life. You were with me during the toughest time of my life and you will always remain very close to my heart no matter how far you are. I honestly thank God that He gave you as one of my true friends. I will also be thankful to Akash for introducing me to another beautiful person:

Mr. Abhijit Sengupta. We fondly call him *Kaku*. Your enthusiasm and great interest in Science always surprised me. Sometimes, I wonder how you can manage to keep your desire to know about every little aspect of Physics despite your busy daily schedules. Perhaps, this attitude of yours will always inspire me for higher studies. I have learned so many useful things from you. Akash and *Kaku*, you have helped me a lot to overcome many difficulties which cannot be described in this small acknowledgement. I can even write a whole book about you - love you guys. I would also like to express my deepest appreciation and heartiest thanks to my love - Sanhita. Without your generous and unselfish support, I could not have completed my PhD. Wherever I go, I will always think about you. Thank you so much for not only being my friend, but also for being an intense source of support and inspiration.

Last but not the least, I would like to convey my heartfelt gratitude and love to my parents and my brother to whom I owe my whole life rather than my PhD for their unconditional love, immense support and constant encouragement. I would not have reached anywhere near where I am today without their unrelenting support and patience. I will always consider myself the luckiest person in the world to have such admirable parents and brother. You are and always will be my strongest source of encouragement, inspiration and motivation. I dedicate this thesis to you - my *Maa, Baba* and *Dada*.

---

# CONTENTS

<b>Synopsis</b>	<b>ix</b>
<b>List of Publications</b>	<b>xv</b>
<b>1 Introduction</b>	<b>1</b>
1.1 Cosmological framework . . . . .	2
1.1.1 The expanding universe . . . . .	3
1.1.2 Cosmic inventory: Components of the universe . . . . .	5
1.1.3 The cosmic microwave background . . . . .	6
1.2 Dynamics of structure formation . . . . .	7
1.2.1 Density perturbation . . . . .	7
1.2.2 Linear gravitational growth . . . . .	8
1.2.3 Non-linear evolution . . . . .	11
1.2.4 Fourier analysis of density perturbations . . . . .	13
1.2.5 Non-linear object formation and evolution . . . . .	16
1.3 Galaxy formation and cosmic reionization . . . . .	20
1.3.1 Baryonic structure formation . . . . .	21
1.3.2 Reionization of the IGM . . . . .	25
1.3.3 Observational probes for reionization . . . . .	28
1.3.4 Modelling the IGM and reionization . . . . .	31
<b>2 Model-independent constraints on reionization</b>	<b>37</b>

2.1	Semi-analytical modelling of reionization . . . . .	38
2.1.1	Features of the model . . . . .	38
2.1.2	Data sets and free parameters . . . . .	40
2.1.3	Reionization constraints . . . . .	43
2.2	Principal component analysis . . . . .	45
2.2.1	Motivation . . . . .	46
2.2.2	Brief theory of PCA . . . . .	47
2.3	Constraining reionization scenario using PCA . . . . .	49
2.3.1	Fiducial model and the Fisher matrix . . . . .	49
2.3.2	Optimum number of modes . . . . .	52
2.3.3	Monte-Carlo Markov Chain analysis on PCA modes . . . . .	54
2.4	Discussion and summary . . . . .	59
<b>3</b>	<b>Escape of ionizing radiation from galaxies</b>	<b>61</b>
3.1	Introduction: Challenges for determining escape fraction . . . . .	61
3.2	Luminosity function of ionizing sources . . . . .	63
3.3	Constraining escape fraction and other crucial parameters . . . . .	65
3.4	Conclusion . . . . .	68
<b>4</b>	<b>Reionization and other cosmological parameters</b>	<b>71</b>
4.1	Effects of reionization on cosmological parameter determinations . . . . .	71
4.1.1	Cosmological parameters and different reionization scenarios . . . . .	72
4.1.2	Analysis method and datasets . . . . .	75
4.1.3	Constraints for different parametrization of reionization . . . . .	76
4.1.4	Summary . . . . .	81
4.2	CMB bounds on neutrino mass from reionization . . . . .	81
4.2.1	Cosmological constraints on neutrino masses . . . . .	82
4.2.2	Models of reionization and free parameters . . . . .	83
4.2.3	Effects of reionization on neutrino mass bounds . . . . .	85
4.2.4	Summary . . . . .	90
<b>5</b>	<b>Formation rate of dark matter haloes</b>	<b>93</b>
5.1	Rate of halo formation . . . . .	96
5.1.1	Sasaki prescription: Press-Schechter mass function . . . . .	97
5.1.2	Sasaki prescription: Sheth-Tormen mass function . . . . .	98

---

5.1.3	Excursion set approach to halo formation rate: Press-Schechter mass function . . . . .	100
5.1.4	Excursion set approach to halo formation rate: Sheth-Tormen mass function . . . . .	101
5.2	N-body simulations . . . . .	105
5.3	Results and discussion . . . . .	106
5.3.1	Halo destruction rate efficiency . . . . .	106
5.3.2	Halo formation rate . . . . .	112
5.3.3	Halo survival probability . . . . .	118
5.3.4	Formation time distribution . . . . .	118
5.3.5	Discussion . . . . .	119
5.4	Conclusions . . . . .	120
<b>6</b>	<b>Post-reionization neutral hydrogen distribution</b>	<b>123</b>
6.1	Introduction . . . . .	123
6.2	Simulation and the bias model . . . . .	125
6.3	HI 21-cm angular power-spectrum . . . . .	128
6.4	PCA constraints for the simulated data . . . . .	132
6.5	Results and discussion . . . . .	136
<b>7</b>	<b>Summary and conclusions</b>	<b>141</b>



---

# LIST OF FIGURES

1.1	Typical spectrum of a QSO at $z = 1.34$ . . . . .	29
1.2	Spectra of quasars at redshifts $z > 6$ . . . . .	30
1.3	Comparison of analytical model predictions with observations . . . . .	36
2.1	MCMC constraints for reionization model with chemical feedback . . . . .	44
2.2	The Fisher matrix $F_{ij}$ . . . . .	50
2.3	Eigenvalues and eigenmodes of the Fisher matrix . . . . .	51
2.4	Risk, error and bias . . . . .	53
2.5	MCMC constraints from PCA analysis using WMAP7 data . . . . .	55
2.6	MCMC constraints from PCA analysis using simulated PLANCK data . . . . .	58
3.1	Redshift evolution of $N_{\text{ion}}$ obtained from PCA using WMAP7 data . . . . .	64
3.2	Luminosity function from our model at different redshifts . . . . .	66
3.3	Redshift evolution of the escape fraction $f_{\text{esc}}$ . . . . .	67
4.1	Ionization histories for different best-fit models . . . . .	77
4.2	Constraints for the PC amplitudes . . . . .	80
4.3	Reionization models with zero and non-zero neutrino masses . . . . .	88
5.1	Destruction rate for Press-Schechter mass function . . . . .	102
5.2	Formation rate efficiency for Press-Schechter and Sheth-Tormen mass function . . . . .	104
5.3	Destruction rates computed using different methods for $n = -0.5$ . . . . .	107
5.4	Destruction rates computed using different methods for $n = -1.5$ . . . . .	108

5.5	Destruction rates computed using different methods for $\Lambda$ CDM model . . . . .	109
5.6	Formation rates computed using different methods for $n = -0.5$ . . . . .	110
5.7	Formation rates computed using different methods for $n = -1.5$ . . . . .	111
5.8	Formation rates computed using different methods for $\Lambda$ CDM model . . . . .	113
5.9	Halo survival probability . . . . .	113
5.10	Halo formation epoch distribution . . . . .	114
5.11	Comparison between two different approaches . . . . .	115
5.12	An alternate method for formation rates . . . . .	116
5.13	Ratio of formation rates estimated using two different approaches . . . . .	116
5.14	Formation rates for $\epsilon = 0.1$ . . . . .	117
5.15	Ratio of formation rates for $\epsilon = 0.1$ . . . . .	117
6.1	Simulated power spectra and HI density field . . . . .	126
6.2	Simulated bias function . . . . .	127
6.3	Theoretical 3D HI power spectrum . . . . .	130
6.4	Theoretical angular power spectrum . . . . .	130
6.5	Degraded Fisher matrix $F_{ij}^{deg}$ . . . . .	132
6.6	Eigenvalues of the degraded Fisher matrix . . . . .	135
6.7	Eigenmodes of the degraded Fisher matrix . . . . .	135
6.8	Reconstruction of the constant bias model . . . . .	136
6.9	MCMC constraints of the binned bias function . . . . .	137
6.10	Reconstructed angular power spectrum . . . . .	138
6.11	Reconstructed HI power spectrum . . . . .	138

---

# LIST OF TABLES

2.1	All the parameters for the reionization model with PopII and PopIII stars . . . .	45
2.2	Derived parameters obtained from MCMC analysis for WMAP7 data . . . . .	56
2.3	Errors on the derived parameters from WMAP7 and simulated PLANCK data .	57
3.1	Best-fit values and $2\text{-}\sigma$ limits of $\epsilon_*$ and $f_{\text{esc}}$ . . . . .	67
4.1	Mean and 95% C.L. constraints on all the parameters from reionization . . . .	74
4.2	68% C.L. constraints for different parametrization of reionization . . . . .	76
4.3	Mean values with the 95% C.L. for different models . . . . .	77
4.4	Amplitudes of the principal components . . . . .	79
4.5	Different models of reionization . . . . .	84
4.6	Constraints for all the cosmological and reionization parameters . . . . .	86
4.7	$\epsilon$ parameters for zero and non-zero neutrino masses . . . . .	89
5.1	Simulation description for power law spectrum . . . . .	104
5.2	Simulation description for $\Lambda$ CDM spectrum . . . . .	104
6.1	Fitting parameters for bias function . . . . .	126
6.2	The $2\text{-}\sigma$ errors for various parameters . . . . .	139



---

# SYNOPSIS

Research presented in this thesis follows mainly two areas of Cosmology: (1) semi-analytical modelling of cosmological reionization and comparison with recent observations and (2) formation and evolution of large-scale structures in the Universe. A brief summary of the thesis work is discussed in the following sections. Publications included in this thesis are listed in the final section.

## **Cosmological Reionization**

Reionization is a process whereby hydrogen (and helium) in the Universe is ionized by the radiation from first luminous sources. In the framework of the hot big bang model, the baryonic matter in the Universe is expected to become almost neutral after the recombination epoch at  $z \sim 1100$ . Given the fact (known from observations of quasar absorption spectra) that the Universe is highly ionized at  $z < 6$ , it is crucial to understand as to when and how did the luminous sources reionize the Universe. In the past few years, the understanding of reionization process has become increasingly sophisticated in both the observational and theoretical communities, thanks to the availability of good quality data related to reionization. However, recent studies suggest that reionization process is too complex to be described as a sudden process, in fact observations suggest that the reionization occurred somewhere between  $z \sim 6 - 15$  (for reviews, see Barkana & Loeb 2001; Loeb & Barkana 2001; Wyithe & Loeb 2003; Choudhury & Ferrara 2006b; Choudhury 2009 and the references therein). Furthermore, the physical processes relevant to reionization are so complex that neither the analytical nor the numerical simulations alone can capture the overall picture. Consequently, it is often studied using semi-analytical models of reionization where a large region of parameter space can be explored even with limited computational resources.

## Model-independent Constraints on Reionization

Using a semi-analytical model developed by Choudhury & Ferrara (2005) and Choudhury & Ferrara (2006b), we study the observational constraints on reionization via a principal component analysis (PCA). The advantage of this approach is that it provides constraints on reionization in a model-independent manner (Mortonson & Hu 2008b). Assuming that reionization at  $z > 6$  is primarily driven by stellar sources, we decompose the unknown function  $N_{\text{ion}}(z)$ , representing the number of photons in the IGM per baryon in collapsed objects, into its principal components and constrain the latter using three different data sets - the photoionization rates  $\Gamma_{\text{PI}}$  obtained using Ly $\alpha$  forest Gunn-Peterson optical depth observations and a large set of hydrodynamical simulations (Bolton & Haehnelt 2007), the redshift distribution of Lyman Limit Systems  $dN_{\text{LL}}/dz$  in  $0.36 < z < 6$  (Songaila & Cowie 2010) and the angular power spectra  $C_l$  for TT, TE and EE modes using WMAP7 (Larson et al. 2011) data which seems to contain somewhat more information than taking the electron scattering optical depth  $\tau_{\text{el}}$  as a single data point (Mitra et al. 2011). Using Markov Chain Monte Carlo methods, we find that all the quantities related to reionization can be severely constrained at  $z < 6$  whereas a broad range of reionization histories at  $z > 6$  are still permitted by the current data sets. With the WMAP7 data, we constrain  $0.080 < \tau_{\text{el}} < 0.112$  (95% CL) and also conclude that reionization is 50% complete between  $9.0 < z(Q_{\text{HII}} = 0.5) < 11.8$  (95% CL) and is 99% complete between  $5.8 < z(Q_{\text{HII}} = 0.99) < 10.4$  (95% CL). With the forthcoming PLANCK data (The Planck Collaboration 2006) on large-scale polarization (ignoring effect of foregrounds), the  $z > 6$  constraints will be improved considerably, e.g., the  $2 - \sigma$  error on  $\tau_{\text{el}}$  will be reduced to 0.009 and the uncertainties on  $z(Q_{\text{HII}} = 0.5)$  and  $z(Q_{\text{HII}} = 0.99)$  would be  $\sim 1$  and 3 (95% CL), respectively (Mitra et al. 2012). For more stringent constraints on reionization at  $z > 6$ , one has to rely on data sets other than CMB. Our method will be useful in such case since it can be used for non-parametric reconstruction of reionization history with arbitrary data sets.

## Constraining the escape fraction of ionizing photons

One of the most crucial issues regarding the evolution of intergalactic medium (IGM) and cosmic reionization is the escape fraction,  $f_{\text{esc}}$ , of ionizing photons from high-redshift galaxies. This parameter remains poorly constrained in spite of many theoretical and observational attempts made in past few years (Wood & Loeb 2000; Gnedin 2008; Fernandez & Shull 2011; Haardt & Madau 2011). We propose a novel, semi-empirical approach based on a simultaneous match of the most recently determined Luminosity Functions (LF) of galaxies in the redshift range  $6 \leq z \leq 10$  (Bouwens & Illingworth 2006; Bouwens et al. 2011b; Oesch et al. 2012) with reionization models constrained by a large variety of experimental data. From this procedure we obtain the evolution of the best-fit values of  $f_{\text{esc}}$  along with their  $2 - \sigma$  limits. We find that, averaged over the galaxy population, (i) the escape fraction increases from  $f_{\text{esc}} = 0.068^{+0.054}_{-0.047}$  at  $z = 6$  to  $f_{\text{esc}} = 0.179^{+0.331}_{-0.132}$  at  $z = 8$ ; (ii) at  $z = 10$  we can only put a lower limit of  $f_{\text{esc}} > 0.146$  (Mitra et al. 2013). Thus, although errors are large, there is an indication of a 2.6 times increase

of the average escape fraction from  $z = 6$  to  $z = 8$ .

## Effects of Reionization on Cosmological Parameters

Reionization process could affect the determination of the cosmological parameters. So, we perform an analysis of the WMAP7 data considering physically motivated and viable reionization scenarios with the aim of assessing their effects on cosmological parameter determinations. The main novelties are: (i) the combination of CMB data with astrophysical results from quasar absorption line experiments; (ii) the joint variation of both the cosmological and astrophysical (governing the evolution of the free electron fraction  $x_e(z)$ ) parameters. Including a realistic, data-constrained reionization history in the analysis induces appreciable changes in the cosmological parameter values deduced through a standard WMAP7 analysis (Pandolfi et al. 2011). Particularly noteworthy are the variations in  $\Omega_b h^2 = 0.02258_{-0.00056}^{+0.00057}$  (WMAP7) vs.  $\Omega_b h^2 = 0.02183 \pm 0.00054$  (WMAP7 + ASTRO), and the new constraints for the scalar spectral index, for which WMAP7 + ASTRO excludes the Harrison-Zel'dovich value  $n_s = 1$  at  $> 3\sigma$ . Finally, the e.s. optical depth value is considerably decreased with respect to the standard WMAP7, i.e.  $\tau_{\text{el}} = 0.080 \pm 0.012$ . So we find that the inclusion of astrophysical datasets, allowing to robustly constrain the reionization history, in the extraction procedure of cosmological parameters leads to relatively important differences in the final determination of their values.

## CMB bounds on neutrino mass from reionization

Neutrinos with non-zero mass can have an intense impression on the evolution of our Universe. Rigorous cosmological observations on cosmic microwave background (CMB) anisotropies and the large-scale structures of galaxies thus can be used to put a stronger constraint on the neutrino masses than that achieved from current laboratory experiments (Hu et al. 1998; Hannestad 2003; Gratton et al. 2008; Jose et al. 2011). Seven years of Wilkinson Microwave Anisotropy Probe (WMAP) data presents the upper bound on the sum of neutrino masses as  $\sum m_\nu < 1.3$  eV at 95% confidence limits (CL) (Komatsu et al. 2011), assuming a *sudden* reionization scenario depicted by a single parameter. Another feasible effect that could put an impact on the CMB bounds for neutrino masses is the detailing of reionization scenario (Archidiacono et al. 2010). So, we also try to investigate the possible effects on neutrino mass bound by considering our data-constrained reionization model based on Choudhury & Ferrara (2005, 2006b) and Mitra et al. (2011, 2012) and we find that, a more strict constraint on the neutrino masses can be achieved using this model.

## **Large Scale Structure Formation of the Universe**

Formation of large-scale structures like galaxies is a crucial ingredient of the models of reionization. In the standard, hierarchical, cold dark matter (CDM) paradigm of cosmological structure formation, galaxy formation begins with the gravitational collapse of overdense regions into bound, virialized halos of dark matter (DM). Bound in the potential wells of dark matter halos, baryons proceed to cool, condense, and form galaxies. Understanding the fundamental properties and abundances of these dark matter halos is the first, necessary step in understanding the properties of galaxies. The subject area of formation of galaxies is quite involved in itself dealing with formation of non-linear structures and various processes. In our reionization model described above, galaxy formation is implemented by calculating the mass function of dark matter haloes (number of haloes per unit volume as a function of halo mass) and their formation rates (number of haloes created per unit volume per unit time) and accounting for the baryonic processes like cooling and feedback to populate haloes with galaxies.

### **Mass function and formation rates of dark matter haloes**

We derive an estimate of the rate of formation of dark matter haloes per unit volume as a function of the halo mass and redshift of formation. Analytical estimates of the number density of dark matter haloes are useful in modeling several cosmological phenomena. We develop a new prescription to calculate halo formation rate, using excursion set formalism (Bond et al. 1991; Lacey & Cole 1993) but avoiding the assumption of scale invariance of halo destruction rate efficiency made by Sasaki (Sasaki 1994). Our approach allows us to differentiate between major and minor mergers, as this is a pertinent issue for semi-analytic models of galaxy formation. We compute the formation rate for the Press-Schechter (Press & Schechter 1974) and the Sheth-Tormen (Sheth et al. 2001) mass function and show that the formation rate computed in this manner is positive at all scales (Mitra et al. 2011) unlike the Sasaki prescription where one can get the unphysical results for the Sheth-Tormen mass function. We compare the destruction rate and the halo formation rates computed using the excursion set approach with N-Body simulations (Bagla & Padmanabhan 1997; Bagla et al. 2009). We find that our approach matches well with simulations for all models at all redshifts.

### **Post-reionization Neutral Hydrogen distribution**

Perhaps the most promising prospect of detecting the fluctuations in the neutral hydrogen (HI) density during the reionization era is through the 21-cm emission experiments like GMRT, MWA and LOFAR. Measurement of the spatial distribution of neutral hydrogen via the redshifted 21-cm line promises to revolutionize our knowledge of the epoch of reionization and the first galaxies, and may provide a powerful new tool for observational cosmology from redshifts  $1 < z < 4$  (Mo & White 1996; Wyithe & Loeb 2007b; Datta et al. 2007). Part of this thesis contains a particular topic of this area - constraining large scale HI bias using 21-cm signal from

the post-reionization epoch.

Assuming a background cosmology, the 21-cm emission from neutral hydrogen (HI) in the post-reionization epoch is modelled through (i) a bias function  $b(k, z)$ , which relates HI to the dark matter distribution and (ii) a mean neutral fraction ( $\bar{x}_{\text{HI}}$ ) which sets its amplitude. In this work, we investigate the nature of large scale HI bias. The post-reionization HI is modelled using gravity only N-Body simulations and a suitable prescription for assigning gas to the dark matter halos. Using the simulated bias as the fiducial model for HI distribution at  $z \leq 4$ , we have generated a hypothetical data set for the 21-cm angular power spectrum using a noise model based on parameters of an extended version of the GMRT and we explore the possibility of constraining  $b(k)$  using the Principal Component Analysis (PCA) on this simulated data (Guha Sarkar et al. 2012). We show that our method can be successfully implemented on future observational data sets to constrain  $b(k, z)$  and  $\bar{x}_{\text{HI}}$  and thereby enhance our understanding of the low redshift Universe.



---

# LIST OF PUBLICATIONS

This thesis is mainly based on the following publications:

1. **Mitra, Sourav**; Choudhury, T. Roy; Ferrara, Andrea, *Reionization constraints using principal component analysis*, *MNRAS* **413**, 1569, (2011), arXiv:1011.2213
2. **Mitra, Sourav**; Kulkarni, Girish; Bagla, J. S.; Yadav, Jaswant K., *Formation rates of Dark Matter Haloes*, *BASl* **39**, 563, (2011), arXiv:1103.5828
3. **Mitra, Sourav**; Choudhury, T. Roy; Ferrara, Andrea, *Joint quasar-cosmic microwave background constraints on reionization history*, *MNRAS* **419**, 1480, (2012), arXiv:1106.4034
4. Pandolfi, S.; Ferrara, A.; Choudhury, T. Roy; Melchiorri, A.; **Mitra, Sourav**, *Data-constrained reionization and its effects on cosmological parameters*, *PhRvD* **84**, 123522, (2011), arXiv:1111.3570
5. Guha Sarkar, Tapomoy; **Mitra, Sourav**; Majumdar, Suman; Choudhury, Tirthankar Roy, *Constraining large scale HI bias using redshifted 21-cm signal from the post-reionization epoch*, *MNRAS* **421**, 3570, (2012), arXiv:1109.5552
6. **Mitra, Sourav**; Ferrara, Andrea; Choudhury, T. Roy, *The escape fraction of ionizing photons from high redshift galaxies from data-constrained reionization models*, *MNRAS Letter*, **428**, L1, (2013), arXiv:1207.3803



---

---

# CHAPTER 1

---

## INTRODUCTION

Our universe, after all, is richly textured, with with structures on a vast range of scales; planets orbit stars, stars are collected into galaxies, galaxies are gravitationally bound into clusters, and even clusters of galaxies are found within larger superclusters. Cosmology is basically the study of the universe, or cosmos, regarded as a whole. It deals with distances that are very large, objects that are very big and time-scales that are very long. Although, the rigorous study of cosmos is extremely complicated dealing with the objects ranging from carbonaceous dust grains to quasars, cosmologists often like to think of the universe as a simple place characterized by some basic physical principles. It can be studied by mainly two approaches: observational aspect of cosmology and the theoretical outlook. In fact, this subject is based on the interplay of theory and observations. One could imagine starting from an overview of the observational results and then moving on to their theoretical interpretation.

The primary aim of observational cosmology is to characterize the thermal, chemical, and structural state of the present universe. For the most of history, astronomers have had to rely on light in the visible part of the spectrum in order to study the universe. One of the greatest astronomical achievements of the 20<sup>th</sup> century was the exploitation of the full electromagnetic spectrum for astrophysical measurements. We now have sophisticated instruments capable of making observations of radio waves, microwaves, infrared light, visible light, ultraviolet light, X-rays and gamma rays. We are even entering an epoch where one can go beyond the electromagnetic spectrum and receive information of other types. Over the past few years remarkable discoveries in physics and astronomy have been achieved with enormous implications for cosmology. In particular, the recent experiments measuring anisotropies on the cosmic microwave background (CMB) and the distance-redshift relation in type Ia supernovae (SNIa) have opened a new era in cosmology, sometimes called the golden years or the high-precision era of cosmology. Perhaps the experiment that started this new era was the one performed by the COBE

satellite team in the early 1990's. This experiment, which was a modern version of that performed by Penzias and Wilson, for the first time revealed that the universe was almost, but not completely homogeneous and isotropic. The other more recent cosmological probes (CP), like BOOMERANG<sup>1</sup> (Balloon Observations Of Millimetric Extragalactic Radiation ANd Geophysics), MAXIMA<sup>2</sup> (Millimeter Anisotropy eXperiment IMaging Array), WMAP<sup>3</sup> (Wilkinson Microwave Anisotropy Probe) and PLANCK<sup>4</sup>, not only confirmed with a great accuracy some of the theoretical predictions of the standard Big Bang model (SBB), but also opened the possibility of testing theories and scenarios of the very early universe. The existence of the components of the universe were originally inferred from a variety of measurements ranging from the observed fluxes from distant supernovae to the spatial correlations between galaxy positions. However, the last few years has seen the emergence of the study of the CMB photons as the dominant tool for measuring precisely the densities of each component. Such discoveries have not only corroborated several theoretical predictions and put stringent bounds on many cosmological models, but also be able to answer many of the unknown puzzles of modern cosmology.

The aim of theoretical cosmology is to explain the present state of the universe in terms of the conditions in the “early universe”. The high precision measurements of most of the cosmological parameters help the theoretical cosmologists to develop the so called “standard model” of cosmology which is consistent with all the observations. Almost a century has passed since the beginning of this era, and in the intervening years increasingly accurate predictions of this model of the cosmos, supplemented only by the presence of a dark matter component, have been confronted with, and spectacularly passed, a host of detailed tests - the existence of the CMB; the abundances of the light elements through Big Bang Nucleosynthesis (BBN); the formation of structure under gravitational instability; the small temperature anisotropies in the CMB; the structure of gravitational lensing maps; and many more. Many of these tests are highly nontrivial and provide remarkable support for the overall big bang model.

In this chapter, we shall introduce the standard Lambda Cold Dark Matter ( $\Lambda$ CDM) cosmological model in order to study the nature and components of the universe, evolution of density perturbation and the structure formation. We shall also briefly review the key observations related to this subject towards the end of this chapter.

## 1.1 Cosmological framework

In this picture, the universe was originated from a point-like singularity, the “Big Bang”, of infinite density and temperature about 13.7 billion years ago. This was immediately followed by a period of accelerated expansion called inflation that lasted for just about  $10^{-34}$  s. At the end of

---

<sup>1</sup><http://www.astro.caltech.edu/lgg/boomerang/>

<sup>2</sup><http://cosmology.berkeley.edu/group/cmb/>

<sup>3</sup><http://wmap.gsfc.nasa.gov/>

<sup>4</sup><http://www.esa.int/SPECIALS/Planck/index.html>

inflation, the universe was highly homogeneous on large scales. This large scale homogeneity and isotropy are the most important feature of our universe. This feature ensures that observations made from our single vantage point are representative of the universe as a whole and can therefore be legitimately used to test cosmological models. For most of the twentieth century, the homogeneity and isotropy of the universe had to be taken as an assumption, known as the ‘‘Cosmological Principle.’’ However, redshift surveys suggest that the universe is homogeneous and isotropic on scales above 100 Mpc (1 Mpc  $\simeq 3.26 \times 10^6$  light years  $\simeq 3.08 \times 10^{24}$  cm); on smaller scales there exist large inhomogeneities, such as galaxies, clusters and superclusters. The standard big bang model accommodates most these known facts regarding our universe. In particular, the success of this big bang model rests on three major observational pillars: the Hubble diagram exhibiting expansion; light element abundances from BBN and the blackbody radiation left over from the first few hundred thousand years known as the CMB. As a matter of fact, big bang is the most successful model of cosmology till now. In this section, we introduce the basic elements of this standard hot big bang model which will help us to deal with the evolution of inhomogeneities in density field and with other established facts.

### 1.1.1 The expanding universe

We have solid evidence that the universe is expanding which means that at early epoch the distance between us and distant galaxies was smaller than it is now. It allows us to introduce the scale factor  $a$ , whose present value is set to one and at earlier times it was smaller than it is today. We can picture this expansion as following. The comoving distance between two points in the universe remains constant as the universe expands, but the physical distance, which is proportional to the comoving distance times the scale factor, gets larger as time evolves. In addition to the scale factor and its evolution, the smooth universe is also characterized by its geometry; it can be flat, open or closed universe.

In General Relativity, kinematics in the most general isotropic and homogeneous space is described by the Friedman-Robertson-Walker line element -

$$ds^2 = dt^2 - a^2(t) \left[ \frac{dR^2}{1 - kR^2} + R^2 (d\theta^2 + \sin^2 \theta d\phi^2) \right] \quad (1.1)$$

where  $a(t)$  is the cosmic scale factor,  $(R, \theta, \phi)$  are spherical comoving coordinates and  $k$  determines the geometry or curvature of the space; it is positive in a closed Universe, zero in a flat Universe, and negative in an open Universe. Observers at rest remain at rest, at fixed  $(R, \theta, \phi)$ , with their physical separation increasing with time in proportion to  $a(t)$ . Thus, to understand the history of the universe, we must determine the evolution of the scale factor  $a$  with cosmic time  $t$ , that is, how the scale factor increases as the universe ages. The dependence of  $a$  on  $t$  is determined by the energy density in the universe. At early times, one form of energy, radiation, dominates resulting  $a \propto t^{1/2}$ , while at later epoch, non-relativistic matter accounts for most of the energy density resulting  $a \propto t^{2/3}$ . In case for the cosmological constant dominated universe, the energy density is constant and the scale factor grows exponentially  $a \propto \exp(\sqrt{\Lambda/3}t)$ .

To quantify the change in the scale factor and its relation to the energy, it is very useful to define the Hubble rate or the Hubble parameter

$$H(t) \equiv \frac{da/dt}{a} \quad (1.2)$$

which measures how rapidly the scale factor changes. Thus a powerful test of the cosmology is to measure the Hubble rate today,  $H_0$ , and the age of the universe today. In a flat, matter-dominated universe, the product  $H_0 t_0$  equals to  $2/3$ . The expansion rate is a measure of how fast the universe is expanding, determined by measuring the velocities of distant galaxies and dividing by their distance from us. So the expansion is often written in units of velocity per distance. Present measure of the Hubble parameter is parameterized by  $h$  defined via

$$H_0 = 100h \text{ km sec}^{-1}\text{Mpc}^{-1} \quad (1.3)$$

Current measurements by Nine years of Wilkinson Microwave Anisotropy Probe (WMAP9) set  $h = 0.70 \pm 0.02$  (Hinshaw et al. 2012) and new PLANCK data release sets that value to  $h = 0.67 \pm 0.01$  (Ade et al. 2013b).

More generally, the evolution of the scale factor is determined by the Friedmann equation (Weinberg 1972, 2008; Kolb & Turner 1990)

$$H^2(t) = \frac{8\pi G}{3}\rho - \frac{k}{a^2} \quad (1.4)$$

which relates the expansion of the universe to its matter-energy content. For each component of the energy density  $\rho$ , with an equation of state  $p = p(\rho)$ , the density varies with  $a(t)$  according to the equation of energy conservation

$$d(\rho a^3) = -pd(a^3) \quad (1.5)$$

So the basic idea is that given  $p$  as a function of  $\rho$ , we can solve equation (1.5) to find  $\rho$  as a function of  $a$ . We then use this in equation (1.4) to determine  $a$  or  $H$  as a function of  $t$ , and thus the Friedmann metric. But before that, let us now introduce one of the most useful quantities in cosmology which we will encounter later very frequently - the cosmological redshift.

As the universe is expanding, the galaxies are moving away from each other and we therefore see them receding from us. The wavelength of light or sound emitted from a receding object is stretched out so that the observed wavelength ( $\lambda_{\text{obs}}$ ) is larger than the emitted one,  $\lambda_{\text{emit}}$ . We define this stretching factor as the cosmological redshift  $z$ :

$$1 + z \equiv \frac{\lambda_{\text{obs}}}{\lambda_{\text{emit}}} = \frac{1}{a} \quad (1.6)$$

Hubble (1920) interpreted the redshifts he observed as instances of the Doppler effect; for recession velocities  $v \ll c$ , we get  $z = v/c \propto d$ . The measured constant of proportionality in

the this relation between  $v$  and  $d$  is basically the Hubble's constant  $H_0$ , that is,  $v = H_0 d$ , or  $z = H_0 d/c$ . This linear relationship between redshift and distance breaks down for larger distances and higher velocities (see Weinberg 1972). Since the redshift is a more easily measured quantity than distance itself, it is commonly used by cosmologists to parameterize the distance to a galaxy or other sources.

### 1.1.2 Cosmic inventory: Components of the universe

To solve equation (1.4), one needs to know about the different constituents of matter which can contribute to the density  $\rho$ , and how they evolve in time. We can now tackle this question quantitatively by considering the different components of the universe.

- One of the components contributing to this density is Hot Matter or the radiation. for relativistic matter like radiation, we know  $p = \rho_r/3$ . Using equation (1.5), we get  $\rho_r \propto a^{-4}$ .
- The density is also contributed by visible, non-relativistic, baryonic matter with density  $\rho_b$ . But unfortunately, models with just radiation and baryonic matters are in strong disagreement with observations, which leads to postulate the existence of a pressure-less ( $p = 0$ ) non-baryonic “dark matter” which does not couple with radiation and has a density  $\rho_{\text{DM}}$ . So the total density for the non-relativistic matter is  $\rho_m = \rho_{\text{DM}} + \rho_b$ . Similarly, equation (1.5) gives the evolution of the form  $\rho_m \propto a^{-3}$ .
- Along with the dark matter, it is also necessary to propose an exotic form of matter having density  $\rho_\Lambda$  with  $p \approx -\rho_\Lambda$ . This is known as “dark energy”<sup>5</sup>. The simplest form of it is the well-known cosmological constant ( $p = -\rho_\Lambda$ , hence  $\rho_\Lambda = \text{constant}$ ).

Using these, our Friedmann equation [equation (1.4)] now becomes

$$\frac{H(t)}{H_0} = \left[ \frac{\Omega_m}{a^3} + \Omega_\Lambda + \frac{\Omega_r}{a^4} + \frac{\Omega_k}{a^2} \right]^{1/2} \quad (1.7)$$

Where  $\Omega_m$ ,  $\Omega_\Lambda$  and  $\Omega_r$  denotes the present contributions to  $\Omega$ ; defined as the ration of the total density to the critical density i.e.  $\Omega \equiv \rho/\rho_c$  with the critical density  $\rho_c(t) \equiv 3H^2(t)/(8\pi G)$ ; from matter (including cold dark matter as well as a contribution  $\Omega_b$  from baryons), vacuum density (cosmological constant), and radiation, respectively. The quantity  $\Omega_k$  is defined as  $\Omega_k \equiv 1 - (\Omega_m + \Omega_\Lambda + \Omega_r)$ . One particular cosmological model with  $\Omega_m = 1$ ,  $\Omega_\Lambda = \Omega_r = \Omega_k = 0$  is very simple and is known as *Einstein-de Sitter model*.

According to the current WMAP nine-year observations, the most favored cosmological model (flat  $\Lambda$ CDM model) has  $\Omega_b = 0.0463 \pm 0.0024$ ,  $\Omega_{\text{DM}} = 0.233 \pm 0.023$ ,  $\Omega_\Lambda = 0.721 \pm$

<sup>5</sup>Although the dark matter and dark energy are the two most dominant components of the energy density in the universe, it is very unfortunate that we still do not have laboratory evidence for their existence

0.025 and  $h = 0.700 \pm 0.022$  (Hinshaw et al. 2012) and a more precise measurement from the recent PLANCK CMB data for temperature power spectrum with a WMAP polarization low-multipole likelihood (Bennett et al. 2012) at  $l \leq 23$  suggests those values to be  $\Omega_b h^2 = 0.02205 \pm 0.00028$ ,  $\Omega_m h^2 = 0.1426 \pm 0.0025$ ,  $\Omega_\Lambda = 0.685_{-0.016}^{+0.018}$  and  $h = 0.673 \pm 0.012$  (Ade et al. 2013b).

### 1.1.3 The cosmic microwave background

Before making further progress, let us spend some time to briefly discuss about one of the greatest discoveries in cosmology of the last century. In the standard hot Big Bang model, the universe initially was very hot and the energy density was dominated by radiation. At redshift  $z \sim 3500$  the transition to matter domination occurs. The universe remains hot enough that the gas is ionized and electron-photon scattering effectively couples the matter and radiation. At  $z \sim 1100$  or when the universe was 300,000 years old, the temperature drops sufficiently low (below 3000 K) that protons and electrons recombine to form neutral hydrogen. Since then the photons decouple and travel freely through space. These photons are observed today as cosmic microwave background (hereafter CMB). When we observe them today, they literally come from the earliest moments of time. They are therefore the most powerful probes of the early universe.

The discovery of the cosmic microwave background radiation (CMBR) established that the early universe was hot as well as dense. The key to this argument is the observed blackbody or thermal spectrum of this radiation. Let us ask what happens to a blackbody radiation field if we extrapolate backwards in time to an epoch when the scale factor  $a$  was smaller i.e.  $z > 0$ . The wavelength of all photons is decreased proportionally to  $a$  or  $(1+z)^{-1}$ . The Planck function, however, depends only on the product of the wavelength and temperature  $\lambda T_{\text{CMB}}$ . It follows that the spectrum of the radiation was also blackbody in the past, but the temperature was higher by a factor  $1 + z$  (see Weinberg 1972; Partridge 1995; Durrer 2008)

$$T_{\text{CMB}}(z) = T_0(1 + z) \tag{1.8}$$

where  $T_0$  is the present temperature of the CMBR, approximately 2.73 K. Knowing the present value of the temperature, we can calculate the temperature at any earlier epoch. For instance, at  $z > 1100$ , the temperature was  $> 3000$  K, sufficient to ionize the atomic hydrogen. At more larger redshifts, corresponding to the earlier times in the history of the expanding universe, the temperature was even greater. However, the strict linear dependence of  $1 + z$  and  $T_{\text{CMB}}$  breaks down at higher temperatures, where the number of light particle species goes up (see Kolb & Turner 1990).

## 1.2 Dynamics of structure formation

So far, we have discussed about the underlying cosmology of Hot Big Bang model and its successes in describing the universe as whole. The basic concept has been the cosmological principle, requiring that the universe be homogeneous and isotropic, and we have seen how this persuades to an explanation for the cosmic microwave background. However, although this cosmological principle is valid for studying the universe as a whole, we know that it does not hold perfectly. The nearby universe is highly inhomogeneous, being made up of stars, planets and galaxies. Attempting to explain these observed structures perhaps is the most active research area in modern cosmology. The existence of these cosmological structures tells us something important about the initial conditions of the big bang, and about the physical processes that have operated subsequently. In this section, we will deal with the gravitational and other processes that are relevant to structure formation and apply these ideas to large-scale structure, galaxy formation etc.

### 1.2.1 Density perturbation

The basic aim of studying cosmological inhomogeneities is to understand the processes that caused the universe to depart from uniform density. Two most promising existing ideas for how this could have happened are either through the amplification of quantum zero-point fluctuations during an inflationary era, or through the effect of topological defects formed in a cosmological phase transition (for details, see Peacock 1999). Unfortunately, neither of these ideas can yet be regarded as established, but it is quite impressive to see that with help of these ideas we are able to contemplate the observational consequences of physical processes that occurred at such remote energies.

However, gravitational instability is a powerful idea, easy to understand, and most likely responsible for the structures in our universe. As time evolves, matter accumulates in initially overdense regions. It doesn't matter how small the initial overdensity was (typically, the overdensity was of the order 1 part in  $10^5$ ); eventually enough matter will be attracted to the region to form galaxies, clusters etc. The first task is to develop the mathematical machinery capable of describing the growth of these structures.

In a universe made of non-baryonic dark matter, baryons and radiation, we need to discuss each component separately. The simplest of the three components is the dark matter, which is collisionless and affected only by gravity. The scales, where formation of structures occurs, are much smaller than the Hubble length  $d_H(z)$ , defined as  $d_H(z) = c/H(z)$ . For such scales, one can neglect the relativistic effects and hence a simple Newtonian treatment can be applied to study the physics of the density perturbation and related quantities. We can treat the dark matter and baryons as fluids and their properties can be governed by the non-relativistic equations of fluid dynamics. In the fluid limit, we can ignore the velocity dispersion of the dark matter particles, and there will be no effective pressure term in the equations. If the velocity dispersion

is important, there will arise an effect called *free streaming* (see Padmanabhan 1993).

A linear solution for how the matter in the expanding universe behaves to its own self-gravity can be found by expressing the equations of motion in terms of a dimension-less density perturbation field  $\delta$ :

$$\delta(\mathbf{x}) \equiv \frac{\rho(\mathbf{x}) - \bar{\rho}}{\bar{\rho}} \quad (1.9)$$

where,  $\rho(\mathbf{x})$  is the density of the ideal pressureless fluid of particles each of which is at  $\mathbf{x}$ , and  $\bar{\rho}$  is the mean fluid density. We will see that, when this density contrast  $\delta$  is small, it is possible to linearize the equations in  $\delta$  and obtain the solutions describing the growth of linear perturbation. In fact, this is a valid approximation for a considerable period of time as the density contrasts are expected to be small in the early universe. In the non-linear regime, where  $\delta \gg 1$ , it turns out that solving the equations in such a case becomes extremely non-trivial for both dark matter and baryons, and they have to be integrated numerically. However, by introducing some simplified ansatz one can tackle this difficulty and can gain some physical insights regarding the dynamics by comparing with the exact numerical results. In the following sections, we will study the perturbations of non-baryonic dark matter, baryons and radiation independently and as well as taking the mixture of them within a linear approximation. Then, with help of some simplified assumptions (e.g. spherical symmetry), we will briefly mention about the non-linear scenarios, when density contrast is comparable with unity.

## 1.2.2 Linear gravitational growth

We start by writing down the fundamental equations describing the fluid motion (non-relativistic case):

$$\begin{aligned} \text{Euler :} & \quad (\partial/\partial t + \mathbf{v} \cdot \nabla) \mathbf{v} = -\nabla p/\rho - \nabla\Phi \\ \text{Energy :} & \quad (\partial/\partial t + \mathbf{v} \cdot \nabla) \rho = -\rho \nabla \cdot \mathbf{v} \\ \text{Poisson :} & \quad \nabla^2 \Phi = 4\pi G \rho \end{aligned} \quad (1.10)$$

where  $\nabla$  is the spatial gradient operator with respect to the proper coordinates  $\mathbf{x}$ ,  $\rho(t, \mathbf{x})$  and  $p(t, \mathbf{x})$  are the fluid density and pressure respectively,  $\mathbf{v}(t, \mathbf{x}) \equiv d\mathbf{x}/dt$  is the proper velocity, and the quantity  $\Phi(t, \mathbf{x})$  is the gravitational potential. We now produce the linearized equation of motion by taking terms of first order in perturbations about a homogeneous background of  $[\rho_0; \mathbf{v}_0; p_0; \Phi_0]$ :  $\rho = \rho_0 + \delta\rho$ ,  $\mathbf{v} = \mathbf{v}_0 + \delta\mathbf{v}$ ,  $p = p_0 + \delta p$  and  $\Phi = \Phi_0 + \delta\Phi$ . Here note that,  $\mathbf{v}_0$  is nothing but the Hubble expansion  $H\mathbf{x}$ . When dealing with the time derivatives of perturbed quantities, we can always replace  $(\partial/\partial t + \mathbf{v} \cdot \nabla)$  by  $d/dt$ , which is the simple time derivative for an observer comoving with the unperturbed expansion of the universe. After linearizing the

equations, we then can write

$$\begin{aligned}\frac{d}{dt}\delta\mathbf{v} &= -\frac{\nabla\delta p}{\rho_0} - \nabla\delta\Phi - (\delta\mathbf{v} \cdot \nabla)\mathbf{v}_0 \\ \frac{d}{dt}\delta &= -\nabla \cdot \delta\mathbf{v} \\ \nabla^2\delta\Phi &= 4\pi G\rho_0\delta\end{aligned}\tag{1.11}$$

where we define the fractional density perturbation  $\delta \equiv \delta\rho/\rho_0$ .

However, the above equations of motion are written in Eulerian coordinates, where the proper length units are used and the Hubble expansion is explicitly present through the velocity  $\mathbf{v}_0$ . An alternative approach is to use the *comoving coordinates*; these label observers who follow the Hubble expansion in an unperturbed universe. Comoving spatial coordinates  $\mathbf{r}(t)$  can be formed by simply dividing the Eulerian coordinates by the scale factor  $a(t)$ :

$$\begin{aligned}\mathbf{x}(t) &= a(t)\mathbf{r}(t) \\ \delta\mathbf{v}(t) &= a(t)\mathbf{u}(t)\end{aligned}\tag{1.12}$$

where  $\mathbf{u}$  is the comoving equivalent of peculiar velocity  $\delta\mathbf{v}$ . Also the spatial derivatives can be now translated in terms of comoving coordinates in a similar manner:  $\nabla_x = \nabla_r/a$ . For simplicity, we will write  $\nabla_r$  as only  $\nabla$ , keeping in mind that the spatial derivatives are now with respect to comoving coordinates. Then the linearized equations for conservation of momentum and matter, experienced by observers moving with the Hubble flow, can be written in comoving coordinates as

$$\begin{aligned}\frac{d}{dt}\mathbf{u} + 2H\mathbf{u} &= -\frac{\nabla\delta p}{\rho_0} - \frac{\nabla\delta\Phi}{a^2} \\ \frac{d}{dt}\delta &= -\nabla \cdot \mathbf{u} \\ \nabla^2\delta\Phi &= 4\pi G\rho_0 a^2\delta\end{aligned}\tag{1.13}$$

The term  $\nabla\delta\Phi/a$  is basically the peculiar gravitational acceleration. But we still have three equations and four unknown variables  $\delta$ ,  $\mathbf{u}$ ,  $\delta\Phi$  and  $\delta p$ . So we need an equation of state in order to solve this system, and this may be specified in terms of the sound speed  $c_s^2 \equiv \partial p/\partial\rho$ . To make further progress, think of a plane-wave disturbance  $\delta \propto e^{-i\mathbf{k}\cdot\mathbf{r}}$ , where  $\mathbf{k}$  is a comoving wavevector. Then we can simplify the equation for the amplitude of  $\delta$  by eliminating  $\mathbf{u}$ :

$$\frac{d^2\delta}{dt^2} + 2H\frac{d\delta}{dt} = \delta \left( 4\pi G\rho_0 - \frac{c_s^2 k^2}{a^2} \right)\tag{1.14}$$

This is the equation that governs the gravitational amplification of density perturbations.

There is a critical proper wavelength at which we switch from the possibility of exponential growth for long-wavelength modes to standing sound waves (oscillatory solution) at short

wavelengths. This length is known as *Jeans length* and defined as

$$\lambda_J = c_s \sqrt{\frac{\pi}{G\rho}} \quad (1.15)$$

This essentially denotes the scale at which sound waves can cross an object in about the time needed for gravitational free-fall collapse.

Let us now see what happens to these equations at early enough times when the universe was radiation dominated ( $p = \rho/3$ ;  $c_s = 1/\sqrt{3}$ ). To treat this problem accurately, one has to apply the full general relativity perturbation theory. However, as the fields are still weak, it is possible to generate the results using special relativity fluid mechanics and Newtonian gravity with a relativistic source term (see Peacock 1999). To keep this analysis simple, assume that the accelerations due to pressure gradients are negligible in comparison with gravitational accelerations (i.e.  $\lambda \gg \lambda_J$ ). Then the basic set of equations will be

$$\begin{aligned} \text{Euler :} & \quad (\partial/\partial t + \mathbf{v} \cdot \nabla) \mathbf{v} = -\nabla\Phi \\ \text{Energy :} & \quad (\partial/\partial t + \mathbf{v} \cdot \nabla) (\rho + p) = \partial p/\partial t - (\rho + p)\nabla \cdot \mathbf{v} \\ \text{Poisson :} & \quad \nabla^2\Phi = 4\pi G(\rho + 3p) \end{aligned} \quad (1.16)$$

It is then easy to linearize these equations as before, and after that, the evolution equation for  $\delta$  will be

$$\frac{d^2\delta}{dt^2} + 2H\frac{d\delta}{dt} = \frac{32\pi}{3}G\rho_0\delta \quad (1.17)$$

so the net result of all the relativistic corrections is a driving term on the right-hand side of this equation, and it is a factor  $8/3$  higher than in the matter-dominated case. In both matter and radiation-dominated universes with  $\Omega = 1$ , we can easily get the solutions for  $\delta(t)$ . The equations for  $\delta$ , in general, has two independent solutions, only one of which grows with time. For the ‘‘growing mode’’, the solutions for matter and radiation-dominated cases can be combined rather conveniently using the *conformal time*  $\eta \equiv \int dt/a$  and we can then get  $\delta \propto \eta^2$ .

It is also interesting to consider the growth of matter perturbations in universe with non-zero vacuum energy. For this general scenario, we can get two linearly independent solutions for  $\delta$  as:

$$\begin{aligned} \text{growing mode :} & \quad \delta \propto H(a) \int_0^a \frac{da}{H^3(a)a^3} \\ \text{decaying mode :} & \quad \delta \propto H(a) \end{aligned} \quad (1.18)$$

where  $H(a)$  is nothing but the Hubble parameter. For structure formation studies, the decaying solution is of no use as it will be dominated by the growing mode solution at the epochs of interest. The right hand side of the above solutions of  $\delta$  for growing mode is also known as *growth factor*  $D(a)$ . The growth factor in the matter-dominated era is given by (Peebles 1980)

$$D(a) \propto \frac{(\Omega_\Lambda a^3 + \Omega_k a + \Omega_m)^{1/2}}{a^{3/2}} \int_0^a \frac{a^{3/2} da}{(\Omega_\Lambda a^3 + \Omega_k a + \Omega_m)^{3/2}} \quad (1.19)$$

where we have neglected  $\Omega_r$  in the matter-dominated regime. In the Einstein-de Sitter model, the growth factor is simply proportional to  $a(t)$ .

We are often concerned about the evolution of perturbations in a universe that contains several distinct components - dark matter, radiation and baryons. It is easy to treat such composite system if only gravity is important (i.e. for large wavelength). Let us first take the mixture of pressureless matter and radiation. They respond to gravity in different ways. The coupled perturbation equations will be

$$L \begin{pmatrix} \delta_m \\ \delta_r \end{pmatrix} = 4\pi G \begin{pmatrix} \rho_m & 2\rho_r \\ 4\rho_m/3 & 8\rho_r/3 \end{pmatrix} \begin{pmatrix} \delta_m \\ \delta_r \end{pmatrix} \quad (1.20)$$

where the operator  $L \equiv \partial^2/\partial t^2 + 2H\partial/\partial t$ . Solutions to these equations are simple if the matrix has time-independent eigenvectors. In fact, one of these eigenmodes is time independent and known as *adiabatic mode* in which  $\delta_r = 4\delta_m/3$  at all times. The other perturbation mode is called *isocurvature mode* as it corresponds to  $\delta\rho/\rho \rightarrow 0$  at  $t \rightarrow 0$ .

Now take the case for dark matter and baryons together. As both of these components have the same equation of state, we can write

$$L \begin{pmatrix} \delta_b \\ \delta_{\text{DM}} \end{pmatrix} = \frac{4\pi G\rho}{\Omega} \begin{pmatrix} \Omega_b & \Omega_{\text{DM}} \\ \Omega_b & \Omega_{\text{DM}} \end{pmatrix} \begin{pmatrix} \delta_b \\ \delta_{\text{DM}} \end{pmatrix} \quad (1.21)$$

where  $\delta_{\text{DM}}(t)$  and  $\delta_b$  are the perturbations in the dark matter and baryons respectively. Both of the eigenvectors are time independent and can be solved easily in the large scale limit, where pressure effects are negligible. In this case, if we set up a perturbation with  $\delta_b = 0$ , this mixture of the eigenstates will quickly evolve to be dominated by the fastest-growing mode with  $\delta_b = \delta_{\text{DM}}$  and the baryonic matter falls into the dark matter potential wells. However, this is the solution on large scales, with negligible effects of pressure. On the small scales, the effect of pressure will prevent the baryons from continuing to follow the dark matter. One has to add the pressure term to the coupled equations and the solutions are slightly more complicated for this case. We get an oscillatory behavior in this solution and this holds as long as pressure forces continue to be important. We shall study this case later in Section 1.3.1.

### 1.2.3 Non-linear evolution

The equations of motion we dealing with are non-linear, and in the previous section we have only solved them in the limit of linear perturbations. The exact evolution of the density field is usually performed by a rigorous *N-body simulation*, in which the density fields are represented by the sum of a set of fictitious discrete particles. The basic idea for this simulation is as follows. With some initial conditions, the equations of motion for each particles are solved for the present gravitational field due to all other particles. We find the change in particle positions and velocities over some small time gap, then we let the particles move and accelerate and

finally re-calculate the gravitational field to start a new iteration. Although the full development of the gravitational instability cannot be solved without the  $N$ -body techniques, there are few useful ideas and approximations that help us to understand the scenario.

One of them is the *Zeldovich approximation*. In this method, we work out the initial displacement of the particles under the assumption that they continue to move in this initial direction. The proper coordinates of a particle under consideration is

$$\mathbf{x}(t) = a(t)\mathbf{q} + b(t)\mathbf{f}(\mathbf{q}) \quad (1.22)$$

This is like the Hubble expansion with some perturbation, which will become insignificant as  $t \rightarrow 0$ . Therefore the coordinates  $\mathbf{q}$  is nothing but the usual comoving coordinates at  $t = 0$ .  $\mathbf{f}(\mathbf{q})$  is the time-independent displacement field and  $b(t)$  is some the scaling function. The coordinate  $\mathbf{x}$  is known as the *Eulerian position*, and  $\mathbf{q}$  the *Lagrangian position*.

Now, if the initial unperturbed density is  $\rho_0$  (which is independent of  $\mathbf{q}$ ), then the conservation of mass implies that the perturbed density in Eulerian coordinate will be (Padmanabhan 1993)

$$\rho(\mathbf{x}, t)d^3\mathbf{x} = \rho_0 d^3\mathbf{q} \quad (1.23)$$

Therefore using the Jacobian of the transformation between  $\mathbf{x}$  and  $\mathbf{q}$ , we get (Peacock 1999)

$$\rho(\mathbf{x}, t) = \rho_0 \left[ \left(1 - \frac{b}{a}\alpha\right) \left(1 - \frac{b}{a}\beta\right) \left(1 - \frac{b}{a}\gamma\right) \right]^{-1} \quad (1.24)$$

where  $(-\alpha, -\beta, -\gamma)$  are the eigenvalues of *strain tensor* or *deformation tensor*  $\partial f_i / \partial q_j$ . Collapse therefore takes place first along the axis corresponding to the largest negative eigenvalue, leading to a flattened structure known as *pancakes*. Here we have assumed that the strain tensor is symmetric, so that it is easy to calculate the Jacobian in a new coordinate system where this tensor is diagonal. The displacement field is then irrotational (in other word, the rotational part of this field decays down in an expanding universe), so to make this obvious, one can write it in terms of a potential as

$$\mathbf{f}(\mathbf{q}) = \nabla\psi(\mathbf{q}) \Rightarrow \frac{\partial f_i}{\partial q_j} = \frac{\partial^2\psi}{\partial q_i\partial q_j} \quad (1.25)$$

After linearizing equation (1.24), we can get the expressions for the density and velocity perturbations:

$$\begin{aligned} \delta &= -\frac{b}{a}(\alpha + \beta + \gamma) = -\frac{b}{a}\nabla \cdot \mathbf{f} \\ \mathbf{u} &= \frac{1}{a} \left( \dot{\mathbf{x}} - \frac{\dot{a}}{a}\mathbf{x} \right) = \left( \frac{\dot{b}}{a} - \frac{\dot{a}b}{a^2} \right) \mathbf{f} \end{aligned} \quad (1.26)$$

Using the Friedmann equation, this gives

$$\frac{\ddot{b}}{b} = -\frac{2\ddot{a}}{a} = \frac{8\pi G\rho_0}{3} \quad (1.27)$$

which yields the growing mode solution  $b \propto t^{4/3}$  for  $\Omega = 1$ . From the linearized density relation, one can also relate  $b$  as  $b(t) = a(t)D(t)$ , where  $D(t)$  is the usual growth function. However, this approximation fails after the shells of matter start crossing each other. In that case, one must take a full non-linear gravitational treatment which we shall briefly mention later in Section 1.2.5.

### 1.2.4 Fourier analysis of density perturbations

So far, we have seen how gravitational instability is expected to produce patterns of inhomogeneity in the universe, with a characteristic dependence on the precise matter content. In this section we will see how these ideas can be used to study the statistics for spatial distribution of the perturbations at different scales.

In cosmology, it is often convenient to assume the initial linear perturbation field to be a Gaussian random field, and can be described in Fourier space, in terms of Fourier components

$$\delta(\mathbf{k}, z) = \int d^3x \delta(\mathbf{x}, z) e^{-i\mathbf{k}\cdot\mathbf{x}} \quad (1.28)$$

Now, the most important quantity regarding the Fourier technique is the *correlation function* and is defined as

$$\xi(\mathbf{r}, z) \equiv \langle \delta(\mathbf{x}, z) \delta(\mathbf{x} + \mathbf{r}, z) \rangle \quad (1.29)$$

The angle brackets denotes averaging over normalization volume  $V$ . Now, let us introduce another important quantity known as the *power spectrum*  $P(k, z)$ , which is basically the Fourier transform of the correlation function in  $k$ -space, and is defined as

$$\langle \delta(\mathbf{k}, z) \delta(\mathbf{k}', z) \rangle \equiv (2\pi)^3 P(k, z) \delta_D(\mathbf{k} - \mathbf{k}') \quad (1.30)$$

where,  $\delta_D$  is the usual *Dirac delta function*. Note that, due to the isotropy of background universe, the power spectrum is only a function of the magnitude of  $\mathbf{k}$ . So the correlation function now becomes

$$\begin{aligned} \xi(r, z) &= \int \frac{d^3k}{(2\pi)^3} P(k, z) e^{-i\mathbf{k}\cdot\mathbf{r}} \\ &= \int_0^\infty \frac{dk}{k} \frac{k^3 P(k, z)}{2\pi^2} \frac{\sin kr}{kr} \end{aligned} \quad (1.31)$$

where the last step follows because of the isotropic nature of the power spectrum, so that we can introduce the spherical polar coordinates with the polar axis along  $\mathbf{k}$ , and the angular part of that integral can therefore be performed independently. Many cosmologists often express the power spectrum in dimensionless form, as the variance per  $\ln k$

$$\Delta^2(k, z) \equiv \frac{d\langle\delta^2\rangle}{d\ln k} = \frac{k^3}{2\pi^2}P(k, z) \quad (1.32)$$

In the standard cold dark matter model,  $\Delta^2(k, z)$  increases with wavenumber, but we observe the density field smoothed over some scale. Therefore, we are particularly interested in the density field smoothed on a particular scale, say  $R$ ,

$$\delta_R(\mathbf{x}, z) \equiv \int d^3x' W(|\mathbf{x}' - \mathbf{x}|; R)\delta(\mathbf{x}', z) \quad (1.33)$$

The function  $W(x; R)$  is called the *window function* or the filter function that weights the density field in a manner that is relevant for the particular reason. Perhaps, the most natural choice of a window function is a simple sphere in real space:

$$\begin{aligned} W(x; R) &= \frac{3}{4\pi R^3} && \text{for } x \leq R \\ &= 0 && \text{for } x > R \end{aligned} \quad (1.34)$$

However, due to the sharp transition in configuration space, this choice of window function has certain disadvantages. Therefore, it is often convenient to use the Fourier transformed real-space *tophat* window of equation (1.34)

$$W(k; R) = \frac{3(\sin kR - kR \cos kR)}{k^3 R^3} \quad (1.35)$$

We can now also define a few more useful quantities, namely, the volume-averaged correlation function

$$\begin{aligned} \bar{\xi}(R, z) &\equiv \frac{3}{4\pi R^3} \int_0^R d^3r \xi(r, z) \\ &= \int_0^\infty \frac{dk}{k} \frac{k^3 P(k, z)}{2\pi^2} W(k; R) \end{aligned} \quad (1.36)$$

and the root mean square fluctuations in mass  $M$  at some comoving radius  $R$  ( $M = 4\pi\rho_m R^3/3$ )

$$\sigma^2(M, z) \equiv \sigma^2(R, z) = \langle\delta_R(\mathbf{x}, z)\rangle = \int_0^\infty \frac{dk}{k} \frac{k^3 P(k, z)}{2\pi^2} |W(k; R)|^2 \quad (1.37)$$

where  $W(k; R)$  is defined as equation (1.35). We will see later that, the function  $\sigma(M, z)$  plays a very crucial role in estimates of the abundance of collapsed objects. We should mention here

that, whenever we want to use these quantities at the present epoch, we shall omit  $z$  in our notations; like  $P(k, z = 0) \equiv P(k)$ .

So, the above shows that the power spectrum is a very crucial quantity in cosmology, but how can we predict its functional form? For simplicity, we assume that the spectrum does not contain any preferred length scale. In standard models, we presume that inflation produces a featureless primordial power-law spectrum  $P(k) \propto k^n$  with spectral index  $n \sim 1$ . Most important case is the scale-invariant spectrum which corresponds to the value  $n = 1$ . This is often known as *Harrison-Zeldovich (HZ) spectrum* (Harrison 1970; Zeldovich 1972). However, the current WMAP or PLANCK data strongly disfavors a pure HZ spectrum;  $n = 0.972 \pm 0.013$  from WMAP9 (Hinshaw et al. 2012) and  $n = 0.9603 \pm 0.0073$  from PLANCK with WMAP low-multipole likelihood (Ade et al. 2013b). Growth of perturbation in the radiation-dominated and then matter-dominated era results in a modified final power spectrum, characterized by a turnover at a scale of order the horizon  $c/H$  at matter-radiation equality. On large scales the spectrum evolves in proportion to the square of the growth factor. On the other hand, at small scales, the power spectrum changes shape due to the additional non-linear gravitational growth of perturbations, resulting a full non-linear power spectrum. However, the overall amplitude of the power spectrum is yet not specified by the recent allowed models of inflation, and it is normally set by the observations from CMB and galaxy clustering.

For a variety class of cold dark matter models, the power spectrum for dark matter fluctuations, calculated at present epoch, can be well approximated by a fitting function of the form

$$P_{\text{DM}}(k) = \frac{A_{\text{DM}} k^n}{(1 + [ak + (bk)^{1.5} + (ck)^2]^\nu)^{\frac{2}{\nu}}} \quad (1.38)$$

where the fitting parameters  $\nu = 1.13$ ,  $a = (6.4/\Gamma)h^{-1}$  Mpc,  $b = (3/\Gamma)h^{-1}$  Mpc,  $c = (1.7/\Gamma)h^{-1}$  Mpc and  $\Gamma = \Omega_m h$  for  $\Omega_b \ll \Omega_m$ . The normalization parameter  $A_{\text{DM}}$  is fixed through the observed value of the root mean square fluctuations in spheres of radius  $8h^{-1}$  Mpc. This quantity is denoted as  $\sigma_8$ . The current best-fit value of  $\sigma_8$  is  $0.821 \pm 0.023$  from WMAP9 (Hinshaw et al. 2012) and  $0.829 \pm 0.012$  from PLANCK using WMAP polarization data (Ade et al. 2013b). For large scales (low  $k$ ) where the growth is linear, we can get the power spectrum for any other epoch  $P_{\text{DM}}(k, z)$  simply by multiplying  $P_{\text{DM}}(k)$  with  $D^2(z)$ , where  $D(z)$  is the growth function [equation (1.19)].

The power spectrum for linear baryonic density fluctuations can be obtained from  $P_{\text{DM}}(k, z)$  as (Fang et al. 1993)

$$P_b(k, z) = \frac{P_{\text{DM}}(k, z)}{[1 + x_b^2(z)k^2]^2} \quad (1.39)$$

where the quantity  $x_b$  is defined as (Choudhury et al. 2001; Choudhury et al. 2001; Choudhury & Ferrara 2005)

$$x_b(z) = \frac{1}{H_0} \sqrt{\frac{2\gamma k_B T_0}{3\mu m_p \Omega_m (1+z)}} \quad (1.40)$$

$\mu$  is the mean molecular weight in atomic units,  $\gamma$  is the specific heat ratio,  $m_p$  is the proton mass and  $k_B$  is the Boltzmann's constant.

### 1.2.5 Non-linear object formation and evolution

In the previous sections, we have introduced the mathematical framework needed to study the structure formation. The formation of bound virialized objects was studied for pressure-less dark matter component using linear theory until the perturbation  $\delta$  is very small. In Section 1.2.3, we mentioned that the full non-linear treatment must be taken into account for a realistic situation. In this section, we will study the formation and abundance of the non-linear objects using such full non-linear theory - the *spherical model*.

Due to the spherical symmetry, an overdense sphere turns out to be a very useful non-linear model. It behaves exactly the same way as a closed sub-universe. Any spherically symmetric perturbation will evolve at a given radius in the same way as a uniform sphere containing the same amount of mass. Now consider the force on a particle in an inertial non-comoving coordinate system, resulting from a point mass at the origin (ignoring the presence of a vacuum energy density). Then the equation of motion for that particle on the shell in a background universe with dark matter only will be

$$\frac{d^2r}{dt^2} = -\frac{GM}{r^2} \quad (1.41)$$

where  $r$  is the distance of the particle from the center of the spherical perturbation, and  $M$  is the total mass within that radius. The mass remains constant in time as long as the shells do not cross each other. We can then write down the cycloid solution (Peacock 1999; Barkana & Loeb 2001):

$$\begin{aligned} r &= A(1 - \cos \theta) \\ t &= B(\theta - \sin \theta) \end{aligned} \quad (0 \leq \theta \leq 2\pi) \quad (1.42)$$

where,  $A^3 = GMB^2$ . Expanding these relations up to order  $\theta^5$  for small  $t$  gives

$$r \simeq \frac{A}{2} \left( \frac{6t}{B} \right)^{\frac{2}{3}} \left[ 1 - \frac{1}{20} \left( \frac{6t}{B} \right)^{\frac{2}{3}} \right] \quad (1.43)$$

and the density perturbation within the sphere will be

$$\delta \simeq \frac{3}{20} \left( \frac{6t}{B} \right)^{\frac{2}{3}} \quad (1.44)$$

This agrees with what we knew already, that is, at early times the sphere expands with  $a \propto t^{2/3}$ , the Hubble flow, and density perturbations grow as  $\delta \propto a$ .

We can now see that, the sphere *turns around* from the general expansion when it reaches a maximum radius at  $\theta = \pi$ ,  $t = \pi B$ . By comparison with the linear theory for an  $\Omega = 1$  background, one can say that, this occurs at a critical overdensity of  $\delta_c^{\text{lin}} \simeq 1.06$ . If only gravity operates, then the sphere will *collapse* to zero radius at  $\theta = 2\pi$ , and this gives  $\delta_c^{\text{lin}} \simeq 1.69$ . But even a slight violation of the exact symmetry of the initial perturbation can prevent the sphere from collapsing to a point. Instead the sphere reaches a state of virial equilibrium. At this point, its kinetic energy  $K$  is related to its potential energy  $U$  by  $U = -2K$  and this is known as *virial theorem*. Some people prefer to assume that this virialized size is achieved only at collapse, in that case the density contrast becomes  $\simeq 178$ . Of course, in real case, objects are not exactly symmetric and the complex anisotropic sequence of events eventually leads to the  $N$ -body version of structure formation. Nevertheless, this procedure is quite accurate as far as determining the time of collapse is concerned.

In the standard hierarchical CDM paradigm of cosmology, the structure formation starts with the gravitational collapse of overdense regions into bound virialized haloes of dark matter. Bound in the potential wells of dark matter haloes, baryons proceed to cool, condense, and eventually form galaxies and other structures. Thus, understanding the fundamental properties and abundances of these dark matter haloes is the first and necessary step in studying the physics of structure formation. The dynamics of dark matter collapse can be solved analytically only in cases of particular symmetry. If we consider a region much smaller than the horizon  $c/H$ , then the halo formation can be treated a problem in Newtonian gravity. The simplest but effective approximation scheme is based on spherical symmetry with an initial top-hat uniform overdensity  $\delta_i$  inside a sphere of radius  $R$ . Although this model is limited in its direct applicability, the results of spherical collapse have turned out to be surprisingly useful in understanding the underlying physics of cold dark matter haloes.

As mentioned earlier, the equation of motion for collapse of a spherical top-hat perturbation in a background universe with dark matter haloes can be described by the equation (1.41). This equation can be solved for a given background cosmology, provided the initial conditions are known (Barkana & Loeb 2001). The initial value for  $r$  should be chosen such that the initial density contrast  $\delta_i$  is much less than unity. The enclosed  $\delta$  initially grows according to the linear theory, but eventually it grows above the linear critical density  $\delta_c = 1.69$ , where the linear approximation breaks down. If the mass shell of radius  $r$  is bound then it reaches a radius of maximum growth and consequently collapses. The critical density for a tophat collapse at any redshift  $z$  can be obtained by extrapolating its linear density contrast to that redshift

$$\delta_c(z) = \frac{1.69}{D(z)} \quad (1.45)$$

where  $D(z)$  is the usual growth function and is set to be 1 at present day  $z = 0$ .

Another important quantity in structure formation studies is the virial density of the collapsed halo of mass  $M$  with respect to the critical density, defined as

$$\Delta_c = \frac{\rho_m}{\rho_c} = \frac{8\pi G \rho_m}{3H^2} = \frac{2GM}{r_{\text{vir}}^3 H^2} \quad (1.46)$$

where  $r_{\text{vir}}$  is the radius of a spherical volume within which the mean density is  $\Delta_c$  times the critical density at that redshift, so that  $M = 4\pi r_{\text{vir}}^3 \rho_c \Delta_c / 3$ . This is known as the *virial radius*. The value of  $\Delta_c$  is taken from the solution of spherical tophat collapse under the assumption that the halo has just virialized (Peebles 1980). Its value is  $18\pi^2$  for the Einstein-de Sitter universe but has a dependence on cosmology through the parameter  $\Omega_m^z$ , defined as

$$\Omega_m^z = \frac{\Omega_m(1+z)^3}{\Omega_m(1+z)^3 + \Omega_\Lambda + \Omega_k(1+z)^2} \quad (1.47)$$

This dependence can be approximated quite well by the fitting formula (Bryan & Norman 1998)

$$\begin{aligned} \Delta_c &= 18\pi^2 + 60x - 32x^2 && \text{if } \Omega_\Lambda = 0 \\ &= 18\pi^2 + 82x - 39x^2 && \text{if } \Omega_\Lambda = 1 - \Omega_m \end{aligned} \quad (1.48)$$

where  $x = \Omega_m^z - 1$ . This results are accurate to 1% in the range  $\Omega_m^z = 0.1 - 1$ .

In practice, we are often interested in the quantity called the *circular velocity*  $v_c$  of the collapsed halo. In a universe with non-zero  $\Lambda$ , it is given by

$$v_c^2 = \frac{GM}{r_{\text{vir}}} - \frac{\Omega_\Lambda H_0^2 r_{\text{vir}}^2}{3} \quad (1.49)$$

where we have assumed that the virialized halo has a singular isothermal density profile  $\rho(r) \propto 1/r^2$ . We can get the mass of the halo in terms of the circular velocity by eliminating  $r_{\text{vir}}$  from the above equation

$$\frac{M}{10^{11} h^{-1} M_\odot} = \left( \frac{v_c}{35.0 \text{ km s}^{-1}} \right)^3 \sqrt{\frac{2H_0^2}{H^2(z)\Delta_c(z)}} \left[ 1 - \frac{2\Omega_\Lambda H_0^2}{3H^2(z)\Delta_c(z)} \right]^{-3} \quad (1.50)$$

We may also then define a *virial temperature* as

$$T_{\text{vir}} = \frac{\mu m_p}{2k_B} v_c^2 \quad (1.51)$$

where  $\mu$  is the mean molecular weight and  $m_p$  is the mass of a proton. The Jeans scale,  $\lambda_J$ , will then be determined by the minimum circular velocity for star-forming haloes

$$\lambda_J = 2\pi \frac{v_c}{H_0} \sqrt{\frac{\gamma}{3\Omega_m(1+z)}} \quad (1.52)$$

However, for baryons, we do not have such a well-established theoretical tools and therefore the non-linear evolution of baryons are very complicated and challenging to study.

In addition to identifying the properties of individual haloes, a critical prediction of any theory of structure formation is the abundance of haloes, i.e. the number density of haloes as a function of mass, at any redshift. This is a very crucial step toward understanding the

abundances of galaxies and galaxy clusters. Although, the correct way to that is to use the numerical simulations, one can gain the physical understanding and explore the dependence of abundances on the cosmological parameters with the help of an analytical model. One can then match the analytical results with that from numerical simulations.

A simple analytic model with particular attention toward applications to dark matter halo formation and growth, halo abundance and clustering, which matches quite successfully most of the numerical simulation was proposed by Press & Schechter (1974). This model is based on the ideas of a Gaussian random field of density perturbations, linear gravitational growth, and spherical collapse. They essentially assumed that the objects will collapse on some small scale, say  $R$ , once the smoothed density contrast  $\delta_R$  [equation (1.33)] on this scale exceeds some threshold value, but that the non-linearities introduced by these virialized objects will not affect the collapse of overdense regions on much larger scales. Although this assumption is not strictly correct, but it is approximately true to some extent (see Williams et al. 1991). Moreover, this assumption leads us to some important ingredients of the non-linear structure formation, like the characterization of the statistical properties of primordial density fluctuations, the evolution of overdensities according to linear perturbation theory etc.

Using a model for the collapse of a spherical tophat overdensity, Press & Schechter prescribed that collapse on some smoothing scale  $R$  should occur roughly when the smoothed density on that scale exceeds the critical value  $\delta_c(z)$ , given in equation (1.45), independent of  $R$ . The mass of the virialized object  $M(R)$  is related to the smoothing scale by the volume of the window function. For a tophat window [equation (1.34)],  $M = 4\pi\rho_m R^3/3$ . Now, the probability of attaining a value of  $\delta_R(z)$  between  $\delta_R$  and  $\delta_R + d\delta_R$  is

$$P(\delta_R; M)d\delta_R = \frac{1}{\sqrt{2\pi\sigma^2(M)}} \exp\left[-\frac{\delta_R^2(z)}{2\sigma^2(M)}\right] d\delta_R \quad (1.53)$$

where the standard deviation  $\sigma(M)$  is calculated using the present power spectrum [equation (1.37)]. By integrating the above equation, one can get the cumulative probability for a region to have a smoothed density  $\delta_R(z)$  greater than the threshold density  $\delta_c(z)$ . This will give the fractional volume occupied by the virialized objects larger than the smoothing scale or having mass greater than  $M$

$$F(> M; z) = \int_{\delta_c(z)}^{\infty} P(\delta_R; M)d\delta_R = \frac{1}{2} \operatorname{erfc}\left(\frac{\nu}{\sqrt{2}}\right) \quad (1.54)$$

where  $\operatorname{erfc}(x)$  is the complementary error function and  $\nu \equiv \delta_c(z)/\sigma(M)$  is the height of the threshold in units of the standard deviation. Note that, as in the hierarchical power spectra  $\sigma(M) \rightarrow \infty$  for  $M \rightarrow 0$ , the function  $F(> 0; z)$  in the above equation should give the fraction of all mass in virialized objects. But,  $\operatorname{erfc}(0) = 1$ , so this equation states that only half of the mass density of the universe is contained in virialized objects. Press & Schechter noted this as a problem associated with not counting underdense regions and multiplied  $F(> M; z)$  by an ad-hoc factor of 2 to account for all masses. However Bond et al. (1991) found an alternative

derivation of this correction factor, using a different ansatz. Also one can get the corrected results using an *excursion set formalism* (see Chapter 5 for details). However, taking this extra factor of two, we get

$$F(> M; z) = \operatorname{erfc} \left( \frac{\nu}{\sqrt{2}} \right) \quad (1.55)$$

Thus the number of virialized objects with masses between  $M$  and  $M + dM$  is

$$\frac{dn}{dM} dM = \frac{\rho_m}{M} \left| \frac{dF(> M; z)}{dM} \right| dM \quad (1.56)$$

and in terms of the mass variance,

$$\frac{dn}{dM} dM = \sqrt{\frac{2}{\pi}} \frac{\rho_m}{M^2} \nu \left| \frac{d \ln \sigma}{d \ln M} \right| \exp \left( -\frac{\nu^2}{2} \right) dM \quad (1.57)$$

So, without regard to the details of the shape of the power spectrum and other quantities, we can see that, the mass function is close to a power-law with  $dn/dM \propto M^{-2}$  for very small masses and is exponentially cut-off for larger masses. The shape of this mass function agrees with numerical results to some reasonable accuracy. Improvements to the Press-Schechter mass function have been made to overcome this limitation. In particular, the *Sheth-Tormen mass function*, which is based on the more realistic ellipsoidal collapse model (Sheth & Tormen 1999; Sheth et al. 2001) fits the numerical results better.

### 1.3 Galaxy formation and cosmic reionization

In the previous sections we have outlined the basic mathematical framework needed to study structure formation. The formation of bound virialized objects was discussed for pressure-less dark matter component first using a linear theory and then some non-linear approximation where the density contrast becomes order of unity. However, the physics for the baryons are too complicated to be studied under this simple approximation schemes. In this chapter, we are concerned in describing the basic physics which guides the baryons, which leads us to introduce models of galaxy formation.

Now start with a very brief thermal history of the baryons in the universe. The two most abundant elements among the baryons are hydrogen and helium. At redshift  $z \sim 1100$  (age of the universe was  $\sim 3 \times 10^5$  years), the electrons and protons combined for the first time to form neutral hydrogen and some amount of helium. This process is usually called the *recombination*. Right after this recombination epoch, the universe entered a phase called *dark age* where no sources of light existed and hydrogen stayed largely neutral at this stage. This is believed to be the most unknown period of the universe spanning from  $z \sim 1100$  to the formation of first stars at  $z \sim 20 - 30$ . However, the small inhomogeneities which were formed by then start to

grow via gravitational instability and form highly non-linear structures like massive dark matter haloes. We have already discussed how to obtain the abundance of such haloes in the previous section. The collapsed haloes then form potential wells whose depths depend on their mass. The neutral baryonic gas falls into these potential wells. If the virial temperature of the halo is high enough, the gas will be able to dissipate its energy, cool via atomic or molecular transitions and fragment within the halo. In the absence of molecules, the lower limit of the halo virial temperature is  $\sim 10^4$  K. This produces conditions appropriate for condensation of gas and forming the first population of stars and galaxies, which can generate ultraviolet (UV) radiation through the nuclear reactions. In addition to the galaxies, perhaps an early population of accreting black holes, known as *quasars* (QSO), also generated considerable amount of UV radiation. The UV radiation contains photons with energies  $> 13.6$  eV which are then able to reheat and reionize most of the hydrogen atoms in the intergalactic space (called the intergalactic medium or IGM). This process is known as *reionization*. Thus after the recombination, reionization is the second major change in the ionization history of the universe. Also, it has an immense theoretical and observational impact in studying the physics of structure formation. This reheating of the IGM can expel the gas and suppress cooling in the low mass haloes. In addition, the nuclear reactions within the stellar sources can alter the chemical composition of the medium via energetic explosion (*supernova*). These processes can change the nature and amount of star formation at later stages. They are commonly known as *feedback mechanisms* (described in Section 1.3.2).

The details of galaxy formation and reionization of the IGM depends on complicated physics of density fluctuations, various feedback mechanisms and non-linearities at small scales - none of which are not well understood as yet in contrast this situation with that for the dark matter. However, in order to model the evolution of baryonic structures, one needs to incorporate all the hydrodynamical processes, heating, cooling, star formation etc., in the N-body simulations. Because of such complications, our understanding of the physics of baryonic structure formation has been limited. In this chapter we will attempt to address some of these complicated issues, starting with the physics of baryonic structure formation.

### 1.3.1 Baryonic structure formation

We begin by exploring the gravitational instability scenario, in which primordial density perturbations grow through gravitational *Jeans instability* to form the complex structures we observe today.

In the Newtonian gravity limit, the Jeans length  $\lambda_J$  is defined as the critical wavelength that separates oscillatory and exponentially growing density perturbations in an infinite, uniform and stationary distribution of gas, defined in equation (1.15). For the scales  $l < \lambda_J$ , the sound crossing time  $l/c_s$  is smaller than the gravitational free-fall time,  $(G\rho)^{-1/2}$ . This allows to build up a pressure force that counteracts gravity. On larger scales, the pressure gradient force is too slow to react to a build up of the attractive gravitational force. The mass within a sphere of

radius  $\lambda_J/2$  is known as *Jeans mass*:

$$M_J = \frac{4\pi}{3}\rho \left(\frac{\lambda_J}{2}\right)^3 \quad (1.58)$$

In a perturbation with a mass  $M > M_J$ , the self-gravity cannot be supported by the pressure gradient, so the gas is unstable to gravitational collapse. However, this Newtonian derivation of the Jeans instability suffers from a conceptual inconsistency, as the unperturbed gravitational force of the uniform background must induce the bulk motions (Binney & Tremaine 2008). This inconsistency must be treated when the analysis is done in an expanding universe.

The perturbative derivation of the Jeans instability criterion can be carried out by taking a sinusoidal perturbation superposed on a uniformly expanding background. Now, consider spherical fluctuations in the baryonic gas and dark matter densities in the form of a single spherical Fourier mode on a scale much smaller than the horizon:

$$\begin{aligned} \frac{\rho_{\text{DM}}(r, t) - \bar{\rho}_{\text{DM}}(t)}{\bar{\rho}_{\text{DM}}(t)} &= \delta_{\text{DM}}(t) \frac{\sin kr}{kr} \\ \frac{\rho_b(r, t) - \bar{\rho}_b(t)}{\bar{\rho}_b(t)} &= \delta_b(t) \frac{\sin kr}{kr} \end{aligned} \quad (1.59)$$

where  $\delta$  are the corresponding overdensity amplitudes and  $r$  is the comoving radial coordinate. Initially, at some time  $t = t_i$  the perturbation amplitudes are small ( $\delta_{\text{DM},i}, \delta_{b,i} \ll 1$ ) and the gas temperature is uniform  $T_b(r, t_i) = T_i$ . We can define a region inside the first zero of  $\sin kr/kr$ , namely  $0 < kr < \pi$ , as the collapsing object. The temperature of baryons is determined by the coupling of its free electrons to the CMB through *Compton scattering* and by the adiabatic expansion. Thus  $T_b$  is generally between the CMB temperature  $T_{\text{CMB}} \propto (1+z)^{-1}$  [see equation (1.8)] and the adiabatically scaled temperature  $T_{\text{ad}} \propto (1+z)^{-2}$ . In the limit of tight coupling to the CMB, the gas temperature remains uniform, whereas in the adiabatic limit, it goes as  $T_b \propto \rho_b^{(\gamma-1)}$ , where  $\gamma$  is the specific heat ratio.

The evolution of the perturbation in dark matter is described in the linear regime by [see equation (1.21)]

$$\ddot{\delta}_{\text{DM}} + 2H\dot{\delta}_{\text{DM}} = \frac{3}{2}H^2(\Omega_b\delta_b + \Omega_{\text{DM}}\delta_{\text{DM}}) \quad (1.60)$$

and with the inclusion of pressure term, the baryon overdensity evolves as (Kolb & Turner 1990; Loeb 2006)

$$\ddot{\delta}_b + 2H\dot{\delta}_b = \frac{3}{2}H^2(\Omega_b\delta_b + \Omega_{\text{DM}}\delta_{\text{DM}}) - \frac{\gamma k_B T_i}{\mu m_p} \left(\frac{k}{a}\right)^2 \left(\frac{a_i}{a}\right)^{1+\beta} \left(\delta_b + \frac{2}{3}\beta[\delta_b - \delta_{b,i}]\right) \quad (1.61)$$

Here the parameter  $\beta$  discriminates between the two limits of evolution of gas temperature:  $\beta = 1$  in the adiabatic limit, and  $\beta = 0$  in the strong coupling limit. The Jeans wavelength

$\lambda_J = 2\pi/k_J$  is then obtained by setting the right hand side of equation (1.61) to zero and solving for the critical wavenumber  $k_J$ . One can see that  $\lambda_J$  (and thus  $M_J$ ) will be time dependent in general and also that perturbations with increasingly smaller initial wavelengths stop oscillating and start to grow.

Following the recombination at  $z \approx 1100$ , the residual ionization of the cosmic gas keeps its temperature locked to the CMB temperature via Compton scattering down to a redshift  $z_t$ , which is (Peebles 1993)

$$1 + z_t \approx 137 \left( \frac{\Omega_b h^2}{0.022} \right)^{2/5} \quad (1.62)$$

In the redshift range between recombination and  $z_t$ , i.e.  $z_t < z < z_{\text{rec}}$ , the parameter  $\beta = 0$ . So, we get

$$k_J \equiv \frac{2\pi}{\lambda_J} = H_0 \sqrt{\frac{3\mu m_p \Omega_m}{2\gamma k_B T_{\text{CMB}}(0)}} \quad (1.63)$$

and the Jeans mass is

$$M_J = \frac{4\pi}{3} \left( \frac{\lambda_J}{2} \right)^3 \bar{\rho}(0) = 1.35 \times 10^5 \left( \frac{\Omega_m h^2}{0.15} \right)^{-1/2} M_\odot \quad (1.64)$$

For  $z < z_t$ , the gas temperature drops adiabatically i.e.  $\beta = 1$ , and the total Jeans mass will be (Padmanabhan 1993)

$$M_J = 5.73 \times 10^3 \left( \frac{\Omega_m h^2}{0.15} \right)^{-1/2} \left( \frac{\Omega_b h^2}{0.022} \right)^{-3/5} \left( \frac{1+z}{10} \right)^{3/2} M_\odot \quad (1.65)$$

However, above expressions for the Jeans mass are just a linear theory estimate and can only describe the initial phase of collapse. Also, it is not clear how the value of the Jeans mass is related to the mass of collapsed, bound objects. As the density perturbations grow with time and become larger than unity, the amount of mass enclosed within a given baryonic shell may increase with time, until eventually the dark matter pulls the baryons with it and causes their collapse even for objects below the Jeans mass. In this linear regime, the Jeans mass is related only to the evolution of perturbation at a given time. When the Jeans mass itself varies with time, the overall suppression in the growth of perturbations will depend on a time-weighted Jeans mass, known as *filtering mass* (Gnedin & Hui 1998; Choudhury & Ferrara 2005). Thus the Jeans condition may only be a necessary but not sufficient condition.

In order to estimate the minimum mass of baryonic objects, we must go beyond the linear theory, and we have to consider the non-linear effects on the evolution of the accreted baryons. Assume that a dark matter halo with a potential well  $\phi(\mathbf{r})$ , with  $\phi \rightarrow 0$  at large distances and

$\phi < 0$  inside the object, is formed at redshift  $z_{\text{vir}}$ . After the gas, with some pressure  $p_b$  and mass density  $\rho_b$  settles into this potential well, it satisfies the hydrostatic equilibrium equation,

$$\nabla p_b = -\rho_b \nabla \phi \quad (1.66)$$

At  $z < 100$ , the gas temperature is decoupled from the CMB, and its pressure evolves adiabatically, so we have  $p_b \propto \rho_b^{5/3}$  (as  $\gamma = 5/3$ ), which immediately gives

$$\frac{\rho_b}{\bar{\rho}_b} = \left( 1 - \frac{2 \mu m_p \phi}{5 k_B \bar{T}} \right)^{3/2} \quad (1.67)$$

$\bar{T} = \bar{p}_b \mu m_p / (k_B \bar{\rho}_b)$  is the background gas temperature (a bar denotes the background conditions). Then the baryonic overdensity can be written as

$$\delta_b \equiv \frac{\rho_b}{\bar{\rho}_b} - 1 = \left( 1 + \frac{6 T_{\text{vir}}}{5 \bar{T}} \right)^{3/2} - 1 \quad (1.68)$$

where  $T_{\text{vir}} = -\mu m_p \phi / (3k_B)$  is the virial temperature corresponding to the potential well of depth  $-\phi$ .

According to the spherical top-hat collapse model, we may say that collapse of baryons happens when their mean overdensity  $\delta_b$  exceeds a value of 100. This implies a minimum halo mass for these collapsed baryonic objects, known as *protogalaxies*, of

$$M_{\text{min}} = 5.0 \times 10^3 \left( \frac{\Omega_m h^2}{0.15} \right)^{-1/2} \left( \frac{\Omega_b h^2}{0.022} \right)^{-3/5} \left( \frac{1+z}{10} \right)^{3/2} M_{\odot} \quad (1.69)$$

This happens to be very close to our earlier linear estimate of Jeans mass, however it takes non-linear effects into account. Note that, unlike the Jeans mass, this minimum mass depends on the choice for an overdensity threshold. Of course, when the first stars and galaxies form, this value of  $M_{\text{min}}$  will be changed due to various feedback effects.

Besides the gravitational instability, another process that affects the structure formation is cooling. As we have discussed above, gravity dominates in objects with baryonic masses greater than  $3 \times 10^4 M_{\odot}$  and for lower masses pressure delays the collapse - resulting to a bottom-up hierarchy of structure formation. Thus the first objects to collapse have a mass scale that separates these two regimes. Such objects can fragment only through cooling. The efficiency of gas cooling is very crucial in determining the minimum mass of protogalaxies. Thus, there are two independent minimum mass thresholds for star formation: the Jeans mass and the cooling mass. The higher of these two decides the actual threshold. The primary molecule that acquires sufficient abundance to affect the thermal state of the gas is molecular Hydrogen  $\text{H}_2$ , produced by various processes in the early universe. Primordial  $\text{H}_2$  forms with a very small fractional abundance of  $\approx 10^{-7}$  at  $z > 400$ . But, at  $z < 110$ , when the CMB radiation intensity becomes weak enough to allow for a significant formation of  $\text{H}^-$  ions, more  $\text{H}_2$  molecules can be formed.

Cooling via  $H_2$  forms objects with mass  $\sim 10^4 M_\odot$ , which are usually called *minihaloes*. This cooling process is known as *molecular cooling*. However, molecular Hydrogens are very fragile and can easily be dissociated by photons with energies of 11.26 – 13.6 eV, to which the IGM is transparent even before reionization. Haiman et al. (1997) showed that the UV flux necessary for dissociating  $H_2$  throughout the collapsed environments is two orders of magnitudes lower than the amount required for IGM reionization. Hence,  $H_2$  is completely destroyed by trace amount of first generation stars. Further star formation is only possible via *atomic cooling*, which happens at  $T_{\text{vir}} \gtrsim 10^4$  K. Such objects correspond to mass of  $\sim 10^8 M_\odot$ .

The final state in the evolution of stars is uncertain, but if their mass loss is not too excessive, they are most likely to end up as black holes (BH) (Bond et al. 1984). Apart from star formation, some massive black hole formations are also expected to happen in the early stages of galaxy formation, they are known as quasars. The quasars are more effective than stars in ionizing the intergalactic hydrogen (Larson 2000). Thus the history of reionization may be greatly affected if quasars form early. Some of the massive stars may end their lives by producing gamma ray bursts (GRBs). Then the broad-band afterglows of these bursts could provide a powerful tool for probing the epoch of reionization (Lamb & Reichart 2000; Ciardi & Loeb 2000).

### 1.3.2 Reionization of the IGM

As mentioned earlier, reionization begins when the first sources of ionizing photons form and start building ionized medium around themselves. In this section, we will discuss the basic stages of reionization: the *pre-overlap*, *overlap* and *post-overlap* phases.<sup>6</sup>

In the initial “pre-overlap” stage, a fraction of the UV radiation emitted by the stars can escape the host galaxy and ionize hydrogen in the surrounding medium. The value of the escape fraction of radiation depends on the mass of the galaxy and the clumping of matter within it, and is quite uncertain. Along with that, the ionizing UV radiation can also be generated by an early population of QSOs. Although the number of QSOs at high redshifts ( $z > 6$ ) is quite small, but the radiation from the QSOs can escape much easily because of the fact that their spectrum is much harder compared to that of galaxies. Since the first galaxies form in the most massive haloes at high redshifts, they are preferentially located in the high density regions. The ionizing photons have to pass through this high density region which is characterized by large recombination rates. At this stage, the IGM acts like a two-phase medium, with highly ionized Hydrogen (HII) regions separated from neutral Hydrogen (HI) regions by the ionization fronts.

The “overlap” stage begins when the ionizing volume increases gradually and the neighboring HII regions start overlapping. The propagation of these ionization front can be studied by taking into account the photoionization and the recombination of the atoms (Shapiro & Giroux 1987). At this stage, the intensity in the HII regions rises very rapidly, allowing them to expand

---

<sup>6</sup>This terminology was first introduced by Gnedin (2000)

into the high density gas that had been able to recombine in the presence of a lower ionizing intensity. By end of this stage, the ionizing radiation reaches most of the IGM regions, except for the gas trapped inside self-shielding, high-density clouds. This process of overlapping seems to be completed around  $z \approx 6 - 8$  at which point the neutral hydrogen fraction  $x_{\text{HI}}$  becomes lower than  $10^{-4}$ .

Following the overlap phase, a never-ending “post-overlap” (or “post-reionization”) phase started which implies that the universe is largely ionized at present epoch. Even at the end of the overlap stage, there remains some neutral regions in very high density structures (with column densities  $N_{\text{HI}} > 10^{17} \text{cm}^{-2}$ ), such as Lyman Limit Systems (LLS) and Damped Ly $\alpha$  systems (DLA), which can be seen in absorption at lower  $z$  (see Section 1.3.3). These too, get gradually ionized in this stage as galaxies form and the mean ionization intensity increases. This post-overlap phase then continues indefinitely, since the collapsed objects retain HI even at the present time.

Although the basic physics behind the reionization is more or less understood, the details are still to be filled in. The numerical resolution in the hydrodynamical simulations is also limited for this purpose and, at present, one has to rely on semi-analytical models for this purpose. Still the nature of the reionization sources and the reionization history remain unclear and highly debated in the literature. This is mainly due to uncertainties in modelling several physical issues, like the properties of the first stars and quasars, the ionizing photon production and radiative transfer, the IGM clumping etc. One of the most crucial parameters needed for modelling reionization is the escape fraction of ionizing radiation; whatever the nature of a source, only a fraction,  $f_{\text{esc}}$ , of the ionizing photons emitted escape the production site and reach the IGM. However, the value of  $f_{\text{esc}}$  is largely unconstrained (see Fernandez & Shull 2011; Mitra et al. 2013 and the references therein). We will come back to this point later in Chapter 3.

We have already mentioned about some of the possible sources of reionization, which include the first stars, galaxies, and QSOs. We will now briefly discuss about them one by one.

The first stars represent the first sources of light and dust in the universe. They can affect the subsequent formation of all later generations of stars and galaxies via several feedback processes. Although feedback effects are quite important, they are also difficult to model. They can be broadly classified into three categories: (i) *Radiative feedback* - it is associated with the radiation from first stars which can heat up the surrounding medium and can increase the mass scale (known as filtering mass) above which baryons can collapse into haloes within those regions. Thus the minimum mass of haloes which are able to cool is much higher in ionized regions than in neutral ones. It can change the cooling rate and suppress the star formation in low mass haloes. (ii) *Mechanical feedback* - the ejection of energy by a supernova driven wind (Dekel & Silk 1986). This can expel the cold gas from galaxies and suppress star formation in low mass haloes. One can parametrize both of these feedback processes through the minimum mass parameter  $M_{\text{min}}(t)$ , defined in equation (1.69). (iii) *Chemical feedback* - stars can expel the gas and associated metals into the *interstellar medium* (ISM) via stellar winds

and supernovae and hence change its chemical composition. Thus the subsequent formation of stars could be in a completely different environment and also the nature of stars could be highly different. The hierarchical models of structure formation predict the first collapsed objects to have a primordial, metal-free composition; their formation and cooling is governed by molecular hydrogen and they have huge masses. They are known as PopIII stars. They dominate the photoionization rate at high redshifts. However, the *initial mass function* (IMF), which specifies the distribution of masses in a newly formed stellar population, is largely unknown for these PopIII objects due to a poor understanding of their fragmentation processes. Although it is quite hard to model the primordial star formation processes, advances have been made along this direction using numerical simulations. By means of various simulations, people have found the first star to be massive with  $M \geq 100M_{\odot}$  (Bromm et al. 1999; Abel et al. 2000; Nakamura & Umemura 2001). However, it is important to note that PopIII star formation is suppressed as soon as the ISM is enriched by metals produced by previous generations of PopIII stars. Then the later generation stars will have sub-solar metallicities. They are known as PopII stars. Since the metal-free composition restricts the stellar energy source to be proton-proton burning rather than the usual CNO cycle, PopIII stars are hotter and have a harder spectra than PopII stars. However, both of their contributions to reionization are highly important. Recent studies suggest that reionization is initially driven by metal-free PopIII stars in low mass ( $M < 10^8 M_{\odot}$ ) haloes, then the conditions for the formation of these objects are soon erased by the combined action of chemical and radiative feedbacks at  $z < 10$  (Choudhury & Ferrara 2007).

According to the bottom-up, hierarchical model of structure formation, it is now well understood that small haloes form first, which later merge to form larger systems like galaxies. However, calculating the contribution of galaxies to reionization is extremely complicated due to the lack of knowledge of their intrinsic ionizing photon rate, which depends on the star formation rate (SFR), as well as the value of  $f_{\text{esc}}$  for each galaxy. Using suitable parameter choices of the SFR and  $f_{\text{esc}}$ , a number of authors have shown that star forming galaxies are capable of reionizing the universe by  $z \sim 6 - 15$ . This includes the work done using semi-analytic models (Fukugita & Kawasaki 1994; Haiman & Loeb 1997; Chiu & Ostriker 2000; Choudhury & Ferrara 2005, 2006b; Mitra et al. 2011) and simulations (Gnedin & Ostriker 1997; Gnedin 2000).

QSOs are powered by accretion of gas onto a black hole (BH), the excess rotation of the gas spiraling in towards the BH yields viscous dissipation of heat that makes the gas glow. The seed BH is generally seemed to be the remnant of a massive PopIII explosion. They are the significant sources of hard photons at  $z \lesssim 6$  but they have negligible effects on the IGM at higher redshifts (Dietrich & Hamann 2004). QSOs are more efficient than stars for reionization as the emission spectrum is harder and the value of  $f_{\text{esc}}$  is larger for QSOs than for stars.

### 1.3.3 Observational probes for reionization

We end this chapter with a brief survey of certain observations available at present and in near future, which shape our understanding of reionization. There are both cosmological and astrophysical constraints on reionization, while the former are from the CMB experiments, and the latter are inferred using spectral data from QSOs, GRBs and LAEs.

**(i) CMBR (Primary Anisotropies) constraints :** According to the standard big bang model, at redshift  $z \sim 1100$ , electrons and protons combine for the first time to form HI atoms. Then the photons decouple from matter, travel freely and are observed today as the CMBR. They carry information about the state of the universe at the decoupling epoch; small fluctuations in density, velocity and gravitational potential lead to anisotropies in the CMB (Sachs & Wolfe 1967; Bennett et al. 1996). The angular power spectrum for the primary anisotropies are able to probe length scales as large as the horizon size ( $\sim 3000 h^{-1}$  Mpc). Small-scale ( $\sim 1 h^{-1}$  Mpc, corresponding to multipoles of order  $l \sim 1000$ ) fluctuations in CMB are damped by Thomson scattering from free electrons produced at reionization. This scattering suppresses the amplitude of the acoustic peaks by  $e^{-2\tau_{\text{el}}}$  on the scales corresponding to perturbation modes with wavelength smaller than the Hubble radius at reionization. The low- $l$  CMBR polarization spectrum depends not just on  $\tau_{\text{el}}$ , but also on the detailed redshift evolution of the number density of free electrons in the IGM,  $x_e(z)$ . Thus, the CMBR polarization data with an improved constraint on  $\tau_{\text{el}}$ , can be used to probe the *epoch of reionization* (EoR). With a simple assumption that the universe was reionized instantaneously at a redshift  $z_{\text{re}}$ , recent WMAP team found that  $\tau_{\text{el}} = 0.089 \pm 0.014$  and  $z_{\text{re}} = 10.6 \pm 1.1$  (Hinshaw et al. 2012). This value is consistent with more precise measurements done by PLANCK (Ade et al. 2013b).

**(ii) Astrophysical constraints on reionization:** The IGM manifests itself in numerous absorption lines along the line of sight (LOS) of observed QSOs, GRBs and galaxies. These absorption lines arise when a LOS intersects with a patch of HI that absorbs the continuum radiation. This radiation is then redshifted into the Ly $\alpha$  (1216 Å) range. According to the amount of absorption, different kinds of absorbers can be distinguished in the observed spectra. Ly $\alpha$  forest arises from absorbers with a column density of  $N_{\text{HI}} \leq 10^{16} \text{ cm}^{-2}$ . These absorbers lie in shallow dark matter potential wells containing gas in various stages of infall and collapse. The Lyman Limit systems (LLS) have a column density  $N_{\text{HI}} \geq 1.6 \times 10^{17} \text{ cm}^{-2}$  and absorption is caused by relatively cool gas associated with star forming galaxies in high density regions. Whereas, the Damped Ly $\alpha$  systems (DLAs) are believed to be the highest density systems having a column density of  $N_{\text{HI}} \geq 2 \times 10^{20} \text{ cm}^{-2}$  (see Fig. 1.1). However, most of the spectral methods of constraining reionization rely on the Ly $\alpha$  line to constrain the amount of HI in the IGM. This is because the Ly $\alpha$  emission line at 1216 Å, corresponding to a energy of 10.6 eV is the strongest emission signal. Furthermore, due to a large Gunn-Peterson (GP) optical depth (Gunn & Peterson 1965a), in the presence of HI, the observed spectra shows a sharp cut-off

blueward of the Ly $\alpha$  line. The effective optical depth to the Ly $\alpha$  absorption by a uniform intergalactic medium can be expressed as (Gunn & Peterson 1965a; Barkana & Loeb 2007)

$$\tau_{\text{GP}}^{\text{eff}} \approx 6.45 \times 10^5 x_{\text{HI}} \left( \frac{\Omega_b h}{0.0315} \right) \left( \frac{\Omega_m}{0.3} \right)^{-1/2} \left( \frac{1+z}{10} \right)^{3/2} \quad (1.70)$$

So, even a trace amount of HI ( $x_{\text{HI}} \sim 10^{-4}$ ) can lead to a significant attenuation of the Ly $\alpha$  line. Therefore, it is important to note that the detection of a GP trough only translates into a lower limit of  $x_{\text{HI}}$ .

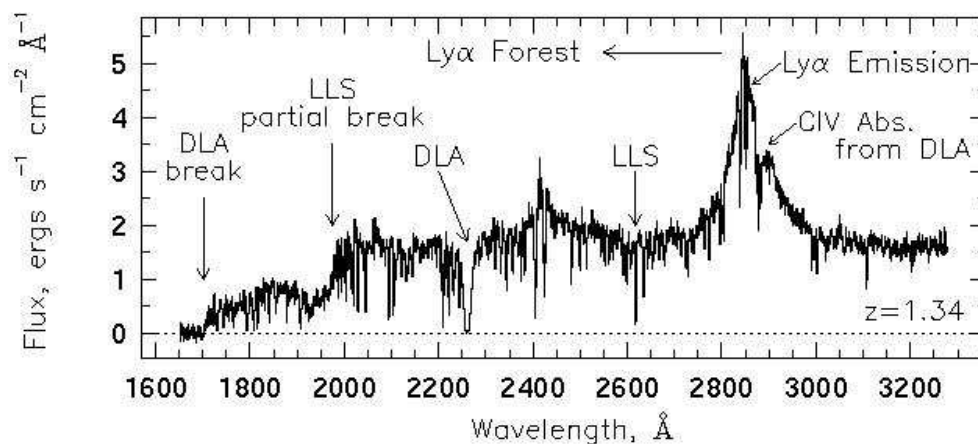


Figure 1.1: Typical spectrum of a QSO at  $z = 1.34$ . Ly $\alpha$  forest with numerous narrow absorption lines is seen at wavelengths below (blueward) the Ly $\alpha$  emission line. There are regions which have very high absorption - the DLAs. LLS absorbs all the photons which are capable of ionizing hydrogen and is observed as a sharp break in this QSO spectrum. [Figure courtesy: Charlton & Churchill (2000)]

Also the QSO spectra are often used for constraining the reionization. Fan et al. (2006) and Fan (2012) have obtained the spectra for several QSOs at  $z > 6$  (shown in Fig. 1.2). One can see that, as the redshift increases, larger portions of the spectra, blueward of the Ly $\alpha$  line, are completely attenuated; increasing  $z$  makes this break shift to longer wavelengths. The detection of Gunn-Peterson troughs indicates a rapid change (Fan et al. 2002; Pentericci et al. 2002; White et al. 2003) in the neutral content of the IGM at  $z \sim 6$  and this rapid change implies that overlap, and hence the reionization epoch, completed near  $z \sim 6$  (Fan et al. 2006). This result is also in agreement with the findings of Becker et al. (2001), who detected the first evidence of a complete GP trough in a QSO at  $z = 6.28$ . Using these spectra, many groups (Gallerani et al. 2006; Becker et al. 2007) have tried to check if reionization was over by  $z \sim 6$ .

Using the distribution of the dark gaps (regions showing no flux) and peaks (regions showing transmission) in the QSO spectra, Gallerani et al. (2008) have found that the data favors a model where reionization completes at  $z \sim 7$  and robustly constrain  $x_{\text{HI}} < 0.36$  at  $z = 6.3$ . Similar conclusions have been made by Dayal et al. (2008) using Ly $\alpha$  emitter (LAE) data.

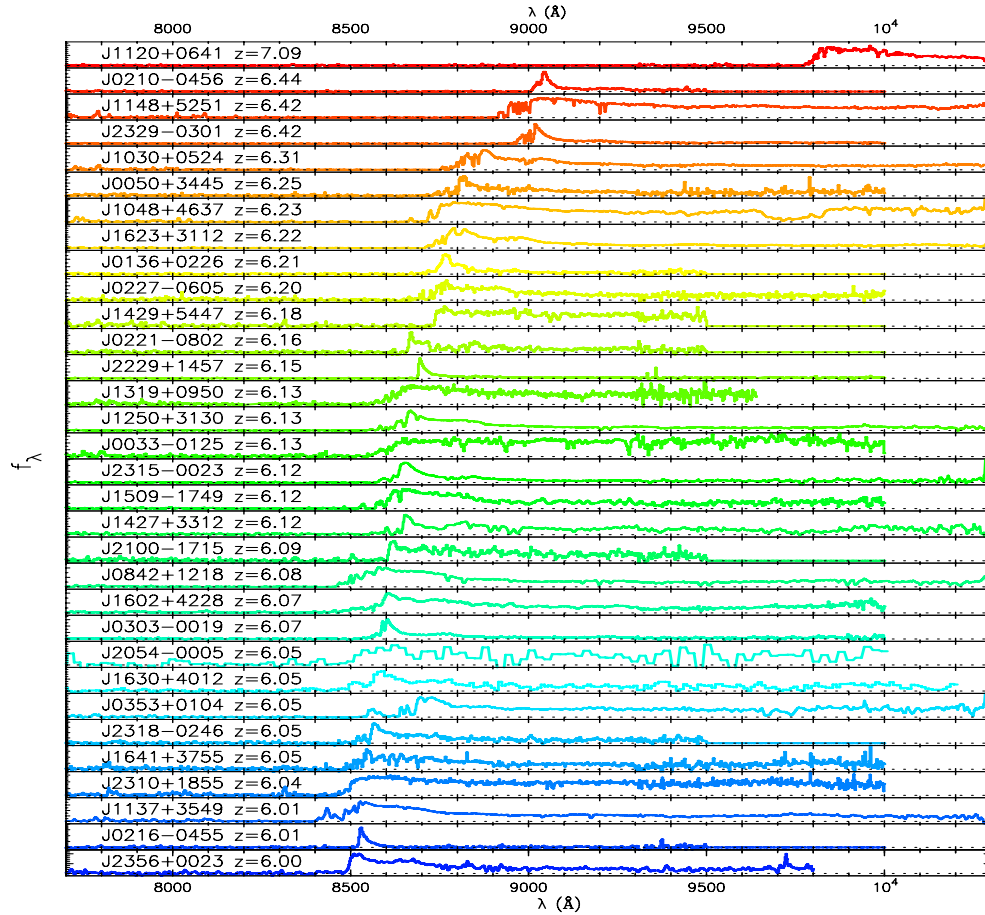


Figure 1.2: Dispersion spectra of all published quasars at  $z > 6$  as of 2012 June (Fan 2012). Some of the QSO spectra show no transmitted flux shortward of the Ly $\alpha$  wavelength at that redshift. These are the so-called Gunn-Peterson trough which indicates a non-negligible HI fraction in the IGM. [Figure courtesy: Fan (2012)]

Spectrum of GRB can also be used to constrain reionization using the same principles mentioned above. Using the spectrum of GRB 050904 at  $z = 6.3$ , Totani et al. (2006) have found the upper limits of  $x_{\text{HI}} < 0.17$  and  $0.60$  at 68% and 95% confidence levels.

An alternative and perhaps the most promising prospect of observing the epoch of reionization is through the detection of the 21 cm signature from neutral hydrogen in the IGM before

and during the reionization era (Carilli et al. 2002; Furlanetto et al. 2006; Pritchard & Loeb 2012; Mack & Wyithe 2012). The ground state of hydrogen exhibits a hyperfine transition involving the spins of the proton and the electron. The triplet state (with parallel spins) has a slightly higher energy than the singlet state (with anti-parallel) spins. This spin-flip transition from the triplet to singlet state corresponds to a rest frame frequency of 1420 MHz or a rest wavelength of 21 cm. This line, when redshifted, can be observed in radio frequencies and is often used to detect neutral hydrogen in the local universe. We will use this method for studying the post-reionization neutral hydrogen distribution later in this thesis (see Chapter 6 for details). However, obtaining the cosmological signal from this experiment is very difficult and hence challenging, because of the fact that it is expected to be a small contribution buried deep in the emission from other astrophysical sources (foregrounds) and in the system noise. But once such difficulties are overcome, this probe will be the strongest probe of not only reionization, but also the matter distribution at very small scales during the dark ages (Pritchard & Loeb 2010).

So, from the above discussion, it is clear that, one of the major challenges for modelling reionization is to match the model prediction with most of the available data sets which are accumulated by the measurements of QSO absorption line spectra (Fan et al. 2006), GRB spectra (Totani et al. 2006) and the CMB data (Hinshaw et al. 2012; Ade et al. 2013b). A major portion of this thesis is involved in modelling reionization by taking into account all these data sets.

### 1.3.4 Modelling the IGM and reionization

After reviewing our current understanding of reionization and the observations that have revealed it, we can now proceed to develop a basic theoretical framework required for modelling reionization of the IGM. In this section we will try to avoid the details of the mathematics and keep the description in a quite simple level. For more detailed information, one can look into some of beautiful reviews by Barkana & Loeb (2001); Loeb & Barkana (2001); Choudhury & Ferrara (2006a); Choudhury (2009) and references therein. For simplicity, we shall assume that the IGM consists only of hydrogen (neglect the presence of helium).

In the standard picture, each sources of reionization (stars or QSOs) generates the UV photons (with energies  $> 13.6$  eV) and ionizes its surrounding region. These regions are gradually expand and overlap. The basic aim for modelling reionization is to follow the evolution of these regions. One can compute the evolution of such expanding ionized region for individual ionizing sources until the reionization process is complete. However, evolution of these individual ionized bubbles will depend on the nature of their sources. So, another way of studying reionization is to take into account the global distribution of the sources and ionized volumes and statistically compute the globally averaged properties and fluctuations. We shall study this statistical approach below.

Let us start with the most useful statistical quantity which is studied in reionization, the volume filling factor of ionized regions  $Q_{\text{HII}}$ . This is the fraction of volume that is ionized and reionization is said to be complete when  $Q_{\text{HII}} = 1$ . The evolution of this quantity is governed

by the equation (Shapiro & Giroux 1987; Madau et al. 1999; Choudhury & Ferrara 2006a; Choudhury 2009)

$$\frac{dQ_{\text{HII}}}{dt} = \frac{\dot{n}_{\text{ph}}}{n_{\text{HI}}} - \frac{Q_{\text{HII}}}{t_{\text{rec}}} \quad (1.71)$$

where  $\dot{n}_{\text{ph}}$  is average number of ionizing photons produced per unit volume per unit time and  $n_{\text{HI}}$  is the mean comoving density of neutral hydrogen. The quantity  $t_{\text{rec}}$  is the recombination timescale of neutral hydrogen and is given by

$$t_{\text{rec}}^{-1} = \mathcal{C} \alpha_R(T) n_{\text{HI}} (1+z)^3 \quad (1.72)$$

In the above relation  $\alpha_R(T)$  is the recombination rate coefficient, which can depend on the temperature, however that dependence is often ignored while studying the volume filling factor.  $\mathcal{C}$  is called the *clumping factor* which takes into account the fact that the recombination rate in an inhomogeneous (clumpy) IGM is higher than a medium of uniform density and it is defined as

$$\mathcal{C} \equiv \frac{\langle n_{\text{HII}} n_e \rangle}{\langle n_{\text{HII}} \rangle \langle n_e \rangle} = \frac{\langle n_{\text{H}}^2 \rangle}{\langle n_{\text{H}} \rangle^2} \quad (1.73)$$

where the angle brackets denote space average.  $n_e$  represents the mean electron density. The last equality in the above relation holds when the IGM has hydrogen alone and is highly ionized, i.e.  $n_e = n_{\text{HII}} \approx n_{\text{H}}$ .

Note that, equation (1.71) implicitly assumes that the sources of ionizing photons are uniformly distributed over the volume we concern. This equation can be solved once we have a model for calculating the evolution of the photon production rate  $\dot{n}_{\text{ph}}$  and  $\mathcal{C}$ . In this description, reionization is said to be complete when  $Q_{\text{HII}}$  reaches unity.

However, in this simple description, we did not take into account the inhomogeneities in the IGM appropriately (except for  $\mathcal{C}$ ). One should have to account for the density distribution of the IGM. The recombination rate (which is  $\propto n_{\text{H}}^2$ ) is higher in high-density regions where the gas becomes neutral very quickly. Thus, the high-density regions will remain neutral for a longer time, whereas the regions of lower densities will be ionized first. This is also in agreement with the observations where we know that there exists such regions of high density which remain neutral even at the post-reionization phase; these regions are being gradually ionized (Miralda-Escudé et al. 2000). Of course, there should be a dependence on how far the high density region is from an ionizing source, but such complexities can only be dealt in a full numerical simulation. So, in this picture: (i) during the post-overlap stage all the low-density regions (with overdensities, say,  $\Delta < \Delta_{\text{HII}}$ ) will be ionized, while there will be some high density peaks which will still remain neutral. (ii) At the pre-overlap stage, a volume fraction  $1 - Q_{\text{HII}}$  of the universe is completely neutral (irrespective of the density), while the remaining  $Q_{\text{HII}}$  fraction of the volume is occupied by the ionized regions. However, within this ionized volume, the high density regions (with  $\Delta > \Delta_{\text{HII}}$ ) will still be neutral. Once reionization is

complete and  $Q_{\text{HII}}$  becomes unity, all regions with  $\Delta < \Delta_{\text{HII}}$  are ionized and the rest are neutral. The high-density neutral regions manifest themselves as the LLS (which we have discussed already in the previous section) in the QSO absorption spectra.

To write the equations incorporating the above picture, one needs to know the probability distribution function  $P(\Delta)d\Delta$  for the overdensities. Then only a mass fraction

$$F_M(\Delta_{\text{HII}}) = \int_0^{\Delta_{\text{HII}}} d\Delta \Delta P(\Delta) \quad (1.74)$$

needs to be ionized, while the remaining high density regions will be completely neutral as their recombination rates are high. Then the generalization of equation (1.71), appropriate for this description will be (Miralda-Escudé et al. 2000; Wyithe & Loeb 2003)

$$\frac{d[Q_{\text{HII}}F_M(\Delta_{\text{HII}})]}{dt} = \frac{\dot{n}_{\text{ph}}(t)}{n_{\text{HI}}} - Q_{\text{HII}}\alpha_R(T)n_{\text{HI}}R(\Delta_{\text{HII}})(1+z)^3 \quad (1.75)$$

where the factor  $R(\Delta_{\text{HII}})$  is the analogous of the clumping factor, and is given by

$$R(\Delta_{\text{HII}}) = \int_0^{\Delta_{\text{HII}}} d\Delta \Delta^2 P(\Delta) \quad (1.76)$$

In order to solve the equation (1.75), we assume that  $\Delta_{\text{HII}}$  does not evolve significantly with time in the pre-overlap stage, it is equal to a critical value  $\Delta_c$ . This critical density is usually determined from the the mean separation of the ionizing sources. Some people (Chiu et al. 2003; Choudhury & Ferrara 2005) suggest that  $\Delta_c$  should be similar to the typical overdensities near the boundaries of the collapsed haloes, which is typically  $\sim 50 - 60$ .

Once  $\Delta_c$  is fixed and we have some functional form for the IGM density distribution  $P(\Delta)$ , one can follow the evolution of  $Q_{\text{HII}}$  taking into account all the three stages of reionization and calculate the clumping factor and the effective recombination rate self-consistently without introducing any extra parameter. As we have outlined our basic formalism here, we can now go forward and discuss other details regarding the modelling of reionization.

The number of ionizing photons  $\dot{n}_{\text{ph}}(t)$  depends on the assumptions made regarding the sources. If we assume that hydrogen reionization is primarily driven by stellar sources, then this quantity should be determined by the star formation rate (SFR) density (i.e. SFR per comoving volume)  $\dot{\rho}_*(t)$ , which is given by (Choudhury 2009)

$$\dot{\rho}_*(t) = \frac{1}{a^3(t)} \frac{\bar{\rho}_b}{\bar{\rho}_m} \int_{M_{\text{min}}(t)}^{\infty} dM' \epsilon_* M' \frac{\partial^2 n(M', t)}{\partial M' \partial t} \quad (1.77)$$

where,  $M_{\text{min}}(t)$  is the lower mass cut-off at a given epoch and is decided by the cooling criteria and different feedback processes (as discussed earlier in Section 1.3.1). For neutral regions, we assume that this quantity is determined by the atomic cooling of gas within haloes (neglect cooling via molecular hydrogen). Within ionized regions, photo-heating of the gas can result

in a further suppression of star formation in low-mass haloes. We compute such (radiative) feedback self-consistently from the evolution of the thermal properties of the IGM.  $\epsilon_*$  is the fraction of baryonic mass,  $(\bar{\rho}_b/\bar{\rho}_m)M$ , which has been converted into stars. One should keep in mind that, many details of the star formation process could have been encoded within this single parameter  $\epsilon_*$ . This should, in principle, be a function of both halo mass  $M$  and time  $t$ . However, the dependencies are not well understood, that's why it is usually taken to be a constant. The quantity  $\partial n(M, t)/\partial M$  is basically the number density of collapsed objects per unit comoving volume within a mass range  $(M, M + dM)$  at an epoch  $t$  and it is already given in equation (1.57).

One can then write the SFR in terms of the fraction of collapsed mass in haloes more massive than  $M_{\min}(t)$  [see equation (1.55)]

$$\begin{aligned} f_{\text{coll}}(t) &= \frac{1}{\bar{\rho}_m} \int_{M_{\min}(t)}^{\infty} dM' M' \frac{\partial n(M', t)}{\partial M'} \\ &= \text{erfc} \left[ \frac{\delta_c}{\sqrt{2} D(t) \sigma(M_{\min})} \right] \end{aligned} \quad (1.78)$$

as

$$\dot{\rho}_*(t) = \epsilon_* \frac{\bar{\rho}_b}{a^3(t)} \frac{df_{\text{coll}}(t)}{dt} \quad (1.79)$$

Given the SFR, we can then calculate the rate of ionizing photons in the IGM per unit volume:

$$\dot{n}_{\text{ph}}(t) = N_{\text{ion}} n_b \frac{df_{\text{coll}}(t)}{dt} \quad (1.80)$$

$n_b$  is the total baryonic number density in the IGM. If we consider only hydrogen and neglect the presence of helium, then  $n_b = n_{\text{H}}$ . The quantity  $N_{\text{ion}}$  is the number of photons entering the IGM per baryon included into stars (Wyithe & Loeb 2007a), and is defined as

$$N_{\text{ion}} = \epsilon_* f_{\text{esc}} N_{\gamma} \quad (1.81)$$

where  $f_{\text{esc}}$  is the escape fraction of photons from the halo and  $N_{\gamma}$  is the specific number of photons emitted per baryon in stars, which depends on the stellar IMF and the corresponding stellar spectrum.

So, using the physics described above, we can now construct a semi-analytical model for studying the thermal and ionization history of the IGM, and suitable choices of corresponding model parameters, we can compare our model predictions with various observations related to reionization. Fig. 1.3 shows an example of one such model developed by Choudhury & Ferrara (2005, 2006b).

Although semi-analytical modelling of IGM can help us to acquire a good understanding of the underlying physics of cosmic reionization, they can take into account the physical processes only in some approximate sense. A detailed and complete description of reionization would require locating the ionizing sources, resolving the inhomogeneities in the IGM, following the scattering processes through a detailed description of radiative transfer. In that case one has to rely on numerical simulations (Abel et al. 1999; Gnedin et al. 2000; Gnedin 2000; Ciardi et al. 2001; Razoumov et al. 2002; Maselli et al. 2003; Bolton et al. 2004; Iliiev et al. 2006).

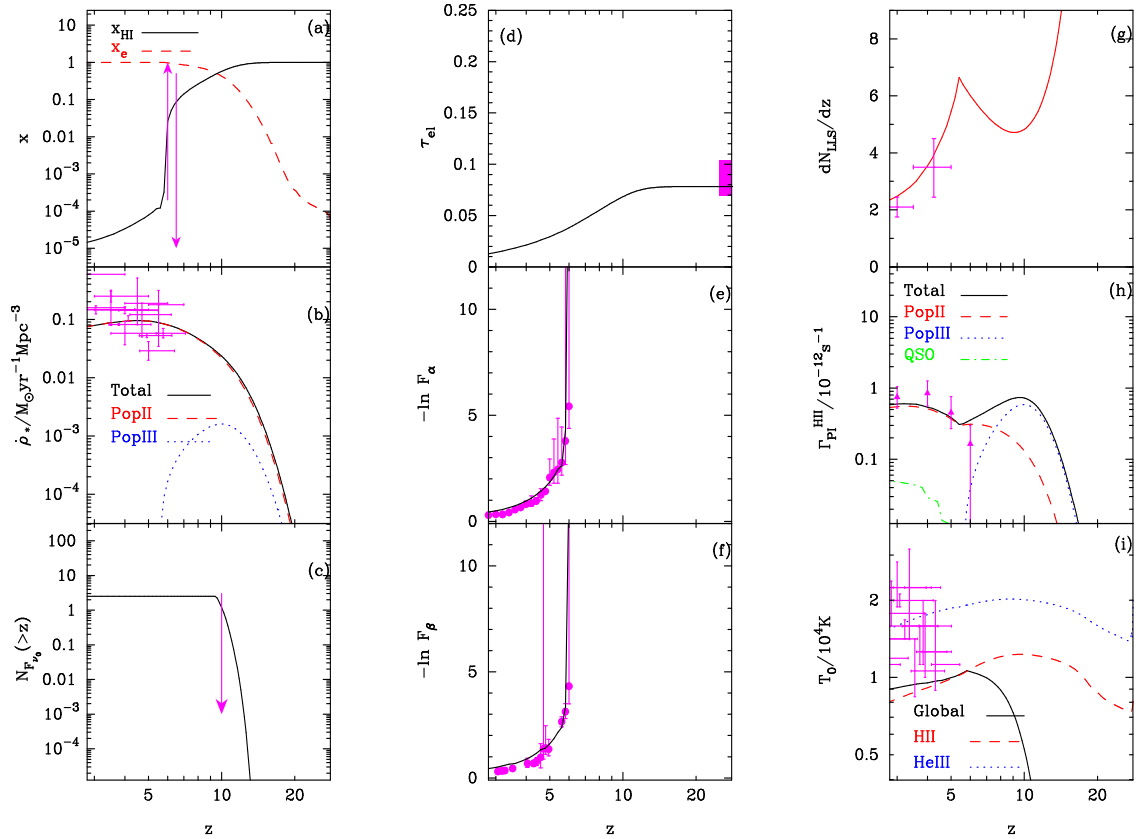


Figure 1.3: Comparison of analytical model (Choudhury & Ferrara 2005, 2006b) predictions with observations for the best-fit model. The different panels indicate: (a) The volume-averaged neutral hydrogen fraction  $x_{\text{HI}}$ , with observational lower limit from quasar absorption lines at  $z = 6$  and upper limit from Ly $\alpha$  emitters at  $z = 6.5$  (shown with arrows). In addition, the ionized fraction  $x_e$  is shown by the dashed line. (b) SFR  $\dot{\rho}_*$  for different stellar populations. (c) The number of source counts above a given redshift, with the observational upper limit from NICMOS HUDF shown by the arrow. The contribution to the source count is zero at low redshifts because of the J-dropout selection criterion. (d) Electron scattering optical depth, with observational constraint from WMAP 3-year data release. (e) Ly $\alpha$  effective optical depth. (f) Ly $\beta$  effective optical depth. (g) Evolution of Lyman-limit systems. (h) Photoionization rates for hydrogen, with estimates from numerical simulations (shown by points with error-bars). (i) Temperature of the mean density IGM. [Figure courtesy: Choudhury (2009)]

---

---

## CHAPTER 2

---

# MODEL-INDEPENDENT CONSTRAINTS ON REIONIZATION

In the previous chapter, we have developed the theoretical tools to understand the basic physics of structure formation and cosmological reionization. Now, in this chapter, we will apply those tools to study the modelling of reionization in detail. In particular, we shall be concerned about finding the constraints on reionization in a model-independent manner and comparing those with the various observations mentioned in Section 1.3.3.

In recent years, studies in reionization have been boosted by the availability of a wide range of data sets and the expectation that the volume of data would increase rapidly over the next few years (for reviews, see Furlanetto et al. 2006; Fan et al. 2006). Theoretically, reionization is modelled either semi-analytically or by numerical simulations. Unfortunately, the physical processes relevant to reionization are so complex that neither of the two approaches can capture the overall picture entirely. The simulations are indispensable for understanding detailed spatial distribution of ionized regions and topology of reionization. However, if one is interested in the evolution of globally-averaged quantities, then semi-analytical models prove to be very useful in providing insights. The main reason for this is that these models can probe a wide range of parameter space which can be quite large depending on our ignorance of the different processes.

The major uncertainty in modelling reionization is to model the star-formation history and transfer of radiation from the galaxies to the intergalactic medium (IGM) which is usually parameterized through  $N_{\text{ion}}$ , the number of photons entering the IGM per baryon in collapsed objects [see equation (1.81)]. This parameter, in principle, has a dependence on  $z$  which can arise from evolution of star-forming efficiency, fraction of photons escaping from the host halo and chemical and radiative feedback processes. Note that this parameter remains uncertain even in

numerical simulations, hence the semi-analytical models can become handy in studying a wide range of parameter values and the corresponding agreement with data sets. In analytical studies,  $N_{\text{ion}}(z)$  is either taken to be a piecewise constant function (Wyithe & Loeb 2003; Choudhury & Ferrara 2005) or parameterized using some known functions (Chiu et al. 2003; Pritchard et al. 2010) or modelled using a physically-motivated prescription (Choudhury & Ferrara 2006b). In particular, a model involving metal-free and normal stars with some prescription for radiative and chemical feedback can match a wide range of observations (Choudhury & Ferrara 2006b; Gallerani et al. 2006) and possibly make prediction regarding search for reionization sources by future experiments (Choudhury & Ferrara 2007).

However, the fact remains that many of the physical processes involved in modelling  $N_{\text{ion}}$  are still uncertain. Given this, it is worthwhile doing a detailed probe of the parameter space and determine the range of reionization histories that are allowed by the data. In other words, rather than working out the uncertain physics, one can ask the question as to what are the forms of  $N_{\text{ion}}(z)$  implied by the data itself. It is expected that in near future, with more data sets becoming available, the allowed range in the forms of  $N_{\text{ion}}(z)$  would be severely constrained, thus telling us exactly how reionization occurred. Now, it is obvious that the constraints on  $N_{\text{ion}}(z)$  will not be same for all redshifts, points where there are more and better data available, the constraint would be more tight. Similarly, since we deal with a heterogeneous set of data, it is expected that the constraints would depend on the nature of data used. It is thus important to know which aspects of reionization history can be constrained by what kind of data sets. A method which is ideally suited to tackle this problem is to use the principal component analysis (PCA); this is a technique to compute the most meaningful basis to re-express the unknown parameter set and the hope is that this new basis will reveal hidden detailed statistical structure.

Here, we make a preliminary attempt to constrain  $N_{\text{ion}}(z)$  using PCA and hence estimate the uncertainties in the reionization history. The main objective of the work would be to find out the widest possible range in reionization histories allowed by the different data sets.

## 2.1 Semi-analytical modelling of reionization

### 2.1.1 Features of the model

The semi-analytical model used in this work is based on Choudhury & Ferrara (2005) and Choudhury & Ferrara (2006b). Let us first summarize the main features of the model along with the modifications made in this work:

- The model accounts for IGM inhomogeneities by adopting a lognormal distribution according to the method outlined in Miralda-Escudé et al. (2000); reionization is said to be complete once all the low-density regions (say, with overdensities  $\Delta < \Delta_{\text{crit}} \sim 60$ ) are ionized. The mean free path of photons is thus determined essentially by the distribution

of high density regions:

$$\lambda_{\text{mfp}}(z) = \frac{\lambda_0}{[1 - F_V(z)]^{2/3}} \quad (2.1)$$

where  $F_V$  is the volume fraction of ionized regions and  $\lambda_0$  is a normalization parameter. In our earlier works, the value of this parameter was fixed by comparing with low redshift observations while in this work, we treat it as a free parameter. We follow the ionization and thermal histories of neutral, HII and HeIII regions simultaneously and self-consistently, treating the IGM as a multi-phase medium.

- The model assumes that reionization is driven by stellar sources. The stellar sources can further be divided into two classes, namely, (i) metal-free (i.e. PopIII) stars having a Salpeter IMF in the mass range  $1 - 100M_\odot$ : they dominate the photoionization rate at high redshifts; (ii) PopII stars with sub-solar metallicities also having a Salpeter IMF in the mass range  $1 - 100M_\odot$ .
- Reionization by UV sources is accompanied by photo-heating of the gas, which can result in a suppression of star formation in low-mass haloes. We compute such (radiative) feedback self-consistently from the evolution of the thermal properties of the IGM.
- Furthermore the *chemical feedback* including PopIII→PopII transition is implemented using merger-tree based genetic approach (Schneider et al. 2006). Under this approach, it is assumed that if a given star-forming halo has a progenitor which formed PopIII stars, then the halo under consideration is enriched and cannot form PopIII stars. In this work, we introduce an analytical formula for the transition from PopIII to PopII phase using the conditional probability of Press-Schechter mass function (Lacey & Cole 1993). The probability that a halo of mass  $M$  at  $z$  never had a progenitor in the mass range  $[M_{\text{min}}(z), M + M_{\text{res}}]$  is given by

$$f_{\text{III}}(M, z) = \frac{2}{\pi} \tan^{-1} \left[ \frac{\sigma(M + M_{\text{res}}) - \sigma(M)}{\sigma(M_{\text{min}}(z)) - \sigma(M + M_{\text{res}})} \right], \quad (2.2)$$

where  $M_{\text{min}}$  is the minimum mass of haloes which are able to form stars and  $M_{\text{res}}$  represents the minimum increase in mass (either by accretion or by merger) of an object so that it may be identified as a new halo. The fraction of collapsed haloes which are able to form PopII and PopIII stars at redshift  $z$  are given by the following relations:

$$\begin{aligned} f_{\text{coll,II}}(z) &= \frac{1}{\bar{\rho}_m} \int_{M_{\text{min}}(z)}^{\infty} dM [1 - f_{\text{III}}(M, z)] M \frac{\partial n(M, z)}{\partial M}, \\ f_{\text{coll,III}}(z) &= \frac{1}{\bar{\rho}_m} \int_{M_{\text{min}}(z)}^{\infty} dM f_{\text{III}}(M, z) M \frac{\partial n(M, z)}{\partial M}. \end{aligned} \quad (2.3)$$

with  $f_{\text{coll,II}}(z) + f_{\text{coll,III}}(z) = f_{\text{coll}}(z)$ . The quantity  $\bar{\rho}_m$  is the comoving density of dark matter and  $\partial n / \partial M$  is number density of collapsed objects per unit comoving volume per unit mass range (Press & Schechter 1974).

- Given the collapsed fraction, this model calculates the production rate of ionizing photons in the IGM as

$$\dot{n}_{\text{ph}}(z) = n_b \left[ N_{\text{ion,II}} \frac{df_{\text{coll,II}}}{dt} + N_{\text{ion,III}} \frac{df_{\text{coll,III}}}{dt} \right] \quad (2.4)$$

where  $n_b$  is the total baryonic number density in the IGM and  $N_{\text{ion,II}}(N_{\text{ion,III}})$  is the number of photons from PopII (PopIII) stars entering the IGM per baryon in collapsed objects. The parameter  $N_{\text{ion}}$  can actually be written as a combination of various other parameters:

$$N_{\text{ion}} \equiv \epsilon_* f_{\text{esc}} m_p \int_{\nu_{\text{HI}}}^{\infty} d\nu \left[ \frac{dN_\nu}{dM_*} \right] \equiv \epsilon m_p \int_{\nu_{\text{HI}}}^{\infty} d\nu \left[ \frac{dN_\nu}{dM_*} \right], \quad (2.5)$$

where  $\epsilon_*$  denotes the star-forming efficiency (fraction of baryons within collapsed haloes going into stars),  $f_{\text{esc}}$  is the fraction of photons escaping into the IGM,  $[dN_\nu/dM_*]$  gives the number of photons emitted per frequency range per unit mass of stars (which depends on the stellar IMF and the corresponding stellar spectrum) and  $\epsilon \equiv \epsilon_* f_{\text{esc}}$ . For PopII stars with sub-solar metallicities having a Salpeter IMF in the mass range  $1 - 100M_\odot$ , we get  $N_{\text{ion,II}} \approx 3200\epsilon_{\text{II}}$ , while for PopIII stars having a Salpeter IMF in the mass range  $1 - 100M_\odot$ , we get  $N_{\text{ion,III}} \approx 35000\epsilon_{\text{III}}$ .

In this Section, we take  $\epsilon_{\text{II}}, \epsilon_{\text{III}}$  (or, equivalently  $N_{\text{ion,II}}, N_{\text{ion,III}}$ ) to be independent of  $z$  and  $M$ , which implies that the star-forming efficiencies and the escape fractions do not depend on the mass of the star-forming halo and also do not evolve. However, note that the effective  $N_{\text{ion}}$  (which is the appropriately weighted average of  $N_{\text{ion,II}}$  and  $N_{\text{ion,III}}$ ) evolves with  $z$

$$N_{\text{ion}}(z) = \frac{N_{\text{ion,II}} \frac{df_{\text{coll,II}}}{dt} + N_{\text{ion,III}} \frac{df_{\text{coll,III}}}{dt}}{\frac{df_{\text{coll,II}}}{dt} + \frac{df_{\text{coll,III}}}{dt}} \quad (2.6)$$

At high redshifts, we expect  $df_{\text{coll,II}}/dt \rightarrow 0$ , hence  $N_{\text{ion}}(z) \rightarrow N_{\text{ion,III}}$ , and similarly at low redshifts where chemical enrichment is widespread, we have  $N_{\text{ion}}(z) \rightarrow N_{\text{ion,II}}$ .

- We also include the contribution of quasars based on their observed luminosity function at  $z < 6$  (Hopkins et al. 2007); we assume that they have negligible effects on IGM at higher redshifts. They are significant sources of photons at  $z \lesssim 4$  and are particularly relevant for studying helium reionization.

## 2.1.2 Data sets and free parameters

Usually, the model is constrained by comparing with a variety of observational data, namely, (i) redshift evolution of Lyman-limit absorption systems (LLS), (ii) IGM Ly $\alpha$  and Ly $\beta$  optical depths, (iii) electron scattering optical depth, (iv) temperature of the mean intergalactic gas, and

(v) cosmic star formation history (see Fig. 1.3). However, most of the constraints on the model come from a subset of the above data sets. In this work, we would like to carry out a detailed likelihood analysis of the parameters. Hence to keep the analysis simple, the likelihood analysis is done using only three particular data sets which are discussed as follows (Mitra et al. 2011, 2012):

(i) We use estimates for the photoionization rates  $\Gamma_{\text{PI}}$  obtained using Ly $\alpha$  forest Gunn-Peterson optical depth observations and a large set of hydrodynamical simulations (Bolton & Haehnelt 2007). The error-bars in these data points take into account the uncertainties in the thermal state of the IGM in addition to the observational errors in the Ly $\alpha$  optical depth. The data points have a mild dependence on the cosmological parameters which has been taken into account in this work. We also find that although the error-bars on  $\Gamma_{\text{PI}}$  are highly asymmetric, those on  $\log(\Gamma_{\text{PI}})$  are relatively symmetric; hence we use values of  $\log(\Gamma_{\text{PI}})$  and the corresponding errors in our likelihood analysis. The photoionization rate can be obtained in our model from  $\dot{n}_{\text{ph}}(z)$  using the relation

$$\Gamma_{\text{PI}}(z) = (1+z)^3 \int_{\nu_{\text{HI}}}^{\infty} d\nu \lambda_{\text{mfp}}(z; \nu) \dot{n}_{\text{ph}}(z; \nu) \sigma_H(\nu) \quad (2.7)$$

where  $\nu$  the frequency of radiation,  $\nu_{\text{HI}}$  is the threshold frequency for photoionization of hydrogen and  $\sigma_H(\nu)$  is the photoionization cross section of hydrogen.

(ii) The second set of observations we have used is the CMBR data sets. We should mention here that, instead of CMB data, one can use the single WMAP7 data of electron scattering optical depth  $\tau_{\text{el}}$  (Mitra et al. 2011). The reported value of this quantity depends on the background cosmological model used. The quantity  $\tau_{\text{el}}$  can be obtained from our model given the global reionization history, in particular the comoving density of free electrons  $n_e(z)$ :

$$\tau_{\text{el}}(z) = \sigma_T c \int_0^{z[t]} dt n_e (1+z)^3 \quad (2.8)$$

where  $\sigma_T$  is the Thomson scattering cross section.

However, the  $\tau_{\text{el}}$  constraint is treated as a single data point which should be thought as a simplification because CMB polarization observations are, in principle, sensitive to the shape of the reionization history (Burigana et al. 2008). We know that, the amplitude of fluctuations in the large-scale (low- $l$ )  $E$ -mode component of CMB polarization provides the best constraint on  $\tau_{\text{el}}$ . Using the data from seven year WMAP and the assumption of instantaneous reionization, Larson et al. (2011) find  $\tau_{\text{el}} = 0.088 \pm 0.015$ . However, recent theoretical and numerical studies suggest that reionization is a fairly complex process. In that case, the low- $l$   $E$ -mode spectrum depends not just on  $\tau_{\text{el}}$  but also on the detailed redshift evolution of the number density of free electrons in the IGM,  $x_e(z)$ . For fixed values of  $\tau_{\text{el}}$  and all other relevant cosmological parameters, differences in  $x_e(z)$  can affect the shape of the large-scale  $E$ -mode angular power spectrum up to multipoles  $l \simeq 40 - 50$ . Because of this dependence, measurements of the low- $l$   $C_l^{\text{EE}}$  should place at least weak constraints on the overall reionization history in addition to the

constraint on the total optical depth. Now, in our model, the change in the parameter  $N_{\text{ion}}(z)$  directly corresponds to the change in  $x_e(z)$  i.e. in other words, changes in  $N_{\text{ion}}$  can affect the shape of low- $l$   $C_l^{\text{EE}}$ . So, incorporating the data sets for large-scale EE polarization signal in our model can provide important information about the evolution of  $N_{\text{ion}}$  at  $z > 6$  beyond the information about  $\tau_{\text{el}}$ . Our hope is this may be most useful for distinguishing the models of reionization with different ionization histories but same optical depth. Keeping this in mind, it would be more prudent to work with the actual data related to the angular power spectra  $C_l$  and obtain constraints on reionization parameters; the constraint on  $\tau_{\text{el}}$  will be determined a posteriori.

The moment we include the  $C_l$ 's (TT+TE+EE) in our analysis, we realize that parameters related to reionization may have strong degeneracies with (some of) the cosmological parameters and hence constraints on reionization without varying cosmological parameters would be misleading. On the other hand, including all the cosmological parameters in the analysis would increase the number of free parameters to a large number. Usually, it is found that  $\tau_{\text{el}}$  is strongly degenerate with the normalization of the matter power spectrum  $\sigma_8$  and also with the slope  $n_s$  (Spergel et al. 2003). Hence, we carry out our analysis by varying only these two parameters (in addition to the parameters related to reionization model) and keeping all the other cosmological parameters fixed to their mean value (for details, see Mitra et al. 2012). However, we should keep in mind that the uncertainties in reionization history would possibly be slightly underestimated as the parameters related to reionization are slightly degenerate with the other cosmological parameters.

(iii) Finally, we use the redshift distribution of LLS  $dN_{\text{LL}}/dz$  over a wide redshift range  $0.36 < z < 6$  (Songaila & Cowie 2010). The data points are obtained using a large sample of QSO spectra which results in extremely small statistical errors. However, there are various systematic effects arising from effects like the incidence of proximate LLS and uncertainties in the continuum. Usually, these effects contribute to about 10–20% uncertainty in the data points. The quantity  $dN_{\text{LL}}/dz$  can be calculated in our model from the mean free path:

$$\frac{dN_{\text{LL}}}{dz} = \frac{c}{\sqrt{\pi} \lambda_{\text{mfp}}(z) H(z) (1+z)} \quad (2.9)$$

Note that inclusion of the Lyman-limit systems in the analysis is crucial for constraining the parameter  $\lambda_0$ , the normalization which determines the mean free path of photons.

The free parameters for this model would be  $\epsilon_{\text{II}}, \epsilon_{\text{III}}$  (or, equivalently  $N_{\text{ion,II}}, N_{\text{ion,III}}$ ),  $\lambda_0$ ,  $n_s$  and  $\sigma_8$ . We shall refer this model as the model with chemical feedback.

We then perform the likelihood calculations using these three data sets. The likelihood function used in our calculations is given by

$$L \propto \exp(-\mathcal{L}) \quad (2.10)$$

where  $\mathcal{L}$  is the negative of the log-likelihood and estimated using the relation

$$\mathcal{L} = \frac{1}{2} \sum_{\alpha=1}^{N_{\text{obs}}} \left[ \frac{\mathcal{J}_{\alpha}^{\text{obs}} - \mathcal{J}_{\alpha}^{\text{th}}}{\sigma_{\alpha}} \right]^2 + \mathcal{L}' \quad (2.11)$$

where  $\mathcal{J}_{\alpha}$  represents the set of  $N_{\text{obs}}$  observational data points related to photoionization rate and distribution of Lyman-limit systems, i.e.,  $\mathcal{J}_{\alpha} = \{\log(\Gamma_{\text{PI}}), dN_{\text{LL}}/dz\}$ ,  $\sigma_{\alpha}$  are the corresponding observational error-bars and  $\mathcal{L}'$  is negative of WMAP7 (or PLANCK) log-likelihood function for  $C_l^{\text{TT}}$ ,  $C_l^{\text{TE}}$  and  $C_l^{\text{EE}}$  up to  $l = 2000$ . We constrain the free parameters by maximizing the likelihood function with a prior that reionization should be completed by  $z = 5.8$ , otherwise it will not match Ly $\alpha$  and Ly $\beta$  forest transmitted flux data.

In this work, we calculate likelihoods using the code based on the publicly available COSMOMC<sup>1</sup> (Lewis & Bridle 2002) code. Besides this, throughout we work in a flat cold dark matter model with a cosmological constant ( $\Lambda$ CDM) cosmology with the cosmological parameters given by the WMAP7 (based on RECFAST 1.5 (Seager et al. 1999, 2000; Wong et al. 2008) and version 4.1 of the WMAP likelihood) best-fit values:  $\Omega_m = \Omega_{\text{DM}} + \Omega_b = 0.27$ ,  $\Omega_{\Lambda} = 1 - \Omega_m$ ,  $\Omega_b h^2 = 0.02249$ ,  $h = 0.704$  and  $dn_s/d \ln k = 0$  (Larson et al. 2011). Note that, here in all cases,  $\tau_{\text{el}}$  is a derived parameter and the error on obtaining this quantity is slightly underestimated because of neglecting the degeneracies between  $\tau_{\text{el}}$  and other cosmological parameters.

### 2.1.3 Reionization constraints

The results of our likelihood analysis using the reionization model described above are summarized in Table 2.1. The evolution of various quantities for models which are allowed within 95% confidence limit is shown in Fig. 2.1.

The top-left panel of the figure shows the evolution of the effective  $N_{\text{ion}}$  as given by equation (2.6). One can see that the quantity attains a constant value  $\approx 10$  at  $z < 6$  which is a consequence of the fact that the photon emissivity at those epochs are purely determined by PopII stars. However at higher redshifts, the value of  $N_{\text{ion}}$  increases with  $z$  because of the presence of PopIII stars. It is clear that the data cannot be fitted with PopII stars with constant  $N_{\text{ion,II}}$  alone, one requires a rise in  $N_{\text{ion}}$  at higher redshifts. For the kind of chemical feedback employed in the model, the rise is rather smooth and gradual.

The mean values of parameters quoted in Table 2.1 are similar to the best-fit model described in Choudhury & Ferrara (2006b) and hence the corresponding reionization history is similar to those described in the same paper. This can be readily verified from Fig. 2.1 where we see that reionization starts around  $z \approx 15$  driven by PopIII stars, and it is 90 per cent complete by  $z \approx 7.3$ . After a rapid initial phase, the growth of the volume filled by ionized regions slows down at  $z \lesssim 10$  due to the combined action of chemical and radiative feedback, making

<sup>1</sup><http://cosmologist.info/cosmomc/>

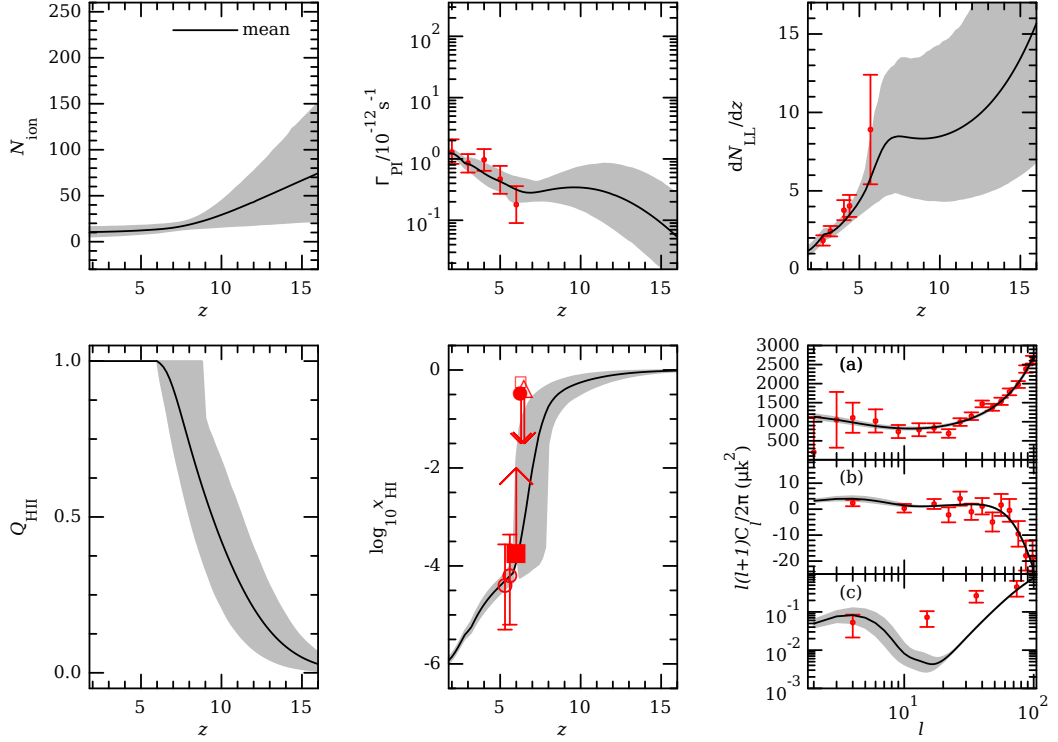


Figure 2.1: The marginalized posteriori distribution of various quantities related to reionization history for a model with chemical feedback (Choudhury & Ferrara 2006). The solid lines correspond to the model described by mean values of the parameters while the shaded regions correspond to  $2\text{-}\sigma$  limits. The points with error-bars denote the observational data points. *Top-left:* the evolution of the effective  $N_{\text{ion}}(z)$ ; *Top-middle:* the hydrogen photoionization rate  $\Gamma_{\text{PI}}(z)$  along with the constraints from Bolton & Haehnelt (2007); *Top-right:* the LLS distribution  $dN_{\text{LL}}/dz$  with data points from Songaila & Cowie (2010); *Bottom-left:* the volume filling factor of HII regions  $Q_{\text{HII}}(z)$ ; *Bottom-middle:* the global neutral hydrogen fraction  $x_{\text{HI}}(z)$  with observational limits from QSO absorption lines (Fan et al. 2006; filled square), Ly $\alpha$  emitter luminosity function (Kashikawa et al. 2006; open triangle) and GRB spectrum analysis (Totani et al 2006; open square). Also shown the constraints using dark gap statistics on QSO spectra (Gallerani et al 2008a; open circles) and GRB spectra (Gallerani et al. 2008b; filled circle); *Bottom-right:* (a) TT, (b) TE and (c) EE power spectra with the data points from WMAP7 (Larson et al. 2010).

Parameters	Mean value	95% confidence limits
$\epsilon_{\text{II}}$	0.003	[0.002, 0.006]
$\epsilon_{\text{III}}$	0.012	[0.001, 0.031]
$\lambda_0$	3.278	[1.512, 5.443]
$n_s$	0.969	[0.956, 0.983]
$\sigma_8$	0.812	[0.795, 0.834]
$\tau_{\text{el}}$	0.084	[0.066, 0.107]
$z(Q_{\text{HII}} = 0.5)$	9.467	[8.050, 11.120]
$z(Q_{\text{HII}} = 0.99)$	6.820	[5.800, 8.017]

Table 2.1: The marginalized posterior probabilities with 95% C.L. errors of all free parameters (top five parameters) and derived parameters (from the sixth parameter down) for the reionization model with PopII and PopIII stars.

reionization a considerably extended process completing only at  $z \approx 6$ . Our likelihood analysis shows that reionization is 50 (99) % complete between redshifts  $z = 8.1 - 11.1$  ( $5.8 - 8.0$ ) at 95% confidence level. Hence, under the assumptions made in the model, we find that completion of reionization cannot occur earlier than  $z \approx 8$ , essentially ruling out models of very early reionization. The reason for this is that the number of photons in the IGM at  $z = 6$  is very low as implied by the Ly $\alpha$  forest data. In order to take the data point into account, the models typically cannot have too high a emissivity at  $z \sim 6$ . On the other hand, the constraints on  $\tau_{\text{el}}$  (or equivalently the CMB data) imply that reionization must be initiated early enough. Thus the IGM has to go through a gradual reionization phase. As we discussed above, the gradual reionization is maintained by a combined action of radiative and chemical feedback effects.

## 2.2 Principal component analysis

Principal component analysis (PCA) has been known as one of the most valuable results from applied linear algebra. PCA is used abundantly in all forms of analysis, because it is a simple, non-parametric method of extracting relevant information from confusing data sets. With minimal additional effort PCA provides a road map for how to reduce a complex data set to a lower dimension to reveal the sometimes hidden, simplified structure that often underlies it. The main aim of principal component analysis is to compute the most meaningful basis to re-express a noisy data set. The hope is that this new basis will filter out the noise and reveal hidden structure. So, PCA is basically a variable reduction procedure. It is useful when we have obtained data on a number of variables (possibly a large number of variables), and believe that there is some redundancy in those variables. Because of this redundancy, we believe that it should be possible to reduce the observed variables into a smaller number of principal components (artificial variables) that will account for most of the variance in the observed variables. The main advantage of this method is that the resulting components will display varying degrees of corre-

lation with the observed variables, but are completely uncorrelated with one another. Because it is a variable reduction procedure, principal component analysis is very similar in many respects to exploratory *factor analysis*. However, there are significant conceptual differences between these two procedures (Hatcher 1994). In this section, we shall outline the principal component method and introduce the notation that we will use throughout this chapter.

### 2.2.1 Motivation

It is most likely that the star-forming efficiencies and escape fractions and hence  $N_{\text{ion}}$  are functions of halo mass and redshift; however since the dependencies are not well understood, they were taken to be constant for each considered stellar population in the previous Section. The question one can ask is that how would the constraints on reionization histories of the previous Section change when the evolution of  $N_{\text{ion}}$  is taken into account. Ideally one would like to do a rigorous likelihood analysis with  $N_{\text{ion}}$  varying with  $z$  and see the possible ranges of reionization histories consistent with available data. One possible approach could be to parameterize  $N_{\text{ion}}(z)$  using some (known) function and constrain the parameters of the function (Pritchard et al. 2010). However, it is possible that the reionization constraints thus obtained could depend on the nature of the function chosen. In addition, it is not clear as to how many parameters should be used to parameterize the function.

An alternative approach is to assume  $N_{\text{ion}}(z)$  to be completely arbitrary and decompose it into principal components. These principal components essentially filters out components of the model which are most sensitive to the data. Obviously, these components are the ones which can be constrained most accurately, while the others cannot be done so. This principal component analysis (PCA), thus, should give an idea as to which aspects of  $N_{\text{ion}}$  can be constrained with available data. This implies that one should get a clear idea about the optimum number of parameters required to model  $N_{\text{ion}}$  to fit the data most accurately.

In order to carry out such analysis, we modify the model described in the previous Section in following respects:

- We take  $N_{\text{ion}}$  to be a function of  $z$ . Unlike in the previous Section, we do not explicitly assume the presence of two population of stars but rather we include only one stellar population; any change in the characteristics of these stars over time would be accounted for in the evolution of  $N_{\text{ion}}$ .
- Clearly, the chemical feedback prescription has to be abandoned in this model, as there are no two different populations of stars anymore. The chemical feedback is rather taken into account indirectly by the evolution of  $N_{\text{ion}}$ . However, we retain radiative feedback in the model given its weak dependence on the specific stellar population properties.

In recent years there has been a wide use of this method in cosmological data analysis. The first set of works were mostly related to CMB data where, e.g., Efstathiou & Bond (1999)

and Efstathiou (2002) used principal component analysis of CMB anisotropy measurements to investigate degeneracies among cosmological parameters. Kadota et al. (2005) applied PCA to study how accurately CMB observables can constrain inflation potential in a model-independent manner. Leach (2006) used PCA techniques for measuring departures from scale-invariance in the primordial power spectrum of density perturbations using cosmic microwave background (CMB)  $C_l$  data. Mortonson & Hu (2008a) developed a model-independent method to study the effects of reionization on the large-scale E-mode polarization for any reionization history with the help of principal component analysis followed by the earlier work by Hu & Holder (2003). In the context of weak lensing surveys, Munshi & Kilbinger (2006) studied the degeneracies between cosmological parameters and measurement errors from cosmic shear surveys using PCA. The PCA has also been employed as an effective tool in the context of type Ia supernova observations to constrain the equation of state of dark energy (Huterer & Starkman 2003; Huterer & Cooray 2005; Crittenden et al. 2009; Clarkson & Zunckel 2010).

## 2.2.2 Brief theory of PCA

Consider a set of  $n_{\text{obs}}$  observational data points labeled by  $\mathcal{G}_\alpha$ ,  $\alpha = 1, 2, \dots, n_{\text{obs}}$ . Recall that  $\mathcal{G}_\alpha$  can represent combinations of different data sets, e.g., in our case photoionization rate  $\Gamma_{\text{PI}}$ , the redshift distribution of Lyman-limit systems  $dN_{\text{LL}}/dz$  and the large-scale E-mode polarization angular power spectrum  $C_l^{\text{EE}}$  ( $l \leq 23$ ).

Now, let us assume that our model contains an unknown function  $N_{\text{ion}}(z)$ , which we wish to constrain through observations. We can divide our entire redshift interval  $[z_{\text{min}}, z_{\text{max}}]$  into (equal) bins of width  $\Delta z$  and represent  $N_{\text{ion}}(z)$  by a set of  $n_{\text{bin}}$  discrete free parameters

$$N_{\text{ion}}(z_i) \equiv N_i; \quad i = 1, 2, \dots, n_{\text{bin}} \quad (2.12)$$

where

$$z_i = z_{\text{min}} + (i - 1)\Delta z \quad (2.13)$$

and the bin width is given by

$$\Delta z = \frac{z_{\text{max}} - z_{\text{min}}}{n_{\text{bin}} - 1}. \quad (2.14)$$

In other words, we have modelled reionization using the value of  $N_{\text{ion}}$  in each redshift bin. We can also include other free parameters apart from  $N_{\text{ion}}(z_i)$  in the analysis, like the normalization of the mean free path  $\lambda_0$ , cosmological parameters etc. We will address the inclusion of other parameters later in this Section.

The next step is to assume a fiducial model for  $N_{\text{ion}}(z_i)$ , which we denote by  $N_{\text{ion}}^{\text{fid}}(z_i)$ . The fiducial model should be chosen such that it is close to the ‘‘true’’ model. The departure from the fiducial model is denoted by

$$\delta N_{\text{ion}}(z_i) = N_{\text{ion}}(z_i) - N_{\text{ion}}^{\text{fid}}(z_i) \equiv \delta N_i. \quad (2.15)$$

We can then construct the  $n_{\text{bin}} \times n_{\text{bin}}$  Fisher matrix

$$F_{ij} = \sum_{\alpha=1}^{n_{\text{obs}}} \frac{1}{\sigma_{\alpha}^2} \frac{\partial \mathcal{G}_{\alpha}^{\text{th}}}{\partial N_i} \frac{\partial \mathcal{G}_{\alpha}^{\text{th}}}{\partial N_j}, \quad (2.16)$$

where  $\mathcal{G}_{\alpha}^{\text{th}}$  is theoretical value of  $\mathcal{G}_{\alpha}$  modelled using the  $N_i$  and  $\sigma_{\alpha}$  is the observational error on  $\mathcal{G}_{\alpha}$ . The derivatives in the above relation are evaluated at the fiducial model  $N_i = N_i^{\text{fid}}$ .<sup>2</sup>

Once the Fisher matrix is constructed, we can determine its eigenvalues and corresponding eigenvectors. The principal value decomposition is then given by the eigenvalue equation

$$\sum_{j=1}^{n_{\text{bin}}} F_{ij} S_{jk} = \lambda_k S_{ik} \quad (2.17)$$

where  $\lambda_k$  are the eigenvalues and the eigenfunctions corresponding to  $\lambda_k$  are the  $k$ -th column of the matrix  $S_{ik}$ , these are the principal components of  $N_i$ . They can be thought of a function of  $z$  i.e.,  $S_{ik} = S_k(z_i)$ .

The eigenvalues  $\lambda_k$  are usually ordered such that  $\lambda_1 \geq \lambda_2 \geq \dots \geq \lambda_{n_{\text{bin}}}$ , i.e.,  $\lambda_1$  corresponds to the largest eigenvalue while  $\lambda_{n_{\text{bin}}}$  the smallest. The eigenfunctions are both orthonormal and complete and hence we can expand any function of  $z$  as linear combinations of them. In particular we can expand the departure from the fiducial model as

$$\delta N_i = \sum_{k=1}^{n_{\text{bin}}} m_k S_k(z_i); \quad m_k = \sum_{i=1}^{n_{\text{bin}}} \delta N_{\text{ion}}(z_i) S_k(z_i) \quad (2.18)$$

where  $m_k$  are the expansion coefficients with  $m_k = 0$  for the fiducial model. We can now describe our model by the coefficients  $m_k$  rather than the original parameters  $\delta N_i$ . The advantage is that, unlike  $N_i$ , the coefficients  $m_k$  are uncorrelated with variances given by the inverse eigenvalue:

$$\langle m_i m_j \rangle = \frac{1}{\lambda_i} \delta_{ij} \quad (2.19)$$

The accuracy with which we can determine  $\delta N_{\text{ion}}$  at a particular  $z_i$  is determined by the Cramer-Rao bound

$$\langle \delta N_{\text{ion}}^2(z_i) \rangle \geq \sum_{k=1}^{n_{\text{bin}}} \frac{S_k^2(z_i)}{\lambda_k} \quad (2.20)$$

So, the largest eigenvalues correspond to minimum variance. The eigenvalues which are smaller would essentially increase the uncertainty in determining  $\delta N_{\text{ion}}(z_i)$ . Hence, most of the information relevant for the observed data points  $\mathcal{G}_{\alpha}$  is contained in the first few modes with the

<sup>2</sup>It is worthwhile to mention that any analysis based on the Fisher matrix  $F_{ij}$ , in principle, depends on the fiducial model chosen. The principal component analysis, which essentially involves diagonalizing  $F_{ij}$ , is thus dependent on the choice of  $N_i^{\text{fid}}$  too. In this sense, the PCA is not completely model-independent.

largest eigenvalues. One may then attempt to reconstruct the function  $\delta N_{\text{ion}}(z_i)$  using only the first  $M \leq n_{\text{bin}}$  modes:

$$\delta N_i^{(M)} = \sum_{k=1}^M m_k S_k(z_i). \quad (2.21)$$

However, in neglecting the last  $n_{\text{bin}} - M$  terms, one introduces a bias in determining  $\delta N_{\text{ion}}(z_i)$ . One has to then use a carefully chosen  $M$  to perform the analysis; the choice usually depends on the particular problem in hand.

In realistic situations, there will be other free parameters (apart from  $m_k$  or  $\delta N_i$ ) in the model. Let there be  $n_{\text{ext}}$  number of extra parameters other than  $m_k$ ; this means that we are now dealing with a total of  $n_{\text{tot}} = n_{\text{bin}} + n_{\text{ext}}$  parameters. In this case, we can still form the Fisher matrix of  $n_{\text{tot}} \times n_{\text{tot}}$  dimensions which can be written as

$$\mathcal{F} = \begin{pmatrix} \mathbf{F} & \mathbf{B} \\ \mathbf{B}^T & \mathbf{F}' \end{pmatrix} \quad (2.22)$$

where  $\mathbf{F}$  is the  $n_{\text{bin}} \times n_{\text{bin}}$ -dimensional Fisher matrix for the  $\delta N_i$ ,  $\mathbf{F}'$  is the  $n_{\text{ext}} \times n_{\text{ext}}$ -dimensional Fisher matrix for the other parameters and  $\mathbf{B}$  is a  $n_{\text{bin}} \times n_{\text{ext}}$ -dimensional matrix containing the cross-terms. One can then invert the above  $\mathcal{F}$  to obtain the corresponding Hessian matrix  $\mathcal{T} = \mathcal{F}^{-1}$ . Following that, one simply retains the sub-block  $\mathbf{T}$  corresponding to  $\delta N_i$  whose principal components will be ‘‘orthogonalized’’ to the effect of the other parameters. The resulting ‘‘degraded’’ sub-block will be (Press et al. 1992)

$$\tilde{\mathbf{F}} = \mathbf{T}^{-1} = \mathbf{F} - \mathbf{B}\mathbf{F}'^{-1}\mathbf{B}^T \quad (2.23)$$

In this work we need to use the above formalism to marginalize over the normalization of the mean free path  $\lambda_0$ , cosmological parameters  $n_s$  and  $\sigma_8$ . So, in this case,  $n_{\text{ext}} = 3$ .

## 2.3 Constraining reionization scenario using PCA

So far, we have outlined the basic formalism of PCA and stated the advantages of applying this non-parametric approach to the datasets related to reionization. In this section, we shall see how this PCA helps us finding the useful constraints on reionization scenario.

### 2.3.1 Fiducial model and the Fisher matrix

The first task is to make an assumption for the fiducial model  $N_{\text{ion}}^{\text{fid}}(z)$ . The model should match the  $\Gamma_{\text{PI}}$  and  $dN_{\text{LL}}/dz$  data points at  $z < 6$  and also produce  $\tau_{\text{el}}$  or the CMBR angular power spectra in the acceptable range. Unfortunately, the simplest model with  $N_{\text{ion}}$  being constant

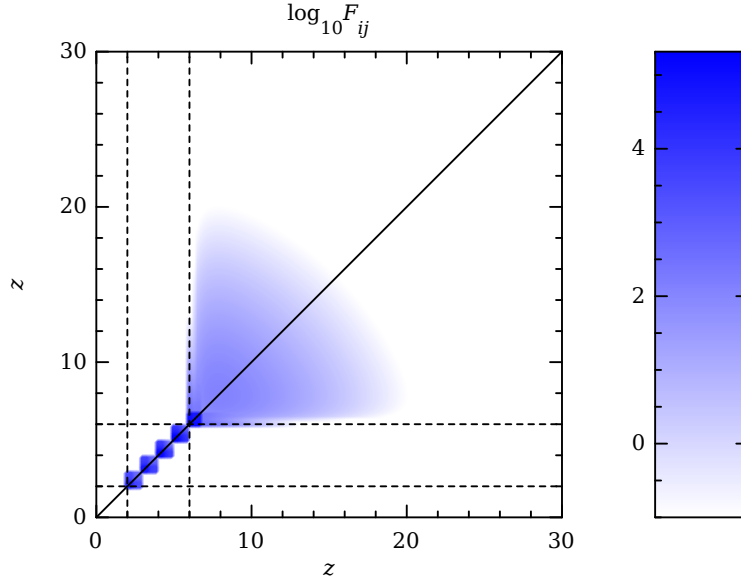


Figure 2.2: The Fisher matrix  $F_{ij}$  in the  $z - z$  plane.

does not have these requirements (recall models with only PopII stars were disfavored in the previous Section). We have found earlier that the effective  $N_{\text{ion}}$  should be higher at early epochs dominated by PopIII stars and should approach a lower value at  $z \sim 6$  determined by PopII stars. In this work we take  $N_{\text{ion}}^{\text{fid}}$  to be the model given by mean values of the free parameters in Section 2.1.3.

The choice of this  $N_{\text{ion}}^{\text{fid}}$  may seem somewhat arbitrary as there could be many other forms of  $N_{\text{ion}}$  which may match the data equally well. We have chosen this to be our fiducial model because of the following reasons: (i) it is obtained from a physically-motivated model of star formation which includes both metal-free and normal stars, (ii) it is characterized by a higher  $N_{\text{ion}}$  at higher redshifts and hence produces a good match with different observations considered in this work, and (iii) the transition from higher to lower values is smooth (i.e., there is no abrupt transition or sharp features). The final conclusions of this work (to be presented later in the Section) would hold true for any fiducial model having these three properties (though the actual functional form might be different). The match with the data for our fiducial model is similar to Fig. 2 of Choudhury (2009).

We have run the reionization models over a redshift range  $[z_{\text{min}} : z_{\text{max}}] = [0 : 30]$ , with a bin width of  $\Delta z = 0.2$ . This gives  $n_{\text{bin}} = 151$ . We have checked and found that our main conclusions are unchanged if we vary the bin width between 0.1–0.5.

The Fisher matrix  $F_{ij}$  defined in equation (2.16) is evaluated at the fiducial model and is shown as a shaded plot in the  $z - z$  plane in Fig. 2.2. Firstly, the components of the the matrix

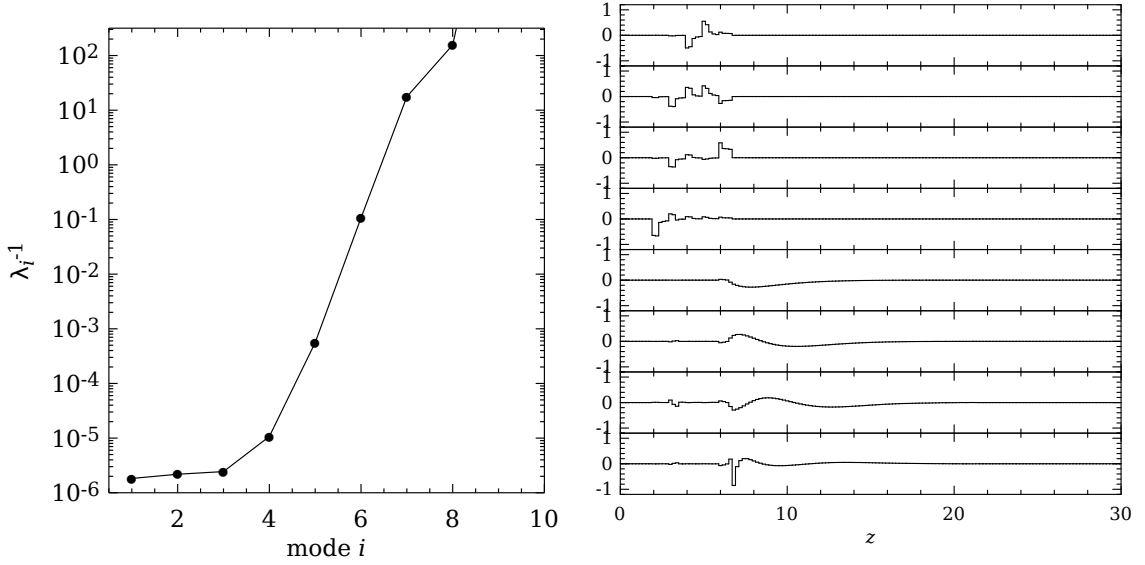


Figure 2.3: *Left panel:* The inverse of eigenvalues of the Fisher matrix  $F_{ij}$  which essentially measures the variance on the corresponding coefficient. For modes larger than 8, the eigenvalues are extremely small. *Right panel:* The first 8 eigenmodes of the Fisher matrix, i.e.,  $S_k(z)$ ;  $k = 1, \dots, 8$ .

vanish for  $z < 2$  because there are no data points considered at these redshifts. The plot shows different characteristics for  $F_{ij}$  at redshift intervals  $2 < z < 6$  and  $z > 6$ . For  $z < 6$ , the values of  $F_{ij}$  are considerably higher because it is determined by the sensitivity of  $\Gamma_{\text{PI}}$  and  $dN_{\text{LL}}/dz$  on  $N_{\text{ion}}$  and it turns out that  $\Gamma_{\text{PI}}$  is extremely sensitive to changes in  $N_{\text{ion}}$ . One can see a band-like structure in the information matrix which essentially corresponds to the presence of data points. The regions where data points are sparse (or non-existent), the value of  $F_{ij}$  is relatively smaller, implying that one cannot constrain  $N_{\text{ion}}$  from the data in those redshift bins. On the other hand, the information at  $z > 6$  is determined by the sensitivity of  $\tau_{\text{el}}$  or equivalently  $C_l^{\text{EE}}$  on  $N_{\text{ion}}$ . One can see that  $F_{ij} \rightarrow 0$  at the highest redshifts considered; this is expected because the collapsed fraction of haloes is negligible at those redshifts and hence there exist no free electrons to contribute to  $\tau_{\text{el}}$ . We find that  $F_{ij}$  is negligible for  $z > 14$ ; thus it is not possible to constrain any parameters related to star formation at redshifts  $z > 14$  using the data sets we have considered in this work.

After diagonalizing  $F_{ij}$ , we obtain its eigenvalues and the corresponding eigenmodes. In the left panel of Fig. 2.3, we show the inverse of the first few larger eigenvalues i.e., the variances of the corresponding modes. Since the eigenvalues  $\lambda_i$  are sorted in ascending order, the variances are larger for higher modes. For modes  $i > 8$ , the eigenvalues are almost zero and the variances are extremely large. This implies that the errors on  $N_{\text{ion}}$  would increase dramatically if we include modes  $i > 8$ . The corresponding first 8 eigenmodes (i.e., those which have the lowest variances) are plotted in the right panel of Fig. 2.3. We find that all

the eigenmodes tend to vanish at  $z > 14$ , which is obvious because of  $F_{ij}$  being negligible at these redshifts. We can see a number of spikes and troughs in the first four modes whose positions correspond to the presence of data points for  $\Gamma_{\text{PI}}$  and  $dN_{\text{LL}}/dz$  at  $2 < z < 6$ . The last four modes contain the information about the sensitivity of  $C_l^{\text{EE}}$ . This sensitivity is maximum around  $z \approx 7-8$  and decreases at  $z > 8$  due to unavailability of free electrons; it also decreases at  $z < 7$  because of the fact that reionization is mostly completed at these redshifts ( $x_e \rightarrow 1$ ) and hence changing  $N_{\text{ion}}$  does not affect the value of  $C_l^{\text{EE}}$  significantly at this redshift range. The modes ( $> 8$ ) with smaller eigenvalues i.e. large variances introduce huge uncertainties in the determination of  $N_{\text{ion}}$ . These modes are characterized by sharp features at different redshifts and they do not contain any significant information about the overall reionization hence do not contain any meaningful information about the reionization history.

### 2.3.2 Optimum number of modes

The next step in our analysis is to decide on how many modes  $M$  to use. In the case where  $M = n_{\text{bin}}$ , all the eigenmodes are included in the analysis and no information is thrown away. However, this would mean that modes with very small eigenvalues (and hence large uncertainties) are included and thus the errors in recovered quantities would be large. Reducing  $M$  is accompanied by a reduction in the error, but an increased chance of getting the recovered quantities wrong (which is known as bias).

It is thus natural to ask what could be the optimum value of  $M$  for calculations. The most straightforward way, which is used often, is to determine it by trial and error, i.e., more and more terms are added till one gets some kind of convergence in the recovered quantities (Mortonson & Hu 2008a).

One possible approach is to use the trial-and-error method to fix  $M$ , i.e. assume an underlying model which is different from the fiducial model but matches the current data sets quite accurately and study its recovery using only first few modes. Using this method we found that, one can recover the input model quite reasonably by considering the first  $M = 8$  modes (see Mitra et al. 2011 for a detailed discussion about this approach). A slightly more formal approach is to estimate  $M$  by minimizing the quantity Risk which is defined as Wasserman et al. (2001)

$$R = \sum_{i=1}^{n_{\text{bin}}} \left( \delta N_i^{(M)} \right)^2 + \sum_{i=1}^{n_{\text{bin}}} \left\langle \left( \delta N_i^{(M)} \right)^2 \right\rangle \quad (2.24)$$

The 1st term in the RHS is the bias contribution which arises from neglecting the higher order terms, and the 2nd term is the uncertainty given by Cramer-Rao bound which rises as higher order terms (i.e., those corresponding to smaller eigenvalues) are included:

$$\left\langle \left( \delta N_i^{(M)} \right)^2 \right\rangle \geq \sum_{k=1}^M \frac{S_k^2(z_i)}{\lambda_k} \quad (2.25)$$

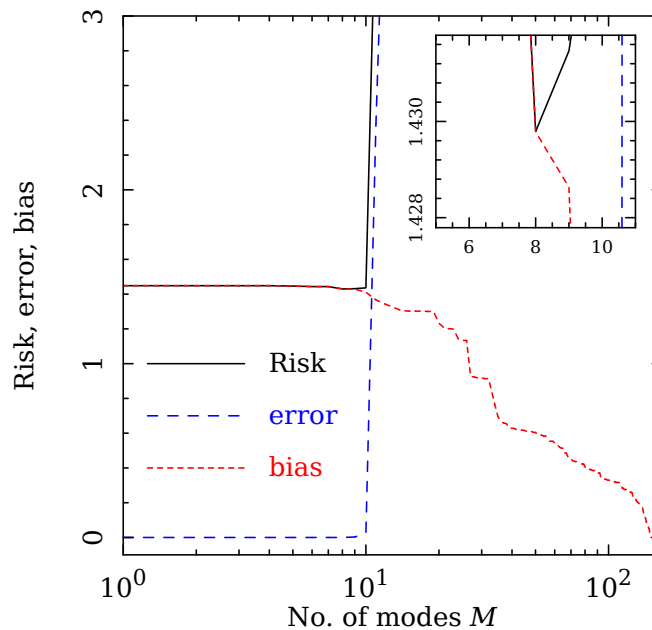


Figure 2.4: Dependence of Risk, error and bias as defined in equation (2.24) on the number of modes  $M$ . The blow-up of a region around  $M = 8$  is shown in the inset which shows that there is a clear minimum in the Risk at  $M = 8$ .

The dependence of the Risk on the number of modes  $M$  is shown in Figure 2.4. In addition, we also show the plots of bias [first term of the rhs in equation (2.24)] and the error [second term of the rhs in equation (2.24)] are also shown. It is clear that the value of error is small for lower  $M$  which is a direct consequence of small eigenvalues. The error shoots up drastically for larger  $M$ . On the other hand, the bias is higher for small  $M$  and decreases gradually as more and more terms in the summation are included. The Risk, which is the sum of these two quantities, has a clear minimum at  $M = 8$  (which is more clear from the inset in Figure 2.4). Hence we conclude that  $M = 8$  is the optimum value to be used.

However, both methods described above, involve the assumption of an “underlying model”, hence the determination of  $M$  using this method would be model-dependent. An alternate prescription is to use Akaike information criterion (Liddle 2007)

$$\text{AIC} = \chi_{\min}^2 + 2M \quad (2.26)$$

where smaller values are assumed to imply a more favored model. Similarly, one can also use the Bayesian information criterion defined by  $\text{BIC} = \chi_{\min}^2 + M \ln n_{\text{obs}}$ . The utility of these criteria over the Risk is that they are computed without knowing the underlying solution (Clarkson & Zunckel 2010). The results using BIC typically give smooth reconstructions by underestimating the errors. The AIC, on the other hand, renders more featured reconstructions at the expense of large errors. However, as  $n_{\text{obs}}$  is fixed for our current analysis, the minimum

value of AIC corresponds to the minimum of BIC, hence we simply carry out our analysis with only AIC. Note that there is no reason to select one particular reconstruction, the minimum of AIC can be accompanied by an increased chance of getting the reconstructed parameters wrong. According to Clarkson & Zunckel (2010), one successful strategy is to select different  $M$  which are near the minimum value of AIC and amalgamate them equally at the Monte Carlo stage when we compute the errors. In this way, we can reduce the inherent bias which exists in any particular choice of  $M$ . We have examined that, in our case, the family of different  $M$  reconstructions, starting from  $M = 2$ , which satisfy

$$\text{AIC} < \text{AIC}_{\min} + \kappa \quad (2.27)$$

where  $\kappa = 10$  (which corresponds to  $M = 8$ ), produces very solid results. For alternative data sets, the value of  $\kappa$  can be adjusted. The choice of this parameter must be treated as a prior. The importance of using the AIC is that the analysis now becomes non-parametric. The method has been successfully used in reconstructing the dark energy equation of state using SN-Ia observations (Clarkson & Zunckel 2010).

### 2.3.3 Monte-Carlo Markov Chain analysis on PCA modes

The constraints on reionization are obtained by performing a Monte-Carlo Markov Chain (MCMC) analysis over the parameter space of the optimum number of PCA amplitudes,  $\lambda_0$ ,  $n_s$  and  $\sigma_8$ . Other cosmological parameters are kept fixed to the WMAP7 best-fit values (see Section 2.1.2). To avoid the confusion about the correct choice of number of modes, we perform the MCMC analysis for PCA amplitudes taking from  $M = 2$  to  $M = 8$ , all of which obey the AIC criterion (equation 2.27). We then weight each choice of  $M$  equally and fold the corresponding errors together to reproduce  $N_{\text{ion}}$  and other related quantities along with their effective errors. In order to carry out the analysis, we have developed a code based on the publicly available COSMOMC (Lewis & Bridle 2002). We run a number of separate chains (varying between 5 to 10) until the Gelman and Rubin convergence statistics,  $R$ , corresponding to the ratio of the variance of parameters between chains to the variance within each chain, satisfies  $R - 1 < 0.01$ . Also we have used the convergence diagnostic of Raftery & Lewis to determine how much each chain must be thinned to obtain independent samples. Both of these are computed automatically by COSMOMC.

We have shown the evolution of various quantities related to reionization using the AIC criterion for  $M = 2$  to  $M = 8$  in figure 2.5. The solid lines represent the mean model while the shaded region correspond to 95% confidence limits. For comparison, we have also plotted the fiducial model (short-dashed) as described in Section 2.3.1. We find that the fiducial model is within the 95% confidence limits for the whole redshift range. Note that all the quantities are highly constrained at  $z < 6$ , which is expected as most of the observational information related to reionization exists only at those redshifts. The errors also decrease at  $z > 14$  as there is practically no information in the PCA modes and hence all models converge towards

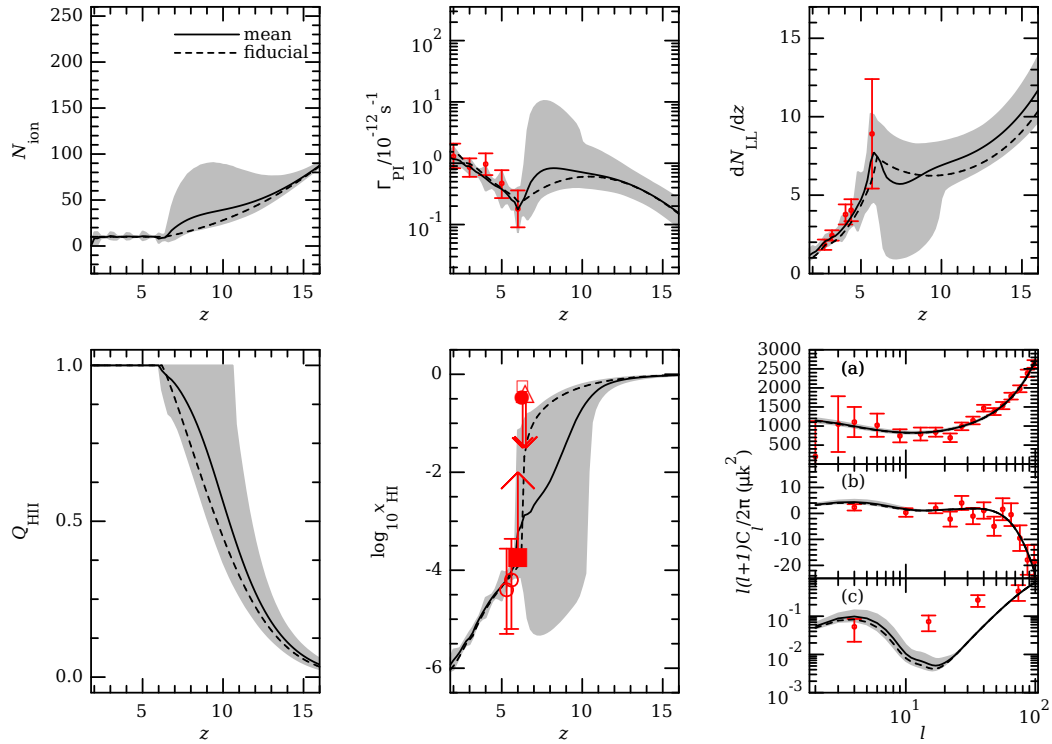


Figure 2.5: The marginalized posteriori distribution of various quantities (same as Fig. 2.1) related to reionization history obtained from the PCA using the AIC criterion with first 8 eigenmodes. The solid lines correspond to the model described by mean values of the parameters while the shaded regions correspond to  $2\sigma$  limits. The points with error-bars denote the observational data points. In addition, we show the properties of the fiducial model (short-dashed lines) as described in Section 2.3.1.

Parameters	Mean value	95% confidence limits
$\tau_{\text{el}}$	0.093	[0.080, 0.112]
$z(Q_{\text{HII}} = 0.5)$	10.206	[8.952, 11.814]
$z(Q_{\text{HII}} = 0.99)$	7.791	[5.800, 10.427]

Table 2.2: The marginalized posterior probabilities with 95% C.L. errors of all the derived parameters for the reionization model obtained from the current analysis using AIC criterion for WMAP7 data.

the fiducial one. The most interesting information regarding reionization is concentrated within a redshift range  $6 < z < 14$ .

It can be seen from the plot of  $N_{\text{ion}}(z)$  (*top-left* panel of figure 2.5) that such quantity must necessarily increase from its constant value at  $z < 6$  which confirms our finding from the earlier analysis using a model with chemical feedback (Sec. 2.1.3). This rules out the possibility of reionization with a single stellar population having non-evolving IMF and/or star-forming efficiency.

From the plot of  $\Gamma_{\text{PI}}(z)$  (*top-middle* panel), we find that the mean model is consistent with the observational data at  $z < 6$ , as expected. The errors corresponding to 95% confidence limits are also smaller at this epoch. The photoionization rate for the fiducial model shows a smooth rise at  $z > 6$  reaching a peak around  $z \approx 11$ ; however, the model described by the mean values of the parameters shows a much sharper rise and much prominent peak around  $z \sim 6.5$ . The prominent peak-like structure is also present in the plot of  $dN_{\text{LL}}/dz$  (*top-right* panel).

From the plot of  $Q_{\text{HII}}(z)$  (*bottom-left* panel), we see that the growth of  $Q_{\text{HII}}(z)$  for the mean model is much faster than that of fiducial model at initial stages, though the completion of reionization takes place only at  $z \approx 6$ . One can also find that reionization can be completed as early as  $z \approx 10.4$  (95% confidence level). Similarly,  $x_{\text{HI}}(z)$  (*bottom-middle* panel) decreases much faster than the fiducial one at  $6 < z < 12$  and then smoothly matches the  $\text{Ly}\alpha$  forest data.

Finally, we have shown the values of (a)  $C_l^{\text{TT}}$ , (b)  $C_l^{\text{TE}}$  and (c)  $C_l^{\text{EE}}$  for the mean model in the *bottom-right* panel of this figure, which is almost the same as the fiducial model. So the WMAP7 EE polarization data alone cannot distinguish between the various models of reionization. One can see that, our mean model includes most of the WMAP7 best-fit CMB data within the error bars, except for a few  $C_l^{\text{EE}}$  data points. Note that these discrepant points at  $l \gtrsim 15$  cannot be reconciled by any *physical* reionization model, implying that the spectra contribution might come from some other cosmological process, as e.g. gravitational lensing.

The mean values and the 95% confidence limits on the parameters obtained from our analysis are shown in the Table 2.2. We have checked that, our fiducial model which is characterized by  $m_1 = m_2 = m_3 = m_4 = m_5 = m_6 = m_7 = m_8 = 0$  and the best-fit values of  $\lambda_0$ ,  $n_s$  and  $\sigma_8$ , is included within the 95% confidence limits of those parameters corresponding to our current analysis using AIC criterion. We find that reionization is 50% complete between redshifts 9.0 – 11.8 (95% confidence level), while it is almost (99%) complete between redshifts 5.8 – 10.4

Parameters	2- $\sigma$ errors	
	WMAP7	PLANCK (forecast)
$\tau_{\text{el}}$	0.032	0.009
$z(Q_{\text{HII}} = 0.5)$	2.862	1.117
$z(Q_{\text{HII}} = 0.99)$	4.627	3.013

Table 2.3: The 95% C.L. errors of derived parameters for the reionization model obtained from the current analyses using AIC criterion for WMAP7 and simulated PLANCK data.

(95% confidence level). Note that the lower limit on the redshift of reionization (5.8) is imposed as a prior on the parameters. Here the mean model for  $\tau_{\text{el}}$  shows a higher value than the best-fit WMAP7 value which is arising from relatively complex reionization histories giving non-zero ionized fractions at high redshifts.

We have checked that, if we take any particular choice of  $M$ , say  $M = 7$  or  $8$ , our main findings are almost the same as the above results, except with the help of AIC criterion, we have reduced the inherent bias which is present for that specific choice of  $M$  and got a mean model which matches the current data sets quite reasonably.

To summarize, we find that using WMAP7  $C_l^{\text{EE}}$  data set we get a higher  $\tau_{\text{el}}$  than the WMAP7 best-fit value. So a wide range of reionization histories is still allowed by the data we have used. Reionization can be quite early or can be gradual and late, depending on the behavior of  $N_{\text{ion}}(z)$ . Hence, using these data, it is somewhat difficult to put strong constraints on chemical feedback and/or the evolution of star-forming efficiencies and/or escape fractions.

Given that the WMAP data allow a large range of reionization models, it is worthwhile computing the level of constraints from the large-scale polarization measurements by PLANCK. To forecast the errors for parameters related to the reionization history, we first generate the simulated PLANCK data of CMB power spectra for our fiducial model up to  $l \leq 2000$  using the exact full-sky likelihood function at PLANCK-like sensitivity (Perotto et al. 2006; Galli et al. 2010). We assume that beam uncertainties are small and that uncertainties due to foreground removal are smaller than statistical errors. More sensitive observations will also require an exact analysis of non-Gaussian likelihood function, here for simplicity we assume isotropic Gaussian noise and neglect non-Gaussianity of the full sky (Lewis 2005) and try to see what we can learn about the global reionization history from PLANCK-like sensitivity. We then repeat the MCMC analysis over the same parameter space using this simulated data. Like the previous case, here we have also varied the number of modes included in the analysis from two to eight using the AIC criterion in order to study the effect of truncating the PCA expansion for the recovery of various quantities related to reionization.

In the Table 2.3, we have shown the comparison of the 2- $\sigma$  errors on the derived parameters obtained for WMAP7 data and the same for forecasts from simulated PLANCK data. It is clear that the uncertainties on all the parameters related to reionization would be reduced considerably. In particular, we find that we should be able to constrain the redshift range at which

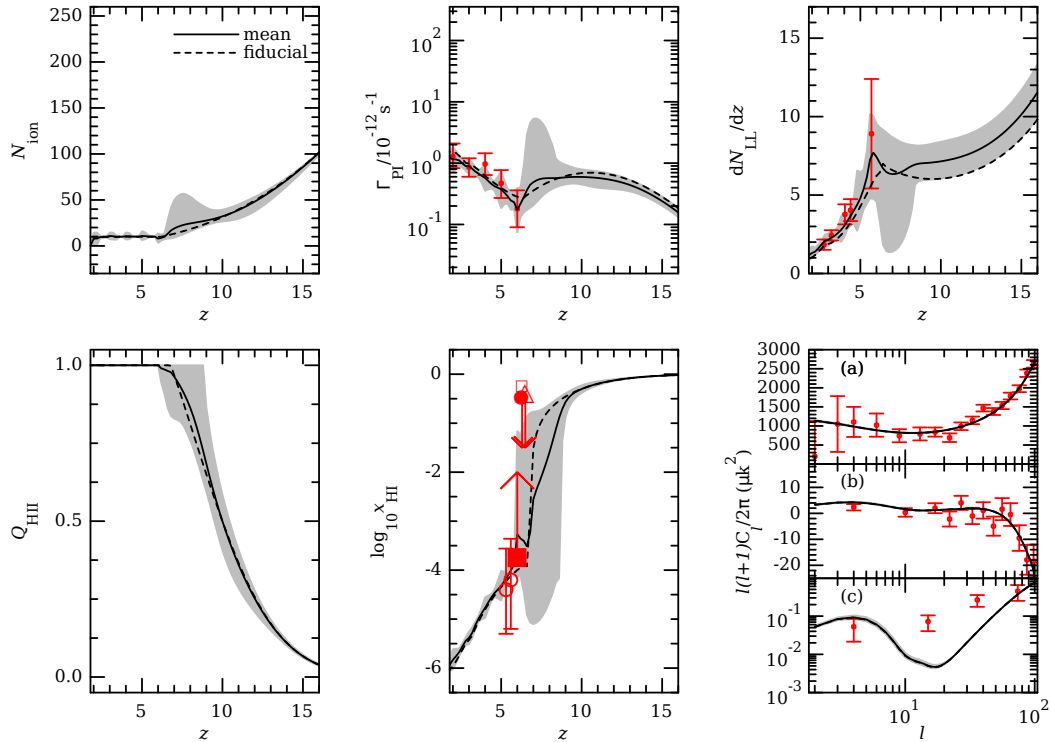


Figure 2.6: Same as Figure 2.5 but for PLANCK likelihood.

reionization was 99% (50%) completed to about 3 (1). This is clearly a significant improvement over what can be achieved through current data sets.

In Figure 2.6, we have illustrated the recovery of the same quantities as mentioned in the earlier section using the AIC criterion taking up to 8 eigenmodes for the simulated PLANCK data. For comparison, here also we have plotted the results for the fiducial model (short-dashed lines) along with the mean results (solid lines) from MCMC analysis with shaded  $2\text{-}\sigma$  limits. We find that our main results are in quite reasonable agreement with those obtained from the WMAP data, except that all the  $2\text{-}\sigma$  (95%) limits are reduced remarkably for all redshift range.

We thus find that we can constrain the global reionization history quite better using the PLANCK forecast data sets, especially the  $2\text{-}\sigma$  limits for  $Q_{\text{HII}}$  reduce significantly for this case. However, there is no room to substantially improve the constraints using large-scale  $E$ -modes for WMAP7 data sets and one still has to rely on other types of data for understanding reionization.

## 2.4 Discussion and summary

We have studied constraints on reionization history using non-parametric methods. To model the unknown function  $N_{\text{ion}}(z)$ , we have applied the principal component method using three different sets of data points - the photoionization rate  $\Gamma_{\text{PI}}(z)$ , the LLS distribution  $dN_{\text{LL}}/dz$  and WMAP7 data for  $C_l^{\text{EE}}$  for  $l \leq 23$ . Following that, we have obtained constraints on the reionization history using MCMC techniques. We have also used the Akaike information criteria (AIC) to extract the underlying information about the PCA model and reduce the intrinsic bias present in any particular choice of fiducial model. We have applied our method to the WMAP7 data as well as the simulated PLANCK data to forecast errors on reionization.

Our main findings can be summarized as follows -

1. We have found that the information about  $N_{\text{ion}}(z)$  or equivalently the star formation and/or chemical feedback lies in the first eight eigenmodes of the Fisher information matrix distributed over the range  $2 < z < 14$ . Using the higher modes costs higher errors.
2. The angular power spectra  $C_l$  of CMB observations contain more information than treating  $\tau_{\text{el}}$  as a single data point.
3. The constraints at  $z < 6$  are relatively tight because of the QSO absorption line data. On the other hand, a wide range of histories at  $z > 6$  is allowed by the data. Interestingly, it is not possible to match the available data related to reionization with a constant  $N_{\text{ion}}(z)$  over the whole redshift range, it must increase at  $z > 6$  from its constant value at lower redshifts.
4. With the data from WMAP7, we constrain  $0.080 < \tau_{\text{el}} < 0.112$  (95% CL) and also conclude that reionization is 50% complete between  $9.0 < z(Q_{\text{HII}} = 0.5) < 11.8$  (95% CL) and is 99% complete between  $5.8 < z(Q_{\text{HII}} = 0.99) < 10.4$  (95% CL).
5. With the forthcoming PLANCK data on large-scale polarization (ignoring effect of foregrounds), the  $z > 6$  constraints will be improved considerably, e.g., the  $2 - \sigma$  error on  $\tau_{\text{el}}$  will be reduced to 0.009 and the uncertainties on  $z(Q_{\text{HII}} = 0.5)$  and  $z(Q_{\text{HII}} = 0.99)$  would be  $\sim 1$  and 3 (95% CL), respectively. The errors could be somewhat larger if the effect of foregrounds are incorporated into the analysis. For more stringent constraints on reionization at  $z > 6$ , one has to rely on data sets other than CMB.

Finally, we try to indicate the data sets (other than CMB) which can possibly be used to better the constraints on reionization. Since most of the information on reionization at  $z < 6$  come from QSO absorption lines, it is natural to expect more constraints from such observations at  $z > 6$ . In addition, spectra of GRBs, which are being observed at much higher redshifts (Salvaterra et al. 2009; Tanvir et al. 2009; Cucchiara et al. 2011) could also provide additional constraints. The difficulty is that the transmission regions (which are the sources for most of the

information) are almost non-existent at high- $z$  spectra, thus making the analysis more difficult. Additional constraints on  $x_{\text{HI}}$  at high redshifts are expected from  $\text{Ly}\alpha$  emitters (Taniguchi et al. 2005; Kashikawa et al. 2006; Iye et al. 2006; Vanzella et al. 2011; Lehnert et al. 2010), however they too are affected highly by systematics. On the positive side, we feel that even a relatively weak constraint on  $x_{\text{HI}}$  at  $z \sim 7 - 10$  could be crucial in ruling out a subset of reionization models as the value of  $N_{\text{ion}}(z)$  is most uncertain at these redshifts.

We also now have observations of Lyman-break galaxies till  $z \sim 10$  (Bouwens et al. 2007, 2011b,a). The luminosity function of such galaxies would be helpful in constraining properties of the galaxies like the IMF and/or the star-forming efficiency. Unfortunately, that would still leave out the escape fraction of ionizing photons, which remain an uncertain parameter till date.

Other indirect observations that could help in constraining reionization are the temperature measurements at  $z < 6$  (Schaye et al. 2000; Ricotti et al. 2000; McDonald et al. 2001; Zaldarriaga et al. 2001; Cen et al. 2009). The temperature evolution can retain memory of how and when the IGM was reionized and thus could provide additional constraints on reionization. Whatever be the case, the principal component method described here, could be a promising tool for extracting the information from the future data sets in a model-independent manner.

---

---

## CHAPTER 3

---

# ESCAPE OF IONIZING RADIATION FROM GALAXIES

In this chapter, we will extend our knowledge to find some of the crucial but still unknown parameters related to reionization scenario with help of the semi-analytical model described in the previous chapter. As we mentioned earlier in Section 1.3.2, The escape fraction,  $f_{\text{esc}}$ , of ionizing photons from high-redshift galaxies is a key parameter to understand cosmic reionization and star formation history. Yet, in spite of many efforts, it remains largely uncertain. Here we shall propose a novel, semi-empirical approach based on a simultaneous match of the most recently determined Luminosity Functions (LF) of galaxies in the redshift range  $6 \leq z \leq 10$  with reionization models constrained by a large variety of experimental data and obtain the evolution of some of these critical parameters.

### 3.1 Introduction: Challenges for determining escape fraction

One of the most crucial issues regarding the evolution of intergalactic medium (IGM) and cosmic reionization is the escape fraction,  $f_{\text{esc}}$ , of ionizing photons from high-redshift galaxies. This parameter remains poorly constrained in spite of the many theoretical and observational attempts made in past few years. The difficulties largely arise from the lack of a full understanding of the physics of star formation, radiative transfer and feedback processes, and from uncertainties on the properties of the high- $z$  galaxy interstellar medium (ISM); as a result, derived values of  $f_{\text{esc}}$  span the large range  $0.01 - 1$  (Fernandez & Shull 2011). Observationally,  $f_{\text{esc}}$  can be reliably estimated only at redshifts  $z \lesssim 3$  (Leitherer et al. 1995; Dove et al. 2000;

Heckman et al. 2001; Ciardi et al. 2002; Giallongo et al. 2002; Fernández-Soto et al. 2003; Inoue et al. 2005; Bergvall et al. 2006; Shapley et al. 2006; Vanzella et al. 2010). On the other hand, theoretical studies (Wood & Loeb 2000; Razoumov & Sommer-Larsen 2006; Gnedin 2008; Gnedin et al. 2008; Srbinovsky & Wyithe 2010; Razoumov & Sommer-Larsen 2010; Yajima et al. 2011; Haardt & Madau 2011; Fernandez & Shull 2011; Kuhlen & Faucher-Giguère 2012) have been rather inconclusive so far, as illustrated by their often conflicting results in terms of  $f_{\text{esc}}$  values and trend with redshift and galaxy mass.

One key aspect of reionization lies in its close coupling with the properties and evolution of first luminous sources (for reviews, see Loeb & Barkana 2001; Barkana & Loeb 2001; Choudhury & Ferrara 2006a; Choudhury 2009). Observations of cosmic microwave background (CMB) and highest redshift QSOs put very tight constraints on the reionization history; these allow to construct self-consistent models of structure formation (Choudhury & Ferrara 2005; Wyithe & Loeb 2005; Gallerani et al. 2006; Choudhury & Ferrara 2006b; Dijkstra et al. 2007; Samui et al. 2007; Iliev et al. 2008; Kulkarni & Choudhury 2011). The most favorable model, which is consistent with the Thomson scattering optical depth  $\tau_{\text{el}} = 0.088 \pm 0.015$  from WMAP7 data (Larson et al. 2011) and the Gunn-Peterson optical depth evolution from QSO absorption line experiments at  $z \gtrsim 6$  (Fan et al. 2006), suggests that reionization is an extended process over the redshift range  $6 \lesssim z \lesssim 15$  (Choudhury & Ferrara 2006b; Mitra et al. 2011, 2012). This model also indicates that reionization feeds back on star formation by suppressing it in the low-mass haloes at early times (Thoul & Weinberg 1996; Choudhury & Ferrara 2006b).

In parallel, direct observations of galaxies at epochs close to the end of reionization have made astonishing progresses over the past few years (Bouwens & Illingworth 2006; Iye et al. 2006; Bouwens et al. 2007, 2008; Ota et al. 2008; Bouwens et al. 2009; Henry et al. 2009; Bouwens et al. 2010a; Oesch et al. 2010; Bouwens et al. 2010b; McLure et al. 2010; Oesch et al. 2012; Bradley et al. 2012). allowing to derive the galaxy UV Luminosity Function (LF) up to  $z \approx 10$  (Bouwens & Illingworth 2006; Bouwens et al. 2010b; Oesch et al. 2012), and to better constrain light production by reionization sources.

Here we aim at combining data-constrained reionization histories and the evolution of the LF of early galaxies to get an empirical determination of the escape fraction. The study also provides relatively tight constraints also on the evolution of the star-forming efficiency  $\epsilon_*$  (Faucher-Giguère et al. 2008; Kuhlen & Faucher-Giguère 2012). Throughout this chapter, we assume a flat Universe with cosmological parameters given by the WMAP7 best-fit values:  $\Omega_m = 0.27$ ,  $\Omega_\Lambda = 1 - \Omega_m$ ,  $\Omega_b h^2 = 0.023$ , and  $h = 0.71$ . The parameters defining the linear dark matter power spectrum are  $\sigma_8 = 0.81$ ,  $n_s = 0.97$ ,  $dn_s/d \ln k = 0$  (Larson et al. 2011). Unless mentioned, quoted errors are  $2\sigma$ .

## 3.2 Luminosity function of ionizing sources

In this work, we have used the semi-analytical model described in Section 2.1, which is basically based on Choudhury & Ferrara (2005) and Choudhury & Ferrara (2006b). Given the collapsed fraction  $f_{\text{coll}}$  of dark matter haloes, the production rate of ionizing photons in the IGM is calculated in this model as [see equation (1.80) and (2.4)]

$$\dot{n}_{\text{ph}}(z) = n_b N_{\text{ion}} \frac{df_{\text{coll}}}{dt} \quad (3.1)$$

We have already mentioned that the parameter  $N_{\text{ion}}$ , the number of photons entering the IGM per baryon included into stars, can actually be written as a combination of three parameters: the star-forming efficiency  $\epsilon_*$ , the escape fraction  $f_{\text{esc}}$ , and the specific number of photons emitted per baryon in stars,  $N_\gamma$ , which depends on the stellar IMF and the corresponding stellar spectrum [see equation (1.81)]:

$$N_{\text{ion}} = \epsilon_* f_{\text{esc}} N_\gamma \quad (3.2)$$

In the last chapter, we assumed  $N_{\text{ion}}$  to be an unknown function of  $z$  and decompose it into its principal components. In the following we assume a single stellar population (PopII) when computing the ionizing radiation properties; any change in the characteristics of these stars over time would be accounted for indirectly by the evolution of  $N_{\text{ion}}$ . We also include the contribution of quasars at  $z < 6$  assuming that they have negligible effects on IGM at higher redshifts; however, they are significant sources of ionizing photons at  $z \lesssim 4$ . From our reionization-PCA model (Mitra et al. 2011, 2012), we obtain the redshift evolution of  $N_{\text{ion}}$  by doing a detailed likelihood analysis using three different data sets - the photoionization rates  $\Gamma_{\text{PI}}$ , the redshift distribution of Lyman Limit Systems  $dN_{\text{LL}}/dz$  in  $0.36 < z < 6$  and the angular power spectra  $C_l$  for TT, TE and EE modes using WMAP7 data (see Section 2.3.3). We show the redshift evolution of  $N_{\text{ion}}(z)$  obtained from our Principal Component Analysis using WMAP7 data in Fig. 3.1. The solid line corresponds to the model described by mean values of the parameters which we obtained by performing a Monte-Carlo Markov Chain (MCMC) analysis over the parameter space of our model, while the shaded region corresponds to its  $2\text{-}\sigma$  limits. This is the same figure as the top-left panel of Fig. 2.5. We concluded that it is not possible to match available reionization data with a constant  $N_{\text{ion}}$  over the whole redshift range. Rather, it must increase at  $z > 6$  from its constant value at lower redshifts. This is a signature of either a varying IMF and/or evolution in the star-forming efficiency and/or photon escape fraction of galaxies, as equation (3.2) clearly shows.

The effect of reionization on the high redshift galaxy LF was studied using the semi-analytical models by Samui et al. (2007) and Kulkarni & Choudhury (2011). In this work, we follow their method to study the evolution of LF for our model.

The LF is derived as follows. We compute the luminosity at  $1500 \text{ \AA}$  of a galaxy having

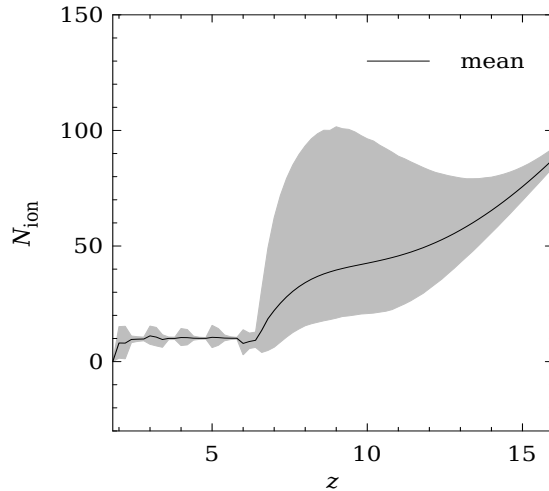


Figure 3.1: Redshift evolution of  $N_{\text{ion}}$  obtained from the Principal Component Analysis using WMAP7 data. The solid line corresponds to the model described by mean values of the parameters while the shaded region corresponds to  $2\text{-}\sigma$  limits. This figure is the same as the top-left panel of Fig. 2.5

the halo mass  $M$  and age  $\Delta t$  using

$$L_{1500}(M, \Delta t) = \epsilon_* \left( \frac{\Omega_b}{\Omega_m} \right) M l_{1500}(\Delta t) \quad (3.3)$$

Here the age of the galaxy formed at  $z'$  and observed at  $z$  is  $\Delta t = t_z - t_{z'}$ ,  $l_{1500}(\Delta t)$  is a template specific luminosity at  $1500 \text{ \AA}$  for the stellar population of age  $\Delta t$ . As we restrict to a single stellar population, i.e. PopII stars,  $\epsilon_*$  indicates the star forming efficiency of PopII stars throughout this chapter.

To compute  $l_{1500}$ , we use stellar population models of Bruzual & Charlot (2003) for PopII stars. The UV luminosity depends on galaxy properties including the IMF, star formation rate (SFR), stellar metallicity ( $Z$ ) and age. Dayal et al. (2009) and Dayal et al. (2010) have shown that the metallicity correlates with stellar mass, and the best fit mass-metallicity relation they find is

$$Z/Z_\odot = (0.25 - 0.05\Delta z) \log_{10}(M_*) - (2.0 - 0.3\Delta z) \quad (3.4)$$

where  $\Delta z = (z - 5.7)$  and  $M_*$  is the total stellar mass of the galaxy. We take all the available stellar population models in the metallicity range  $Z = 0.0001 - 0.05$  for PopII stars and interpolate them to compute  $l_{1500}$  following the mass-metallicity relation given by the above relation for our model galaxies.

The luminosity can be converted to a standard absolute AB magnitude (Oke & Gunn 1983; Samui et al. 2007; Kulkarni & Choudhury 2011) using

$$M_{AB} = -2.5 \log_{10} \left( \frac{L_{\nu_0}}{\text{erg s}^{-1} \text{Hz}^{-1}} \right) + 51.60 \quad (3.5)$$

The luminosity function  $\Phi(M_{AB}, z)$  at any redshift  $z$  is then given by

$$\Phi(M_{AB}, z) = \frac{dn}{dM_{AB}} = \frac{dn}{dL_{1500}} \frac{dL_{1500}}{dM_{AB}}, \quad (3.6)$$

where

$$\frac{dn}{dL_{1500}} = \int_z^\infty dz' \frac{dM}{dL_{1500}}(L_{1500}, \Delta t) \frac{d^2n}{dM dz'}(M, z') \quad (3.7)$$

is the comoving number of objects at redshift  $z$  with observed luminosity within  $[L_{1500}, L_{1500} + dL_{1500}]$ . The quantity  $d^2n/dM dz'$  gives the formation rate of haloes of mass  $M$ , which we obtain as in Choudhury & Ferrara (2007). Note that, we can vary the star-forming efficiency  $\epsilon_*$  in equation (3.3), as a free parameter and obtain its best-fit value by comparing the high-redshift LFs computed using the above equations with observations.

### 3.3 Constraining escape fraction and other crucial parameters

Our strategy to constrain  $f_{\text{esc}}$  exploits the combination between the previously derived (Sec. 2.3.3) evolution of  $N_{\text{ion}}$ , and the constraints on  $\epsilon_*$  that can be derived from matching LFs at different redshifts. Once the (Salpeter) IMF of the (PopII) stars is fixed,  $N_\gamma$  is also fixed and equal to  $\approx 3200$ ; from equation (3.2) we then get the value of  $f_{\text{esc}}$  as follows:

$$f_{\text{esc}} = \frac{N_{\text{ion}}}{\epsilon_* N_\gamma} \quad (3.8)$$

As the uncertainties on  $[N_{\text{ion}}/N_\gamma]$  and  $\epsilon_*$  are independent, the fractional uncertainty in  $f_{\text{esc}}$  can be obtained from the quadrature method (Taylor 1997), i.e.

$$\frac{\delta f_{\text{esc}}}{f_{\text{esc}}} = \sqrt{\left(\frac{\delta [N_{\text{ion}}/N_\gamma]}{[N_{\text{ion}}/N_\gamma]}\right)^2 + \left(\frac{\delta \epsilon_*}{\epsilon_*}\right)^2} \quad (3.9)$$

In this work, we are interested in the  $z \geq 6$  evolution of the escape fraction. In principle, our approach can also be used for the lower redshift range  $3 \leq z \leq 5$ , provided that a detailed treatment of dust extinction is added to our model. The underlying assumption in the present work is that dust effects on the escape fraction can be safely neglected at early times.

The observationally determined LFs are taken from Bouwens & Illingworth (2006) for  $z = 6$ , Bouwens et al. (2011b) for  $z = 7, 8$  and Oesch et al. (2012) for  $z = 10$ . Figure 3.2 shows the globally averaged LFs calculated using our model for  $z = 6, 7, 8, 10$  compared to the observational data points. The  $z = 10$  data are obtained from the detection of a single galaxy

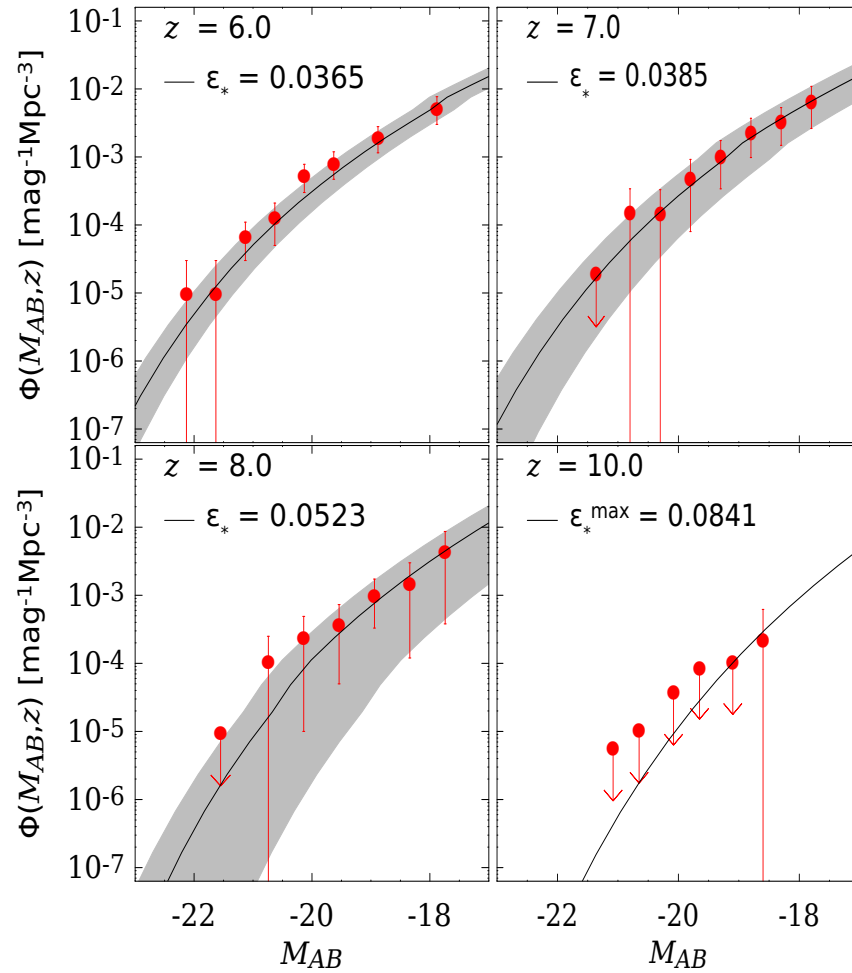


Figure 3.2: Luminosity function from our model for best-fit  $\epsilon_*$  (black curve) and its  $2\text{-}\sigma$  limits (shaded region) at  $z = 6, 7, 8$  and  $10$ . Data points with  $2\text{-}\sigma$  errors are from Bouwens & Illingworth (2006) ( $z = 6$ ), Bouwens et al. (2010) ( $z = 7, 8$ ) and Oesch et al. (2012) ( $z = 10$ ). For  $z = 10$ , we show the luminosity function from our model for the maximum value of  $\epsilon_*$  for which the LF curve does not exceed the experimental upper limits.

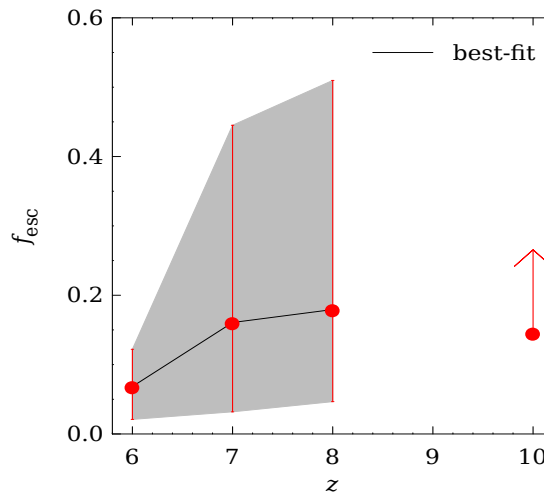


Figure 3.3: Redshift evolution of the escape fraction  $f_{\text{esc}}$  with  $2\text{-}\sigma$  errors. The  $z = 10$  data point shows the lower limit of  $f_{\text{esc}}$ . The solid line corresponds to its best-fit value while the shaded region corresponds to  $2\text{-}\sigma$  limits.

Redshift	Best-fit $\epsilon_*$	$2\text{-}\sigma$ limits	Best-fit $f_{\text{esc}}$	$2\text{-}\sigma$ limits
$z = 6$	0.0365	[0.0253, 0.0481]	0.0684	[0.0210, 0.1221]
$z = 7$	0.0385	[0.0193, 0.0576]	0.1607	[0.0319, 0.4451]
$z = 8$	0.0523	[0.0129, 0.0822]	0.1794	[0.0466, 0.5098]
$z = 10$	$< 0.0841$		$> 0.1456$	

Table 3.1: Best-fit values and  $2\text{-}\sigma$  limits of  $\epsilon_*$  and the derived parameter  $f_{\text{esc}}$  for the reionization model obtained from the LF calculation at different redshifts. At  $z = 10$ , we get only an upper limit of  $\epsilon_*$  and a corresponding lower limit of  $f_{\text{esc}}$ .

candidate by Oesch et al. (2012); hence, we only show results for the maximum value of  $\epsilon_*$  for which the LF curve does not exceed the experimental upper limits.

Our model reproduces the observed LFs reasonably well, especially at lower redshifts. From such a match we find that the best-fit value of the star-formation efficiency  $\epsilon_*$  nominally increases from 3.6% at  $z = 6$  to 5.2% at  $z = 8$ . Such a small variation is statistically consistent with a constant value of  $\epsilon_*$ , i.e. no evolution (Mitra et al. 2013).

The corresponding values of  $f_{\text{esc}}$  calculated using equation (3.8) and (3.9) are plotted in Fig. 3.3 along with the  $2\text{-}\sigma$  confidence limits (shaded region). The numerical values for  $\epsilon_*$  and  $f_{\text{esc}}$  are also reported in Table 3.1 for different redshifts ( $z = 6, 7, 8$ ). The escape fraction shows a moderately increasing trend from  $f_{\text{esc}} = 0.068^{+0.054}_{-0.047}$  at  $z = 6$  to  $f_{\text{esc}} = 0.179^{+0.331}_{-0.132}$  at  $z = 8$ ; at  $z = 10$  we can only put a lower limit of  $f_{\text{esc}} > 0.146$ , corresponding to the maximum allowed value of  $\epsilon_* = 0.0841$ .

The reported  $2\text{-}\sigma$  errors are however relatively large and we cannot exclude a non-evolving

galaxy-averaged trend for  $f_{\text{esc}}$ . The uncertainties become larger with redshift as a consequence of the fact that the larger LF errors at higher redshifts.

### 3.4 Conclusion

We have used our semi-analytical reionization model to compare the UV luminosity functions at different epochs predicted from our model with the observed LF to constrain the parameters related to star formation history in the redshift range  $6 \leq z \leq 10$ . In particular, by varying the star formation efficiency as a free parameter, we have constrained one of the most unknown parameters of reionization models, the escape fraction  $f_{\text{esc}}$  of ionizing photons from high-redshift galaxies. The main findings of our work (Mitra et al. 2013) are that, averaged over the galaxy population, (i) the escape fraction shows a moderate increase from  $f_{\text{esc}} = 0.068_{-0.047}^{+0.054}$  at  $z = 6$  to  $f_{\text{esc}} = 0.179_{-0.132}^{+0.331}$  at  $z = 8$ ; (ii) at  $z = 10$  we can only put a lower limit of  $f_{\text{esc}} > 0.146$ . Thus, although errors are large, there is an indication of a 2.6 times increase of the average escape fraction from  $z = 6$  to  $z = 8$  which might partially release the ‘‘starving reionization’’ problem. At the same time, the best-fit value of the star formation efficiency  $\epsilon_*$  nominally increases from 3.6% at  $z = 6$  to 5.2% at  $z = 8$ . Such a small variation is statistically consistent with a constant value of  $\epsilon_*$ , i.e. no evolution.

Parallel to our more phenomenological approach, in the past few years many numerical and analytical studies have attempted to constrain  $f_{\text{esc}}$  reaching often contradictory conclusions, likely due to uncertainties on star formation history, feedback, radiation transfer and the geometry of the ISM distribution (Fernandez & Shull 2011). Increasing (Razoumov & Sommer-Larsen 2006, 2010; Haardt & Madau 2011), decreasing (Wood & Loeb 2000) or un-evolving (Gnedin 2008; Yajima et al. 2011) trends have been suggested as a function of redshift.

A strong redshift evolution of the escape fraction was recently found by Kuhlen & Faucher-Giguère (2012). They show that, models in which star formation is strongly suppressed in low-mass haloes, can simultaneously satisfy reionization and lower redshift Lyman- $\alpha$  forest constraints only if the escape fraction of ionizing radiation increases from  $\sim 4\%$  at  $z = 4$  to  $\sim 1$  at higher redshifts. Although broadly in agreement with their conclusions, our results show instead that reionization and LF data can be satisfied simultaneously if  $f_{\text{esc}}$  grows from  $\sim 7\%$  at  $z = 6$  to  $\sim 18\%$  at  $z = 8$ , but without requiring an escape fraction of order of unity at these redshifts. We believe that this discrepancy can be understood as due to the fact that unlike Kuhlen & Faucher-Giguère (2012), we are fitting the *full CMB spectrum* rather than the single value of  $\tau_{\text{el}}$ ; the latter choice can be thought as a simplification of CMB polarization observations. In addition, we have used a PCA analysis to optimize model parameters to reionization data, yielding a more robust statistical analysis (Mitra et al. 2013).

Although here we have only considered the evolution of  $z \geq 6$  luminosity functions, our approach can also be applied to model the LFs at  $3 \leq z \leq 5$ . As hydrogen reionization mostly occurs at  $z \gtrsim 6$ , the LFs in this lower redshift range are very unlikely to be sensitive to the

details of reionization history. Also, dust extinction at  $z < 6$  can decrease  $f_{\text{esc}}$  by absorbing the ionizing photons at these epochs (Yajima et al. 2011). As a caveat we mention that the present results can be responsive to changes in some cosmological parameters, mainly  $\sigma_8$  and  $n_s$  (Pandolfi et al. 2011). A larger  $\sigma_8$  or  $n_s$  may lead to an increase in the number of collapsed haloes at all redshifts. In principle then, one should include these two quantities in the analysis as additional free parameters. Also, it could be interesting to evaluate the effects of PopIII stars and other feedback processes in our LF calculation. We hope to revisit some of these topics in more detail in future work.

Finally we should mention that, for constraining  $N_{\text{ion}}$ , which is linked to the rate of ionizing photon production via the collapse fraction, we performed the MCMC run using 2 – 8 PCA modes (Mitra et al. 2012). Truncating a PCA expansion can reduce the variance in the estimation of the reionization history, but also introduces a bias towards the fiducial history. Being aware of this fact, we used the Akaike information criteria (AIC) to reduce the intrinsic bias present in any particular choice of fiducial model. We found that at  $z \leq 6$ , the strong Lyman- $\alpha$  forest constraints essentially fix  $N_{\text{ion}}$ , so that the efforts to reconstruct the reionization history are very promising at this region. While it does not seem very reliable to recover  $N_{\text{ion}}$  or the other various quantities related to reionization history at  $z > 6$  in a truly model-independent manner as there exists a considerable amount of bias at this high redshift end (Mitra et al. 2011, 2012). In other word, statistical uncertainty may have been hidden here as systematic uncertainty (Huterer & Starkman 2003). So, including bias at the level of variance might eliminate the ability to make the claim of increasing  $f_{\text{esc}}$  from  $z = 6$  to  $z = 8$ . However, with more data it would be possible to apply this technique in a regime where the variance in  $N_{\text{ion}}$  is small enough to produce a useful constraint on the reionization history without the need to truncate the PCA modes so severely and so without introducing any bias. This technique will become more applicable as more data becomes available for  $z > 6$  region.



---

---

## CHAPTER 4

---

# REIONIZATION AND OTHER COSMOLOGICAL PARAMETERS

So far, we have discussed about the semi-analytical modeling of reionization and how we can use that model to constrain the reionization scenario and various crucial but unknown parameters related to it. In order to do so, for simplicity we have taken most of the cosmological parameters to be fixed at their best-fit WMAP values keeping in mind that the uncertainties in reionization history would possibly be slightly underestimated. In this chapter, we shall concentrate on finding the impacts of realistic reionization premises on the cosmological parameters by varying all the relevant cosmological parameters along with the parameters related to our reionization model. In the first half of this chapter, we will see how the inclusion of a physically motivated reionization history induces changes in the cosmological parameter values and in the later half we will use this data-constrained reionization model to achieve the constraints on the neutrino masses as allowed by the current datasets related to reionization.

### **4.1 Effects of reionization on cosmological parameter determinations**

In this section, we shall focus on assessing the effects of physically motivated and viable reionization scenarios on cosmological parameter determinations. The main novelties are: (i) the combination of CMB data with astrophysical results from quasar absorption line experiments; (ii) the joint variation of both the cosmological and astrophysical [governing the evolution of the free electron fraction  $x_e(z)$ ] parameters. Our aim is to see whether the inclusion of a realistic, data-constrained reionization history, as described in the previous chapters, in the analysis can

induce appreciable changes in the cosmological parameter values deduced through a standard WMAP7 analysis.

### 4.1.1 Cosmological parameters and different reionization scenarios

It is well known from a large set of astrophysical observables that after primordial recombination (which occurred at a redshift of  $z \sim 1100$ ) the universe “reionized” at a redshift  $z > 6$ . It is common practice in Cosmic Microwave Background (CMB) studies to parametrize the reionization as an instantaneous process occurring at some redshift  $z_{\text{re}}$ , with  $4 < z_{\text{re}} < 32$ , and to marginalize over  $z_{\text{re}}$  when deriving constraints on the other cosmological parameters. In the absence of any precise astrophysical model of the reionization process, the electron ionization fraction  $x_e(z)$  is parametrized by  $z_{\text{re}}$  in the following way:  $x_e(z) = 1$  for  $z \ll z_{\text{re}}$  (possibly  $x_e(z) = 1.08$  or  $x_e(z) = 1.16$  for  $z < 3$  in order to take into account the first and second Helium ionization) and  $x_e(z) < 2 \times 10^{-4}$  for  $z > z_{\text{re}}$  in order to join the ionization fraction value after the recombination. In the following we will refer to this parametrization as “sudden” or “instantaneous” reionization. With this choice of parametrization there exist a one-to-one relation between the redshift of sudden reionization  $z_{\text{re}}$  and the electron scattering optical depth  $\tau_{\text{el}}$ . The most recent constraints on the optical depth that come from the analysis of the Wilkinson Microwave Anisotropy Probe team on their seven-year data (WMAP7), in which it is assumed a sudden reionization scenario, is  $\tau_{\text{el}} = 0.088 \pm 0.015$ .

However, as already noticed, e.g. in Mortonson & Hu (2008b), and further emphasized by Pandolfi et al. (2010) and Pandolfi et al. (2010), the assumption of a general reionization scenario could affect the extraction of the constraints of cosmological parameters. In particular, they studied the effects of non-instantaneous reionization on the two principal inflationary parameters (the scalar spectral index of primordial perturbations  $n_s$  and the tensor-to-scalar ratio parameter  $r$ ), and on the optical depth  $\tau_{\text{el}}$ . The method used in the above cited works to describe a general reionization scenario, developed in Mortonson & Hu (2008b), is based on a principal components (PC) analysis of the reionization history,  $x_e(z)$ . PCs provide a complete basis for describing the effects of reionization on large-scale  $E$ -mode polarization spectrum. Following Mortonson & Hu (2008b), one can treat  $x_e(z)$  as a free function of redshift by decomposing it into its principal components:

$$x_e(z) = x_e^f(z) + \sum_{\mu} m_{\mu} S_{\mu}(z), \quad (4.1)$$

where the principal components  $S_{\mu}(z)$  are the eigenfunctions of the Fisher matrix describing the dependence of the polarization spectra on  $x_e(z)$ ; the  $m_{\mu}$  are the PC amplitudes for a particular reionization history, and  $x_e^f(z)$  is the WMAP *fiducial* model for which the Fisher matrix is computed and from which the PCs are obtained. Therefore the amplitude of eigenmode  $\mu$  for a perturbation around the fiducial reionization history  $\delta x_e(z) \equiv x_e(z) - x_e^f(z)$  is

$$m_{\mu} = \frac{1}{z_{\text{max}} - z_{\text{min}}} \int_{z_{\text{min}}}^{z_{\text{max}}} dz S_{\mu}(z) \delta x_e(z). \quad (4.2)$$

In what follows we refer to this parametrization of reionization as the “Principal Components”(PC) reionization. Since the ionization fraction is bounded in  $0 < x_e(z) < 1$  (neglecting helium reionization and the small residual ionized fraction after recombination) in the range of redshifts in which PCs are defined, it is necessary to impose some limits on the amplitudes of the eigenmodes of equation (4.2) to let the reionization fraction be within these limits, if only for the definition of reionization fraction. In Mortonson & Hu (2008b) the authors find the ranges of values for the amplitudes  $m_\mu$  compatible with  $x_e(z) \in [0, 1]$  for all the redshifts in range of interest. Pandolfi et al. (2010) and Pandolfi et al. (2010) used the publicly available  $S_\mu(z)$  functions and varied the amplitudes  $m_\mu$  for the first five eigenfunctions (i.e. for  $\mu = 1, \dots, 5$ ). The principal components were computed only in the range of redshifts  $z \in [6 - 30]$ . They performed a Monte Carlo Markov Chains analysis assuming a flat prior on (only) the ranges of values of the amplitudes  $m_\mu$  whose linear combination with the function  $S_\mu$  give a  $x_e(z)$  in the allowed range. These values are reported in left part of Table 4.4 and are labeled “PC Bounds”.

However, these limits for the values of the PC amplitudes are a necessary but not sufficient condition for the reionization fraction to lie in  $0 < x_e(z) < 1$ . In fact, as noticed also by Mortonson & Hu (2008b), if any  $m_\mu$  violates those bounds  $x_e(z)$  is guaranteed to be unphysical in some redshift range, but the opposite is not true, because the full reionization history depends on the linear combinations of the product of the amplitudes times their corresponding PC principal component. Indeed, even if all the amplitudes  $m_\mu$  satisfy the bounds reported in Table 4.4,  $x_e(z)$  could assume an unphysical value for some redshifts. To overcome this potential problem, we have added in the version of the `cosmomc` package used in Pandolfi et al. (2010) and Pandolfi et al. (2010), the condition that the value of  $x_e(z)$  computed at each step of a Markov Chain must be in the range  $0 < x_e(z) < 1$  for every  $z$ . In these studies, this was the only “physicality” condition imposed on the possible reionization history. However, experimental data gathered in the last few years can be used to discard at least some of the possible  $x_e(z)$  histories on well understood (astro)physical grounds. It is now possible to use reionization histories that are physically motivated and tested with known probes of the reionization epoch, such as the Gunn-Peterson optical depth, or the distribution in redshift of the Ly $\alpha$  emitters.

In this work we adopt the results of a well-tested semi-analytical reionization model proposed in Choudhury & Ferrara (2005) and Choudhury & Ferrara (2006b) (in what follows we will refer to this model as the CF model). This model takes into account a large number of parameters and physical processes that are involved in modeling reionization, including (e.g.) the radiative and chemical feedbacks of the first sources of ionizing light on the evolution of the intergalactic medium (IGM), and constrain the model by comparing it with a variety of observational data, such as the redshift evolution of Lyman Limit Systems (LLS), the IGM temperature and the cosmic star formation density. Thus we will be able to build up an ensemble of reionization histories that is more robust from both the theoretical and the observational point of view, rather than rely on purely phenomenological, albeit model-independent, parameterization schemes as the PCs.

We will combine the CF model with a standard  $\Lambda$ CDM cosmological model and we per-

form a Monte Carlo Markov Chains analysis of the joint CMB and reionization data. We will thus be able to test the impact of considering a detailed physical model for reionization on the constraints of the cosmological parameters, and conversely to test the dependence of the CF model on the underlying cosmological model.

At the end of such analysis we will moreover derive the subsequent constraints on the amplitudes of the reionization principal components  $m_\mu$  [applying directly the equation (4.2)]. By construction then, these limits on the values of amplitudes of the principal components will be compatible and constrained both by the CMB and by the astrophysical probes of the reionization process. The main objectives of the present work are then:

- Verify the impact of considering a data-constrained and realistic reionization model on the determination cosmological parameters.
- Verify the impact on the constraints of the reionization parameters produced by variations of the cosmological parameters, i.e. refraining from fixing them a priori from the most updated best fit values of the WMAP experiment.
- Obtain the PC amplitudes  $m_\mu$  from the allowed reionization histories.

As such an analysis with combined cosmological parameters characterizing the background evolution of the universe and astrophysical parameters modeling the reionization history has not yet been made, it is worthwhile to explore their mutual implications on the extraction of the constraints of the two ensemble of parameters.

Parameter	Mean	95% C.L. limits
$\Omega_m$	0.2733	[0.2260, 0.3305]
$\Omega_b h^2$	0.2184	[0.0208, 0.0229]
$h$	0.6984	[0.6553, 0.7422]
$n_s$	0.9579	[0.9330, 0.9838]
$\sigma_8$	0.7941	[0.7434, 0.8491]
$\epsilon_{II}$	0.0037	[0.0016, 0.0067]
$\epsilon_{III}$	0.0165	[0.0000, 0.0398]
$\lambda_0$	3.0152	[1.0000, 5.1739]
$\tau_{\text{el}}$	0.0803	[0.0625, 0.1042]
$z_{\text{re}}$	6.7469	[5.8563, 8.2000]

Table 4.1: Mean and 95% C.L. constraints on the cosmological, astrophysical and derived parameters obtained with the reionization parametrized with the CF model of reionization.

### 4.1.2 Analysis method and datasets

The details of the CF model are already summarized in Chapter 2 and 3; in the present work we assume the following settings:

- We consider here a flat  $\Lambda$ CDM cosmology described by a set of cosmological parameters:

$$\{\Omega_m, \Omega_b h^2, h, \sigma_8, n_s\}, \quad (4.3)$$

where  $\Omega_m$  is the total matter density relative to the critical density,  $\Omega_b h^2$  is the baryonic matter density,  $h$  is the reduced Hubble parameter  $H_0 = 100h$ ,  $\sigma_8$  is the r.m.s. density fluctuation in spheres of radius  $8h^{-1}$  Mpc and  $n_s$  is the scalar spectral index of primordial perturbations. We want to stress that these cosmological parameters are considered here as free parameters, so that they are not assumed a priori, as in our previous works (Mitra et al. 2011, 2012).

- The CF reionization model contains additional three free parameters. These are  $\epsilon_{\text{II,III}} = [\epsilon_* f_{\text{esc}}]_{\text{II,III}}$ , the product of the star-forming efficiency (fraction of baryons within collapsed haloes going into stars)  $\epsilon_*$  and the fraction of photons escaping into the IGM  $f_{\text{esc}}$  for PopII and PopIII stars; the normalization  $\lambda_0$  of the ionizing photons mean free path (see the previous chapters for details). In what follows we refer to these three parameters as the ‘‘astrophysical’’ parameters, to distinguish them from the five ‘‘cosmological’’ ones described in the previous point.
- The ranges of variation adopted for the three free astrophysical parameters are  $\epsilon_{\text{II}} \in [0; 0.02]$ ,  $\epsilon_{\text{III}} \in [0; 0.1]$ ,  $\lambda_0 \in [1; 10]$ .
- The observational data used to compute the likelihood analysis are (i) the photo-ionization rates  $\Gamma_{\text{PI}}$  obtained using Ly $\alpha$  forest Gunn-Peterson optical depth observations and a large set of hydrodynamical simulations (Bolton & Haehnelt 2007) and (ii) the redshift distribution of LLS  $dN_{\text{LL}}/dz$  in the redshift range of  $0.36 < z < 6$  (Songaila & Cowie 2010). The data points are obtained using a large sample of QSO spectra.
- In order to make the analysis self-consistent, the WMAP7 constraint on the total electron scattering optical depth  $\tau_{\text{el}}$  is not considered in this analysis. This prevents a possible loophole in our analysis: WMAP7 constraints on  $\tau_{\text{el}}$  have been obtained using the assumption of instantaneous reionization at  $z = z_{\text{re}}$ . Once this idealized evolution of  $x_e(z)$  is dropped, the value of  $\tau_e$  must be a byproduct of the new analysis rather than being inserted artificially as an external constraint into it. Moreover, as already pointed out in Mitra et al. (2011, 2012), the CMB polarization spectra are sensitive to the shape of the reionization history and considering a more general reionization scenario could lead to a tighter optical depth constraint than derived by WMAP7 (Pandolfi et al. 2010).

- Finally, we impose the prior that reionization should be completed by  $z = 5.8$  to match the flux data of Ly $\alpha$  and Ly $\beta$  forest.

With these hypotheses we have then modified the Boltzmann CAMB code (Lewis et al. 2000) to incorporate the CF model and performed a MCMC analysis based on an adapted version of the public available MCMC package COSMOMC Lewis & Bridle (2002). Our basic data set is the seven-yr WMAP data (Larson et al. 2011) (temperature and polarization), on top of which we add two “astrophysical” datasets, i.e. the LLS redshift evolution,  $dN_{LL}/dz$  (Songaila & Cowie 2010), and the Gunn-Peterson optical depth measurements presented in Bolton & Haehnelt (2007). To extract the constraints on free parameters from such combined data set we consider a total likelihood function  $L \propto \exp(-\mathcal{L})$  made up by two parts:

$$\mathcal{L} = \frac{1}{2} \sum_{\alpha=1}^{N_{\text{obs}}} \left[ \frac{\mathcal{J}_{\alpha}^{\text{obs}} - \mathcal{J}_{\alpha}^{\text{th}}}{\sigma_{\alpha}} \right]^2 + \mathcal{L}' \quad (4.4)$$

where  $\mathcal{L}'$  refers to the WMAP7 likelihood function and is computed using the routine supplied by the WMAP team;  $\mathcal{J}_{\alpha}$  represents the set of  $N_{\text{obs}}$  observational points referring to Gunn-Peterson optical depth LLS distribution data; finally,  $\sigma_{\alpha}$  are the corresponding observational error-bars. We constrain the free parameters by maximizing  $\mathcal{L}$  with flat priors on the allowed parameter ranges and the aforementioned prior on the end of reionization at  $z = 5.8$ .

The Monte Carlo-Markov Chain convergence diagnostics are done on 4 chains applying the Gelman and Rubin “variance of chain mean”/“mean of chain variances”  $R$  statistic for each parameter. We considered the chains to be converged at  $R - 1 < 0.03$ .

Parameter	WMAP7	WMAP7 + PC	WMAP7 + ASTRO
$\Omega_m$	$0.266 \pm 0.029$	$0.243 \pm 0.032$	$0.273 \pm 0.027$
$\Omega_b h^2$	$0.02258^{+0.00057}_{-0.00056}$	$0.02321 \pm 0.00076$	$0.02183 \pm 0.00054$
$h$	$0.710 \pm 0.025$	$0.735 \pm 0.033$	$0.698 \pm 0.023$
$n_s$	$0.963 \pm 0.014$	$0.994 \pm 0.023$	$0.958 \pm 0.013$
$\sigma_8$	$0.801 \pm 0.030$	—	$0.794 \pm 0.027$
$\tau_{\text{el}}$	$0.088 \pm 0.015$	$0.093 \pm 0.010$	$0.080 \pm 0.012$
$z_{\text{re}}^*$	$10.5 \pm 1.2$	—	$6.7 \pm 0.6$

Table 4.2: Comparison of the 68% C.L. posterior probability constraints obtained for different parametrization of reionization. The  $z_{\text{re}}$  parameter has a different definition in the different reionization scenarios (see text for details).

### 4.1.3 Constraints for different parametrization of reionization

The results of the MCMC analysis described above are summarized in Table 4.1, where we list the marginalized posterior probabilities at 95% confidence level (C.L.) errors on the free cosmological and astrophysical parameters. We also report the constraints for two derived parameters:

Parameter	WMAP7 + ASTRO		CF	
	Mean	95% CL	Mean	95% CL
$\epsilon_{II}$	0.0037	[0.0016, 0.0067]	0.003	[0.001, 0.005]
$\epsilon_{III}$	0.0165	[0.0000, 0.0398]	0.020	[0.0000, 0.043]
$\lambda_0$	3.0152	[1.0000, 5.1739]	5.310	[2.317, 9.474]
$\tau_{el}$	0.0803	[0.0625, 0.1042]	0.089	[0.0635, 0.1104]
$z_{re}$	6.7469	[5.8563, 8.2000]	6.762	[5.800, 7.819]

Table 4.3: Comparison between the mean value and the 95% C.L. posterior constraints between the present work (WMAP7 + ASTRO) and the CF model (Mitra et al. 2011) (MCF).

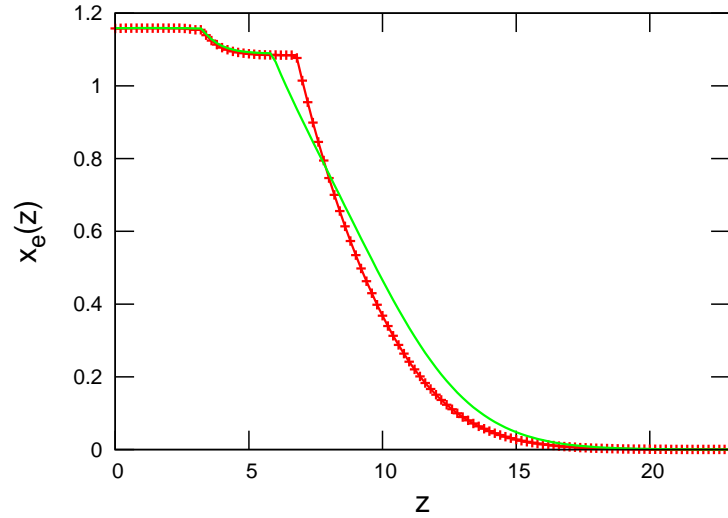


Figure 4.1: Ionization histories for the best-fit model for the two cases WMAP7+ASTRO (red dotted solid curve) and CF (green solid curve) Mitra et al. (2011).

the electron scattering optical depth  $\tau_e$  and reionization redshift  $z_r$ , to be intended as the redshift at which the reionization is 99% complete. In Table 4.2 we show the 68% C.L. constraints obtained by the WMAP team for the standard 6-parameter  $\Lambda$ CDM model (“WMAP7”) and the constraints obtained on the cosmological parameters from the present analysis (“WMAP7 + ASTRO”).

As we can see from the Table 4.2 the results of our work mildly differ from the WMAP7 results for the parameters of the standard  $\Lambda$ CDM model. The most sensitive parameter for the presence of the “astrophysical” datasets (LLS and Gunn-Peterson data) is  $\Omega_b h^2$  whose mean values in the two cases differ by more than a standard deviation from each other. It is important to note that even when considering a complex reionization history implying three new parameters the errors remain practically the same as in the standard case.

Table 4.2 reports the results obtained in Pandolfi et al. (2010) for the WMAP7 dataset with the PC reionization (“WMAP7 + PC”). This method produces two main differences with respect to the WMAP7 + ASTRO case: the first is related to the constraints obtained for  $n_s$ . In Pandolfi et al. (2010) the constraints for the scalar spectral index were compatible with  $n_s = 1$ , i.e. the Harrison-Zel’dovich (HZ) primordial power spectrum, when instead WMAP7+ASTRO excludes the value  $n_s = 1$  at  $> 3\sigma$ . The second difference concerns  $\tau_{\text{el}}$  in the two cases: for WMAP7 + PC this quantity is in the range  $\tau_{\text{el}} = 0.093 \pm 0.010$ , while the WMAP+ASTRO case gives a mean value lower by  $> 1 - \sigma$ , i.e.  $\tau_{\text{el}} = 0.080 \pm 0.012$ . Note that in the WMAP7 + PC case we did not consider constraints on the  $\sigma_8$  parameter, so in Table 4.2 the corresponding value is missing.

There is a caveat in comparing the constraints obtained on  $z_{\text{re}}$ . Indeed, in the WMAP7 case  $z_{\text{re}}$  is the redshift at which the universe undergoes an instantaneous and complete reionization process. In the more realistic, extended reionization scenarios considered here instead,  $z_{\text{re}}$  is defined as the redshift at which the IGM is 99% re-ionized by volume. With this clarification in mind, WMAP7+ASTRO results predict  $5.8 < z_{\text{re}} < 8.2$  at 95% C.L. (see Table 4.1).

In Table 4.3 we report the 95% C.L. posterior probability constraints for the reionization parameters  $\epsilon_{II}$ ,  $\epsilon_{III}$  and  $\lambda_0$  obtained in the present work (WMAP7 + ASTRO case, cosmological parameters free to vary) compared to those obtained in Mitra et al. (2011) in which the cosmological parameters were fixed to the WMAP7 best fit values (CF case). Figure 4.1 shows the comparison between the best-fit model for the  $x_e(z)$  evolution for the two cases of WMAP7 + ASTRO and CF. For the WMAP7 + ASTRO case, full hydrogen reionization is not only achieved earlier than in the CF model, but the evolution is faster, resulting in an initially lower  $x_e(z)$  above  $z = 8$ . These differences are entirely induced by the fact that we have now allowed the cosmological parameters to vary together with the astrophysical ones, but they are relatively small (Pandolfi et al. 2011). The fact that the astrophysical parameters do not show much dependence on cosmology is understandable because the cosmological parameters affect the reionization process mostly through structure formation. The next obvious step is to include large scale structure information in the analysis. In conclusion, including astrophysical datasets in the analysis seems to lead to relatively important effects on the extraction of the cosmological

parameters.

Parameter	PC Bounds	Astrophysical Bounds
$m_1$	$[-0.1236, 0.7003]$	$[-0.1229, -0.0866]$
$m_2$	$[-0.6165, 0.2689]$	$[-0.2594, 0.0002]$
$m_3$	$[-0.3713, 0.5179]$	$[0.0763, 0.2941]$
$m_4$	$[-0.4729, 0.3817]$	$[-0.2107, -0.1080]$
$m_5$	$[-0.3854, 0.4257]$	$[0.0418, 0.1319]$

Table 4.4: Ranges of variation for the amplitudes of the principal component, in the case of the Principal Components and in the case of the 99% C.L. reconstructed amplitudes of the present analysis (see text for details).

For each reionization history allowed by the MCMC likelihood analysis, we use equation (4.2) to reconstruct the amplitudes of the first five PC amplitudes,  $m_\mu$ , with  $\mu = 1\dots 5$ . By construction now, the amplitudes  $m_\mu$  not only fulfill the necessary physicality conditions (see Sec. 1) but also they are compatible with the additional astrophysical data sets considered in this analysis, i.e. the Ly $\alpha$  Gunn-Peterson test and the LLS redshift distribution.

In Fig. 4.2 we show the two dimensional 68% and 99% c.l constraints for the amplitudes  $m_\mu$  obtained here compared with those obtained in Pandolfi et al. (2010) for which we show the two dimensional 68% and 95% C.L. distributions for each of the cases considered. We choose to report the 99% C.L. instead of the usual 95% C.L. to be as conservative as possible in showing the reionization histories allowed by the MCMC likelihood analysis. The color (layer) code is the following: in pink (top layer) there is the case WMAP7 + ASTRO considered in the present work. In the background there are the cases considered in Pandolfi et al. (2010): in blue is the WMAP7 case (bottom layer), in red (next layer up) is the case called ‘‘CMB All’’ (i.e. WMAP7 + ACBAR + BICEP+ QUAD + BOOMERanG), green (next layer) is CMB All + LRG-7 and yellow (next layer) is simulated PLANCK data. Pandolfi et al. (2010) considered an ensemble of CMB dataset along with WMAP7, and also we forecasted future constraints from the PLANCK experiment, simulating a set of mock data with a fiducial model given by the best fit WMAP5 model with the following experimental noise:

$$N_\ell = \left( \frac{w^{-1/2}}{\mu\text{K-rad}} \right)^2 \exp \left[ \frac{\ell(\ell + 1)(\theta_{\text{FWHM}}/\text{rad})^2}{8 \ln 2} \right], \quad (4.5)$$

where  $w^{-1/2}$  is the temperature noise level (a factor  $\sqrt{2}$  larger for polarization noise) and  $\theta$  is the beam size. For the PLANCK mission we use  $w^{1/2} = 58\mu\text{K}$  and  $\theta_{\text{FWHM}} = 7.1'$  equivalent to expected sensitivity of the 143 GHz channel.

The region spanned by PC amplitude values is much smaller than that allowed by when the PC bounds only are imposed. The 99% C.L. constraints values are reported in the right part of the Table (4.4) (‘‘Astrophysical Bounds’’). As seen from Table (4.4) the amplitudes of all the principal components (except for  $m_2$ ) obtained with the above procedure are constrained at 99%

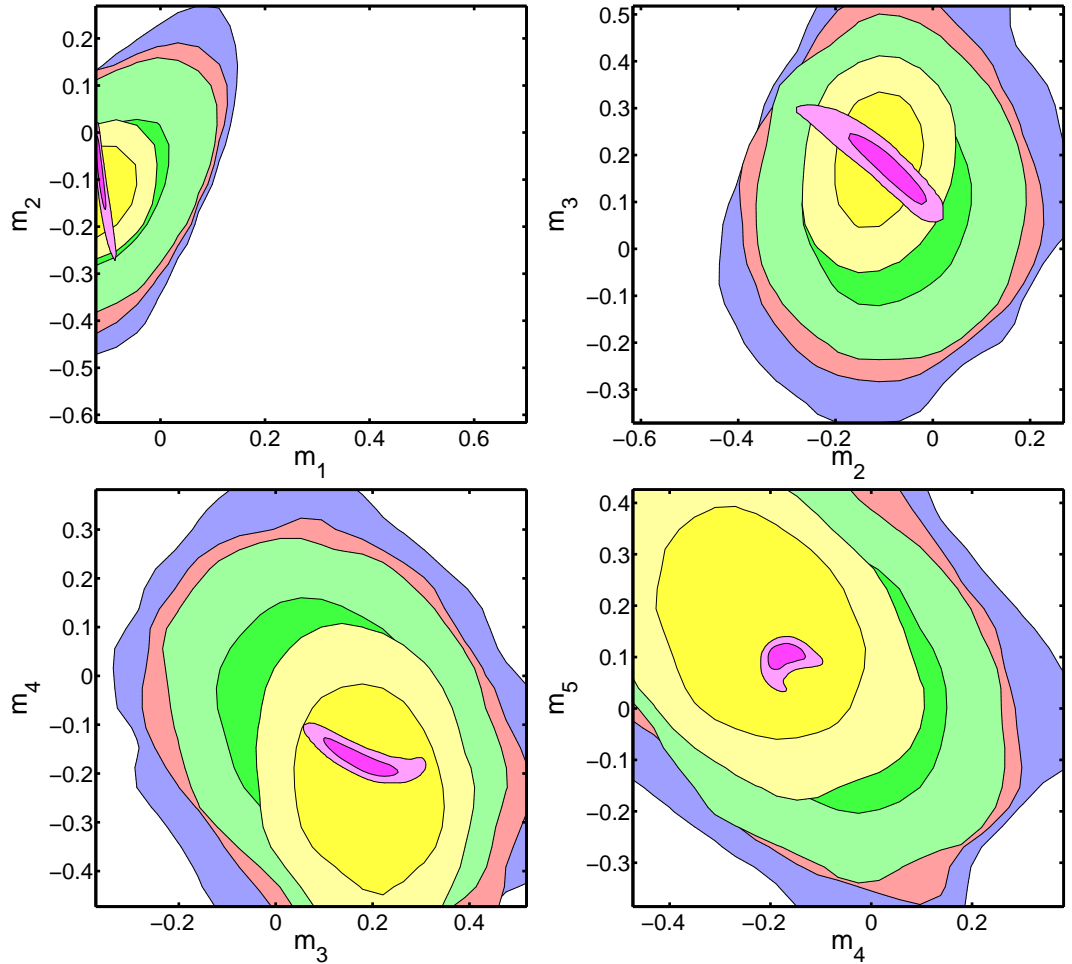


Figure 4.2: 68% and 99% reconstructed C.L. constraints for the values of the PC amplitudes computed from CF model and equation (4.2) (top layer, pink). Background contours refer to 68% and 95% C.L. constraints obtained in Pandolfi et al. (2010) with the PC reionization for WMAP7 (bottom layer, blue), WMAP7 + QUAD + ACBAR + BICEP (CMBAll, next layer up, red), CMB All + LRG-7 (next layer, green) and simulated PLANCK data (next layer, yellow), respectively.

C.L. to take a definite sign, negative for  $m_1$  and  $m_4$  and positive for  $m_3$  and  $m_5$ . Moreover, even if the 99% C.L. upper bound of  $m_2$  is positive, this second amplitude is mostly constrained to be always negative. These results are in qualitative agreement with Pandolfi et al. (2010), who also found that the same amplitude signature, albeit with errors large enough that the 95% C.L. bounds encompass values of both possible signs (Pandolfi et al. 2011).

#### 4.1.4 Summary

With the aim of constraining the evolution of cosmic reionization, we have extended previous work based on the use of Principal Components analysis. The main novelty of the present work is represented on one hand by complementing available CMB data with additional astrophysical results from quasar absorption line experiments, as the Gunn-Peterson test and the redshift evolution of Lyman Limit Systems. In addition, we have for the first time explored the effects of a joint variation of both the cosmological ( $\Omega_m, \Omega_b h^2, h, \sigma_8, n_s$ ) and astrophysical ( $\epsilon_{\text{II}}, \epsilon_{\text{III}}, \lambda_0$ , see Sec 4.1.2 for their physical meaning) parameters. Note that, differently from the vastly used approach in the literature, we do not impose a priori any bound on the electron scattering optical depth  $\tau_{\text{el}}$ , which instead we calculate a posteriori. This is to prevent a possible loophole in the calculation, as the WMAP determination of such quantity is based on the assumption of an instantaneous reionization which we do not make here.

Including a realistic (i.e physically motivated) reionization history in the analysis induces mild changes in the cosmological parameter values deduced through a standard WMAP7 analysis. Particularly noteworthy are the variations in  $\Omega_b h^2 = 0.02258^{+0.00057}_{-0.00056}$  (WMAP7) vs.  $\Omega_b h^2 = 0.02183 \pm 0.00054$  (WMAP7 + ASTRO), and the new constraints for the scalar spectral index, for which WMAP7+ASTRO excludes the Harrison-Zel'dovich value  $n_s = 1$  at  $> 3\sigma$  (Pandolfi et al. 2011). Finally, the electron scattering optical depth values is considerably decreased with respect to the standard WMAP7, i.e.  $\tau_{\text{el}} = 0.080 \pm 0.012$ . We conclude that inclusion of astrophysical datasets, allowing to robustly constrain the reionization history, in the extraction procedure of cosmological parameters leads to relatively important differences in the final determination of their values.

## 4.2 CMB bounds on neutrino mass from reionization

Now, we want to further exploit our data-constrained reionization model to achieve the plausible constraint on the neutrino masses as allowed by the current datasets related to reionization. Neutrinos with non-zero mass can have an intense impression on the evolution of our Universe. Rigorous cosmological observations on cosmic microwave background (CMB) anisotropies and the large-scale structures of galaxies thus can be used to put a stronger constraint on the neutrino masses than that achieved from current laboratory experiments. Current release of Nine years Wilkinson Microwave Anisotropy Probe (WMAP) data presents the upper bound on the sum

of neutrino masses assuming a *sudden* reionization scenario depicted by a single parameter. In this section, we shall focus on constraining the CMB neutrino mass bounds for a more general and realistic reionization model. Our aim is to investigate the possible effects of considering a data-constrained reionization scenario on neutrino mass limits.

### 4.2.1 Cosmological constraints on neutrino masses

The availability of good quantity observational data from Wilkinson Microwave Anisotropy Probe (WMAP) satellite significantly contributes to a stringent constraint on cosmological parameters and models of structure formation. According to the widely accepted flat cold dark matter model with a cosmological constant ( $\Lambda$ CDM) cosmology, the universe is mostly made of Dark energy (73%) and Dark matter (23%) dominating over the baryonic contribution. But despite of many efforts, the nature of the dark components remains one of the biggest mysteries in cosmology over past few decades. Nonetheless, recent cosmological data have indeed allowed much progress in constraining dark matter properties and neutrino masses (Mapelli & Ferrara 2005; Slatyer et al. 2009; Natarajan 2012; Zhao et al. 2012; Carbone et al. 2012; Evoli et al. 2012). In particular, neutrino mass bound now becomes one of the most intriguing goals in cosmology as well as experimental particle physics (for reviews, see Dolgov 2002; Hannestad 2004; Tegmark 2005; Lesgourgues & Pastor 2006; Hannestad 2006, 2010 and the references therein).

Atmospheric and solar neutrino oscillation experiments set a promising impression for particle physics models by strongly indicating that neutrinos have mass and that the sum of their masses is  $\sum m_\nu \gtrsim 0.05$  eV (Maltoni et al. 2004; Ashie et al. 2005; Fogli et al. 2006). However, recent cosmological data, in particular, observations related to cosmic microwave background radiation (CMBR) and the growth of structures in the universe can also make a room to deliver a potentially stronger constraint on neutrino masses (Elgarøy & Lahav 2005; Fukugita et al. 2006; Lesgourgues & Pastor 2006; Komatsu et al. 2011; Joudaki 2013; Riemer-Sørensen et al. 2013). Although, CMB data alone can constrain neutrino masses, but there is a large degeneracy between neutrino masses and the Hubble constant  $H_0$  (Ichikawa et al. 2005). An useful combination of different data sets along with the CMB data and matter power spectrum measurements can significantly tighten the limits (Hu et al. 1998; Eisenstein et al. 1999; Hannestad 2003; Seljak et al. 2005; Seljak et al. 2006; Gratton et al. 2008; Hannestad 2010). In particular, current release of Wilkinson Microwave Anisotropy Probe (WMAP) nine-year data (Hinshaw et al. 2012) can alone give a bound on the total neutrino masses as  $\sum m_\nu < 1.3$  eV at 95% confidence limits (CL) (which is the same as WMAP7 data by Komatsu et al. (2011)). Combining CMB data with the measurements of baryon acoustic oscillation (BAO) scale, constituted by luminosity distance measurements from type-Ia supernovae can put more tighter constraint (Jarosik et al. 2011). BAO data and the priors on  $H_0$  measurements obtained from both Hubble Space Telescope (HST) Key Project (KP) (Freedman et al. 2001; Sandage et al. 2006; Freedman et al. 2012) and Supernovae and  $H_0$  for the Equation of state (SHOES) program (Riess et al.

2009, 2011) along with CMB can make this constraint even tighter (Sekiguchi et al. 2010). Moreover, WMAP team found  $\sum m_\nu < 0.44$  eV at 95% CL (Hinshaw et al. 2012; Bennett et al. 2012) combining CMB data with the BAO data using the third Sloan Digital Sky Survey (SDSS) data from the Baryon Oscillation Spectroscopic Survey (BOSS)<sup>1</sup> (Schlegel et al. 2009; Dawson et al. 2012; Ahn et al. 2012; Anderson et al. 2013) and with the recent  $H_0$  prior (Riess et al. 2011), which is  $H_0 = 73.8 \pm 2.4$ . Note that, this bound for  $\sum m_\nu$  is 25% lower than the bound of 0.58 eV set by WMAP7 data (Komatsu et al. 2011).

Another feasible effect that could put an impact on the CMB bounds for neutrino masses is the detailing of reionization scenario. Although, the WMAP observation of cosmological data analysis is based on the assumption that reionization is a sudden and instantaneous incident, but recent studies (Barkana & Loeb 2001; Wyithe & Loeb 2003; Choudhury & Ferrara 2006b; Choudhury 2009; Pritchard et al. 2010; Mitra et al. 2011) suggest that reionization process is too complex to be described as a sudden event. Archidiacono et al. (2010) indicates that the sum of the neutrino masses from CMB data alone can be relaxed to  $\sum m_\nu < 1.66$  eV (95% CL) if one considers a generalized reionization model (named as MH reionization) based on a Principal Component Analysis (PCA) suggested by Mortonson & Hu (2008b). Recently, Jose et al. (2011) suggests that a more strict constraint on the neutrino masses ( $\sum m_\nu < 0.52$  eV at 95% CL) can be achieved using a well-measured galaxy luminosity function (LF) of high-redshift Lyman break galaxies (LBGs) at  $z \sim 4$  from a semi-analytical structure formation model combining with WMAP7 data. An additional constraint using the prior on Hubble constant can stiffen their limit to  $\sum m_\nu < 0.29$  eV at 95% CL. Also, the low-frequency radio observations of the redshifted 21 cm signal from the epoch of reionization can be used to further constrain neutrino mass limits (Pritchard & Pierpaoli 2008, 2009; Oyama et al. 2012). Furthermore, the recent PLANCK<sup>2</sup> CMB data for temperature power spectrum with a WMAP polarization low-multipole likelihood (Bennett et al. 2012) at  $l \leq 23$ , set a limit of  $\sum m_\nu < 0.93$  eV (95% CL). Along with the BAO data, this value becomes much lower;  $< 0.25$  eV (Ade et al. 2013b).

## 4.2.2 Models of reionization and free parameters

In this work, we try to investigate the possible effects on neutrino mass bound by considering our data-constrained reionization model based on Choudhury & Ferrara (2005, 2006b) and Mitra et al. (2011, 2012). This model constrains the reionization history using a set of reionization parameters  $\{\epsilon_{\text{II}}, \epsilon_{\text{III}}, \lambda_0\}$ , where  $\epsilon_{\text{II}}$  (or  $\epsilon_{\text{III}}$ ) is the product of the star-forming efficiency (fraction of baryons within collapsed haloes going into stars)  $\epsilon_*$  and the fraction of photons escaping into the IGM  $f_{\text{esc}}$  for PopII (or PopIII) stars and  $\lambda_0$  is the normalization of the ionizing photons mean free path. The analysis is done using only three particular data sets: the photoionization rates  $\Gamma_{\text{PI}}$ , the redshift distribution of Lyman Limit Systems  $dN_{\text{LL}}/dz$  and the angular power spectra  $C_l$  of the CMB temperature (T) and polarization (E) modes using WMAP7. In principal, our

<sup>1</sup><http://www.sdss3.org/surveys/boss.php>

<sup>2</sup><http://www.esa.int/SPECIALS/Planck/index.html>

Model	Cosmological parameters	Reionization parameters
Reion-Sudden	$\{\Omega_b h^2, \Omega_c h^2, \Omega_\nu, h, \sigma_8, n_s\}$	$\tau_{\text{el}}$
Reion-CF	same as above	$\{\epsilon_{\text{II}}, \epsilon_{\text{III}}, \lambda_0\}$

Table 4.5: Two different models of reionization considered in this work and their free parameters. For both models, cosmological parameter space is same, but the number and nature of reionization parameters differ.

reionization model parameters can have some degeneracies with the cosmological parameters, as we include the CMB data in our analysis (Mitra et al. 2012). So, we should vary all the relevant cosmological parameters along with the parameters related to our reionization model. Thus, our main goal is to see how the data-constrained reionization scenario can affect the bounds on neutrino masses and also how the inclusion of other data sets can improve that result.

We start with assuming the universe to be described by a flat cold dark matter model with a cosmological constant ( $\Lambda$ CDM) which is parametrized by a set of cosmological parameters  $\{\Omega_b h^2, \Omega_c h^2, \Omega_\nu, h, \sigma_8, n_s\}$ , where  $\Omega_b$ ,  $\Omega_c$  and  $\Omega_\nu$  are the energy density for baryon, cold dark matter and massive neutrinos, respectively, relative to the critical energy density.  $h$  is the reduced Hubble parameter  $H_0 = 100h$ ,  $\sigma_8$  is the r.m.s. density fluctuation in spheres of radius  $8h^{-1}$  Mpc and  $n_s$  is the scalar spectral index of primordial perturbations. Remember that these cosmological parameters are considered here as free parameters. We assume 3 degenerate, massive neutrinos with the same mass of  $m_\nu$ , so the sum of the neutrino masses will be  $\sum m_\nu = 3m_\nu$  and it is related to  $\Omega_\nu$  by (Lesgourgues & Pastor 2006; Archidiacono et al. 2013):

$$\sum m_\nu = 93.14 eV \times \Omega_\nu h^2 \quad (4.6)$$

Now, we will consider two different models of reionization based on the extra parameter(s) needed to describe the reionization process. They are as follows:

- The extra parameter needed to describe the *sudden* reionization is basically one single parameter the Thomson scattering optical depth  $\tau_{\text{el}}$ . We refer to this model as ‘‘Reionization-Sudden’’ or in short ‘‘Reion-sudden’’ model.
- As we mentioned earlier that for a more complex and realistic reionization model, one needs more than one parameter to describe it. For example, we can model the reionization scenario with additional three free parameters -  $\{\epsilon_{\text{II}}, \epsilon_{\text{III}}, \lambda_0\}$  (Mitra et al. 2011; Pandolfi et al. 2011). This well-tested semi-analytical reionization model was first proposed by Choudhury & Ferrara (2005, 2006b) and hereafter we will call this model as ‘‘Reionization-CF’’ or in short ‘‘Reion-CF’’ model.

To summarize the differences between these two model parameters, we listed them in Table 4.5. For both of the models described above, cosmological parameter space is same, but the number and nature of reionization parameters differ.

Furthermore we checked that, for our CF reionization model, a large value of  $m_\nu$  is compensated by a very high value of  $\epsilon_{\text{III}}$ . So we investigate whether this high  $\epsilon_{\text{III}}$  is allowed by the observations on high redshift galaxies. We have already studied the constraints on the star-forming efficiency ( $\epsilon_*$ ) and escape fraction  $f_{\text{esc}}$  of population II stars using observed luminosity function (LF) data earlier in Chapter 3 (Mitra et al. 2013). Following the same approach mentioned there, we compute the LF using our reionization model and match the observed galaxy LF data for  $6 \leq z \leq 10$  (Bouwens et al. 2007, 2011b; Oesch et al. 2012). This time, we include both PopII and PopIII stars and vary only  $\epsilon_*^{\text{III}}$  to find the upper limit on  $\epsilon_{\text{III}}$  as allowed by the observed data. Here  $f_{\text{esc}}$  has been set to its maximum value and the upper limit on  $\epsilon_*^{\text{III}}$  has been obtained by matching the LF data, hence the result is an upper limit on  $\epsilon_{\text{III}}$ . In addition, we also find that, this upper limit depends on the cosmological parameters as well. So, while varying all the parameters, we compute this upper bound within the MCMC chains and put that value as a prior to  $\epsilon_{\text{III}}$ .

We then perform a Monte-Carlo Markov Chain (MCMC) analysis over all the parameter space of each model. In order to carry out the analysis, we have developed a code based on the publicly available COSMOMC<sup>3</sup> (Lewis & Bridle 2002) code. Using the usual Gelman and Rubin convergence statistics, we run a number of separate chains until  $R$ , corresponding to the ratio of the variance of parameters between chains to the variance within each chain, achieves  $R - 1 < 0.03$ . First we have done the analysis using WMAP7 CMB data only to see how the CMB data alone can constrain the neutrino mass bound for different models of reionization. We then carry out the same analysis by taking the BAO data (Percival et al. 2010) along with the WMAP7 data set (we denote this case as WMAP7+BAO). And finally, to see how the prior on  $H_0$  affects the constraint on  $m_\nu$ , we have also included the prior obtained from the SHOES program i.e.  $H_0 = 74.2 \pm 3.6$  (Riess et al. 2009) into our analysis (denoted as WMAP7+BAO+ $H_0$ ).

### 4.2.3 Effects of reionization on neutrino mass bounds

The constraints on several cosmological and other parameters, along with their 95% ( $2\text{-}\sigma$ ) confidence limits, obtained from our MCMC analysis for different reionization scenarios are summarized in Table 4.6. First we investigate the usual WMAP7 case i.e. the case with sudden reionization (second column of Table 4.6). For this case, we get an upper limit  $\sum m_\nu < 1.25$  eV at the  $2\text{-}\sigma$  CL. The other cosmological parameters are in well agreement with those obtained by Archidiacono et al. (2010), Jose et al. (2011) and Feeney et al. (2013). We present our results using additional BAO data and BAO data with  $H_0$  prior along with the WMAP7 data in column 4 and 6 of Table 4.6 respectively for this sudden reionization case. We find a relatively lower value for  $\sum m_\nu$  ( $< 0.63$  eV) using the WMAP7+BAO data and even a more tighter value ( $< 0.56$  eV) using WMAP7+BAO+ $H_0$  data. Note that, the last value is almost identical with that obtained by WMAP team (Komatsu et al. 2011).

<sup>3</sup><http://cosmologist.info/cosmomc/>

Parameters	WMAP7		WMAP7+BAO		WMAP7+BAO+ $H_0$	
	Reion-Sudden	Reion-CF	Reion-Sudden	Reion-CF	Reion-Sudden	Reion-CF
$\Omega_b h^2$	$0.0218^{+0.0012}_{-0.0011}$	$0.0213^{+0.0012}_{-0.0010}$	$0.0212^{+0.0010}_{-0.0010}$	$0.0211^{+0.0010}_{-0.0010}$	$0.0213^{+0.0010}_{-0.0010}$	$0.0211^{+0.0011}_{-0.0010}$
$\Omega_c h^2$	$0.1168^{+0.0480}_{-0.0408}$	$0.1151^{+0.0471}_{-0.0474}$	$0.1184^{+0.0345}_{-0.0310}$	$0.1168^{+0.0338}_{-0.0301}$	$0.1173^{+0.0307}_{-0.0298}$	$0.1153^{+0.0303}_{-0.0250}$
$h$	$0.670^{+0.075}_{-0.067}$	$0.657^{+0.087}_{-0.071}$	$0.672^{+0.039}_{-0.038}$	$0.668^{+0.038}_{-0.037}$	$0.689^{+0.036}_{-0.035}$	$0.686^{+0.033}_{-0.034}$
$\sigma_8$	$0.715^{+0.119}_{-0.129}$	$0.714^{+0.110}_{-0.119}$	$0.694^{+0.117}_{-0.133}$	$0.657^{+0.093}_{-0.081}$	$0.719^{+0.125}_{-0.134}$	$0.677^{+0.115}_{-0.091}$
$n_s$	$0.957^{+0.030}_{-0.029}$	$0.944^{+0.029}_{-0.028}$	$0.962^{+0.024}_{-0.024}$	$0.955^{+0.023}_{-0.022}$	$0.969^{+0.025}_{-0.025}$	$0.961^{+0.022}_{-0.022}$
$\sum m_\nu(\text{eV})$	$< 1.25$	$< 1.04$	$< 0.63$	$< 0.52$	$< 0.56$	$< 0.46$
$\tau_{\text{el}}$	$0.086^{+0.030}_{-0.028}$	$0.081^{+0.022}_{-0.018}$	$0.084^{+0.027}_{-0.024}$	$0.080^{+0.018}_{-0.015}$	$0.086^{+0.027}_{-0.024}$	$0.081^{+0.019}_{-0.016}$
$\epsilon_{\text{II}}$	—	$0.004^{+0.005}_{-0.003}$	—	$0.006^{+0.004}_{-0.004}$	—	$0.005^{+0.004}_{-0.003}$
$\epsilon_{\text{III}}$	—	$0.008^{+0.014}_{-0.007}$	—	$0.010^{+0.013}_{-0.009}$	—	$0.010^{+0.013}_{-0.009}$
$\lambda_0$	—	$2.378^{+2.690}_{-0.786}$	—	$1.783^{+1.882}_{-0.891}$	—	$1.978^{+2.176}_{-1.080}$

Table 4.6: Best-fit values and 95% confidence limits on the cosmological parameters (top six) and reionization parameters (last four) in the case of sudden reionization and CF reionization model for WMAP7 CMB data only, WMAP7+BAO and WMAP7+BAO+SHOES prior of  $H_0 = 74.2 \pm 3.6$ . Note that,  $\tau_{\text{el}}$  is a derived parameter in case of CF reionization model.

Now, to see how the detailing of reionization history affects this bound, we show the constraints on all the parameters for our reionization model using WMAP7, WMAP7+BAO and WMAP7+BAO+ $H_0$  datasets in column 3, 4 and 5 respectively. One can see that, by considering a more physical reionization picture, the upper bound on  $\sum m_\nu$  is improved considerably for all the cases. In particular, the constraint on the neutrino mass is improved by  $\sim 17\%$  for WMAP7 alone and about 18% for WMAP7+BAO+ $H_0$  when a data-constrained reionization scenario is considered. We should refer here that, Archidiacono et al. (2010) found an increase in neutrino masses considering the MH reionization model based on PCA. The discrepancy between these results is due to the fact that, their reionization model is even more general with larger number of parameters and greater degeneracies between the those parameters than ours. Also, on contrary to their results, we found the spectral index  $n_s$  is always  $< 1$  at 95% CL for all cases even we consider the complex reionization premises, thus ruling out the Harrison-Zeldovich (HZ) spectrum ( $n_s = 1$ ). We have shown the values for our reionization model parameters and the electron scattering optical depth  $\tau_{\text{el}}$ , which is a derived parameter for this case, in last four rows in Table 4.6. Although, we get slightly lower values of  $\tau_{\text{el}}$  than the WMAP7 best-fit value, but they are still well inside within the  $2\text{-}\sigma$  limit obtained from WMAP7 data.

Furthermore, we also examine what would be the effects of a non-zero neutrino mass on reionization histories in Figure 4.3. We know that, massive neutrinos can affect the amplitude of cosmological perturbations at high redshifts ( $z \simeq 1000$ , probed by CMB) and as well as at very low redshifts ( $z \simeq 1$ , probed by galaxy surveys). But, recent studies show that they can also affect the power spectrum of perturbation at an intermediate redshift ( $6 \leq z \leq 20$ ) through the expansion of the universe and their *free-streaming* effects (Eisenstein & Hu 1999; Lesgourgues & Pastor 2006; Pritchard & Pierpaoli 2008). Thus the growth of the fluctuations and hence the shape of the power spectrum in this regime are influenced by the presence of these massive neutrinos. This essentially puts an imprint on the reionization scenarios.

In Figure 4.3, we show the evolution of various quantities related to reionization for zero and non-zero neutrino masses for our semi-analytical CF reionization model with WMAP7 data only. The solid (green) lines correspond to the best-fit model from our current MCMC analysis having  $\Omega_\nu = 0.01$ , while the long-dashed (black) lines correspond to the best-fit model from the previous chapter (see Chapter 2) with zero neutrino mass ( $\Omega_\nu = 0$ ). For comparison, we have also plotted a model having  $\Omega_\nu = 0.022$  or  $\sum m_\nu \approx 1.04$  eV (still allowed within the  $2\text{-}\sigma$  limits of our current analysis with WMAP7 data) by the short-dashed (blue) lines. The points with error-bars denote the recent observational data points related to reionization. We should mention here that, as we want to understand the effect of  $m_\nu$  alone on the reionization models, we keep the same efficiency parameters ( $\epsilon_{\text{II/III}}$ ) for these three models.

One can see that, the evolution of the quantities related to reionization are very similar for the model with zero neutrino mass and the best-fit model with  $\Omega_\nu = 0.01$  at lower redshifts ( $z < 6$ ), then they depart at higher redshifts. For the model with relatively higher neutrino mass ( $\Omega_\nu = 0.022$ ), this deviation becomes very large, even at smaller redshifts. It can be seen from the plots of redshift distribution of Lyman Limit Systems  $dN_{\text{LL}}/dz$  (*Top-left panel*)

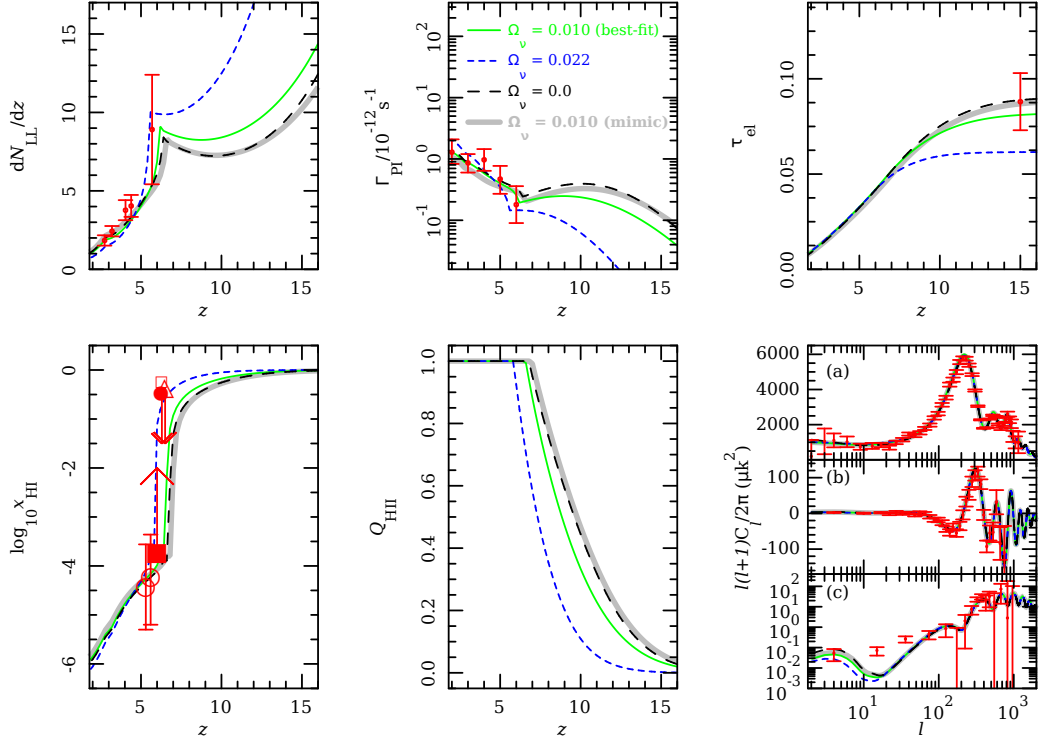


Figure 4.3: Evolution of various quantities related to reionization for zero and non-zero neutrino masses for our semi-analytical CF reionization model with WMAP7 data. The solid (green) lines correspond to the best-fit model from our MCMC analysis having  $\Omega_\nu = 0.01$ , while the short-dashed (blue) lines corresponds to the model having  $\Omega_\nu = 0.022$  or  $\sum m_\nu \approx 1.04$  eV and still allowed within the  $2\text{-}\sigma$  limits. The long-dashed (black) lines are for the model with  $\Omega_\nu = 0$  (i.e. the best-fit model from our previous chapters). These three models have the same efficiency parameters ( $\epsilon_{II/III}$ ). To illustrate the degeneracy between  $\epsilon$ 's and  $m_\nu$ , a fourth model with same  $\Omega_\nu = 0.01$  but having different  $\epsilon$ 's are plotted by the thick shaded (gray) curves. This model mimics the model with zero neutrino mass. The points with error-bars denote the observational data points. *Top-left*: the LLS distribution  $dN_{LL}/dz$  with data points from Songaila & Cowie (2010); *Top-middle*: the hydrogen photoionization rate  $\Gamma_{PI}(z)$  along with the constraints from Bolton & Haehnelt (2007); *Top-right*: the electron scattering optical depth  $\tau_{el}$  with WMAP7 data point. *Bottom-left*: the global neutral hydrogen fraction  $x_{HI}(z)$  with observational limits from QSO absorption lines (Fan et al. 2006; filled square), Ly $\alpha$  emitter luminosity function (Kashikawa et al. 2006; open triangle) and GRB spectrum analysis (Totani et al 2006; open square). Also shown the constraints using dark gap statistics on QSO spectra (Gallerani et al 2008a; open circles) and GRB spectra (Gallerani et al. 2008b; filled circle); *Bottom-middle*: the volume filling factor of HII regions  $Q_{HII}(z)$ ; *Bottom-right*: (a) TT, (b) TE and (c) EE power spectra with the data points from WMAP7 (Larson et al. 2010).

Model	$\epsilon_{\text{II}}$	$\epsilon_{\text{III}}$
$\Omega_\nu = 0.010$ (best-fit)	0.0044	0.0077
$\Omega_\nu = 0.022$		
$\Omega_\nu = 0.0$		
$\Omega_\nu = 0.010$ (mimic)	0.0038	0.0157

Table 4.7: Values of the  $\epsilon$  parameters for different models with zero and non-zero neutrino masses. The top three models have the same efficiency parameters, whereas the last model has a non-zero neutrino mass same as the best-fit model of our present analysis but with different  $\epsilon$ 's so that it can mimic the zero neutrino mass model.

and the hydrogen photoionization rate  $\Gamma_{\text{PI}}(z)$  (*Top-middle panel*), where the higher neutrino mass models clearly shows larger departures, even at  $z < 6$ . However this model is still within the corresponding current observational error-bars. So, any sighting of LLS at higher redshifts would be helpful in putting more constraints on reionization and shrinking the allowed limits on neutrino masses. Similar behavior of non-zero neutrino masses can also be obtained from the evolution of the global neutral hydrogen fraction  $x_{\text{HI}}(z)$  (*Bottom-left panel*) and the volume filling factor of HII regions  $Q_{\text{HII}}(z)$  (*Bottom-middle panel*). For the model with very high neutrino mass we see that, reionization is completed at a relatively lower redshift compared to the models having zero or low neutrino masses. This could happen because of the fact that the presence of very massive neutrinos could suppress the number density of galaxies and hence the formation rate of halos at lower redshifts allowing reionization to be completed lately (Jose et al. 2011).

Moreover, we know that, during reionization the re-scattering of photons can suppress the anisotropies on smaller angular scales by a damping factor  $e^{-\tau_{\text{el}}}$ , where the electron scattering optical depth  $\tau_{\text{el}}$  can be obtained from reionization (*Top-right panel*). From the plot for  $C_l^{\text{TT}}$  power spectra (top row of the *Bottom-right panel*), one can see that, this quantity remains almost the same for zero or non-zero neutrino masses for all  $l$ , even for  $l < 30$  where the effect of reionization is seemed to be important. This is expected as the measurements at such low  $l$  are limited by the *cosmic variance*, and thus we cannot see the effects of different reionization histories in the temperature spectrum. However, we can recognize the reionization effects in the polarization spectra  $C_l^{\text{EE}}$  (last row of the *Bottom-right panel*) at  $l < 30$ . The plot shows a clear departures of low- $l$  polarization spectra for non-zero neutrino masses from the model with zero neutrino mass. These differences are larger for the models with higher neutrino masses.

Remember that, these three models have the same efficiency parameters ( $\epsilon_{\text{II/III}}$ ). Now, we include a fourth model with different  $\epsilon$ 's but having a same non-zero  $m_\nu$  (i.e.  $\Omega_\nu = 0.01$ ) as our best-fit model for the current analysis. We vary the efficiency parameters of this fourth model so that it can mimic the zero  $m_\nu$  model. The values of the  $\epsilon$  parameters for all these four neutrino mass models are tabulated in Table 4.7. We have shown the mimic model by the thick shaded (gray) curves in Figure 4.3. We see that, the evolution of all the quantities for this model are almost identical to those for the model with zero neutrino mass. This essentially guarantees that

there exists a degeneracy between  $\epsilon$ 's and  $m_\nu$ . The constraints on  $m_\nu$  can be further improved if we can constrain the  $\epsilon$  parameters independently. Thus, it is the degeneracy with astrophysics which is not giving good constraints here. Nevertheless, it is important to include reionization data sets in the analysis to improve the constraints on neutrino masses.

#### 4.2.4 Summary

One key aspect of studying reionization lies in the fact that it is strongly related to the properties of first luminous sources and subsequent galaxy formation. Due to the lack of knowledge about an accurate evolution of ionization fraction during reionization period, it is sometimes parametrized by a single parameter, the Thomson scattering optical depth  $\tau_{\text{el}}$ , assuming the universe was reionized instantaneously at some redshift denoted as  $z_{\text{re}}$ . However, recent studies favor for a fairly complex and extended reionization process over the redshift range  $6 \lesssim z \lesssim 15$  (Choudhury & Ferrara 2006a,b; Mitra et al. 2011), and thus it cannot be described by a single parameter. In this work, we explore the constraints on the cosmological parameters, particularly the sum of the neutrino masses  $\sum m_\nu$ , using such data-constrained reionization model. With a relatively complex and realistic reionization model (Choudhury & Ferrara 2005, 2006b) described by three parameters ( $\epsilon_{\text{II}}, \epsilon_{\text{III}}, \lambda_0$ ), we try to determine the upper bounds on neutrino masses and compare our results with those obtained using a simple sudden reionization scenario.

We find that, using WMAP7 data alone, a more physically reasonable treatment of reionization can tighten the upper limit on neutrino masses by  $\sim 17\%$  than that for standard sudden reionization scheme. The BAO dataset and a prior on  $H_0$  obtained from the SHOES program along with the WMAP7 data have been used in this work in order to further reduce the uncertainty on the neutrino masses. We get an  $\sim 18\%$  improvement for this case using our data-constrained reionization model. Although, the results presented here shows that the constraints improve with reionization data sets, but still we do not get much better constrains. So, we need to identify the reason why the high masses are allowed by the data we considered here. For that, we then examine the possible effects of non-zero neutrino masses on reionization histories. We find that, one of the possible reasons for not getting better constrains lies in the fact that there could exist a large degeneracy between the efficiency parameters  $\epsilon$ 's and  $m_\nu$ . Thus, an independent bound on  $\epsilon$  could be crucial in ruling out the models having higher neutrino masses. Even so, we establish that the constraints on neutrino masses can be improved up to a reasonable amount by considering the realistic data-constraint reionization scenario and also the future observations associated with reionization can possibly further reduce the present bounds on neutrino masses.

Finally, we should mention that, although the new WMAP (Bennett et al. 2012), BAO (Anderson et al. 2013) and PLANCK (Ade et al. 2013b) datasets have already become public, we have not included them in this analysis. However, as long as we are concern in finding the bounds on  $m_\nu$ , the old WMAP7 data are fully in agreement with the recently released WMAP9

data (Hinshaw et al. 2012). So, the disparity between using WMAP7 and WMAP9 data is very insignificant for this analysis. Also, remember that, our main aim in this work is to compare the limits on neutrino masses for different reionization scenarios. The current release of BAO data with WMAP9 and the  $H_0$  prior or the recent PLANCK will of course lower the bound of  $\sum m_\nu$  for both cases but by the same amount. Furthermore, the new PLANCK data release does not include the polarization data in their likelihood, instead they rely on the WMAP polarization likelihood (Page et al. 2007; Bennett et al. 2012) at low multipoles to constrain the optical depth from reionization (Ade et al. 2013a,b). As most of the constraints related to reionization models come from the polarization data, we postpone the analysis with the next data release of PLANCK to a later project. So, in this case, the impact of these new datasets, especially when considered as a combination with other datasets, is very marginal and thus will not significantly change our main conclusions.



---

---

## CHAPTER 5

---

# FORMATION RATE OF DARK MATTER HALOES

We have seen that, one of the most crucial ingredient of any analytical models discussed in the previous chapters is the global star formation rate  $\dot{\rho}_*(t)$  and the formation rate of dark matter halos is directly involved in calculating this quantity. As a matter of fact, the hierarchical formation of dark matter halos is the extremely significant process which leads to formation and evolution of galaxies and clusters of galaxies. Thus it is worthy of spending some time in discussing about the formation rate of dark matter halos here.

Gravitational amplification of density perturbations is thought to be responsible for formation of large scale structures in the Universe (Peebles 1980; Shandarin & Zeldovich 1989; Peacock 1999; Padmanabhan 2002). Much of the matter is the so called dark matter that is believed to be weakly interacting and non-relativistic (Trimble 1987; Komatsu et al. 2009). Dark matter responds mainly to gravitational forces, and by virtue of a larger density than baryonic matter, assembly of matter into haloes and large scale structure is primarily driven by gravitational instability of initial perturbations in dark matter. Galaxies are believed to form when gas in highly over-dense haloes cools and collapses to form stars in significant numbers (Hoyle 1953; Rees & Ostriker 1977; Silk 1977; Binney 1977). Thus the hierarchical formation of dark matter haloes is the key driver that leads to formation and evolution of galaxies and clusters of galaxies.

The halo mass function describes the comoving number density of dark matter haloes as a function of mass and redshift in a given cosmology. It is possible to develop the theory of mass functions in a manner that makes no reference to the details of the cosmological model or the power spectrum of fluctuations. That is, we expect the mass function to take a universal form, when scaled appropriately. Simple theoretical arguments have been used to obtain this

universal functional form of the mass function (Press & Schechter 1974; Bond et al. 1991; Sheth et al. 2001). Bond et al. (1991) and Sheth et al. (2001) used the excursion set theory to derive the mass function. Much work has also been done to determine the extent to which this form is consistent with results from N-body simulations (Jenkins et al. 2001; White 2002; Reed et al. 2003; Warren et al. 2006; Reed et al. 2007; Lukić et al. 2007; Cohn & White 2008; Tinker et al. 2008) with the conclusion that the agreement is fairly good. It is remarkable that a purely local approach provides a fairly accurate description of the manifestly non-linear and strongly coupled process of gravitational clustering. The success of the local description has been exploited in developing the semi-analytic theories of galaxy formation (White & Frenk 1991; Kauffmann et al. 1993; Chiu & Ostriker 2000; Madau et al. 2001; Samui et al. 2007).

The Press-Schechter mass function (Press & Schechter 1974) that is commonly used in these semi-analytic models assumes spherical collapse of haloes (Gunn & Gott 1972). The shape of this mass function agrees with numerical results qualitatively, but there are deviations at a quantitative level (Efstathiou et al. 1988; Jenkins et al. 2001). Improvements to the Press-Schechter mass function have been made to overcome this limitation. In particular, the Sheth-Tormen mass function, which is based on the more realistic ellipsoidal collapse model (Sheth & Tormen 1999; Sheth et al. 2001) fits numerical results better. Many fitting functions with three or four fitting parameters have been proposed, these are based on results of simulations of the Lambda-Cold Dark Matter ( $\Lambda$ CDM) model (Jenkins et al. 2001; Reed et al. 2003; Warren et al. 2006; Fakhouri et al. 2010).

In the application of the theory of mass functions to the semi-analytic models for galaxy formation, we often need to know comoving number density of haloes of a certain age. Naturally, this quantity is related to the halo formation rates and the survival probability. While these details are known and well understood for the Press-Schechter mass function (Press & Schechter 1974), the situation is not as clear for other models of the mass function. Furthermore, analytic estimates for the halo formation rate and survival probability are important in spite of the availability of accurate fitting functions for these quantities in the  $\Lambda$ CDM model. This is because analytic estimates can be used to study variation in these quantities with respect to, for instance, the underlying cosmology or the power spectrum of matter perturbations. Studying such variation with the help of simulations is often impractical. In this work, we focus on the computation of halo formation rates.

Several approaches to calculating halo formation rates have been suggested (Blain & Longair 1993; Sasaki 1994; Kitayama & Suto 1996). In particular, Sasaki (1994) suggested a very simple approximation for the formation rate as well as survival probability for haloes. The approximation was suggested for the Press-Schechter mass function, though it does not use any specific aspect of the form of mass function. The series of arguments is as follows:

- Merger and accretion lead to an increase in mass of individual haloes. Formation of haloes of a given mass from lower mass haloes leads to an increase in the number density, whereas destruction refers to haloes moving to a higher mass range. The net change in number density of haloes in a given interval in mass is given by the difference between

the formation and destruction rate.

- Given the net rate of change, we can find the formation rate if we know the destruction rate.
- A simple but viable expression for the destruction rate is obtained by assuming that the probability of destruction per unit mass (also known as the halo destruction efficiency) is independent of mass.
- This approximate expression for the destruction rate is then used to derive the formation rate as well as the survival probability.

The resulting formulae have been applied freely to various cosmologies and power spectra, including the CDM class of power spectra. The Sasaki approach has been used in many semi-analytic models of galaxy formation (Chiu & Ostriker 2000; Choudhury & Ferrara 2005; Samui et al. 2007) mainly due to its simplicity. Attempts have also been made to generalize the approximation to models of mass function other than the Press-Schechter mass function (Samui et al. 2009), though it has been found that a simple extension of the approximation sometimes leads to unphysical results. In particular, when applied to the Sheth-Tormen mass function, the Sasaki approach yields negative halo formation rates.

In this chapter, we investigate the application of the Sasaki approach to the Sheth-Tormen mass function. We test the Sasaki approach by explicitly computing the halo formation and destruction rates for the Press-Schechter mass function using the excursion set formalism. We then generalize this same method to compute the halo formation rates for the Sheth-Tormen mass function. We find that halo formation rates computed in this manner are always positive. Finally, we compare our analytical results with N-body simulations.

A reason for choosing the approach presented here, as compared to other competing approaches based on the excursion set formalism, is that we wish to be able to differentiate between major and minor mergers. This is an essential requirement in semi-analytical models of galaxy formation and is not addressed by other approaches for halo formation rate (Percival & Miller 1999; Percival et al. 2000; Percival 2001; Giocoli et al. 2007; Moreno et al. 2008, 2009).

Many previous studies of merger rates using analytical or numerical techniques are present in the literature. Benson et al. (2005) recognized that the Sasaki approach of calculating halo formation rate was fundamentally inconsistent. They showed that a mathematically consistent halo merger rate should yield current halo abundances when inserted in the Smoluchowski coagulation equation. They applied this technique to obtain merger rates for the Press-Schechter mass function. The original formulation of halo merger rates in the excursion set picture (Lacey & Cole 1994) was also improved by Neistein & Dekel (2008) and Neistein et al. (2010) to include the effect of finite merger time interval. They found that the resultant merger rates are about 20% more accurate than the estimate of Lacey & Cole (1994) for minor mergers and about three times more accurate for major mergers. However, most of these studies have focused on the overall merger rates (Cohn & White 2008) rather than halo formation rates.

In this chapter we discuss the Sasaki and the excursion set formalisms in Section 5.1. We describe our simulations in Section 5.2, discuss our results in Section 5.3 and finally summarize our conclusions at the end of this chapter.

## 5.1 Rate of halo formation

The total change in number density of collapsed haloes at time  $t$  with mass between  $M$  and  $M + dM$  per unit time is denoted by  $\dot{N}(M, t)dM$  and is due to haloes gaining mass through accretion or mergers. Lower-mass haloes gain mass so that their mass is now between  $M$  and  $M + dM$ , and some of the haloes with mass originally between  $M$  and  $M + dM$  gain mass so that their mass now becomes higher than this range. We call the former process halo formation and the latter as halo destruction, even though the underlying physical process is the same in both cases; the different labels of formation or destruction arise due to our perspective from a particular range of mass. We denote the rate of halo formation by  $\dot{N}_{\text{form}}(M, t)dM$  and the rate of halo destruction by  $\dot{N}_{\text{dest}}(M, t)dM$ . We immediately have

$$\dot{N}(M, t) = \dot{N}_{\text{form}}(M, t) - \dot{N}_{\text{dest}}(M, t). \quad (5.1)$$

Following Sasaki (1994), in general we can formulate each term in the above expression as follows. The rate of halo destruction can be written as

$$\dot{N}_{\text{dest}}(M, t) = \int_M^{\infty} N(M, t) \tilde{Q}(M, M'; t) dM' \quad (5.2)$$

$$\equiv \phi(M, t) N(M, t), \quad (5.3)$$

where,  $\tilde{Q}(M, M'; t)$  represents the probability of a halo of mass  $M$  merging with another halo to form a new halo of mass  $M'$  per unit time. The fraction of haloes that are destroyed per unit time is denoted by  $\phi(M, t)$ . This quantity is also referred to as the efficiency of halo destruction. The rate of halo formation can be written as

$$\dot{N}_{\text{form}}(M, t) = \int_0^M N(M', t) Q(M', M; t) dM' \quad (5.4)$$

where  $Q(M', M; t)$  represents the probability of a halo of mass  $M'$  evolving into another halo of mass  $M$  per unit time. We can now write, from equation (5.1) and from our definitions in equations (5.3) and (5.4),

$$\dot{N}_{\text{form}}(M, t) = \dot{N}(M, t) + \phi(M, t) N(M, t). \quad (5.5)$$

This reduces the calculation of rate of halo formation to a computation of  $\phi(M, t)$ .

Sasaki (1994) proposed a simple ansatz to compute  $\phi(M, t)$ : if we assume that the efficiency of halo destruction has no characteristic mass scale and we require that the destruction rate remains finite at all masses then it can be shown that  $\phi$  does not depend on mass.

### 5.1.1 Sasaki prescription: Press-Schechter mass function

Let us first describe the Sasaki prescription for Press-Schechter mass function. To understand the Press-Schechter formalism (Press & Schechter 1974; Bond et al. 1991), which gives the co-moving number density of collapsed haloes at a time  $t$  with mass between  $M$  and  $M + dM$ , consider a dark matter inhomogeneity centered around some point in the Universe. The smoothed density contrast within a smoothing scale of radius  $R$  around this point is defined as  $\delta(R) = [\rho(R) - \bar{\rho}]/\bar{\rho}$ , where  $\rho(R)$  is the density of dark matter within  $R$  and  $\bar{\rho}$  is the mean background density of the Universe. If this density contrast  $\delta(R)$  is greater than the threshold density contrast for collapse  $\delta_c$  obtained from spherical collapse model (Gunn & Gott 1972), the matter enclosed within the volume collapses to form a bound object. In hierarchical models, density fluctuations are larger at small scales so with decreasing  $R$ ,  $\delta(R)$  will eventually reach  $\delta_c$ . The problem then is to compute the probability that the first up-crossing of the barrier at  $\delta_c$  occurs on a scale  $R$ . This problem can be addressed by excursion set approach.

The excursion set approach consists of the following principles: consider a trajectory  $\delta(R)$  as a function of the filtering radius  $R$  at any given point and then determine the largest  $R$  at which  $\delta(R)$  up crosses the threshold  $\delta_c(t)$  corresponding to the formation time  $t$ . The solution of the problem can be enormously simplified for Brownian trajectories (Chandrasekhar 1943), that is for sharp  $k$ -space filtered density fields, as in this case contribution of each wave mode is independent of all others. In such a case we have to solve the Fokker-Planck equation for the probability density  $\Pi(\delta, S)d\delta$ , where  $S \equiv \sigma^2(R)$  and  $\sigma(R)$  is the standard deviation of fluctuations in the initial density field, smoothed at a scale  $R$ ,

$$\frac{\partial \Pi(\delta, S)}{\partial S} = \frac{1}{2} \frac{\partial^2 \Pi(\delta, S)}{\partial \delta^2} \quad (5.6)$$

The solution (Porciani et al. 1998; Zentner 2007) can be obtained using the absorbing boundary condition  $\Pi(\delta_c(t), S) = 0$  and the initial condition  $\Pi(\delta, S=0) = \delta_D(\delta)$ , where  $\delta_D(\delta)$  is the Dirac delta function

$$\Pi(\delta, S; \delta_c) d\delta = \frac{1}{\sqrt{2\pi S}} \times \left[ \exp\left(-\frac{\delta^2}{2S}\right) - \exp\left(-\frac{(\delta - 2\delta_c(t))^2}{2S}\right) \right] d\delta \quad (5.7)$$

Now define  $F(S, \delta_c(t)) = \int_{-\infty}^{\delta_c(t)} d\delta \Pi(\delta, S; \delta_c(t))$  as the survival probability of trajectories and obtain the differential probability for a first barrier crossing:

$$f(S) = -\frac{\partial F(S, \delta_c(t))}{\partial S} = \frac{\delta_c(t)}{\sqrt{2\pi S^3}} \exp\left(-\frac{\delta_c(t)^2}{2S}\right) \quad (5.8)$$

From this, one can obtain the co-moving number density of collapsed haloes at time  $t$  with mass between  $M$  and  $M + dM$

$$\begin{aligned} N_{\text{PS}}(M, t) dM &= \frac{\rho_{\text{nr}}}{M} f(S) \left| \frac{dS}{dM} \right| dM \\ &= \sqrt{\frac{2}{\pi}} \frac{\rho_{\text{nr}}}{M} (\nu)^{\frac{1}{2}} \left| \frac{d \ln \sigma}{dM} \right| \exp\left[-\frac{\nu}{2}\right] dM. \end{aligned} \quad (5.9)$$

here  $\rho_{\text{nr}}$  is the average comoving density of non-relativistic matter and  $\nu \equiv [\delta_c(t)/\sigma(M)]^2 \equiv [\delta_c/(D(t)\sigma(M))]^2$ , where  $\delta_c$  is the threshold density contrast for collapse,  $D(t)$  is the linear rate of growth for density perturbations and  $\sigma(M)(\equiv S^{1/2})$  is the standard deviation of fluctuations in the initial density field, which is smoothed over a scale that encloses mass  $M$ .

In the following discussion, we will denote the mass function by  $N(M, t)$  if the statement is independent of the specific form of the mass function. We will use a subscript PS when the statements apply only to the Press-Schechter form of the mass function.

With Sasaki's ansatz, the destruction rate efficiency  $\phi$  can be written in this case as

$$\phi(t) = \frac{1}{D(t)} \frac{dD(t)}{dt}. \quad (5.10)$$

With this, we can write down the rate of halo formation for the Press-Schechter mass function from equation (5.5) as:

$$\begin{aligned} \dot{N}_{\text{form}}(M, t) &= \dot{N}_{\text{PS}}(M, t) + \frac{1}{D(t)} \frac{dD(t)}{dt} N_{\text{PS}}(M, t) \\ &= \frac{1}{D(t)} \frac{dD(t)}{dt} N_{\text{PS}}(M, t) \frac{\delta_c^2}{\sigma^2(M) D^2(t)}. \end{aligned} \quad (5.11)$$

Note that for haloes with large mass, that is in the limit  $\delta_c \gg \sigma(M)D(t)$ ,  $\dot{N}_{\text{form}}$  approaches  $\dot{N}_{\text{PS}}$ . In other words, the total change in the number of haloes is determined by formation of new haloes. For haloes with low mass, where  $\sigma$  is much larger than unity, although  $\dot{N}_{\text{form}}$  remains positive, the total change is dominated by destruction and  $\dot{N}_{\text{PS}}$  becomes negative.

We can also define two related, useful quantities now. Firstly, the probability  $p(t_1, t_2)$  that a halo which exists at  $t_1$  continues to exist at  $t_2$  without merging is given by

$$p(t_1, t_2) = \exp \left[ - \int_{t_1}^{t_2} \phi(t') dt' \right] = \frac{D(t_1)}{D(t_2)} \quad (\text{where } t_2 > t_1) \quad (5.12)$$

This is usually known as the survival probability of haloes, and is independent of halo mass in the Sasaki prescription. In this picture, the distribution of epochs  $t_f$  of formation of haloes with mass  $M$  at time  $t$  is given by

$$F(M; t_f, t) dM dt_f = \dot{N}_{\text{form}}(M, t_f) p(t_f, t) dM dt_f. \quad (5.13)$$

### 5.1.2 Sasaki prescription: Sheth-Tormen mass function

The Press-Schechter mass function does not provide a very good fit to halo mass function obtained in N-body simulations. In particular, it under-predicts the number density of large mass

haloes, and over-predicts that of small mass haloes. Hence it is important to generalize the calculation of formation rates to other models for mass function that are known to fit simulations better. The Sheth-Tormen form of mass function (Sheth & Tormen 1999) is known to fit simulations much better than the Press-Schechter form.<sup>1</sup> (For a comparison of both of these forms of halo mass function with simulations, see Fig. 3 of Jenkins et al. 2001.) The Sheth-Tormen mass function is given by

$$N_{\text{ST}}(M, t)dM = A\sqrt{\frac{2}{\pi}}\frac{\rho_{\text{nr}}}{M}(a\nu)^{1/2}\left|\frac{d\ln\sigma}{dM}\right|\times[1+(a\nu)^{-p}]\exp\left[-\frac{a\nu}{2}\right]dM, \quad (5.14)$$

where the parameters  $a$ ,  $p$ , and  $A$  have best fit values of  $a = 0.707$ ,  $p = 0.3$  and  $A = 0.322$  (Sheth & Tormen 1999), and the quantity  $\nu$  is as defined before. This form of mass function has the added advantage of being similar to the mass function derived using a variable barrier motivated by ellipsoidal collapse of overdense regions (Sheth et al. 2001; Sheth & Tormen 2002). Note that if we choose  $A = 0.5$ ,  $p = 0$  and  $a = 1$  then we recover the Press-Schechter mass function derived using spherical collapse. Recently, it has been shown that the best fit values of these parameters depend on the slope of the power spectrum (Bagla et al. 2009).

We can now apply the Sasaki prescription to this form of mass function and calculate the rates of halo formation and destruction (Ripamonti 2007). We get for the destruction rate efficiency

$$\phi(t) = \frac{1}{D}\frac{dD}{dt}[1 - 2p]. \quad (5.15)$$

Note that the destruction rate efficiency is independent of mass. The rate of halo formation is then given by

$$\dot{N}_{\text{form}}^{\text{ST}}(M, t) = -\frac{1}{D}\frac{dD}{dt}\left[\frac{2p}{1+(a\nu)^{-p}} - a\nu\right]N_{\text{ST}}(M, t). \quad (5.16)$$

Note that in this case, because of the extra term, the halo formation rate can be negative for some values of halo mass. Since negative values of rate of halo formation are unphysical, this indicates that the generalization of Sasaki approximation to the Sheth-Tormen mass function is incorrect. The same problem is encountered if we use other models of the halo mass function (Samui et al. 2009).

However, since the basic framework outlined in the beginning of this section is clearly correct, there should not be any problems in generalizing it to other mass functions. It is therefore likely that the simplifying assumptions of the Sasaki method that led to the estimate of the halo destruction rate efficiency of equation (5.15) are responsible for negative halo formation rate.

---

<sup>1</sup>Even this form of halo mass function has poor accuracy in some cases, namely, for conditional mass functions with large mass ratios and for mass function in overdense regions (Sheth & Tormen 2002). In applications involving these regimes it is perhaps advisable to use more accurate fitting functions to simulation data. However, the Sheth-Tormen form still has the property of being considerably better than the Press-Schechter form while having a physical interpretation. It is thus preferable in many semi-analytic models where the Press-Schechter form is used.

### 5.1.3 Excursion set approach to halo formation rate: Press-Schechter mass function

To check this assertion we perform an explicit calculation of the rate of halo formation using the excursion set formalism. Recall that from equations (5.2) and (5.3), we can write for the halo destruction rate efficiency as

$$\phi(M_1, t) = \int_{M_1}^{\infty} \tilde{Q}(M_1, M_2; t) dM_2, \quad (5.17)$$

where  $\tilde{Q}(M_1, M_2; t)$  represents the probability that an object of mass  $M_1$  grows into an object of mass  $M_2$  per unit time through merger or accretion at time  $t$ . This quantity is also known as the transition rate.

In the excursion set formalism, the conditional probability for a halo of mass  $M_1$  present at time  $t_1$  to merge with another halo to form a larger halo of mass between  $M_2$  and  $M_2 + dM_2$  at time  $t_2 > t_1$  (Lacey & Cole 1993, 1994) can be written for the extended Press-Schechter mass function as

$$f(M_2, \delta_2 | M_1, \delta_1) dM_2 = \sqrt{\frac{2}{\pi}} \frac{\delta_2(\delta_1 - \delta_2)}{\delta_1} \sigma_2^2 \left[ \frac{\sigma_1^2}{\sigma_2^2(\sigma_1^2 - \sigma_2^2)} \right]^{\frac{3}{2}} \times \exp \left[ -\frac{(\delta_2 \sigma_1^2 - \delta_1 \sigma_2^2)^2}{2\sigma_1^2 \sigma_2^2 (\sigma_1^2 - \sigma_2^2)} \right] \left| \frac{d\sigma_2}{dM_2} \right| dM_2. \quad (5.18)$$

Here,  $\sigma_1$  and  $\sigma_2$  are values of the standard deviation of the density perturbations when smoothed over scales that contain masses  $M_1$  and  $M_2$  respectively, and  $\delta_1$  and  $\delta_2$  are the values of the threshold density contrast for spherical collapse at time  $t_1$  and  $t_2$  respectively. Taking the limit  $t_2$  tends to  $t_1$ , i. e.  $\delta_2$  tends to  $\delta_1$ , we can determine the mean transition rate at time  $t = t_1$ :

$$\tilde{Q}(M_1, M_2; t) dM_2 = \sqrt{\frac{2}{\pi}} \sigma_2^2 \left[ \frac{\sigma_1^2}{\sigma_2^2(\sigma_1^2 - \sigma_2^2)} \right]^{\frac{3}{2}} \left| \frac{d\delta}{dt} \right| \times \exp \left[ -\frac{\delta^2(\sigma_1^2 - \sigma_2^2)}{2\sigma_1^2 \sigma_2^2} \right] \left| \frac{d\sigma_2}{dM_2} \right| dM_2. \quad (5.19)$$

This represents the probability that a halo of mass  $M_1$  will accrete or merge to form another halo of mass  $M_2$  at time  $t$ . We can use this with equation (5.17) to explicitly compute the destruction rate, and hence the halo formation rate.

However, in the excursion set method, an arbitrarily small change in the halo mass is treated as creation of a new halo. As a result, the integral in equation (5.17) diverges unless we specify a ‘‘tolerance’’ parameter. We assume that a halo is assumed to have *survived* unless its mass increases such that  $M_1 \rightarrow M_2 \geq M_1(1 + \epsilon)$  due to either accretion or merging, where  $\epsilon$  is a small number. This assumption allows us to introduce a lower cutoff in the integral in

equation (5.17) and the lower limit changes to  $M_1(1 + \epsilon)$ , leading to a convergent integral. This is also physically pertinent for our application as infinitesimal changes do not lead to variations in dynamical structure of haloes, and hence we do not expect any changes in galaxies hosted in haloes that do not undergo a major merger. This is similar in spirit to the assumption made elsewhere in the literature that a halo is assumed to survive until its mass increases by a factor two (Lacey & Cole 1994; Kitayama & Suto 1996). Note that N-body simulations have a natural cutoff due to the discrete nature of N-body particles. With the introduction of this new parameter, the modified formula for the halo destruction rate efficiency is given by

$$\phi(M_1, t) = \int_{M_1(1+\epsilon)}^{\infty} \tilde{Q}(M_1, M_2; t) dM_2 \quad (5.20)$$

This can then be used to calculate the rate of halo formation using equation (5.5).

Fig. 5.1 shows the destruction rate efficiency  $\phi(M, t)$  computed in this manner for the Press-Schechter mass function for an Einstein-de Sitter cosmology with power law spectrum of density perturbations with index  $-1.5$ . Curves have been plotted for  $\epsilon = 0.1$  and  $\epsilon = 0.5$ . We have also shown the Sasaki approximation in the same panel. The excursion set result has three features:

1. At small  $M$ , the excursion set value approaches the destruction rate computed using the Sasaki approximation.
2. The destruction rate has a peak, more pronounced for smaller  $\epsilon$ , near the scale of non-linearity.
3. At larger scales the destruction rate falls rapidly; this is the region where deviations from the Sasaki result are the largest. Thus the halo destruction rate efficiency vanishes at large masses.

A similar trend is seen for other power spectra. We postpone a detailed discussion of these issues to the end of this section.

#### 5.1.4 Excursion set approach to halo formation rate: Sheth-Tormen mass function

As discussed in Subsection 5.1.2, the Sheth-Tormen mass function is known to be a much better fit to N-body simulations than the Press-Schechter mass function. Several other forms of halo mass function have also been fitted to results of high resolution N-body simulations (Jenkins et al. 2001; Reed et al. 2003; Warren et al. 2006). But here we only focus on the Sheth-Tormen mass function. Recall that the Sasaki prescription gave unphysical results when applied to this form of the mass function. Therefore, we now derive the halo destruction rate efficiency, and

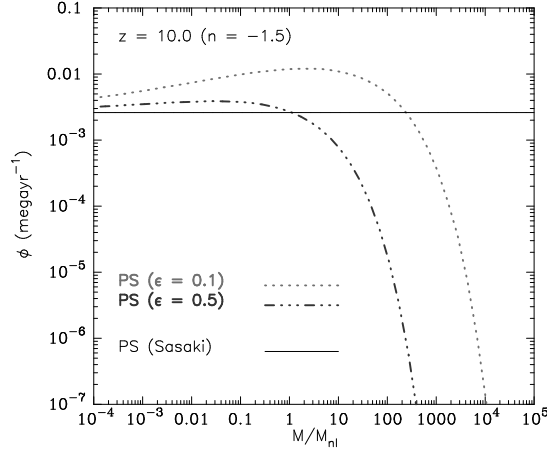


Figure 5.1: Destruction rate  $\phi(M, t)$  at  $z = 10$  for the Press-Schechter mass function for a power law model with index  $-1.5$ . Curves have been plotted for  $\epsilon = 0.1$  and  $\epsilon = 0.5$ .

the halo formation rates for the Sheth-Tormen mass function. This requires obtaining analogs of equations (5.18) and (5.19).

Sheth et al. (2001) showed that once the barrier shape is known, all the predictions of the excursion set approach, like the conditional mass function, associated with that barrier can be computed easily<sup>2</sup>. Further, they showed that the barrier shape for ellipsoidal collapse is

$$B(\sigma, t) \equiv \delta_{ec}(\sigma, t) = \sqrt{a}\delta_c(t) [1 + \beta(av)^{-\gamma}], \quad (5.21)$$

where  $a = 0.75$ ,  $\beta = 0.485$ ,  $\gamma = 0.615$ , and,  $\delta_c(t)$  is the threshold value of overdensity required for spherical collapse (also see Sheth & Tormen 2002). They also found that, for various barrier shapes  $B(S)$ , the first-crossing distribution of the excursion set theory is well approximated by

$$f(S)dS = \frac{|T(S)|}{\sqrt{2\pi}S^{3/2}} \exp\left[-\frac{B(S)^2}{2S}\right] dS, \quad (5.22)$$

where  $T(S)$  denotes the sum of the first few terms in the Taylor series expansion of  $B(S)$

$$T(S) = \sum_{n=0}^{\infty} \frac{(-S)^n}{n!} \frac{\partial^n B(S)}{\partial S^n}. \quad (5.23)$$

(Here, for conformity with the literature, we use the symbol  $S \equiv \sigma^2$ .) This expression gives the exact answer in the case of constant and linear barriers. For the ellipsoidal barrier, we can get convergence of the numerical result if we retain terms in the Taylor expansion up to  $n = 5$ .

For Press-Schechter mass function, the conditional mass function  $f(S_1, \delta_1 | S_2, \delta_2)$  can be obtained from the first crossing  $f(S)$  by just changing the variables  $\delta \rightarrow \delta_1 - \delta_2$  and  $S \rightarrow$

<sup>2</sup>These can be calculated for non-Gaussian initial conditions, see, e.g., de Simone et al. (2011)

$S_1 - S_2$ . This can be done because, despite the shift in the origin, the second barrier is still one of constant height. This is no longer true for Ellipsoidal collapse and hence we cannot simply rescale the function of equation to get the conditional mass function. Instead, this can be done by making the replacements  $B(S) \rightarrow B(S_1) - B(S_2)$  and  $S \rightarrow S_1 - S_2$  in equation (5.22).

$$f(S_1|S_2)dS_1 = \frac{|T(S_1|S_2)|}{\sqrt{2\pi}(S_1 - S_2)^{3/2}} \times \exp \left[ -\frac{(B(S_1) - B(S_2))^2}{2(S_1 - S_2)} \right] dS_1, \quad (5.24)$$

where we now have

$$T(S_1|S_2) = \sum_{n=0}^5 \frac{-(S_1 - S_2)^n}{n!} \frac{\partial^n (B(S_1) - B(S_2))}{\partial S_1^n}. \quad (5.25)$$

Using Bayes' theorem, we now have

$$f(S_2|S_1) dS_2 = \frac{|T(S_1|S_2)||T(S_2)|}{|T(S_1)|} \frac{1}{\sqrt{2\pi}} \left[ \frac{S_1}{S_2(S_1 - S_2)} \right] \times \exp \left[ -\frac{[B(S_1) - B(S_2)]^2}{2(S_1 - S_2)} - \frac{B^2(S_2)}{2S_2} + \frac{B^2(S_1)}{2S_1} \right] dS_2. \quad (5.26)$$

A change of variables from  $S$  to  $M$  now gives us an analog of equation (5.18) for the Sheth-Tormen mass function. In other words, we get the conditional probability  $f_{\text{ST}}(M_2|M_1)d \ln M_2$  that a halo of mass  $M_1$  present at time  $t_1$  will merge to form a halo of mass between  $M_2$  and  $M_2 + dM_2$  at time  $t_2 > t_1$ . Further, taking the limit as  $t_2$  tends to  $t_1 (= t)$ , we obtain  $\tilde{Q}(M_1, M_2; t)$ . As before, we can then use it to calculate the halo destruction rate efficiency  $\phi(M, t)$  and the rate of halo formation  $\dot{N}_{\text{form}}^{\text{ST}}(M_1, z)$  using equations (5.5) and (5.20). We perform this part of the calculation numerically. However, it is also possible to use this formalism to calculate formation rates for the square-root barrier (Moreno et al. 2009, 2008; Giocoli et al. 2007), which is a good approximation for the ellipsoidal collapse model.

Fig. 5.2 is the analog of Fig. 5.1 for the Sheth-Tormen mass function. It shows the destruction rate per halo  $\phi(M, t)$  computed using the excursion set method for an Einstein-de Sitter cosmology with power law spectrum of density perturbations with index  $-1.5$  at  $z = 10.0$ . Curves have been plotted for  $\epsilon = 0.1$  and  $\epsilon = 0.5$ . We have also shown the Sasaki approximation for ST mass function in the same panel for comparison. This result for the Sheth-Tormen mass function has the same features as the result for the Press-Schechter mass function. We also see that the destruction rate efficiency is far from constant at small  $M/M_{nl}$ . Thus the central assumption of the Sasaki prescription is invalid in the case of Sheth-Tormen mass function as well.

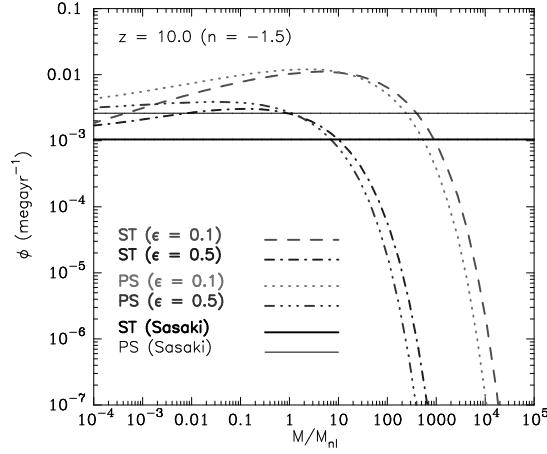


Figure 5.2: Same as Fig. 5.1 but for the Sheth-Tormen (as well as Press-Schechter) mass function.

$n$	$N_{\text{box}}$	$N_{\text{part}}$	$r_{\text{nl}}^i$	$r_{\text{nl}}^f$	$r_{\text{nl}}^{\text{max}}$	$z_i$
-1.5	$400^3$	$400^3$	2.5	12.0	10.0	103.38
-0.5	$256^3$	$256^3$	2.5	12.0	18.2	291.53

Table 5.1: For power law: here  $n$  is the index of the power spectrum,  $N_{\text{box}}$  is the size of the simulation box,  $N_{\text{part}}$  represents the number of particles,  $r_{\text{nl}}^i$  is the scale of non-linearity at the earliest epoch,  $r_{\text{nl}}^f$  is the actual scale of non-linearity for the last epoch,  $r_{\text{nl}}^{\text{max}}$  represents the maximum scale of non-linearity and  $z_i$  is the starting redshift of the simulations for every model.

$L_{\text{box}}$	$N_{\text{part}}$	$m_{\text{part}}$	$\epsilon$	$z_f$	$z_{\text{out}}$
23.04	$512^3$	$6.7 \times 10^6$	1.35	5.0	5.04
51.20	$512^3$	$7 \times 10^7$	3.00	3.0	3.34
76.80	$512^3$	$2.3 \times 10^8$	4.50	1.0	1.33

Table 5.2: For LCDM: columns 1 and 2 list the size of the box (in Mpc/ $h$ ) and the number of particles used in the simulations. Columns 3 and 4 give the mass (in  $M_{\odot}/h$ ) and force resolution (in kpc/ $h$ ; not to be confused with the  $\epsilon$  used in the text) of the simulations, while columns 5 and 6 tell us the redshift at which the simulations were terminated and the redshift for which the analyses were done.

## 5.2 N-body simulations

From the excursion set calculation described in the previous section, we thus find that the halo destruction rate efficiency is not independent of mass as is assumed in the Sasaki prescription. Clearly, this is the reason why Sasaki prescription yields unphysical values for the rate of halo formation. In this section and the next, we now compare the results of our excursion set calculation with results of *N*-body simulations.

We used the TreePM code (Khandai & Bagla 2009) for these simulations. The TreePM (Bagla 2002; Bagla & Ray 2003) is a hybrid *N*-body method which improves the accuracy and performance of the Barnes-Hut (BH) Tree method (Barnes & Hut 1986) by combining it with the PM method (Miller 1983; Klypin & Shandarin 1983; Bouchet et al. 1985; Bouchet & Kandrup 1985; Hockney & Eastwood 1988; Bagla & Padmanabhan 1997; Merz et al. 2005). The TreePM method explicitly breaks the potential into a short-range and a long-range component at a scale  $r_s$ : the PM method is used to calculate the long-range force and the short-range force is computed using the BH Tree method. Use of the BH Tree for short-range force calculation enhances the force resolution as compared to the PM method.

The mean inter-particle separation between particles in the simulations used here is  $l_{\text{mean}} = 1.0$  in units of the grid-size used for the PM part of the force calculation. In our notation this is also cube root of the ratio of simulation volume  $N_{\text{box}}^3$  to the total number of particles  $N_{\text{part}}$ .

Power law models do not have any intrinsic scale apart from the scale of non-linearity introduced by gravity. We can therefore identify an epoch in terms of the scale of non-linearity  $r_{\text{nl}}$ . This is defined as the scale for which the linearly extrapolated value of the mass variance at a given epoch  $\sigma_L(a, r_{\text{nl}})$  is unity. All power law simulations are normalized such that  $\sigma^2(a = 1.0, r_{\text{nl}} = 8.0) = 1.0$ . The softening length in grid units is 0.03 in all runs.

The  $\Lambda$ CDM simulations were run with the set of cosmological parameters favored by *Wilkinson Microwave Anisotropy Probe* 5-yr data (WMAP; Komatsu et al. 2009) as the best fit for the  $\Lambda$ CDM class of models:  $\Omega_{nr} = 0.2565$ ,  $\Omega_{\Lambda} = 0.7435$ ,  $n_s = 0.963$ ,  $\sigma_8 = 0.796$ ,  $h = 0.719$  and  $\Omega_b h^2 = 0.02273$ . The simulations were done with  $512^3$  particles in a comoving cube of three different values of the physical volume as given in Table 5.2.

Simulations introduce an inner and an outer scale in the problem and in most cases we work with simulation results where  $L_{\text{box}} \gg r_{\text{nl}} \geq L_{\text{grid}}$ , where  $L_{\text{grid}}$ , the size of a grid cell is the inner scale in the problem.  $L_{\text{box}}$  is the size of the simulation and represents the outer scale. In Table (5.1) we list the power law models simulated for the present study. We list the index of the power spectrum  $n$  (column 1), size of the simulation box  $N_{\text{box}}$  (column 2), number of particles  $N_{\text{part}}$  (column 3), the scale of non-linearity at the earliest epoch used in this study (column 4), and, the maximum scale of non-linearity,  $r_{\text{nl}}^{\text{max}}$  (column 6) given our tolerance level of 3% error in the mass variance at this scale. For some models with very negative indices we have run the simulations beyond this epoch. This can be seen in column 5 where we list the actual scale of non-linearity for the last epoch. The counts of haloes in low mass bins are relatively unaffected by finite box considerations. We therefore limit errors in the mass function

by running the simulation up to  $r_{\text{nl}}^{\text{max}}$ . Column 7 lists the starting redshift of the simulations for every model. Similarly, in Table (5.2), we mention the details of the LCDM simulations used in this work. We list the size of the simulation box  $L_{\text{box}}$  in Mpc/ $h$  (column 1), number of particles used in the simulations  $N_{\text{part}}$  (column 2), mass of the particles  $m_{\text{part}}$  in  $M_{\odot}/h$  (column 3), force resolution  $\epsilon$  (not to be confused with the  $\epsilon$  used in the text) of the simulations in kpc/ $h$  (column 4), the redshift  $z_{\text{f}}$  at which the simulations were terminated (column 5) and the redshift  $z_{\text{out}}$  for which the analyses were done (column 6).

In order to follow the merger history of dark matter haloes in each of these simulations, we store the particle position and velocities at different redshifts. A friend-of-friend group finding algorithm is used to locate the virialized haloes in each of these slices. We adopt a linking length that is 0.2 times the mean inter-particle separation, corresponding to the density of virialized haloes. Only groups containing at least 20 particles are included in our halo catalogs. A merger tree is then constructed out of the halo catalogs by tracking the evolution of each particle through various slices. This lets us identify a halo as it evolves with time through mergers with other haloes. We then describe the formation and destruction of haloes in terms of change in number of particles between consecutive snapshots of the simulation. When a halo of mass  $M$  at redshift  $z$  turns into a halo of mass  $M'$  at  $z' (< z)$ , then we say that a halo of mass  $M$  was destroyed at redshift  $z$  and a halo of mass  $M'$  has formed at  $z'$  if  $M' \geq M(1 + \epsilon)$ . We identify the resolution parameter  $\epsilon$  with that used in our excursion set calculation and experiment with different values as described in the next section.

We find that a tolerance parameter  $\epsilon$ , similar to the one defined before, also occurs while analyzing the results of N-body simulations. We identify these two quantities. As we will see in the next section, the formation rate in our model has a dependence on  $\epsilon$ , which reproduces the dependence of the results of N-body simulations on this quantity. Thus, the presence of  $\epsilon$  in our analytical model is crucial in comparing our results with the N-body results.

## 5.3 Results and discussion

In this section we present the results of a comparison of our calculations presented in Section 5.1 with N-body simulations. We present comparison of the destruction rate efficiency and the rate of halo formation and then discuss our results at the end of this section. We also consider two related quantities, the halo survival probability and the distribution of halo formation times, that were defined in Section 5.1.

### 5.3.1 Halo destruction rate efficiency

Figs. 5.3 and 5.4 show the halo destruction rate efficiency  $\phi(M, t)$  for Sheth-Tormen and Press-Schechter mass functions in an Einstein-de Sitter universe with a power law power spectrum of density fluctuations with indices  $n = -0.5$  and  $n = -1.5$  respectively. The top row of

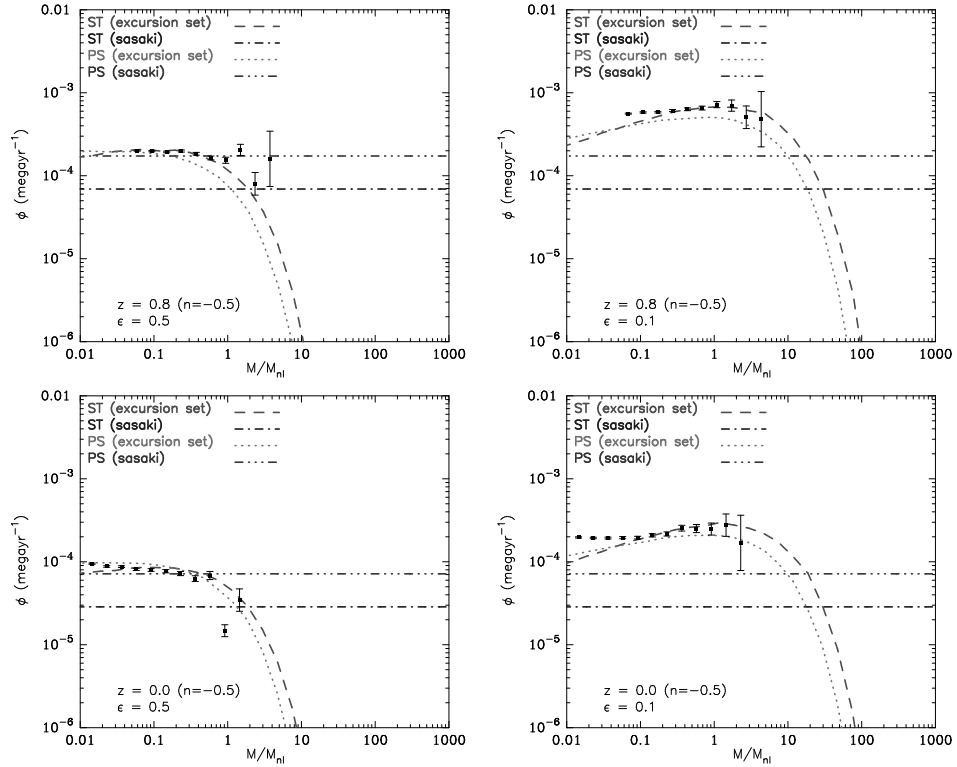


Figure 5.3: Comparison of the destruction rate efficiencies computed using our method and Sasaki formalism for both ST and PS mass function at  $r_{nl} = 5$  grid lengths (top row) and  $r_{nl} = 8$  grid lengths (second row). All curves are plotted for power-law model with index  $n = -0.5$ . Curves for  $\epsilon = 0.5$  are shown in the left panel and  $\epsilon = 0.1$  in the right panel. Points with error bars represent the corresponding results obtained from N-body simulations.

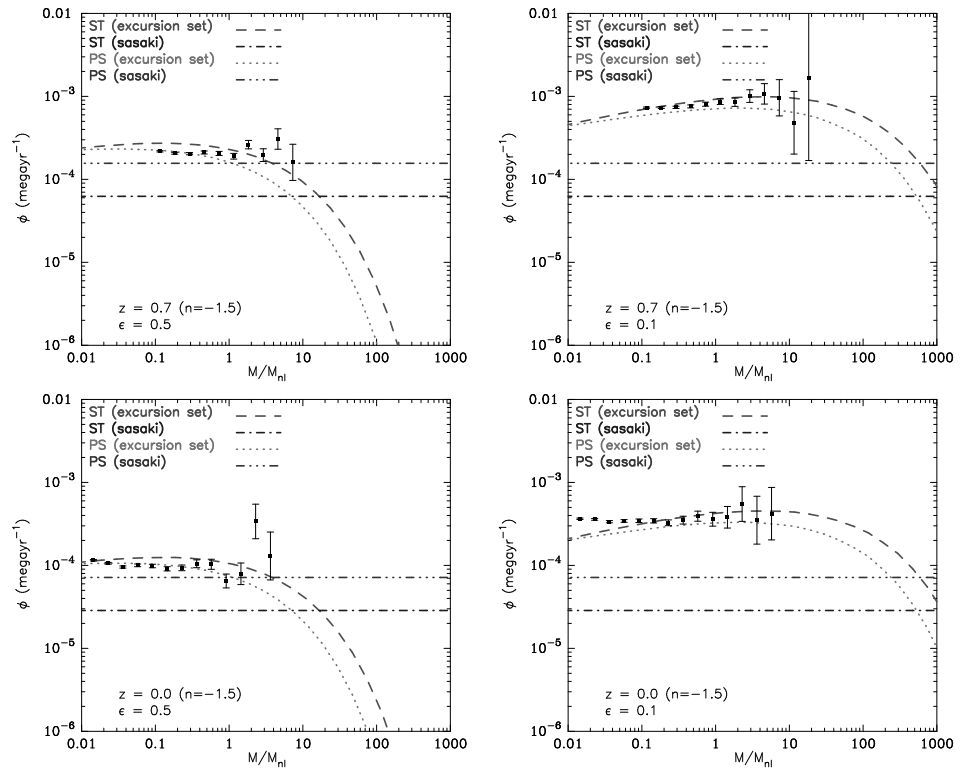


Figure 5.4: Same as Fig. 5.3 but now for  $n = -1.5$ . The two epochs correspond to  $r_{nl} = 4$  and  $r_{nl} = 8$  grid lengths respectively.

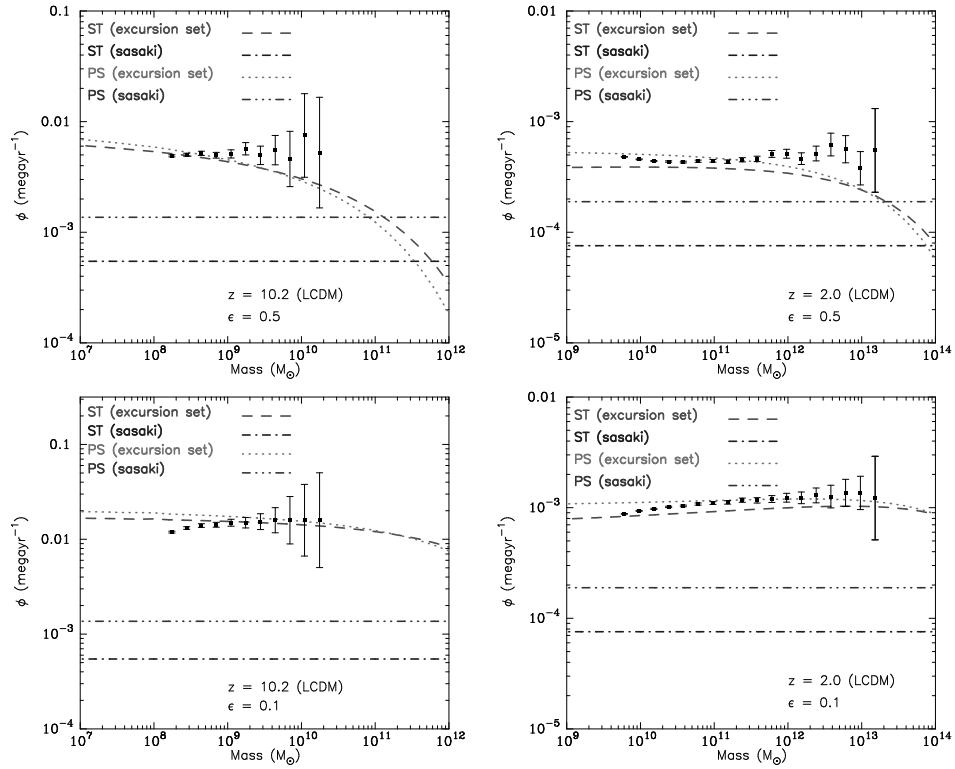


Figure 5.5: Destruction rates for  $\Lambda$ CDM model for both PS and ST mass functions using different thresholds ( $\epsilon = 0.5$  for first;  $\epsilon = 0.1$  for second) and different redshifts ( $z = 10.2$  for left panel,  $z = 2.0$  for right panel). Again, points with error bars represent the corresponding results obtained from N-body simulations.

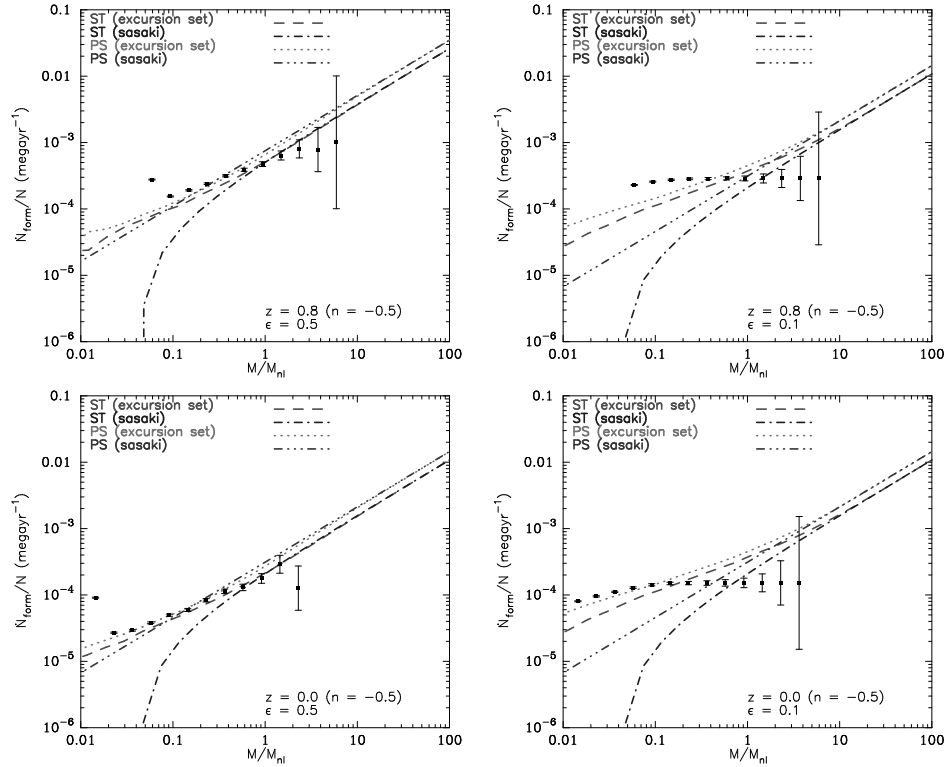


Figure 5.6: Comparison of the formation rates computed using our method and Sasaki formalism for both ST and PS mass functions for  $r_{nl} = 5$  (top row) and  $r_{nl} = 8$  (bottom row). All curves are plotted for power-law model with index  $n = -0.5$ . Curves for  $\epsilon = 0.5$  are shown in the left panel and  $\epsilon = 0.1$  in the right panel. Points with error bars represent the corresponding results obtained from N-body simulations.

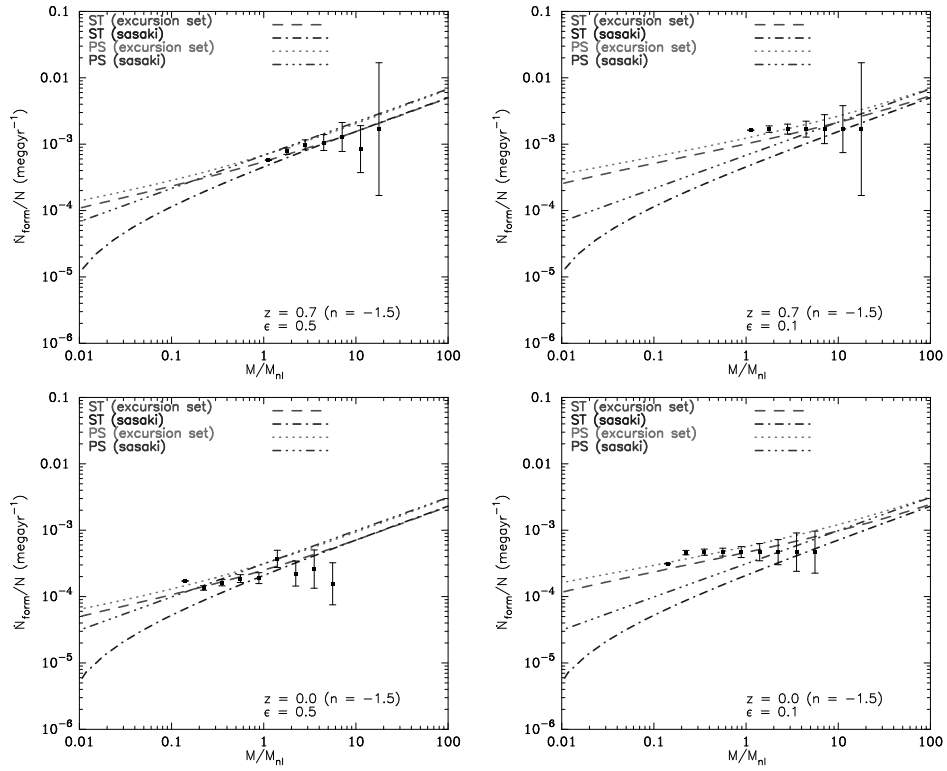


Figure 5.7: Same as Fig. 5.6 but now for  $n = -1.5$ . The two epochs correspond to  $r_{\text{nl}} = 4$  and  $r_{\text{nl}} = 8$  grid lengths respectively.

both figures shows the halo destruction rate efficiency at  $z = 0.8$  and the second row shows the same at  $z = 0.0$ . In each case, we compute the halo destruction rate efficiency using the Sasaki method as well as our excursion set method. We then derive  $\phi(M, t)$  from our N-body simulations for a comparison: see Bagla et al. (2009) for details of the simulations and best fit parameters for the ST mass function. These results are superimposed on the plots. For the excursion set calculation and for the comparison with simulations, we use  $\epsilon = 0.5$  (left column) and  $\epsilon = 0.1$  (right column). For the two power spectra, the two redshifts that we consider correspond to  $r_{\text{nl}} = 5$  and  $r_{\text{nl}} = 8$  grid lengths, and  $r_{\text{nl}} = 4$  and  $r_{\text{nl}} = 8$  grid lengths respectively.

As we saw in Figs. 5.1 and 5.2, we find that Sasaki's assumption is not valid for ST or PS mass functions, that is  $\phi(M, t)$  depends on the halo mass. We also see that the value of  $\phi(M, t)$  derived from simulations matches well with that calculated by our method. On the other hand, the predictions of Sasaki's approximation do not match the simulations. This difference is more pronounced for the smaller value of  $\epsilon$ . Note that the points from N-body simulations have large error-bars at higher mass as the number of haloes decreases at these scales. The most notable feature of the destruction rate efficiency in the excursion set picture is that it cuts off very sharply for large masses. Another aspect is that for small  $\epsilon$ , there is a pronounced peak in  $\phi$  and it drops off towards smaller masses.

We have also calculated the destruction rate efficiency for the  $\Lambda$ CDM cosmological model for both Press-Schechter and Sheth-Tormen mass functions and compared it with derived values from simulations. The results are shown in Fig. 5.5 for two redshifts (2.0 and 10.2) and two values of  $\epsilon$  (0.5 and 0.1). We can see that results calculated by our technique fit numerical results better.

### 5.3.2 Halo formation rate

Having calculated the destruction rate efficiency, we can now calculate the halo formation rate using the formalism described in Section 5.1 and compare it with the derived halo formation rates from our simulations. The results are shown in Figs. 5.6 and 5.7 for an Einstein-de Sitter Universe with a power law power spectrum of density fluctuations with indices  $n = -0.5$  and  $n = -1.5$  respectively. The first row of both figures shows the formation rate at redshift  $z = 0.8$  and the second row shows the same at redshift  $z = 0.0$ . Note the quantity plotted here is the ratio  $\dot{N}_{\text{form}}(M, t)/N(M, t)$ . We have shown the results from the Sasaki prescription and the excursion set calculations and have superimposed formation rates derived from N-body simulations. As before, for the excursion set calculation and for the comparison with simulations, we use  $\epsilon = 0.5$  (left column) and  $\epsilon = 0.1$  (right column). For the two power spectra, the two redshifts that we consider correspond to  $r_{\text{nl}} = 5$  and  $r_{\text{nl}} = 8$  grid lengths, and  $r_{\text{nl}} = 4$  and  $r_{\text{nl}} = 8$  grid lengths respectively. The corresponding results for the  $\Lambda$ CDM cosmological model are shown in Fig. 5.8 for two redshifts (2.0 and 10.2) and two values of  $\epsilon$  (0.5 and 0.1).

Again, we see that the excursion set results fit simulation data much better as compared to

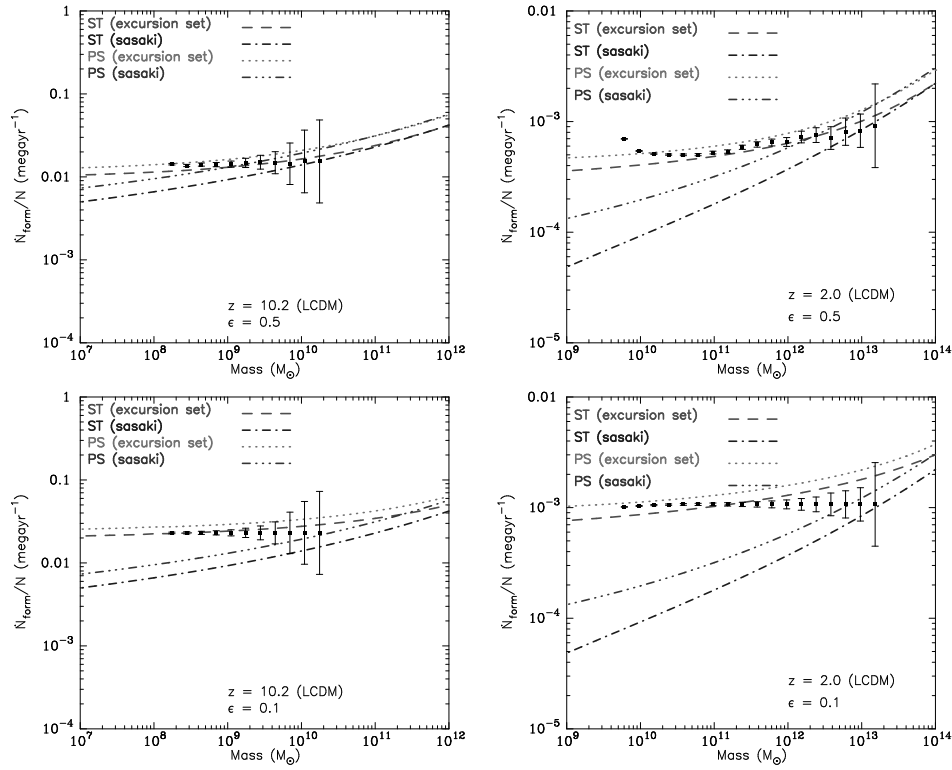


Figure 5.8: Formation rates for  $\Lambda$ CDM model for both PS and ST mass functions using different thresholds ( $\epsilon = 0.5$  for first;  $\epsilon = 0.1$  for second row) and different redshifts ( $z = 10.2$  for left panel,  $z = 2.0$  for right panel). As usual, points with error bars represent the corresponding results obtained from N-body simulations.

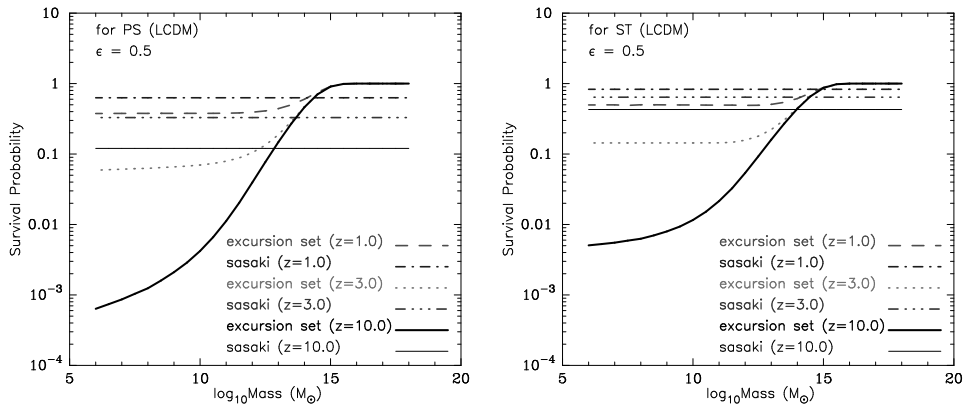


Figure 5.9: Comparison of the survival probabilities computed using our method and Sasaki formalism for both PS (left panel) and ST (right panel) mass functions with different redshifts ( $z = 1, 3$  and  $10$ ) for  $\epsilon = 0.5$ . Curves have been plotted for the  $\Lambda$ CDM model. These curves show the probability that the halo survives from that redshift up to the present epoch.

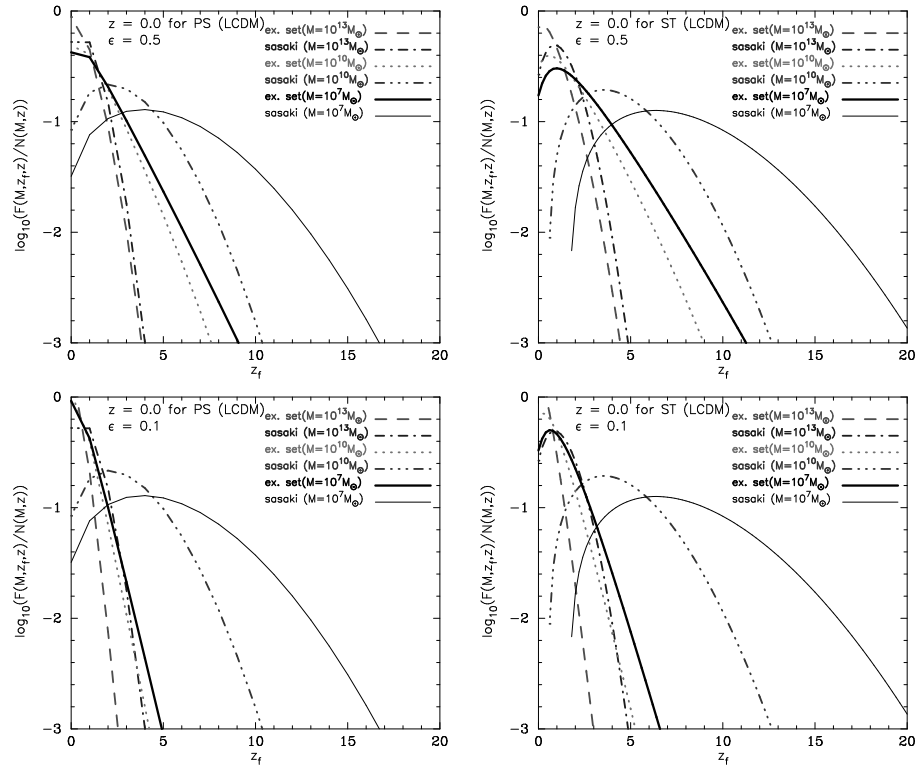


Figure 5.10: Plots for formation epoch distribution of haloes. Left column is for the PS and the right column is for the ST mass function. Curves have been plotted for the LCDM model. The formation epoch distribution as computed using the Sasaki formalism and the excursion set approach described in this work is shown in the top panel.

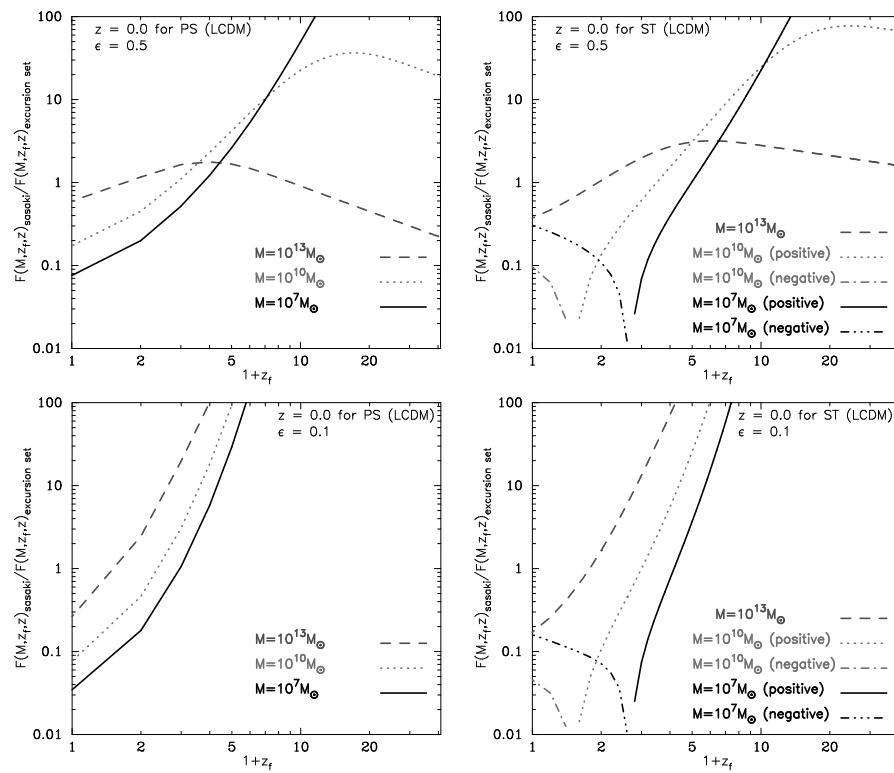


Figure 5.11: Ratio of the two different approaches used in Fig. 5.10 to highlight less obvious differences.

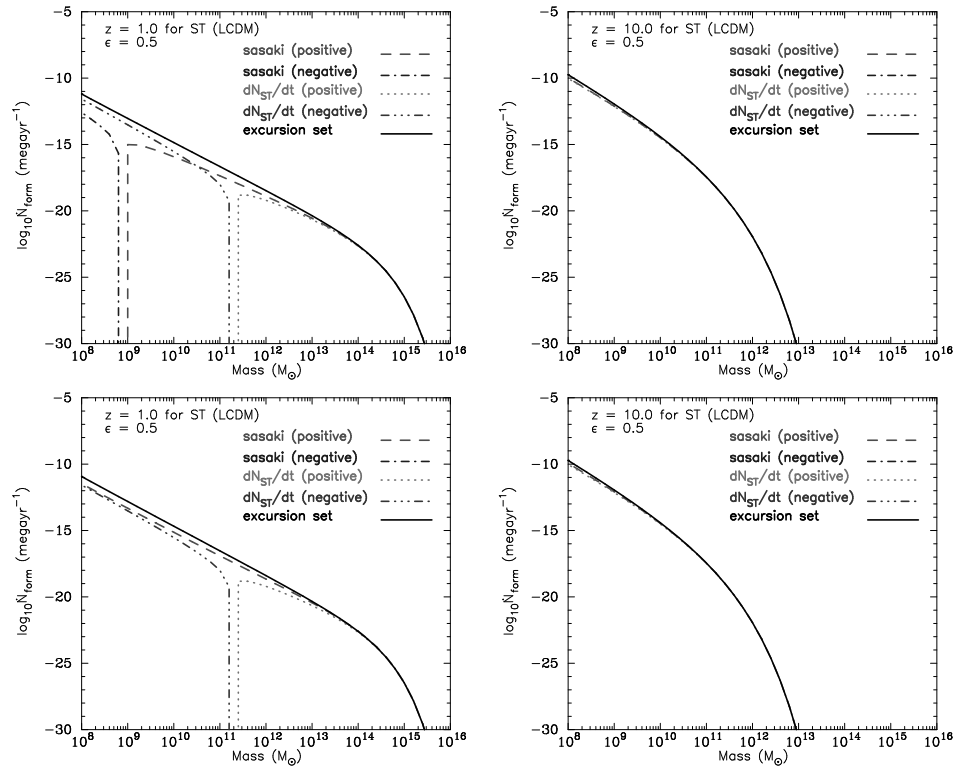


Figure 5.12: Upper panels show formation rates for ST mass function. Lower panels show the same where we used  $\phi$  computed from excursion set approach in the PS mass function and used that to compute the formation rate in the ST mass function.

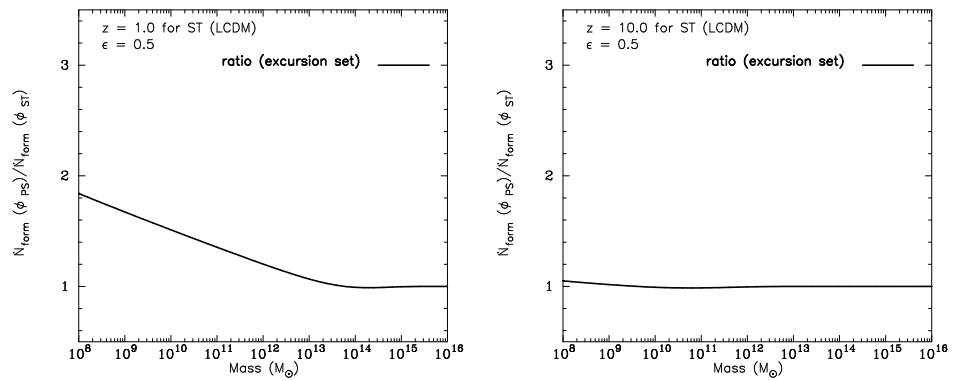
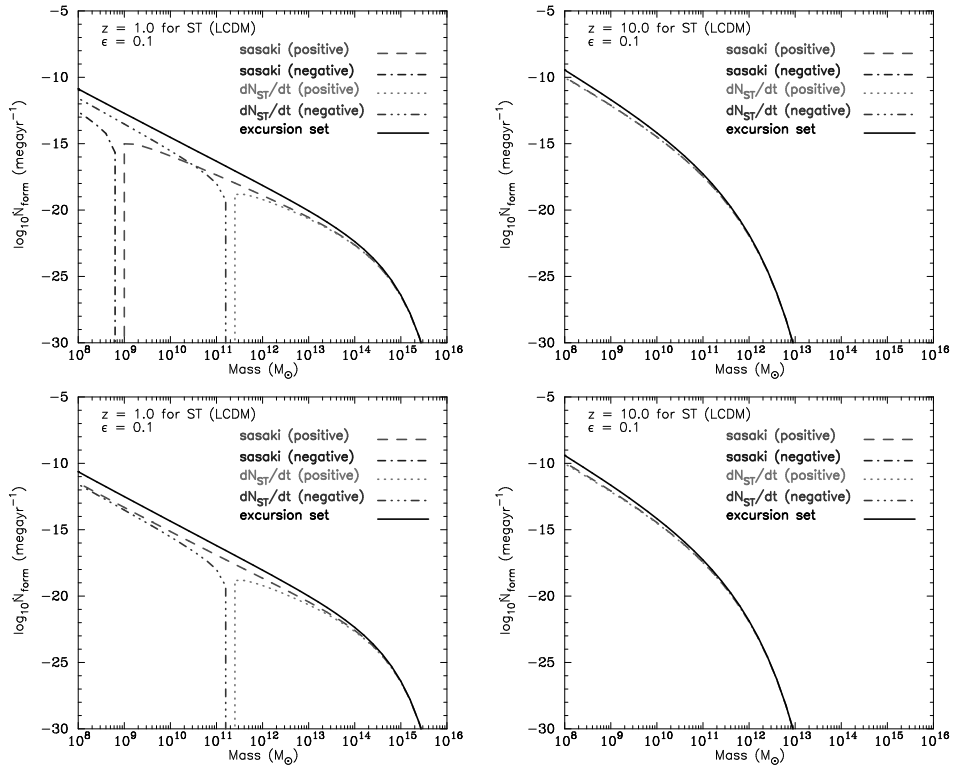
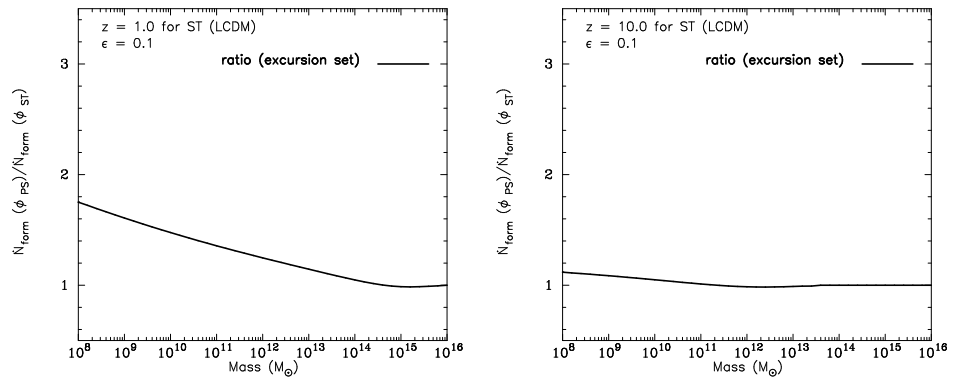


Figure 5.13: Ratio of formation rates estimated in the two approaches shown in Fig. 5.12.

Figure 5.14: Same as Fig. 5.12 but for  $\epsilon = 0.1$ Figure 5.15: Same as Fig. 5.13 but for  $\epsilon = 0.1$

the results from Sasaki prescription. The Sasaki method underestimates the formation rates by a large factor for low mass haloes. Results from the two methods tend to converge in the large mass limit, although a systematic difference remains between the Sheth-Tormen and Press-Schechter estimates, with the former always being larger than the latter. The difference in the Sasaki estimate and the excursion set estimate for the destruction rate efficiency and the formation rate is as high as an order of magnitude at some scales so the close proximity of simulation points to the excursion set calculations is a clear vindication of our approach. It is worth noting that there is a clear deviation of simulation points from the theoretical curves at small mass scales and this deviation is more pronounced at small mass scales for  $\epsilon = 0.5$ . It may be that some of the deviations arise due to a series representation of the barrier shape, and the number of terms taken into account may not suffice for the estimate. We have found that truncation of the series can affect results at small masses, though in most cases results converge with the five terms that we have taken into account for the range of masses considered here.

### 5.3.3 Halo survival probability

An important auxiliary quantity in the ongoing discussion is the halo survival probability, defined in Section 5.1. From our calculation of the halo destruction rate efficiency, we calculated the survival probability of dark matter haloes using both the excursion set formalism and the Sasaki prescription and compared results. These results are shown in Fig. 5.9, which shows the survival probabilities in the  $\Lambda$ CDM cosmological model for the Press-Schechter (left panel) and Sheth-Tormen (right panel) mass functions using the two approaches at three different redshifts ( $z = 1, 3$  and  $10$ ). In this case, we have used  $\epsilon = 0.5$  for the excursion set calculation.

In Sasaki approximation, the destruction rate is independent of mass and hence the survival probability is also independent of mass. Our calculations show that this approximation is not true, and hence the survival probability of haloes must also depend on mass. We note that the survival probability is high for large mass haloes: if a very large mass halo forms at a high redshift then it is likely to survive without a significant addition to its mass. Smaller haloes are highly likely to merge or accrete enough mass and hence do not survive for long periods. Survival probability drops very rapidly as we go to smaller masses. While this is expected on physical grounds, it is an aspect not captured by the Sasaki approximation where equal survival probability is assigned to haloes of all masses. The mass dependence of survival probability is qualitatively similar to that obtained by Kitayama & Suto (1996). There is no significant qualitative difference between the curves for the Press-Schechter and the Sheth-Tormen mass functions.

### 5.3.4 Formation time distribution

Finally, another interesting quantity is the distribution  $F(M; t_f, t)$  of formation epochs  $t_f$  of haloes with mass  $M$  at  $t$ , defined in Section 5.1. This distribution can be obtained once the

survival probability and formation rate of haloes is known. We calculated the formation time distribution using the excursion set formalism and the Sasaki prescription. The results are shown in Fig. 5.10. We plot  $F(M; z_f, z = 0)/N(M, z = 0)$  versus the formation redshift  $z_f$  for three different masses ( $10^{13}$ ,  $10^{10}$  and  $10^7 M_\odot$ ) in the standard  $\Lambda$ CDM model for both Press-Schechter (left column) and Sheth-Tormen (right column) mass functions with  $\epsilon = 0.5$  (first row) and  $\epsilon = 0.1$  (second row). A common feature is that  $F$  as a function of  $z_f$  increases up to a certain redshift and then starts to decline. The epochs at which  $F$  drops by an order of magnitude from its peak can be interpreted as typical range of redshifts for the formation of bound systems of respective masses which exist at  $z = 0$ .

The differences between the formation redshift distribution for  $\epsilon = 0.5$  and  $\epsilon = 0.1$  are along expected lines: the formation redshifts are smaller for the lower value of  $\epsilon$  as a smaller change in mass is required for us to declare that a new halo has formed and hence typical haloes do not survive for a very long time. We see that the excursion set calculation suggests that haloes formed more recently as compared to the Sasaki approximation based estimate. This can be understood in terms of the equal survival probability assigned by the Sasaki approximation to haloes of all masses. For a clearer comparison, the ratio of the estimate based on Sasaki approximation and the excursion set calculation is shown in Fig. 5.11. We note that for very low mass haloes these two estimates differ by more than an order of magnitude. The main qualitative difference between the plots for the Press-Schechter and the Sheth-Tormen mass functions is caused by the negative formation rates in the Sasaki approximation.

### 5.3.5 Discussion

The results described above show conclusively that the excursion set approach predicts halo formation and destruction rates that match with simulations much better than the Sasaki approximation.

Another noteworthy aspect is that the destruction and formation rates depend on the value of  $\epsilon$  in simulations as well as the excursion set calculation thereby allowing us to differentiate between major and minor mergers. In comparison, there is no natural way to bring in this dependence in the Sasaki approximation. While the match between simulations and the excursion set approach for the two values of  $\epsilon$  is satisfying, it raises the question of the appropriate value of this parameter. In our view the appropriate value of the parameter should depend on the application in hand. In semi-analytic galaxy formation models, we should use a value of  $\epsilon$  that corresponds to the smallest ratio of masses of the infalling galaxy and the host galaxy where we expect a significant dynamical influence on star formation rate. For instance, Kauffmann et al. (1999) use  $\epsilon = 0.3$  in their semi-analytic galaxy formation model while considering formation of bulges in merger remnants. In case of galaxy clusters we may base this on the smallest ratio of masses where the intra-cluster medium is likely to be disturbed in a manner accessible to observations in X-ray emission or the Sunyaev-Zel'dovich effect (Sunyaev & Zeldovich 1972; Navarro et al. 1995; Kay 2004).

While the close match between simulations and the excursion set calculation is useful, it also implies that we should not use the simpler Sasaki approximation. The excursion set calculation of the halo destruction rate is fairly simple for the Press-Schechter mass function, but the corresponding calculation for the Sheth-Tormen mass function is much more complicated. Plots of the destruction rate efficiency  $\phi(M)$  for all the models suggest that its variation with mass and  $\epsilon$  is very similar for the PS and ST mass function. This suggests an approximation where we use  $\phi(M, z; \epsilon)$  computed using the Press-Schechter mass function and use that to compute the halo formation rate in the Sheth-Tormen mass function. Figs. 5.12 and 5.14 show the halo formation rate for the  $\Lambda$ CDM model at different redshifts and compare the excursion set calculation, the Sasaki approximation and the intermediate approximation suggested above. We have also shown the ratios of formation rates estimated in these two approaches mentioned above in Figs. 5.13 and 5.15. We find that the intermediate approximation is not plagued by negative halo formation rates and that it is an excellent approximation at all mass scales at higher redshifts. At lower redshifts, the approximation is still good at high masses but not so at smaller masses (Mitra et al. 2011).

While comparing our analytical results with those of N-body simulations, we find a systematic deviation between the two at the high mass end. This is possibly related to the problem of ‘halo fragmentation’ while deriving halo merger trees from the simulations. In about 5% of all haloes, particles in a given progenitor halo can become part of two independent haloes at a future epoch. This is usually attributed to the fact that the FOF algorithm groups particles based on the inter-particle distance. This can result in the identification of two haloes separated by a thin ‘bridge’ of particles to be treated as a single halo. Such halo fragmentation has been treated using different techniques in various halo formation rate studies. Fakhouri & Ma (2008) compare these techniques and find that the effect of halo fragmentation is maximum of high mass haloes.

## 5.4 Conclusions

Key points presented in this chapter can be summarized as follows:

- We revisit the Sasaki approximation for computing the halo formation rate and compute the destruction rate explicitly using the excursion set approach.
- We introduce a parameter  $\epsilon$ , the smallest fractional change in mass of a halo before we consider it as destruction of the old halo and formation of a new halo.
- We show that the halo destruction rate is not independent of mass even for power law models and hence the basis for the Sasaki ansatz does not hold. Two prominent features of the halo destruction rate are the rapid fall at large masses, and a pronounced peak close to the scale of non-linearity. The peak is more pronounced for smaller values of  $\epsilon$ .

- Using the excursion set approach for the Sheth-Tormen mass function leads to positive halo formation rates, unlike the generalization of the Sasaki ansatz where formation rates at some mass scales are negative.
- We compare the destruction rate and the halo formation rates computed using the excursion set approach with N-body simulations. We find that our approach matches well with simulations for all models, at all redshifts and also for different values of  $\epsilon$ .
- In some cases there are deviations between the simulations and the theoretical estimate. However, these deviations are much smaller for the excursion set based method as compared to the Sasaki estimate.
- It may be that some of the deviations arise due to a series representation of the barrier shape, and the number of terms taken into account may not suffice for the estimate. We have found that truncation of the series can affect results at small masses, though in most cases results converge with the five terms that we have taken into account for the range of masses considered here.
- We show that we can use the halo destruction rate computed for the Press-Schechter mass function to make an approximate estimate of the halo formation rate in Sheth-Tormen mass function using equation (5.5). This approximate estimate is fairly accurate at all mass scales in the  $\Lambda$ CDM model at high redshifts.
- The halo survival probability is a strong function of mass of haloes, unlike the mass independent survival probability obtained in the Sasaki approximation.
- The halo formation redshift distribution for haloes of different masses is also very different from that obtained using the Sasaki approximation. This is especially true for the Sheth-Tormen mass function where the Sasaki approximation gives negative halo formation rates in some range of mass scales and redshifts.

The formalism used here for calculation of halo formation rate and other related quantities can be generalized to any description of the mass function if the relevant probabilities can be calculated. Within the framework of the universal approach to mass functions, it can also be used to study formation rates of haloes in different cosmological models (Linder & Jenkins 2003; Macciò et al. 2004). This allows for an easy comparison of theory with observations for quantities like the major merger rate for galaxy clusters (Cohn et al. 2001).

In case of semi-analytic models of galaxy formation, our approach allows for a nuanced treatment where every merger need not be treated as a major merger and we may only consider instances where mass ratios are larger than a critical value for any affect on star formation in the central galaxy.



---

---

# CHAPTER 6

---

## POST-REIONIZATION NEUTRAL HYDROGEN DISTRIBUTION

In the previous chapters, we studied the evolution of neutral hydrogen (HI) fraction in the IGM at high redshifts. We saw how the current observations can constrain this evolution from unity at redshift  $z \sim 15$  to less than  $10^{-4}$  at  $z \sim 6$  due to the presence of luminous sources which reionize the universe. In this chapter, we shall continue our study of neutral hydrogen distribution in the universe in the post-reionization epoch i.e. at  $z < 6$ .

### 6.1 Introduction

Following the epoch of reionization ( $z \sim 6$ ), the low density gas gets completely ionized (Becker et al. 2001; Fan et al. 2006). However, a small fraction of neutral hydrogen (HI) survives, and is confined to the over-dense regions of the IGM. At this redshifts the bulk of the neutral gas is contained in clouds with column density greater than  $2 \times 10^{20}$  atoms/cm<sup>2</sup>. Observations indicate that these regions can be identified as Damped Ly- $\alpha$  (DLA) systems (Wolfe et al. 2005), which are self-shielded from further ionization and house  $\sim 80\%$  of the HI at  $1 < z < 4$ . In this redshift range the neutral fraction remains constant with  $\Omega_{\text{HI}} \sim 0.001$  (Lanzetta et al. 1995; Storrie-Lombardi et al. 1996; Rao & Turnshek 2000; Péroux et al. 2003).

The distribution and clustering properties of DLAs suggest that they are associated with galaxies, which represent highly non-linear matter over densities (Haehnelt et al. 2000). These clumped HI regions saturate the Gunn-Peterson optical depth (Gunn & Peterson 1965b) and hence cannot be probed using Ly- $\alpha$  absorption. They are, however the dominant source for the 21-cm radiation. In the post reionization epoch, Ly- $\alpha$  scattering and the Wouthuysen-Field

coupling (Wouthuysen 1952; Purcell & Field 1956; Furlanetto et al. 2006) increases the population of the hyperfine triplet state of HI. This makes the spin temperature  $T_s$  much greater than the CMB temperature  $T_\gamma$ , whereby the 21-cm radiation is seen in emission (Madau et al. 1997; Bharadwaj & Ali 2004; Loeb & Zaldarriaga 2004). The 21-cm flux from individual HI clouds is too weak ( $< 10\mu\text{Jy}$ ) for detection in radio observations with existing facilities, unless the effect of gravitational lensing by intervening matter enhances the image of the clouds significantly (Saini et al. 2001). The redshifted 21-cm signal however forms a diffuse background in all radio observations at  $z < 6$  (frequencies  $> 203$  MHz). Several radio telescopes, like the presently functioning GMRT<sup>1</sup>, and future instruments MWA<sup>2</sup> and SKA<sup>3</sup> aim to detect this weak cosmological signal submerged in large astrophysical foregrounds (Santos et al. 2005; McQuinn et al. 2006; Ali et al. 2008).

The study of large scale structures in redshift surveys and numerical simulations reveal that the galaxies (for that matter any non linear structure) trace the underlying dark matter distribution with a possible bias (Mo & White 1996; Dekel & Lahav 1999). Associating the post-reionization HI with dark matter halos implies that the gas traces the underlying dark matter distribution with a possible bias function  $b(k) = [P_{\text{HI}}(k)/P(k)]^{1/2}$ , where  $P_{\text{HI}}(k)$  and  $P(k)$  denote the power spectra of HI and dark matter density fluctuations respectively. This function is believed to quantify the clustering property of the neutral gas. It is believed that on small scales (below the Jean's length), the bias is a scale dependent function. However, it is reasonably scale-independent on large scales (Fang et al. 1993). Further, the bias depends on the redshift. The use of the post-reionization 21-cm signal (Bharadwaj & Sethi 2001; Bharadwaj et al. 2001; Wyithe & Loeb 2007b; Loeb & Wyithe 2008; Wyithe & Loeb 2008; Visbal et al. 2009) as a tracer of dark matter opens up new avenues towards various cosmological investigations (Wyithe et al. 2007; Chang et al. 2008; Bharadwaj et al. 2009; Mao et al. 2008) and cross-correlation studies (Guha Sarkar et al. 2009; Guha Sarkar 2010; Guha Sarkar et al. 2011). The underlying bias model is crucial while forecasting or interpreting some of these results.

In this chapter, we have investigated the nature of HI bias in the post-reionization epoch. The HI fluctuations are simulated at redshifts  $z < 6$  and HI bias is obtained at various redshifts from the simulated dark matter and HI power spectra. This is similar to the earlier work by Bagla et al. (2010) and Marín et al. (2010). The simulated bias function is assumed to be our fiducial model for HI distribution at low redshifts. We have studied the feasibility of constraining this fiducial model with observed data. Here we have focused on the multi frequency angular power spectrum (MAPS) (Datta et al. 2007)– measurable directly from observed radio data and dependent on the bias model. Assuming a standard cosmological model and a known dark matter power spectrum we have used the Principal Component Analysis (PCA) on simulated MAPS data for a hypothetical radio-interferometric experiment to put constraints on the bias model. The method is similar to the one used for power spectrum estimation using the

---

<sup>1</sup><http://www.gmrt.ncra.tifr.res.in/>

<sup>2</sup><http://www.mwatelescope.org/>

<sup>3</sup><http://www.skatelescope.org/>

CMB data (Efstathiou & Bond 1999; Hu & Holder 2003; Leach 2006) and constraining reionization (Mitra et al. 2011, 2012). Stringent constraints on the bias function with future data sets would be crucial in modelling the distribution of neutral gas at low redshifts and justify the use of HI as a tracer of the underlying dark matter field. This would be useful for both analytical and numerical work involving the post-reionization HI distribution.

In the next section, we discuss the simulation of HI distribution and the general features of the bias function. Following that, we discuss the HI multi-frequency angular power spectrum (MAPS), a statistical quantifier directly measurable from radio-interferometric experiments. Finally we use the principal component analysis to investigate the possibility of constraining the bias model with simulated MAPS Datta et al. (2007) data.

## 6.2 Simulation and the bias model

We have obtained the dark matter distribution using the PM N-body code developed by Bharadwaj & Srikant (2004), assuming a fiducial cosmological model (used throughout this chapter)  $\Omega_m = 0.2726$ ,  $\Omega_\Lambda = 0.726$ ,  $\Omega_b = 0.0456$ ,  $h = 0.705$ ,  $T_{cmb} = 2.728K$ ,  $\sigma_8 = 0.809$ ,  $n_s = 0.96$  (all parameters from WMAP 7 year data (Komatsu et al. 2011; Jarosik et al. 2011)). We simulate  $608^3$  particles in  $1216^3$  grids with grid spacing 0.1 Mpc in a  $121.6 \text{ Mpc}^3$  box. The mass assigned to each dark matter particle is  $m_{\text{part}} = 2.12 \times 10^8 M_\odot h^{-1}$ . The initial particle distribution and velocity field generated using Zel'dovich approximation (at  $z \sim 25$ ) are evolved only under gravity. The particle position and velocities are then obtained as output at different redshifts  $1.5 \leq z \leq 4$  at intervals of  $\delta z = 0.5$ . We have used the Friends-of-Friends algorithm (Davis et al. 1985) to identify dark matter over-densities as halos, taking linking length  $b = 0.2$  (in units of mean inter-particle distance). This gives a reasonably good match with the theoretical halo mass function (Jenkins et al. 2001; Sheth & Tormen 2002) for masses as small as  $= 10m_{\text{part}}$ . The halo mass function obtained from simulation is found to be in excellent agreement with the Sheth-Tormen mass function in the mass range  $10^9 \leq M \leq 10^{13} h^{-1} M_\odot$ .

We follow the prescription of Bagla et al. (2010), to populate the halos with neutral hydrogen and thereby identify them as DLAs. Equation (3) of Bagla et al. (2010) relates the virial mass of halos,  $M$  with its circular velocity  $v_{\text{circ}}$ . The neutral gas in halos can self shield itself from ionizing radiation only if the circular velocity is above a threshold of  $v_{\text{circ}} = 30 \text{ km/sec}$  at  $z \sim 3$ . This sets a lower cutoff for the halo mass  $M_{\text{min}}$ . Further, halos are populated with gas in a way, such that the very massive halos do not contain any HI. An upper cut-off scale to halo mass  $M_{\text{max}}$  is chosen using  $v_{\text{circ}} = 200 \text{ km/sec}$ , above which we do not assign any HI to halos. This is consistent with the observation that very massive halos do not contain any gas in neutral form (Pontzen et al. 2008). The total neutral gas is then distributed such that the mass of the gas assigned is proportional to the mass of the halo between these two cut-off limits. We note that there is nothing canonical about this scheme. However, with the basic physical picture in the background this is the simplest model. Results obtained using alternative HI assignment

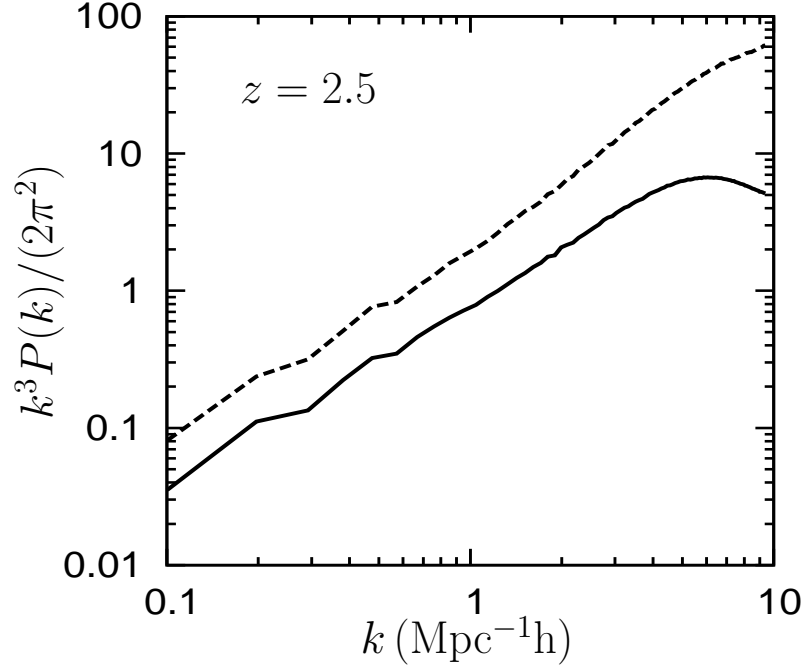


Figure 6.1: The simulated power spectra for dark matter distribution (solid line) and the HI density field (dashed line) at redshift  $z = 2.5$ .

schemes are not expected to be drastically different (Bagla et al. 2010).

Figure 6.1 shows the simulated power spectra of dark matter and HI distribution at a fiducial redshift  $z = 2.5$ . The dark matter power spectrum is seen to be consistent with the transfer function given by Eisenstein & Hu (1998) and the scale invariant primordial power spectrum (Harrison 1970; Zeldovich 1972). The HI power spectrum has a greater amplitude than its dark matter counterpart in the entire  $k$ -range allowed by the simulation parameters. Figure 6.2 shows the behavior of the bias function  $b(k, z)$ . We have obtained the scale dependence of the HI bias for various redshifts in the range  $1.5 \leq z \leq 4$ . At these redshifts, the bias is seen to be greater

$z$	$c_3$	$c_2$	$c_1$	$c_0$
1.5	0.0029	0.0365	-0.1561	1.1402
2.0	0.0052	0.0177	0.0176	1.5837
2.5	0.0101	-0.0245	0.3951	2.1672
3.0	0.0160	-0.0884	1.0835	2.9287
3.5	0.0234	-0.1537	2.1854	3.8050
4.0	0.0248	-0.1655	3.6684	4.9061

Table 6.1: The fit parameters for bias function of the form  $b^2(k) = c_3 k^3 + c_2 k^2 + c_1 k + c_0$  for various redshifts  $1.5 \leq z \leq 4.0$ .

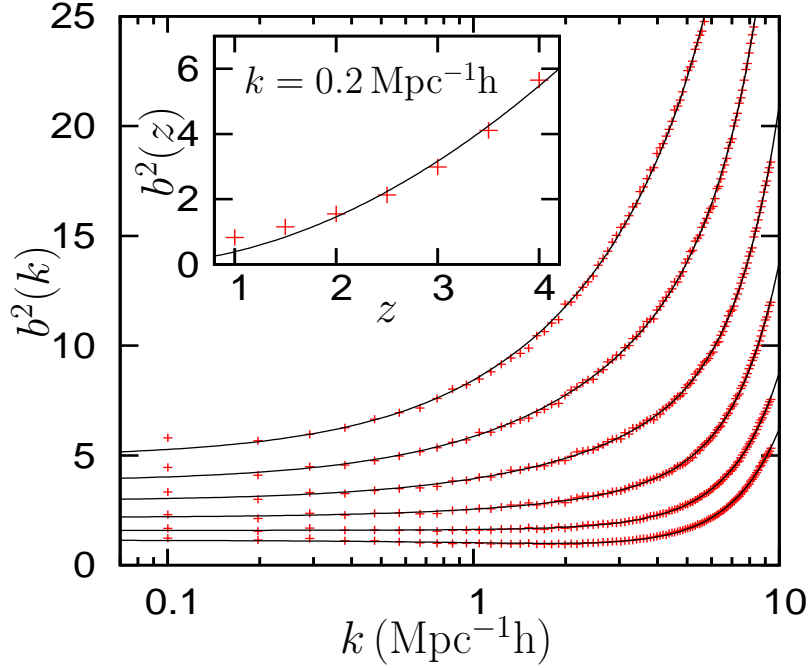


Figure 6.2: The simulated bias function for  $z = 1.5, 2.0, 2.5, 3.0, 3.5$  and  $4.0$  (bottom to top) showing the scale dependence. The inset shows the variation of the large-scale linear bias as a function of redshift.

than unity, a feature that is observed in the clustering of high redshift galaxies (Mo & White 1996; Wyithe & Brown 2009). On large cosmological scales the bias remains constant and grows monotonically at small scales, where non-linear effects are at play. This is a generic feature seen at all redshifts. The  $k$ -range over which the bias function remains scale independent is larger at the lower redshifts. The linear bias model is hence seen to hold reasonably well on large scales. The scale dependence of bias for a given redshift is fitted using a cubic polynomial with parameters summarized in Table 6.1. The inset in Figure 6.2 shows the redshift dependence of the linear bias which indicates a monotonic increase. This is also consistent with the expected  $z$ -dependence of high redshift galaxy bias. The behavior of the linear bias for small  $k$ -values as a function of redshift is non-linear and can be fitted by an approximate power law of the form  $\sim z^2$ . This scaling relationship of bias with  $z$  is found to be sensitive to the mass resolution of the simulation. The similar dependence of HI bias with  $k$  and  $z$  has been observed earlier by Bagla et al. (2010) with a computationally robust Tree N-body code. Here we show that, the same generic features and similar scaling relations for bias can be obtained by using a simpler and computationally less expensive PM N-body code. Our aim is to use this scale and redshift dependence of bias, obtained from our simulation as the fiducial model for the post reionization HI distribution. We shall subsequently investigate the feasibility of constraining this model using Principal Component Analysis (PCA) on simulated MAPS data.

### 6.3 HI 21-cm angular power-spectrum

Redshifted 21-cm observations have an unique advantage over other cosmological probes since it maps the 3D density field and gives a tomographic image of the Universe. Here, the statistical properties of the fluctuations in the redshifted 21-cm brightness temperature  $T(\hat{\mathbf{n}}, z)$  on the sky is quantified through the multi frequency angular power spectrum MAPS, defined as  $C_\ell(\Delta z) = \langle a_{\ell m}(z) a_{\ell m}^*(z + \Delta z) \rangle$ , where  $a_{\ell m}(z) = \int d\Omega_{\hat{\mathbf{n}}} Y_{\ell m}^*(\hat{\mathbf{n}}) T(\hat{\mathbf{n}}, z)$ . This measures the correlation of the spherical harmonic components of the temperature field at two redshift slices separated by  $\Delta z$ . In the flat-sky approximation and incorporating the redshift space distortion effect we have (Datta et al. 2007)

$$C_\ell = \frac{\bar{T}^2}{\pi r^2} \int_0^\infty dk_{\parallel} \cos(k_{\parallel} \Delta r) P_{\text{HI}}^s(\mathbf{k}) \quad (6.1)$$

for correlation between HI at comoving distances  $r$  and  $r + \Delta r$ ,  $\bar{T} = 4\text{mK}(1+z)^2 \left( \frac{\Omega_b h^2}{0.02} \right) \frac{H_0}{H(z)} \times \left( \frac{0.7}{h} \right)$ ,  $k = \sqrt{\left( \frac{\ell}{r} \right)^2 + k_{\parallel}^2}$  and  $P_{\text{HI}}^s$  denotes the redshift space HI power spectrum given by

$$P_{\text{HI}}^s(\mathbf{k}) = \bar{x}_{\text{HI}}^2 b^2(k, z) D_+^2 \left[ 1 + \beta \left( \frac{k_{\parallel}}{k} \right)^2 \right]^2 P(k) \quad (6.2)$$

where the mean neutral fraction  $\bar{x}_{\text{HI}}$  is assumed to have a fiducial value  $2.45 \times 10^{-2}$ ,  $\beta = f/b(k, z)$ ,  $f = d \ln D_+ / d \ln a$  where,  $D_+$  represents the growing mode of density perturbations,  $a$  is the cosmological scale factor and  $P(k)$  denotes the present day matter power spectrum.

We use MAPS as an alternative to the more commonly used 3D power spectrum since it has a few features that makes its measurement more convenient. Firstly we note that as a function of  $\ell$  (angular scales) and  $\Delta z$  (radial separations) the MAPS encapsulate the entire three dimensional information regarding the HI distribution. In this approach, the fluctuations in the transverse direction are Fourier transformed, while the radial direction is kept unchanged in the real frequency space. No cosmological information is however lost. Secondly, 21-cm signal is deeply submerged in astrophysical foregrounds. These foregrounds are known to have a smooth and slow variation with frequency, whereas the signal is more localized along the frequency axis. The distinct spectral ( $\Delta z$ ) behavior has been proposed to be an useful method to separate the cosmological signal from foreground contaminants. In fact it has been shown that foregrounds can be completely removed by subtracting out a suitable polynomial in  $\Delta \nu$  from  $C_\ell(\Delta \nu)$  (Ghosh et al. 2011). It is hence advantageous to use MAPS which maintains the difference between the frequency and angular information in an observation. The 3D power spectrum on the contrary mixes up frequency and transverse information through the full 3D Fourier transform. Further, for a large band width radio observation, covering large radial separations light cone effect is expected to affect the signal. This can also be easily incorporated

into MAPS unlike the 3D power spectrum which mixes up the information from different time slices. The key advantage, however, in using the angular power spectrum is that it can be obtained directly from radio data. The quantity of interest in radio-interferometric experiments is the complex Visibility  $\mathcal{V}(\mathbf{U}, \nu)$  measured for a pair of antennas separated by a distance  $d$  as a function of baseline  $\mathbf{U} = d/\lambda$  and frequency  $\nu$ . The method of Visibility correlation to estimate the angular power spectrum has been well established (Bharadwaj & Sethi 2001; Bharadwaj & Ali 2005). This follows from the fact that  $\langle \mathcal{V}(\mathbf{U}, \nu) \mathcal{V}^*(\mathbf{U}, \nu + \Delta\nu) \rangle \propto C_\ell(\Delta\nu)$ . Here the angular multipole  $\ell$  is identified with the baseline  $U$  as  $\ell = 2\pi U$  and one has assumed that the antenna primary beam is either de-convolved or is sufficiently peaked so that it may be treated as a Dirac delta function. Further the constant of proportionality takes care of the units and depends on the various telescope parameters.

The angular power spectrum at a multipole  $\ell$  is obtained by projecting the 3D power spectrum. The integral in Equation 6.1, sums over the modes whose projection on the plane of the sky is  $\ell/r$ . Hence,  $C_\ell$  has contributions from matter power spectrum only for  $k > \ell/r$ . The shape of  $C_\ell$  is dictated by the matter power spectrum  $P(k)$  and the bias  $b(k)$ . The amplitude depends on quantities dependent on the background cosmological model as well as the astrophysical properties of the IGM. We emphasize here that, the mean neutral fraction and the HI bias are the only two non-cosmological parameters in our model for the HI distribution at low redshifts. Predicting the nature of  $C_\ell$  in a given cosmological paradigm is then crucially dependent on the underlying bias model and the value of the neutral fraction.

The  $\Delta\nu$  dependence of the MAPS  $C_\ell(\Delta\nu)$  measures the correlation between the various 2D modes as a function of radial separation  $\Delta r$  ( $\Delta\nu$ ). The signal is seen to decorrelate for large radial separations, the decorrelation being faster for larger  $\ell$  values. For a given  $\ell$ , one gets independent estimates of  $C_\ell$  for radial separations greater than the correlation length. Projection of the 3D power spectrum leads to the availability of fewer Fourier modes. However, for a given band width  $B$ , one may combine the signals emanating from epochs separated by the correlation length  $\Delta\nu_C$  in the radial direction. Noting that the amplitude of the signal does not change significantly over the radial separation corresponding to the band width, one has  $\sim B/\Delta\nu_c$  independent measurements of  $C_\ell(\Delta z = 0)$ . We have adopted the simplified picture where the noise in  $C_\ell(\Delta z = 0)$  gets reduced owing to the combination of these  $B/\Delta\nu_c$  realizations. A more complete analysis would incorporate the correlation for  $\Delta\nu < \Delta\nu_c$ . We plan to take this up in a future work.

Figure 6.3 shows the 3D HI power spectrum at the fiducial redshift  $z = 2.5$  obtained using the dark matter power spectrum of Eisenstein & Hu (1998). We have used the WMAP 7 year cosmological model throughout. Figure 6.4 shows the corresponding HI angular power spectrum. The shape of  $C_\ell$  is dictated by the shape of the matter power spectrum, the bias function, and the background cosmological model. The amplitude is set by various quantities that depend on the cosmological model and the growth of linear perturbations. The global mean neutral fraction also appears in the amplitude and plays a crucial role in determining the mean level for 21-cm emission. Hence, for a fixed cosmological model, the bias and the neutral

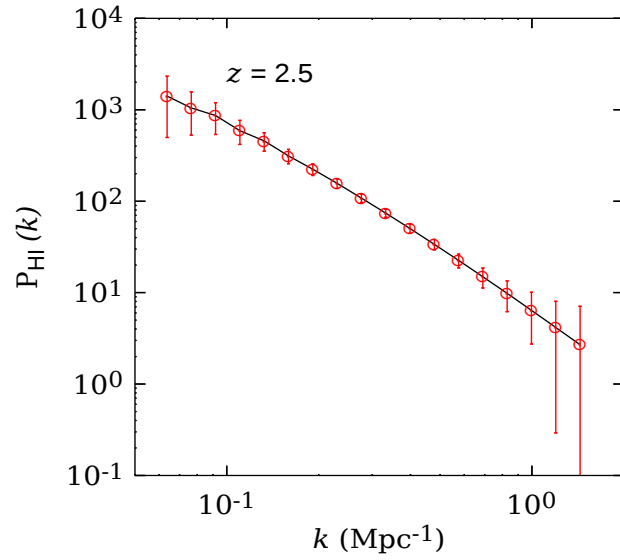


Figure 6.3: The theoretical 3D HI power spectrum  $P_{\text{HI}}^s(k)$  for  $z = 2.5$  as a function of  $k$ , at  $\mu = 0.5$ . The points with  $2\text{-}\sigma$  error-bars represent the hypothetical binned data.

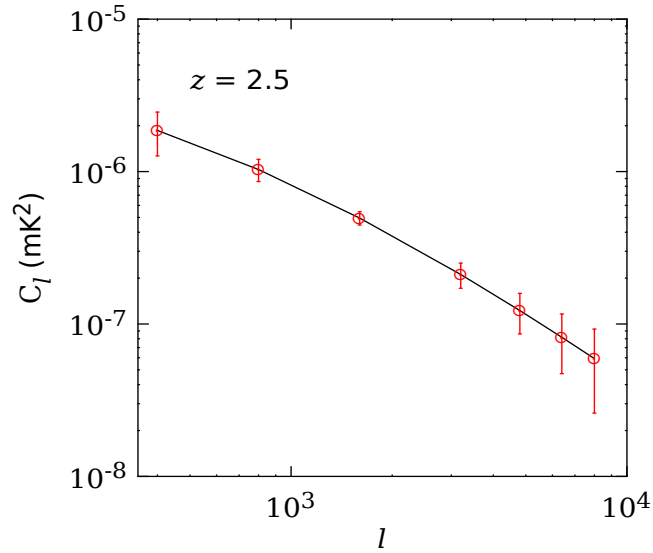


Figure 6.4: The theoretical angular power spectrum  $C_\ell$  for  $z = 2.5$  as a function of a  $\ell$ . The points with  $2\text{-}\sigma$  error-bars represent the hypothetical data.

fraction, solely determine the fluctuations of the post-reionization HI density field. We have used the bias model obtained from numerical simulations in the last section to evaluate the  $C_\ell$ . We assume that the binned angular power spectrum is measured at seven  $\ell$  bins – the data being generated using Equation 6.1 using the fiducial bias model.

The noise estimates are presented using the formalism used by Mao et al. (2008) for the 3D power spectrum and Bharadwaj & Ali (2005) and Bagla et al. (2010) for the angular power spectrum. We have used hypothetical telescope parameters for these estimates. We consider radio telescope with 60 GMRT like antennae (diameter 45 m) distributed randomly over a region  $1\text{km} \times 1\text{km}$ . We assume  $T_{sys} \sim 100\text{K}$ . We consider a radio-observation at frequency  $\nu = 405\text{MHz}$  with a bandwidth  $B = 32\text{MHz}$  for an observation time of 1000 hrs.

In order to attain desired sensitivities we have assumed that the data is binned whereby several nearby  $\ell$ – modes are combined to increase the SNR. Further, in the radial direction, the signal is assumed to decorrelate for  $\Delta\nu > 0.5\text{MHz}$ , so that we have 64 independent measurements of  $C_\ell$  for the given band width of 32MHz. The 7- $\ell$  bins chosen here allows the binned power spectrum to be measured at a SNR  $\gtrsim 4$  in the entire range  $400 \leq \ell \leq 8000$ . One would ideally expect to measure the power spectrum at a large number of  $\ell$  values which would necessarily compromise the obtained sensitivities. With the given set of observational parameters, one may, in principle choose a finer binning. It shall however degrade the SNR below the level of detectability. Choosing arbitrarily fine  $\ell$ – bins and simultaneously maintaining the same SNR would require improved observational parameters which may be unreasonable if not impossible. The same reasoning applies to noise estimation for the 3D power spectrum where for a given set of observational parameters, the choice of  $k$ – bins is dictated by the requirement of sensitivity. In the figure 6.3, showing the 3D power spectrum a  $4 - \sigma$  detection of  $P_{\text{HI}}(k)$  in the central bin requires the full  $k$ – range to be divided into 18 equal logarithmic bins for the same observational parameters.

The noise in  $C_\ell$  and  $P_{\text{HI}}(k)$  is dominated by cosmic variance at small  $\ell/k$  (large scales), whereas, instrumental noise dominates at large  $\ell/k$  values (small scales). We point out that the error estimates predicted for a hypothetical observation are based on reasonable telescope parameters and future observations are expected to reflect similar sensitivities.

We note here that several crucial observational difficulties hinder  $C_\ell$  to be measured at a high SNR. Separating the astrophysical foregrounds, which are several order larger in magnitude than the signal is a major challenge (Santos et al. 2005; McQuinn et al. 2006; Ali et al. 2008; Ghosh et al. 2010, 2011). Several methods have been suggested for the removal of foregrounds most of which uses the distinct spectral property of the 21 cm signal as against that of the foreground contaminants. The multi frequency angular power spectrum (MAPS)  $C_\ell(\Delta\nu)$  is itself useful for this purpose (Ghosh et al. 2010, 2011). Whereas this signal  $C_\ell(\Delta\nu)$  decorrelates over large  $\Delta\nu$ , the foregrounds remain correlated – a feature that maybe used to separate the two. In our subsequent discussions we assume that the foregrounds have been removed. As mentioned earlier, the angular power spectrum can directly be measured from raw visibility data. One requires to incorporate the primary beam of the antenna in establishing this con-

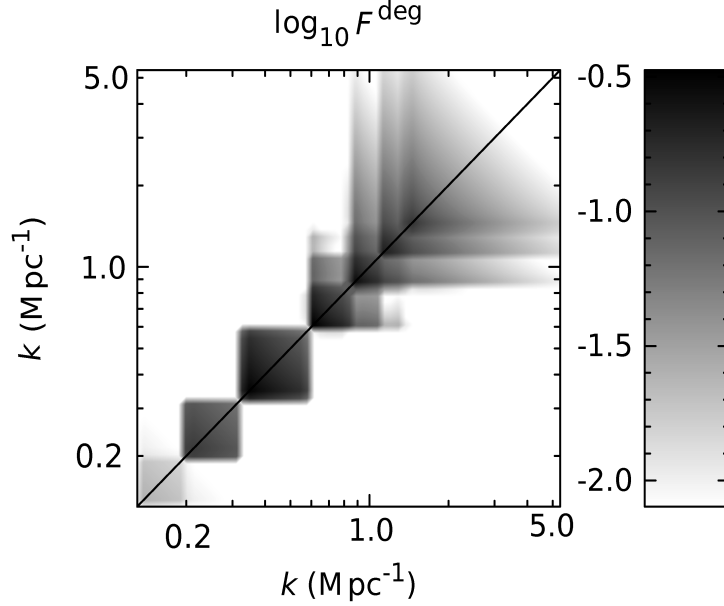


Figure 6.5: The degraded Fisher matrix  $F_{ij}^{deg}$  in the  $k - k$  plane.

nection (Bharadwaj & Ali 2005). Here we assume that such difficulties are overcome and the angular power spectrum is measured with sufficiently high SNR.

In the next section we use the  $C_\ell$  data generated with these assumptions to perform the PCA. If the 3D HI power spectrum is measured at some  $(k, \mu)$  it would be possible to determine the bias directly from a knowledge of the dark matter power spectrum. The bias would be measured at the  $k$ -values where the data is available. The results for the 3D analysis is summarized in section 6.5.

## 6.4 PCA constraints for the simulated data

We have already discussed the principal component method in details in Section 2.2. Here, we will follow that same approach towards constraining the bias function using  $C_\ell$  data. We consider a set of  $n_{\text{obs}}$  observational data points labeled by  $C_{\ell_{\text{obs}}}$  where  $\ell_{\text{obs}}$  runs over the different  $\ell$  values for which  $C_\ell$  is obtained (Fig. 6.4).

In our attempt to reconstruct  $b(k)$  in the range  $[k_{\text{min}}, k_{\text{max}}]$ , we assume that the bias which is an unknown function of  $k$ , can be represented by a set of  $n_{\text{bin}}$  discrete free parameters  $b_i = b(k_i)$  where the entire  $k$ -range is binned such that  $k_i$  corresponds to the  $i^{\text{th}}$  bin of width given

by

$$\Delta \ln k_i = \frac{\ln k_{\max} - \ln k_{\min}}{n_{\text{bin}} - 1} \quad (6.3)$$

We have chosen  $n_{\text{bin}} = 61$  and a  $k$ -range  $0.13 \leq k \leq 5.3 \text{ Mpc}^{-1}$ . Our choice is dictated by the fact that for  $k < 0.13 \text{ Mpc}^{-1}$ , the  $C_\ell$  corresponding to the smallest  $\ell$  is insensitive to  $b(k)$  and for  $k > 5 \text{ Mpc}^{-1}$  there is no data probing those scales. This truncation is also justified as the Fisher information matrix, we shall see, tends to zero beyond this  $k$ -range.

The Fisher matrix is constructed as

$$F_{ij} = \sum_{\ell_{\text{obs}}} \frac{1}{\sigma_{\ell_{\text{obs}}}^2} \frac{\partial C_{\ell_{\text{obs}}}^{\text{th}}}{\partial b^{\text{fid}}(k_i)} \frac{\partial C_{\ell_{\text{obs}}}^{\text{th}}}{\partial b^{\text{fid}}(k_j)}, \quad (6.4)$$

where  $C_{\ell_{\text{obs}}}^{\text{th}}$  is the theoretical [equation (6.1)]  $C_\ell$  evaluated at  $\ell = \ell_{\text{obs}}$  using the fiducial bias model  $b^{\text{fid}}(k)$  and  $\sigma_{\ell_{\text{obs}}}$  is the corresponding observational error. The data is assumed to be such that the covariance matrix is diagonal whereby only the variance  $\sigma_{\ell_{\text{obs}}}$  suffices.

The fiducial model for bias is, in principle, expected to be close to the underlying “true” model. In this work we have taken  $b^{\text{fid}}(k)$  to be the fitted polynomial obtained in the earlier section which matches the simulated bias up to an acceptable accuracy.

In the model for HI distribution at low redshifts, the mean neutral fraction crucially sets the amplitude for the power spectrum. However, a lack of precise knowledge about this quantity makes the overall amplitude of  $C_\ell$  largely uncertain. To incorporate this we have treated the quantity  $\bar{x}_{\text{HI}}$  as an additional free parameter over which the Fisher matrix is marginalized. The corresponding degraded Fisher matrix is given by

$$F^{\text{deg}} = F - \mathbf{B}F'^{-1}\mathbf{B}^T \quad (6.5)$$

where  $F$  is the original  $n_{\text{bin}} \times n_{\text{bin}}$  Fisher matrix corresponding to the parameters  $b_i$ ,  $F'$  is a  $1 \times 1$  Fisher matrix for the additional parameter  $\bar{x}_{\text{HI}}$ , and  $\mathbf{B}$  is a  $n_{\text{bin}} \times 1$ -dimensional matrix containing the cross-terms. We shall henceforth refer to  $F^{\text{deg}}$  as the Fisher matrix and implicitly assume that the marginalization has been performed.

The Fisher matrix obtained using equation (6.4) and equation (6.5) is illustrated in Figure 2.2 as a shaded plot in the  $k - k$  plane. The matrix shows a band diagonal structure with most of the information accumulated in discrete regions especially corresponding to the  $k$ -modes for which the data is available. In the region  $k > 2$  and  $k < 0.2 \text{ Mpc}^{-1}$ , the value of  $F_{ij}$  is relatively small, implying that one cannot constrain  $b(k)$  in those  $k$ -bins from the data set we have considered in this work.

A suitable choice of basis ensures that the parameters are not correlated. This amounts to writing the Fisher matrix in its eigen basis. Once the Fisher matrix is constructed, we determine its eigenvalues and corresponding eigenvectors. The orthonormality and completeness of the

eigenfunctions, allows us to expand the deviation of  $b(k_i)$  from its fiducial model,  $\delta b_i = b(k_i) - b^{\text{fid}}(k_i)$ , as

$$\delta b_i = \sum_{p=1}^{n_{\text{bin}}} m_p S_p(k_i) \quad (6.6)$$

where  $S_p(k_i)$  are the principal components of  $b(k_i)$  and  $m_p$  are the suitable expansion coefficients. The advantage is that, unlike  $b(k_i)$ , the coefficients  $m_p$  are uncorrelated.

Figure 6.6 shows the inverse of the largest eigenvalues. Beyond the first six, all the eigenvalues are seen to be negligibly small. It is known that the largest eigenvalue corresponds to minimum variance set by the Cramer-Rao bound and vice versa. This implies that the errors in  $b(k)$  would increase drastically if modes  $i > 6$  are included. Hence, most of the relevant information is essentially contained in the first six modes with larger eigenvalues. These normalized eigenmodes are shown in the Figure 6.7. One can see that, all these modes almost tend to vanish for  $k > 2$  and  $k < 0.2 \text{ Mpc}^{-1}$ , as the Fisher matrix is vanishingly small in these regions. The positions of the spikes and troughs in these modes are related to the presence of data points and their amplitudes depend on the corresponding error-bars (smaller the error, larger the amplitude).

The fiducial model adopted in our analysis may be different from the true model which dictates the data. Clearly, the reconstruction would be poor for wide discrepancies between the two. In our analysis, the simulated bias serves as the input. In the absence of many alternative models for large scale HI bias, this serves as a reasonable fiducial model.

We assume that one can then reconstruct the function  $\delta b_i$  using only the first  $M \leq n_{\text{bin}}$  modes [see equation ( 6.6)]. Considering all the  $n_{\text{bin}}$  modes ensures that no information is thrown away. However this is achieved at the cost that errors in the recovered quantities would be very large owing to the presence of the negligibly small eigenvalues. On the contrary, lowering the number of modes can reduce the error but may introduce large biases in the recovered quantities. An important step in this analysis is therefore, to decide on the number of modes  $M$  to be used. In order to test this we consider a constant bias model to represent the true model as against the fiducial model. For a given data, figure 6.8 shows how the true model is reconstructed through the inclusion of more and more PCA modes. The reconstruction is directly related to the quality of the data. In the  $k$ -range where data is not available, the reconstruction is poor and the fiducial model is followed. The reconstruction is also poor for large departures of the true model from the fiducial model. We see that a reasonable reconstruction is obtained using the first 5 modes for  $k < 1$  where the data is available.

In order to fix the value of  $M$ , we have used the Akaike information criterion (Liddle 2007)  $\text{AIC} = \chi_{\text{min}}^2 + 2M$ , whose smaller values are assumed to imply a more favored model (see Section 2.3.2). Following the strategy used by Clarkson & Zunckel (2010) and Mitra et al. (2012), we have used different values of  $M$  (2 to 6) for which the AIC is close to its minimum and amalgamated them equally at the Monte Carlo stage when we compute the errors. In this way, we ensure that the inherent bias which exists in any particular choice of  $M$  is reduced.

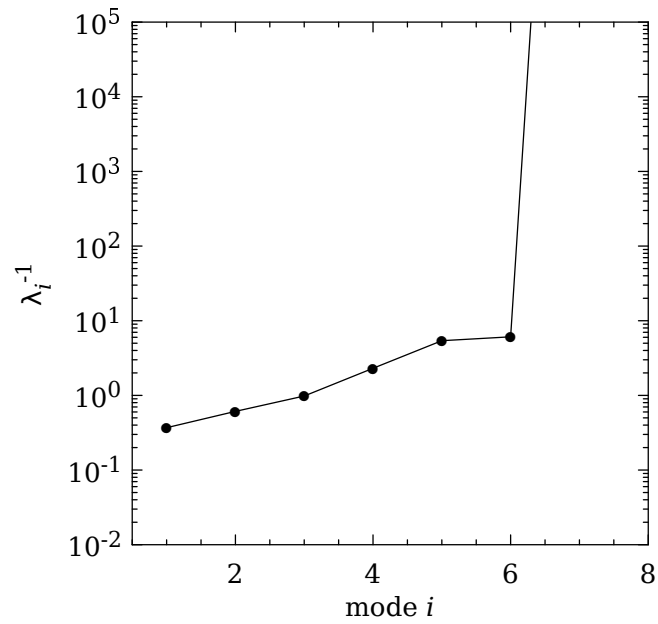


Figure 6.6: The inverse of eigenvalues of the degraded Fisher matrix  $F_{ij}^{deg}$  which essentially measures the variance on the corresponding coefficient.

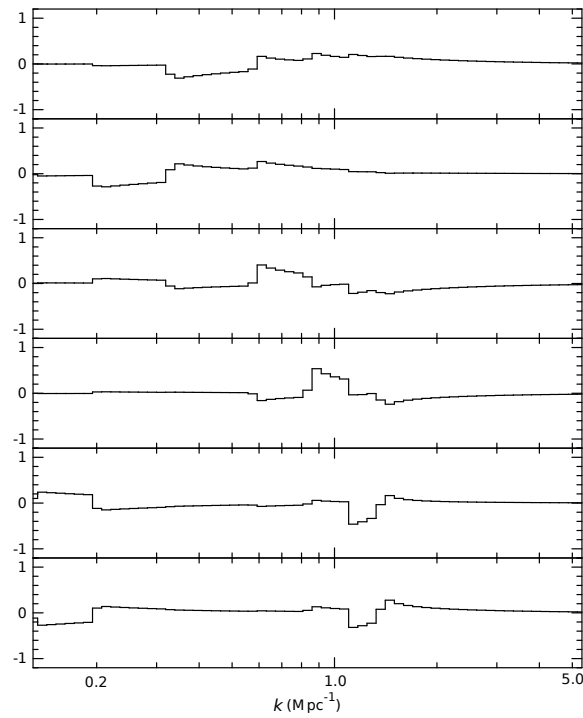


Figure 6.7: The first 6 eigenmodes of the degraded Fisher matrix.

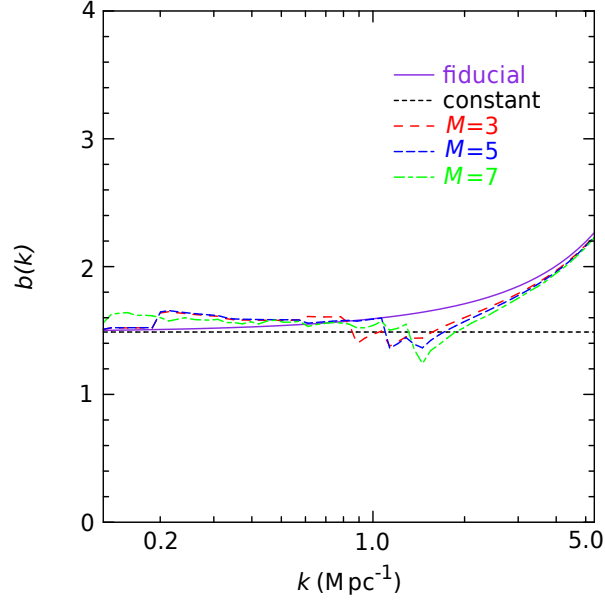


Figure 6.8: The fiducial and constant (true) bias models are shown. The reconstruction of the true model is shown for cases where number of PCA modes considered are  $M = 3, 5, 7$

We next perform the Monte-Carlo Markov Chain (MCMC) analysis over the parameter space of the optimum number of PCA amplitudes  $\{m_p\}$  and  $\bar{x}_{\text{HI}}$ . Other cosmological parameters are held fixed to the WMAP7 best-fit values (see Subsection 6.2). We carry out the analysis by taking  $M = 2$  to  $M = 6$  for which the AIC criterion is satisfied. By equal choice of weights for  $M$  and folding the corresponding errors together we reconstruct  $b(k)$  and thereby  $C_\ell$  along with their effective errors. We have developed a code based on the publicly available COSMOMC Lewis & Bridle (2002) for this purpose. A number of distinct chains are run until the Gelman and Rubin convergence statistics satisfies  $R - 1 < 0.001$ . We have also used the convergence diagnostic of Raftery & Lewis to choose suitable thinning conditions for each chain to obtain statistically independent samples.

## 6.5 Results and discussion

The reconstructed bias function obtained using the analysis described in the last section is shown in Figure 6.9. The solid line represents the mean model while the shaded region corresponds to 95% confidence limits ( $2\sigma$ ). We have also shown the fiducial model (short-dashed) as well as the popularly used constant bias,  $b \sim 1.5$  model (long-dashed) for comparison. We find that the

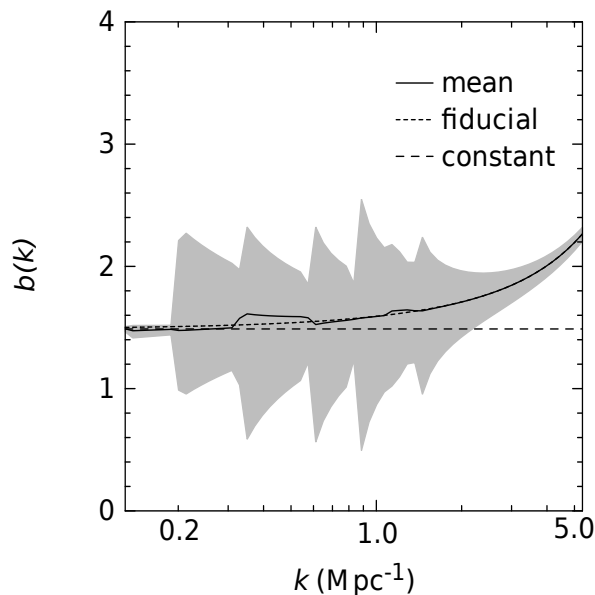


Figure 6.9: The marginalized posteriori distribution of the binned bias function obtained from the MCMC analysis using the AIC criterion up to first 6 PCA eigenmodes. The solid lines shows the mean values of bias parameters while the shaded regions represent the  $2\text{-}\sigma$  confidence limits. In addition, we show the fiducial and constant bias models.

fiducial model is within the 95% confidence limits for the entire  $k$ -range considered, while the constant bias is within the same confidence limits only up to  $k \approx 2 \text{ Mpc}^{-1}$ . We note that the errors decrease drastically for  $k > 2$  and  $k < 0.2 \text{ Mpc}^{-1}$ . This is expected from the nature of the Fisher matrix which shows that there is practically no information in the PCA modes from these  $k$ -regions. Therefore, all models show a tendency to converge towards the fiducial one. This is a direct manifestation of lack of data points probing these scales. Thus, most of the information is concentrated in the range  $0.2 < k < 2 \text{ Mpc}^{-1}$  within which reconstruction of the bias function is relevant with the given data set.

The mean reconstructed bias simply follows the fiducial model for  $0.2 < k < 2 \text{ Mpc}^{-1}$ . This is expected as the simulated  $C_\ell$  data is generated using the fiducial bias model itself (Section 6.2). In the case of analysis using real observed data this matching would have statistical significance, whereas here this just serves as an internal consistency check. The shaded region depicting the errors around the mean is however meaningful and tells us how well the given data can constrain the bias. The outline of the  $2\text{-}\sigma$  confidence limits shows a jagged feature which is directly related to the presence of the data points. We observe that apart from the fiducial model, a constant bias model is also consistent with the data within the  $2\text{-}\sigma$  limits. In

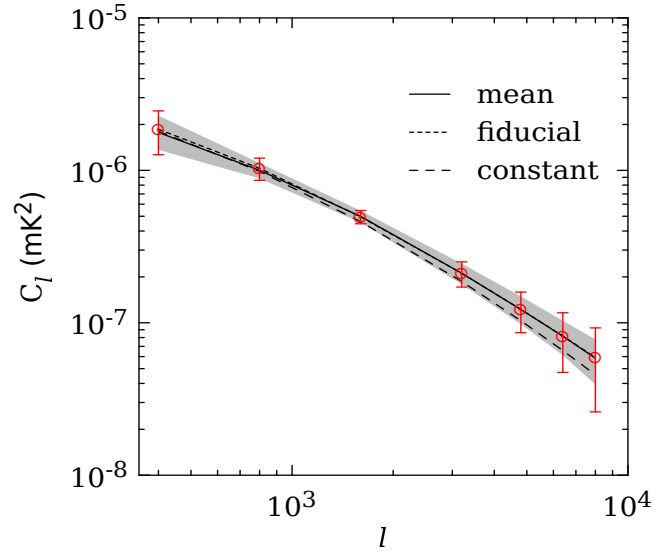


Figure 6.10: The reconstructed  $C_\ell$  with its  $2\text{-}\sigma$  confidence limits. The points with error-bars denote the observational data. The solid, short-dashed and long-dashed lines represent  $C_\ell$  for the mean, fiducial and constant bias models respectively.

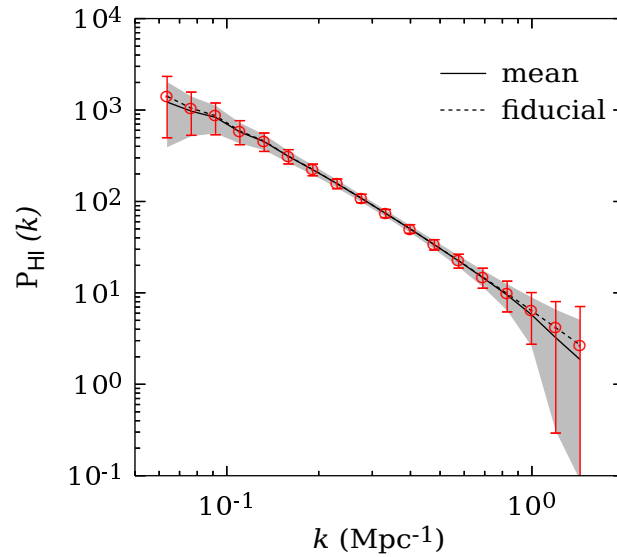


Figure 6.11: The reconstructed  $P_{\text{HI}}(k)$  with its  $2\text{-}\sigma$  confidence limits. The points with error-bars denote the observational data. We have taken  $\mu = 0.5$  and  $z = 2.5$

Parameters	2- $\sigma$ errors
$\bar{x}_{\text{HI}}$	$1.06 \times 10^{-3}$
$b_{\text{lin}}$	0.453

Table 6.2: The 2- $\sigma$  errors for  $\bar{x}_{\text{HI}}$  and  $b_{\text{lin}}(k = 0.3 \text{ Mpc}^{-1})$  obtained from the current analysis using AIC criterion.

fact, other than imposing rough bounds  $1 \lesssim b(k) \lesssim 2$ , the present data can hardly constrain the scale-dependence of bias. It is also not possible for the  $C_\ell$  data with its error-bars to statistically distinguish between the fiducial and the constant bias model in  $0.2 < k < 2 \text{ Mpc}^{-1}$ . Figure 6.10 illustrates the recovered angular power spectrum with its 95% confidence limits. Superposed on it are the original data points with error-bars. We also show the angular power spectrum calculated for the fiducial and the constant bias models. The 2- $\sigma$  contour follows the pattern of the error-bars on the data points. It is evident that the data is largely insensitive (within its error-bars) to the different bias models. Hence the  $k$ -dependence of bias on these scales does not affect the observable quantity  $C_\ell$  within the bounds of statistical precision.

While constructing the Fisher matrix, we had marginalized over the largely unknown parameter  $\bar{x}_{\text{HI}}$ . Treating it as an independent free parameter, we have investigated the possibility of constraining the neutral fraction using the simulated  $C_\ell$  data. The 2- $\sigma$  error in this parameter obtained from our analysis is shown in Table 6.2. We had used the fiducial value  $\bar{x}_{\text{HI}} = 2.45 \times 10^{-2}$  in calculating  $C_\ell$ . It is not surprising that our analysis gives a mean  $\bar{x}_{\text{HI}} = 2.44 \times 10^{-2}$  which is in excellent agreement with the fiducial value. It is however more important to note that the given data actually constrains  $\bar{x}_{\text{HI}}$  reasonable well at  $\sim 4\%$  (Guha Sarkar et al. 2012).

Noting that, on large scales ( $k \lesssim 0.3 \text{ Mpc}^{-1}$ ), one cannot distinguish between the mean, fiducial and the constant bias models, we use  $b_{\text{lin}} (= 1.496)$  to denote the bias value on these scales. The 2- $\sigma$  error on  $b_{\text{lin}}$  is evaluated at  $k = 0.3 \text{ Mpc}^{-1}$  (shown in Table 6.2).

In the  $k$ -range of our interest, the fiducial model does not reflect significant departure from the constant bias. Further, the confidence interval obtained from the data also reflects that the observed  $C_\ell$  is insensitive to the form of bias function  $b(k)$  in this range - provided that it is bound between approximate cut-offs ( $1 \lesssim b(k) \lesssim 2$ ). Moreover, the bias largely affects the amplitude of the angular power spectrum and has only a weak contribution towards determining its shape. A scale independent large-scale bias seems to be sufficient in modelling the data. The mean neutral fraction which globally sets the amplitude of the power spectrum is hence weakly degenerate with the bias. This is manifested in the fact that though  $\bar{x}_{\text{HI}}$  is rather well constrained, the bias reconstruction which uses the degraded Fisher information (after marginalizing over  $\bar{x}_{\text{HI}}$ ) is only weakly constrained from the same data. A prior independent knowledge about the post reionization neutral fraction would clearly ensure a more statistically significant bias reconstruction with smaller errors.

Figure 6.11 shows the reconstructed 3D HI power spectrum. The direct algebraic relationship between the observable  $P_{\text{HI}}(k)$  and the bias  $b(k)$  makes the 3D analysis relatively straightforward. This is specifically evident since the Fisher matrix elements in this case are non-zero only along the diagonal at specific  $k$ - values corresponding to the data points. The entire routine repeated here yields similar generic features. However, the key difference is that we have a larger number of bins with high sensitivity leading to an improved constraining of bias  $1.3 < b(k) < 1.7$  in the range  $0.2 < k < 0.7 \text{ Mpc}^{-1}$ .

In the absence of real observed data, our proposed method (Guha Sarkar et al. 2012) applied on a simulated data set, reflects the possibility of constraining large-scale HI bias. The method is expected to yield better results if one has precise knowledge about the neutral content of the IGM and the underlying cosmological paradigm. We note that the problem of constraining an unknown function given a known data dealt in this work is fairly general and several alternative methods maybe used. The chief advantage of the method adopted here, apart from its effective data reduction, is its model independence. The non-parametric nature of the analysis is specially useful in the absence of any specific prior information. A straightforward fitting of a polynomial and estimating the coefficients may turn out to be effective but there is no a priori reason to believe that it would work. It is logically more reasonable not to impose a model (with its parameters) upon the data, and instead, let the data reconstruct the model.

With the anticipation of upcoming radio observations towards measurement of HI power spectrum, our method holds the promise for pinning down the nature of HI bias thereby throwing valuable light on our understanding of the HI distribution in the diffuse IGM.

---

---

## CHAPTER 7

---

### SUMMARY AND CONCLUSIONS

A major constituent of this thesis is involved in dealing with one of the most intriguing and developing field of modern cosmology: reionization of the universe. In the first part of the thesis, we develop step by step the building blocks of cosmological reionization processes starting from very basic picture of cosmology. In order to understand the physical processes during reionization, one need to know the physics of structure formation. We have studied here the dynamics of non-linear structure formation in certain details. We argue that, due to the poor understanding of various complex processes like cooling and fragmentation of dark haloes, primordial star formation and different feedback processes, one cannot completely solve the problem associated with structure formation analytically without the help of approximation schemes. Off course, the correct way to tackle the problem is to use the numerical simulations. Over the last few years, there has been an enormous increase in the computational power to address various issues of structure formation through simulations. However, due to the limited resources of computational power, in this thesis, we mostly restrict ourselves in using analytical or semi-analytical tools along with some reasonable assumptions to explore the physical understandings of structure formation. Following the same argument, we have developed our basic knowledge regarding the reionization process through the semi-analytical modelling which helped us to acquire a good insight of the physics behind cosmic reionization. This, off course, introduces a few free parameters in the model which needed to be regulated by comparing with relevant observations. So, a successful reionization model should be able to match simultaneously the model predictions with most of the available data sets. In the introductory part of this thesis, we have also mentioned several observational probes of reionization. The most crucial data sets among them come from the measurements of QSO absorption line spectra (Fan et al. 2006), GRB spectra (Totani et al. 2006) and the CMB data (Hinshaw et al. 2012; Ade et al. 2013b). In this thesis, we have used one of the successful semi-analytical reionization models, based on

the model proposed by Choudhury & Ferrara (2005, 2006b), and try to compare our model predictions with such observations related to reionization. We have addressed some of the crucial but critical issues of star-formation history and reionization of the IGM using that model.

First, we have looked into one of the major uncertainties present in modelling reionization scenario, the parameter  $N_{\text{ion}}$ , the number of photons entering the IGM per baryon in collapsed objects. In spite of the fact that, this parameter can have a dependence on redshift  $z$  (which can arise from evolution of star-forming efficiency  $\epsilon_*$ , fraction of photons escaping from the host halo  $f_{\text{esc}}$  and chemical and radiative feedback processes), it is usually taken to be a constant as most of the physical processes involved in modelling  $N_{\text{ion}}$  are still uncertain. We make a preliminary attempt to constrain  $N_{\text{ion}}(z)$  using an emerging technique of cosmological data analysis namely the principal component analysis (PCA) and estimate the uncertainties in the reionization history in Chapter 2. In past few years, PCA has been successfully used in many areas of cosmology due to the fact that, it is a simple, non-parametric method of extracting relevant information from noisy data sets. We assume  $N_{\text{ion}}(z)$  to be completely arbitrary and decompose it into principal components. We have applied the principal component method using three different data sets - the photoionization rate  $\Gamma_{\text{PI}}(z)$ , the LLS distribution  $dN_{\text{LL}}/dz$  and WMAP7 (as well as simulated PLANCK) CMB data and obtained constraints on the reionization history by means of Monte-Carlo Markov Chain (MCMC) techniques. We found that the constraints at  $z < 6$  are relatively tight because of the QSO data, where as a wide range of histories at  $z > 6$  is still allowed by the present data. We have also indicated that, to get a more strict constraints on reionization at  $z > 6$ , one has to rely on data sets other than CMB and the PCA method will be a very promising tool for extracting the useful information from any future data sets in a model-independent manner. In Chapter 3, we extend our discussion about the crucial but still unknown parameters related to reionization -  $\epsilon_*$  and  $f_{\text{esc}}$ . With help of our semi-analytical PCA-reionization model, we try to constrain these parameters using the observed Luminosity Functions (LF) of galaxies in the redshift range  $6 \leq z \leq 10$ . We found that, there is a clear indication of a 2.6 times increase of the average escape fraction from  $z = 6$  to  $z = 8$  and the best-fit value of the star formation efficiency  $\epsilon_*$  nominally increases from 3.6% at  $z = 6$  to 5.2% at  $z = 8$ . Although we have only considered only the evolution of  $z \geq 6$  luminosity functions, our approach can be applied to model the LFs at  $3 \leq z \leq 5$  and also it will become more applicable as more data becomes available for  $z > 6$  region.

In Chapter 2 and 3, we have taken most of the cosmological parameters to be fixed at their best-fit WMAP values to keep the analysis simple. Because of that, the uncertainties in reionization history remained slightly underestimated. So, we then try to find the effects of reionization on cosmological parameter determinations in Chapter 4. This time, we vary all the relevant cosmological parameters along with our model parameters. Using the combination of CMB data with astrophysical results from QSO absorption line experiments and the joint variation of both the cosmological and astrophysical parameters, we found that, a realistic, data-constrained reionization history indeed can induce appreciable changes in the cosmological parameter values. Particularly significant variations among them are the  $\Omega_b h^2$ , the scalar spectral index  $n_s$

and the electron scattering optical depth  $\tau_{\text{el}} = 0.080 \pm 0.012$  which is notably decreased with respect to the standard WMAP7 value  $0.088 \pm 0.015$ . In the later half of that chapter, we further exploit our model to achieve the better constraint on the neutrino masses  $m_\nu$  as allowed by the current datasets related to reionization. We obtained that, our model with a more physically reasonable treatment of reionization can tighten the upper limit on neutrino masses by  $\sim 17\%$  than the usual WMAP7 value where they assume the standard sudden reionization scheme. We also established that, there could exist a large degeneracy between the efficiency parameters  $\epsilon$ 's and  $m_\nu$  and one can get a further stringent constraint on  $m_\nu$ , once this degeneracy will be removed by the future observations associated with reionization.

The next chapter of the thesis is devoted to understanding one of the crucial ingredients of formation of large-scale structures - the mass function and formation rates of dark matter haloes. Understanding the fundamental properties and abundances of the dark matter halos is almost inevitable for understanding the properties of reionization sources like galaxies. In this chapter, we mentioned about several approaches to calculating halo formation rate. One of them is the Sasaki approximation which does not use any specific aspect of the form of mass function. We investigate the application of this approximation scheme to different mass function by explicitly computing the halo formation and destruction rates using the excursion set formalism. We have found that, extension of this approximation sometimes leads to an unphysical negative formation rate, particularly when applied to the Sheth-Tormen mass function. We then generalize this same method for the Sheth-Tormen mass function and find that halo formation rates computed in our manner are always positive. Our approach matches well with simulations for all models at all redshifts. In case of any semi-analytic models of galaxy formation, our approach can be applied successfully.

Finally, in Chapter 6, we have extended our study of neutral hydrogen distribution in the universe to post-reionization redshifts ( $z < 6$ ). Measurement of the spatial distribution of neutral hydrogen (HI) via the redshifted 21-cm line is perhaps the most auspicious tool in developing our knowledge of the epoch of reionization and the first galaxies. Here, we have investigated the nature of large scale HI bias  $b(k)$  which is one of the crucial ingredients for modelling the 21-cm emission from neutral hydrogen in the post-reionization epoch. Using the simulated bias as the fiducial model for HI distribution at  $z \leq 4$ , we have generated a hypothetical data set for the 21-cm angular power spectrum and we explore the possibility of constraining  $b(k)$  using the Principal Component Analysis (PCA) on this simulated data. We have demonstrated that our approach can be successfully implemented on future observational data sets.

In this thesis, we have addressed several issues regarding the structure formation of the universe, semi-analytical modelling of cosmological reionization and the neutral hydrogen distribution at the post-reionization epoch. Based on some simple approximation schemes and data analysis techniques, we have dealt with those problems. We have rigorously tested our approaches and models with all available relevant observational or numerical data sets. In some cases, we have also successfully examined our methods for simulated or future data sets. How-

ever, there are still many unsolved and challenging questions related to this subject which can be resolved by future observations and/or some meticulous computational techniques. Nevertheless, all the ideas and techniques used in this thesis will be very useful for future science in this area.

---

# BIBLIOGRAPHY

- Abel T., Bryan G. L., Norman M. L., 2000, *ApJ*, 540, 39
- Abel T., Norman M. L., Madau P., 1999, *ApJ*, 523, 66
- Ade P., et al., 2013a
- Ade P., et al., 2013b
- Ahn C. P., et al., 2012, *Astrophys.J.Suppl.*, 203, 21
- Ali S. S., Bharadwaj S., Chengalur J. N., 2008, *MNRAS*, 385, 2166
- Anderson L., Aubourg E., Bailey S., Bizyaev D., Blanton M., et al., 2013, *Mon.Not.Roy.Astron.Soc.*, 427, 3435
- Archidiacono M., Cooray A., Melchiorri A., Pandolfi S., 2010, *Phys. Rev. D*, 82, 087302
- Archidiacono M., Fornengo N., Giunti C., Hannestad S., Melchiorri A., 2013
- Ashie Y., et al., 2005, *Phys.Rev.*, D71, 112005
- Bagla J., Ray S., 2003, *New Astron.*, 8, 665
- Bagla J. S., 2002, *Journal of Astrophysics and Astronomy*, 23, 185
- Bagla J. S., Khandai N., Datta K. K., 2010, *MNRAS*, 407, 567
- Bagla J. S., Khandai N., Kulkarni G., 2009, *arXiv:0908.2702*
- Bagla J. S., Padmanabhan T., 1997, *Pramana*, 49, 161

- Barkana R., Loeb A., 2001, *Phys. Rep.*, 349, 125
- Barkana R., Loeb A., 2007, *Reports on Progress in Physics*, 70, 627
- Barnes J., Hut P., 1986, *Nature*, 324, 446
- Becker G. D., Rauch M., Sargent W. L. W., 2007, *ApJ*, 662, 72
- Becker R. H., et al., 2001, *Astron.J.*, 122, 2850
- Bennett C., Larson D., Weiland J., Jarosik N., Hinshaw G., et al., 2012
- Bennett C. L., Banday A. J., Gorski K. M., Hinshaw G., Jackson P., Keegstra P., Kogut A., Smoot G. F., Wilkinson D. T., Wright E. L., 1996, *ApJL*, 464, L1
- Benson A. J., Kamionkowski M., Hassani S. H., 2005, *MNRAS*, 357, 847
- Bergvall N., Zackrisson E., Andersson B.-G., Arnberg D., Masegosa J., Östlin G., 2006, *A&A*, 448, 513
- Bharadwaj S., Ali S. S., 2004, *MNRAS*, 352, 142
- Bharadwaj S., Ali S. S., 2005, *MNRAS*, 356, 1519
- Bharadwaj S., Nath B. B., Sethi S. K., 2001, *Journal of Astrophysics and Astronomy*, 22, 21
- Bharadwaj S., Sethi S. K., 2001, *Journal of Astrophysics and Astronomy*, 22, 293
- Bharadwaj S., Sethi S. K., Saini T. D., 2009, *Phys. Rev. D*, 79, 083538
- Bharadwaj S., Srikant P. S., 2004, *Journal of Astrophysics and Astronomy*, 25, 67
- Binney J., 1977, *ApJ*, 215, 483
- Binney J., Tremaine S., 2008, *Galactic Dynamics: Second Edition*. Princeton University Press
- Blain A. W., Longair M. S., 1993, *MNRAS*, 264, 509
- Bolton J., Meiksin A., White M., 2004, *MNRAS*, 348, L43
- Bolton J. S., Haehnelt M. G., 2007, *MNRAS*, 382, 325
- Bond J. R., Arnett W. D., Carr B. J., 1984, *ApJ*, 280, 825
- Bond J. R., Cole S., Efstathiou G., Kaiser N., 1991, *ApJ*, 379, 440
- Bouchet F. R., Adam J.-C., Pellat R., 1985, *A&A*, 144, 413
- Bouchet F. R., Kandrup H. E., 1985, *ApJ*, 299, 1

- Bouwens R., Illingworth G., 2006, *New Astronomy Reviews*, 50, 152
- Bouwens R. J., et al., 2009, *ApJ*, 705, 936
- Bouwens R. J., et al., 2010a, *ApJL*, 709, L133
- Bouwens R. J., et al., 2010b, *ApJ*, 725, 1587
- Bouwens R. J., et al., 2011a, *Nature*, 469, 504
- Bouwens R. J., et al., 2011b, *ApJ*, 737, 90
- Bouwens R. J., Illingworth G. D., Franx M., Ford H., 2007, *ApJ*, 670, 928
- Bouwens R. J., Illingworth G. D., Franx M., Ford H., 2008, *ApJ*, 686, 230
- Bradley L. D., et al., 2012, *ApJ*, 760, 108
- Bromm V., Coppi P. S., Larson R. B., 1999, *ApJL*, 527, L5
- Bruzual G., Charlot S., 2003, *MNRAS*, 344, 1000
- Bryan G. L., Norman M. L., 1998, *ApJ*, 495, 80
- Burigana C., Popa L. A., Salvaterra R., Schneider R., Choudhury T. R., Ferrara A., 2008, *MNRAS*, 385, 404
- Carbone C., Fedeli C., Moscardini L., Cimatti A., 2012, *JCAP*, 3, 23
- Carilli C. L., Gnedin N. Y., Owen F., 2002, *ApJ*, 577, 22
- Cen R., McDonald P., Trac H., Loeb A., 2009, *ApJL*, 706, L164
- Chandrasekhar S., 1943, *Reviews of Modern Physics*, 15, 1
- Chang T., Pen U., Peterson J. B., McDonald P., 2008, *Physical Review Letters*, 100, 091303
- Charlton J., Churchill C., 2000, *Quasistellar Objects: Intervening Absorption Lines*
- Chiu W. A., Fan X., Ostriker J. P., 2003, *ApJ*, 599, 759
- Chiu W. A., Ostriker J. P., 2000, *ApJ*, 534, 507
- Choudhury T. R., 2009, *Current Science*, 97, 841
- Choudhury T. R., Ferrara A., 2005, *MNRAS*, 361, 577
- Choudhury T. R., Ferrara A., 2006a, *ArXiv Astrophysics e-prints*

- Choudhury T. R., Ferrara A., 2006b, MNRAS, 371, L55
- Choudhury T. R., Ferrara A., 2007, MNRAS, 380, L6
- Choudhury T. R., Padmanabhan T., Srianand R., 2001, MNRAS, 322, 561
- Choudhury T. R., Srianand R., Padmanabhan T., 2001, *Astrophys.J.*, 559, 29
- Ciardi B., Bianchi S., Ferrara A., 2002, MNRAS, 331, 463
- Ciardi B., Ferrara A., Marri S., Raimondo G., 2001, MNRAS, 324, 381
- Ciardi B., Loeb A., 2000, *ApJ*, 540, 687
- Clarkson C., Zunckel C., 2010, *Physical Review Letters*, 104, 211301
- Cohn J. D., Bagla J. S., White M., 2001, MNRAS, 325, 1053
- Cohn J. D., White M., 2008, MNRAS, 385, 2025
- Crittenden R. G., Pogosian L., Zhao G.-B., 2009, *JCAP*, 12, 25
- Cucchiara A., et al., 2011, *ApJ*, 736, 7
- Datta K. K., Choudhury T. R., Bharadwaj S., 2007, MNRAS, 378, 119
- Davis M., Efstathiou G., Frenk C. S., White S. D. M., 1985, *ApJ*, 292, 371
- Dawson K. S., et al., 2012
- Dayal P., Ferrara A., Gallerani S., 2008, MNRAS, 389, 1683
- Dayal P., Ferrara A., Saro A., 2010, MNRAS, 402, 1449
- Dayal P., Ferrara A., Saro A., Salvaterra R., Borgani S., Tornatore L., 2009, MNRAS, 400, 2000
- de Simone A., Maggiore M., Riotto A., 2011, MNRAS, 418, 2403
- Dekel A., Lahav O., 1999, *ApJ*, 520, 24
- Dekel A., Silk J., 1986, *ApJ*, 303, 39
- Dietrich M., Hamann F., 2004, *ApJ*, 611, 761
- Dijkstra M., Wyithe J. S. B., Haiman Z., 2007, MNRAS, 379, 253
- Dolgov A. D., 2002, *Phys. Rep.*, 370, 333
- Dove J. B., Shull J. M., Ferrara A., 2000, *ApJ*, 531, 846

- Durrer R., 2008, *The Cosmic Microwave Background*. Cambridge University Press
- Efstathiou G., 2002, *MNRAS*, 332, 193
- Efstathiou G., Bond J. R., 1999, *MNRAS*, 304, 75
- Efstathiou G., Frenk C. S., White S. D. M., Davis M., 1988, *MNRAS*, 235, 715
- Eisenstein D. J., Hu W., 1998, *ApJ*, 496, 605
- Eisenstein D. J., Hu W., 1999, *ApJ*, 511, 5
- Eisenstein D. J., Hu W., Tegmark M., 1999, *ApJ*, 518, 2
- Elgarøy Ø., Lahav O., 2005, *New Journal of Physics*, 7, 61
- Evoli C., Pandolfi S., Ferrara A., 2012, *ArXiv e-prints*
- Fakhouri O., Ma C.-P., 2008, *MNRAS*, 386, 577
- Fakhouri O., Ma C.-P., Boylan-Kolchin M., 2010, *MNRAS*, 406, 2267
- Fan X., 2012, *Research in Astronomy and Astrophysics*, 12, 865
- Fan X., Carilli C. L., Keating B., 2006, *ARA&A*, 44, 415
- Fan X., Narayanan V. K., Strauss M. A., White R. L., Becker R. H., Pentericci L., Rix H.-W., 2002, *AJ*, 123, 1247
- Fan X., Strauss M. A., Becker R. H., White R. L., Gunn J. E., Knapp G. R., Richards G. T., Schneider D. P., Brinkmann J., Fukugita M., 2006, *AJ*, 132, 117
- Fan X.-H., et al., 2006, *Astron.J.*, 131, 1203
- Fang L.-Z., Bi H., Xiang S., Boerner G., 1993, *ApJ*, 413, 477
- Faucher-Giguère C.-A., Lidz A., Hernquist L., Zaldarriaga M., 2008, *ApJ*, 688, 85
- Feeney S. M., Peiris H. V., Verde L., 2013, *JCAP*, 4, 36
- Fernandez E. R., Shull J. M., 2011, *ApJ*, 731, 20
- Fernández-Soto A., Lanzetta K. M., Chen H.-W., 2003, *MNRAS*, 342, 1215
- Fogli G. L., Lisi E., Marrone A., Palazzo A., 2006, *Progress in Particle and Nuclear Physics*, 57, 742
- Freedman W., et al., 2001, *Astrophys.J.*, 553, 47

- Freedman W. L., Madore B. F., Scowcroft V., Burns C., Monson A., Persson S. E., Seibert M., Rigby J., 2012, *ApJ*, 758, 24
- Fukugita M., Ichikawa K., Kawasaki M., Lahav O., 2006, *Phys. Rev. D*, 74, 027302
- Fukugita M., Kawasaki M., 1994, *MNRAS*, 269, 563
- Furlanetto S. R., Oh S. P., Briggs F. H., 2006, *Phys. Rep.*, 433, 181
- Gallerani S., Choudhury T. R., Ferrara A., 2006, *MNRAS*, 370, 1401
- Gallerani S., Ferrara A., Fan X., Choudhury T. R., 2008, *MNRAS*, 386, 359
- Gallerani S., Salvaterra R., Ferrara A., Choudhury T. R., 2008, *MNRAS*, 388, L84
- Galli S., Martinelli M., Melchiorri A., Pagano L., Sherwin B. D., Spergel D. N., 2010, *Phys. Rev. D*, 82, 123504
- Ghosh A., Bharadwaj S., Ali S. S., Chengalur J. N., 2010, *ArXiv e-prints*
- Ghosh A., Bharadwaj S., Saiyad Ali S., Chengalur J. N., 2011, *ArXiv e-prints*
- Giallongo E., Cristiani S., D'Odorico S., Fontana A., 2002, *ApJL*, 568, L9
- Giocoli C., Moreno J., Sheth R. K., Tormen G., 2007, *MNRAS*, 376, 977
- Gnedin N. Y., 2000, *ApJ*, 535, 530
- Gnedin N. Y., 2008, *ApJL*, 673, L1
- Gnedin N. Y., Ferrara A., Zweibel E. G., 2000, *ApJ*, 539, 505
- Gnedin N. Y., Hui L., 1998, *MNRAS*, 296, 44
- Gnedin N. Y., Kravtsov A. V., Chen H.-W., 2008, *ApJ*, 672, 765
- Gnedin N. Y., Ostriker J. P., 1997, *ApJ*, 486, 581
- Gratton S., Lewis A., Efstathiou G., 2008, *Phys. Rev. D*, 77, 083507
- Guha Sarkar T., 2010, *Journal of Cosmology and Astro-Particle Physics*, 2, 2
- Guha Sarkar T., Bharadwaj S., Choudhury T. R., Datta K. K., 2011, *MNRAS*, 410, 1130
- Guha Sarkar T., Datta K. K., Bharadwaj S., 2009, *Journal of Cosmology and Astro-Particle Physics*, 8, 19
- Guha Sarkar T., Mitra S., Majumdar S., Choudhury T. R., 2012, *MNRAS*, 421, 3570

- Gunn J. E., Gott III J. R., 1972, *ApJ*, 176, 1
- Gunn J. E., Peterson B. A., 1965a, *ApJ*, 142, 1633
- Gunn J. E., Peterson B. A., 1965b, *ApJ*, 142, 1633
- Haardt F., Madau P., 2011, arXiv:1103.5226
- Haehnelt M. G., Steinmetz M., Rauch M., 2000, *ApJ*, 534, 594
- Haiman Z., Loeb A., 1997, *ApJ*, 483, 21
- Haiman Z., Rees M. J., Loeb A., 1997, *ApJ*, 476, 458
- Hannestad S., 2003, *Phys. Rev. D*, 67, 085017
- Hannestad S., 2004, *New Journal of Physics*, 6, 108
- Hannestad S., 2006, *Annual Review of Nuclear and Particle Science*, 56, 137
- Hannestad S., 2010, ArXiv e-prints
- Harrison E. R., 1970, *Phys. Rev. D*, 1, 2726
- Hatcher L., 1994, *A Step-By-Step Approach to Using SAS for Factor Analysis and Structural Equation Modeling*. Cary, NC: SAS Institute Inc.
- Heckman T. M., Sembach K. R., Meurer G. R., Leitherer C., Calzetti D., Martin C. L., 2001, *ApJ*, 558, 56
- Henry A. L., et al., 2009, *ApJ*, 697, 1128
- Hinshaw G., et al., 2012
- Hockney R. W., Eastwood J. W., 1988, *Computer simulation using particles*
- Hopkins P. F., Richards G. T., Hernquist L., 2007, *ApJ*, 654, 731
- Hoyle F., 1953, *ApJ*, 118, 513
- Hu W., Eisenstein D. J., Tegmark M., 1998, *Physical Review Letters*, 80, 5255
- Hu W., Holder G. P., 2003, *Phys. Rev. D*, 68, 023001
- Huterer D., Cooray A., 2005, *Phys. Rev. D*, 71, 023506
- Huterer D., Starkman G., 2003, *Physical Review Letters*, 90, 031301
- Ichikawa K., Fukugita M., Kawasaki M., 2005, *Phys. Rev. D*, 71, 043001

- Iliev I. T., Mellema G., Pen U.-L., Merz H., Shapiro P. R., Alvarez M. A., 2006, MNRAS, 369, 1625
- Iliev I. T., Shapiro P. R., McDonald P., Mellema G., Pen U.-L., 2008, MNRAS, 391, 63
- Inoue A. K., Iwata I., Deharveng J.-M., Buat V., Burgarella D., 2005, A&A, 435, 471
- Iye M., et al., 2006, Nature, 443, 186
- Jarosik N., et al., 2011, Astrophys.J.Suppl., 192, 14
- Jenkins A., Frenk C. S., White S. D. M., Colberg J. M., Cole S., Evrard A. E., Couchman H. M. P., Yoshida N., 2001, MNRAS, 321, 372
- Jose C., Samui S., Subramanian K., Srianand R., 2011, Phys. Rev. D, 83, 123518
- Joudaki S., 2013, Phys. Rev. D, 87, 083523
- Kadota K., Dodelson S., Hu W., Stewart E. D., 2005, Phys. Rev. D, 72, 023510
- Kashikawa N., et al., 2006, ApJ, 648, 7
- Kauffmann G., Colberg J. M., Diaferio A., White S. D. M., 1999, MNRAS, 303, 188
- Kauffmann G., White S. D. M., Guiderdoni B., 1993, MNRAS, 264, 201
- Kay S. T., 2004, MNRAS, 347, L13
- Khandai N., Bagla J. S., 2009, Research in Astronomy and Astrophysics, 9, 861
- Kitayama T., Suto Y., 1996, MNRAS, 280, 638
- Klypin A. A., Shandarin S. F., 1983, MNRAS, 204, 891
- Kolb E. W., Turner M. S., 1990, The early universe.
- Komatsu E., Dunkley J., Nolte M. R., et al., 2009, ApJS, 180, 330
- Komatsu E., et al., 2011, Astrophys.J.Suppl., 192, 18
- Kuhlen M., Faucher-Giguère C.-A., 2012, MNRAS, 423, 862
- Kulkarni G., Choudhury T. R., 2011, MNRAS, 412, 2781
- Lacey C., Cole S., 1993, MNRAS, 262, 627
- Lacey C., Cole S., 1994, MNRAS, 271, 676
- Lamb D. Q., Reichart D. E., 2000, ApJ, 536, 1

- Lanzetta K. M., Wolfe A. M., Turnshek D. A., 1995, *ApJ*, 440, 435
- Larson D., et al., 2011, *Astrophys.J.Suppl.*, 192, 16
- Larson R. B., 2000, in Favata F., Kaas A., Wilson A., eds, *Star Formation from the Small to the Large Scale Vol. 445 of ESA Special Publication, The Formation of the First Stars*. p. 13
- Leach S., 2006, *MNRAS*, 372, 646
- Lehnert M. D., et al., 2010, *Nature*, 467, 940
- Leitherer C., Ferguson H. C., Heckman T. M., Lowenthal J. D., 1995, *ApJL*, 454, L19
- Lesgourgues J., Pastor S., 2006, *Phys. Rep.*, 429, 307
- Lewis A., 2005, *Phys. Rev. D*, 71, 083008
- Lewis A., Bridle S., 2002, *Phys. Rev. D*, 66, 103511
- Lewis A., Challinor A., Lasenby A., 2000, *ApJ*, 538, 473
- Liddle A. R., 2007, *MNRAS*, 377, L74
- Linder E. V., Jenkins A., 2003, *MNRAS*, 346, 573
- Loeb A., 2006, *ArXiv Astrophysics e-prints*
- Loeb A., Barkana R., 2001, *ARA&A*, 39, 19
- Loeb A., Wyithe J. S. B., 2008, *Physical Review Letters*, 100, 161301
- Loeb A., Zaldarriaga M., 2004, *Physical Review Letters*, 92, 211301
- Lukić Z., Heitmann K., Habib S., Bashinsky S., Ricker P. M., 2007, *ApJ*, 671, 1160
- Macciò A. V., Quercellini C., Mainini R., Amendola L., Bonometto S. A., 2004, *Phys. Rev. D*, 69, 123516
- Mack K. J., Wyithe J. S. B., 2012, *MNRAS*, 425, 2988
- Madau P., Ferrara A., Rees M. J., 2001, *ApJ*, 555, 92
- Madau P., Haardt F., Rees M. J., 1999, *ApJ*, 514, 648
- Madau P., Meiksin A., Rees M. J., 1997, *ApJ*, 475, 429
- Maltoni M., Schwetz T., Tórtola M., Valle J. W. F., 2004, *New Journal of Physics*, 6, 122
- Mao Y., Tegmark M., McQuinn M., Zaldarriaga M., Zahn O., 2008, *Phys. Rev. D*, 78, 023529

- Mapelli M., Ferrara A., 2005, *MNRAS*, 364, 2
- Marín F. A., Gnedin N. Y., Seo H.-J., Vallinotto A., 2010, *ApJ*, 718, 972
- Maselli A., Ferrara A., Ciardi B., 2003, *MNRAS*, 345, 379
- McDonald P., Miralda-Escudé J., Rauch M., Sargent W. L. W., Barlow T. A., Cen R., 2001, *ApJ*, 562, 52
- McLure R. J., Dunlop J. S., Cirasuolo M., Koekemoer A. M., Sabbi E., Stark D. P., Targett T. A., Ellis R. S., 2010, *MNRAS*, 403, 960
- McQuinn M., Zahn O., Zaldarriaga M., Hernquist L., Furlanetto S. R., 2006, *ApJ*, 653, 815
- Merz H., Pen U.-L., Trac H., 2005, *New Astron.*, 10, 393
- Miller R. H., 1983, *ApJ*, 270, 390
- Miralda-Escudé J., Haehnelt M., Rees M. J., 2000, *ApJ*, 530, 1
- Mitra S., Choudhury T. R., Ferrara A., 2011, *MNRAS*, 413, 1569
- Mitra S., Choudhury T. R., Ferrara A., 2012, *MNRAS*, 419, 1480
- Mitra S., Ferrara A., Choudhury T. R., 2013, *MNRAS*, 428, L1
- Mitra S., Kulkarni G., Bagla J. S., Yadav J. K., 2011, *Bulletin of the Astronomical Society of India*, 39, 563
- Mo H. J., White S. D. M., 1996, *MNRAS*, 282, 347
- Moreno J., Giocoli C., Sheth R. K., 2008, *MNRAS*, 391, 1729
- Moreno J., Giocoli C., Sheth R. K., 2009, *MNRAS*, 397, 299
- Mortonson M. J., Hu W., 2008a, *ApJ*, 672, 737
- Mortonson M. J., Hu W., 2008b, *ApJL*, 686, L53
- Munshi D., Kilbinger M., 2006, *A&A*, 452, 63
- Nakamura F., Umemura M., 2001, *ApJ*, 548, 19
- Natarajan A., 2012, *Phys. Rev. D*, 85, 083517
- Navarro J. F., Frenk C. S., White S. D. M., 1995, *MNRAS*, 275, 720
- Neistein E., Dekel A., 2008, *MNRAS*, 388, 1792

- Neistein E., Macciò A. V., Dekel A., 2010, *MNRAS*, 403, 984
- Oesch P. A., et al., 2010, *ApJL*, 709, L16
- Oesch P. A., et al., 2012, *ApJ*, 745, 110
- Oke J. B., Gunn J. E., 1983, *ApJ*, 266, 713
- Ota K., et al., 2008, *ApJ*, 677, 12
- Oyama Y., Shimizu A., Kohri K., 2012, *ArXiv e-prints*
- Padmanabhan T., 1993, *Structure Formation in the Universe*
- Padmanabhan T., 2002, *Theoretical Astrophysics - Volume 3, Galaxies and Cosmology*
- Page L., Hinshaw G., Komatsu E., et al., 2007, *ApJS*, 170, 335
- Pandolfi S., Cooray A., Giusarma E., Kolb E. W., Melchiorri A., Mena O., Serra P., 2010, *Phys. Rev. D*, 81, 123509
- Pandolfi S., Ferrara A., Choudhury T. R., Melchiorri A., Mitra S., 2011, *Phys. Rev. D*, 84, 123522
- Pandolfi S., Giusarma E., Kolb E. W., Lattanzi M., Melchiorri A., Mena O., Peña M., Cooray A., Serra P., 2010, *Phys. Rev. D*, 82, 123527
- Partridge R. B., 1995, *3K: The Cosmic Microwave Background Radiation*
- Peacock J. A., 1999, *Cosmological Physics*
- Peebles P. J. E., 1980, *The large-scale structure of the universe*
- Peebles P. J. E., 1993, *Principles of Physical Cosmology*
- Pentericci L., et al., 2002, *Astron.J.*, 123, 2151
- Percival W., Miller L., 1999, *MNRAS*, 309, 823
- Percival W. J., 2001, *MNRAS*, 327, 1313
- Percival W. J., et al., 2010, *Mon.Not.Roy.Astron.Soc.*, 401, 2148
- Percival W. J., Miller L., Peacock J. A., 2000, *MNRAS*, 318, 273
- Perotto L., Lesgourgues J., Hannestad S., Tu H., Y Y Wong Y., 2006, *JCAP*, 10, 13
- Péroux C., McMahon R. G., Storrìe-Lombardi L. J., Irwin M. J., 2003, *MNRAS*, 346, 1103

- Pontzen A., Governato F., Pettini M., Booth C. M., Stinson G., Wadsley J., Brooks A., Quinn T., Haehnelt M., 2008, *MNRAS*, 390, 1349
- Porciani C., Matarrese S., Lucchin F., Catelan P., 1998, *MNRAS*, 298, 1097
- Press W. H., Schechter P., 1974, *ApJ*, 187, 425
- Press W. H., Teukolsky S. A., Vetterling W. T., Flannery B. P., 1992, *Numerical recipes in FORTRAN. The art of scientific computing*
- Pritchard J. R., Loeb A., 2010, *Phys. Rev. D*, 82, 023006
- Pritchard J. R., Loeb A., 2012, *Reports on Progress in Physics*, 75, 086901
- Pritchard J. R., Loeb A., Wyithe J. S. B., 2010, *MNRAS*, 408, 57
- Pritchard J. R., Pierpaoli E., 2008, *Phys. Rev. D*, 78, 065009
- Pritchard J. R., Pierpaoli E., 2009, *Nuclear Physics B Proceedings Supplements*, 188, 31
- Purcell E. M., Field G. B., 1956, *ApJ*, 124, 542
- Rao S. M., Turnshek D. A., 2000, *The Astrophysical Journal Supplement*, 130, 1
- Razoumov A. O., Norman M. L., Abel T., Scott D., 2002, *ApJ*, 572, 695
- Razoumov A. O., Sommer-Larsen J., 2006, *ApJL*, 651, L89
- Razoumov A. O., Sommer-Larsen J., 2010, *ApJ*, 710, 1239
- Reed D., Gardner J., Quinn T., Stadel J., Fardal M., Lake G., Governato F., 2003, *MNRAS*, 346, 565
- Reed D. S., Bower R., Frenk C. S., Jenkins A., Theuns T., 2007, *MNRAS*, 374, 2
- Rees M. J., Ostriker J. P., 1977, *MNRAS*, 179, 541
- Ricotti M., Gnedin N. Y., Shull J. M., 2000, *ApJ*, 534, 41
- Riemer-Sørensen S., Parkinson D., Davis T. M., 2013, *PASA*, 30, 29
- Riess A. G., et al., 2009, *Astrophys.J.*, 699, 539
- Riess A. G., Macri L., Casertano S., Lampeitl H., Ferguson H. C., et al., 2011, *Astrophys.J.*, 730, 119
- Ripamonti E., 2007, *MNRAS*, 376, 709

- Sachs R. K., Wolfe A. M., 1967, *ApJ*, 147, 73
- Saini T. D., Bharadwaj S., Sethi S. K., 2001, *ApJ*, 557, 421
- Salvaterra R., et al., 2009, *Nature*, 461, 1258
- Samui S., Srianand R., Subramanian K., 2007, *MNRAS*, 377, 285
- Samui S., Subramanian K., Srianand R., 2009
- Sandage A., Tammann G. A., Saha A., Reindl B., Macchetto F. D., Panagia N., 2006, *ApJ*, 653, 843
- Santos M. G., Cooray A., Knox L., 2005, *ApJ*, 625, 575
- Sasaki S., 1994, *Pub. Astron. Soc. Japan*, 46, 427
- Schaye J., Theuns T., Rauch M., Efstathiou G., Sargent W. L. W., 2000, *MNRAS*, 318, 817
- Schlegel D., White M., Eisenstein D., 2009, in *astro2010: The Astronomy and Astrophysics Decadal Survey Vol. 2010 of Astronomy, The Baryon Oscillation Spectroscopic Survey: Precision measurement of the absolute cosmic distance scale.* p. 314
- Schneider R., Salvaterra R., Ferrara A., Ciardi B., 2006, *MNRAS*, 369, 825
- Seager S., Sasselov D. D., Scott D., 1999, *ApJL*, 523, L1
- Seager S., Sasselov D. D., Scott D., 2000, *ApJS*, 128, 407
- Sekiguchi T., Ichikawa K., Takahashi T., Greenhill L., 2010, *JCAP*, 3, 15
- Seljak U., et al., 2005, *Phys.Rev.*, D71, 103515
- Seljak U., Slosar A., McDonald P., 2006, *JCAP*, 10, 14
- Shandarin S. F., Zeldovich Y. B., 1989, *Reviews of Modern Physics*, 61, 185
- Shapiro P. R., Giroux M. L., 1987, *ApJL*, 321, L107
- Shapley A. E., Steidel C. C., Pettini M., Adelberger K. L., Erb D. K., 2006, *ApJ*, 651, 688
- Sheth R. K., Mo H. J., Tormen G., 2001, *MNRAS*, 323, 1
- Sheth R. K., Tormen G., 1999, *MNRAS*, 308, 119
- Sheth R. K., Tormen G., 2002, *MNRAS*, 329, 61
- Silk J., 1977, *ApJ*, 211, 638

- Slatyer T. R., Padmanabhan N., Finkbeiner D. P., 2009, *Phys. Rev. D*, 80, 043526
- Songaila A., Cowie L. L., 2010, *ApJ*, 721, 1448
- Spergel D., et al., 2003, *Astrophys.J.Suppl.*, 148, 175
- Srbínovsky J. A., Wyithe J. S. B., 2010, *PASA*, 27, 110
- Storrie-Lombardi L. J., McMahon R. G., Irwin M. J., 1996, *MNRAS*, 283, L79
- Sunyaev R. A., Zeldovich Y. B., 1972, *Comments on Astrophysics and Space Physics*, 4, 173
- Taniguchi Y., et al., 2005, *Pub. Astron. Soc. Japan*, 57, 165
- Tanvir N. R., et al., 2009, *Nature*, 461, 1254
- Taylor J. R., 1997, *An Introduction to Error Analysis: The Study of Uncertainties in Physical Measurements*. University Science Books, 1997, 2nd ed., 327 pages
- Tegmark M., 2005, *Physica Scripta Volume T*, 121, 153
- The Planck Collaboration 2006, arXiv:astro-ph/0604069
- Thoul A. A., Weinberg D. H., 1996, *ApJ*, 465, 608
- Tinker J., Kravtsov A. V., Klypin A., Abazajian K., Warren M., Yepes G., Gottlöber S., Holz D. E., 2008, *ApJ*, 688, 709
- Totani T., Kawai N., Kosugi G., Aoki K., Yamada T., Iye M., Ohta K., Hattori T., 2006, *Pub. Astron. Soc. Japan*, 58, 485
- Trimble V., 1987, *ARA&A*, 25, 425
- Vanzella E., et al., 2010, *ApJ*, 725, 1011
- Vanzella E., et al., 2011, *ApJL*, 730, L35
- Visbal E., Loeb A., Wyithe S., 2009, *Journal of Cosmology and Astro-Particle Physics*, 10, 30
- Warren M. S., Abazajian K., Holz D. E., Teodoro L., 2006, *ApJ*, 646, 881
- Wasserman L., Miller C. J., Nichol R. C., Genovese C., Jang W., Connolly A. J., Moore A. W., Schneider J., the PICA group 2001, ArXiv Astrophysics e-prints
- Weinberg S., 1972, *Gravitation and Cosmology: Principles and Applications of the General Theory of Relativity*
- Weinberg S., 2008, *Cosmology*. Oxford University Press

- White M., 2002, *ApJS*, 143, 241
- White R. L., Becker R. H., Fan X., Strauss M. A., 2003, *AJ*, 126, 1
- White S. D. M., Frenk C. S., 1991, *ApJ*, 379, 52
- Williams B. G., Heavens A. F., Peacock J. A., Shandarin S. F., 1991, *MNRAS*, 250, 458
- Wolfe A. M., Gawiser E., Prochaska J. X., 2005, *Annual Review of Astronomy & Astrophysics*, 43, 861
- Wong W. Y., Moss A., Scott D., 2008, *MNRAS*, 386, 1023
- Wood K., Loeb A., 2000, *ApJ*, 545, 86
- Wouthuysen S. A., 1952, *ApJ*, 57, 31
- Wyithe J. S. B., Loeb A., 2003, *ApJ*, 586, 693
- Wyithe J. S. B., Loeb A., 2005, *ApJ*, 625, 1
- Wyithe J. S. B., Loeb A., 2007a, *MNRAS*, 375, 1034
- Wyithe S., Brown M. J. I., 2009, *ArXiv e-prints*
- Wyithe S., Loeb A., 2007b, *arXiv:0708.3392*
- Wyithe S., Loeb A., 2008, *ArXiv e-prints*
- Wyithe S., Loeb A., Geil P., 2007, *ArXiv e-prints*
- Yajima H., Choi J.-H., Nagamine K., 2011, *MNRAS*, 412, 411
- Zaldarriaga M., Hui L., Tegmark M., 2001, *ApJ*, 557, 519
- Zeldovich Y. B., 1972, *MNRAS*, 160, 1P
- Zentner A. R., 2007, *International Journal of Modern Physics D*, 16, 763
- Zhao G.-B., Saito S., Percival W. J., Ross A. J., Montesano F., et al., 2012